Low Load Operation of Turbine-Driven Boiler Feed Pumps

University of Cape Town

Prepared by:

John Shaun Clark

CLRJOH015

Department of Mechanical Engineering

University of Cape Town

Supervisor:

A/Prof. Wim Fuls

September 2019

Submitted to the Department of Mechanical Engineering at the University of Cape Town in partial fulfilment of the academic requirements for a Master of Science degree in Mechanical Engineering

Key Words: turbine, nozzle model, power generation, *Flownex*, boiler feed pump turbine, low load operation, Eskom

The copyright of this thesis vests in the author. No quotation from it or information derived from it is to be published without full acknowledgement of the source. The thesis is to be used for private study or non-commercial research purposes only.

Published by the University of Cape Town (UCT) in terms of the non-exclusive license granted to UCT by the author.

University of Cape Town

Abstract

Boiler feed pump turbines (BFPTs) are in use at a number of Eskom power stations. They utilise bled steam extracted from the main turbine in order to drive multistage centrifugal pumps which supply the boilers with feedwater. With an increase of renewables in the energy mix, the need for Eskom's coal-fired power stations to run for extended periods at very low loads has arguably never been this great. Various systems affect the ability of these generation units to run economically at low loads. One such system is the boiler feed pump turbine and its associated pumps.

A station was selected from Eskom's fleet based on access to information and the station being a relatively typical plant. The Unit (a boiler and turbogenerator set) selected for study was one with the most thorough instrumentation available for remote monitoring. The BFPT system of this Unit was modelled in *Flownex,* a one-dimensional thermofluid process modelling package. The model included individual pump stages, steam admission valves and a stage-by-stage turbine model utilising custom stage components. These turbine stage components represent each stage with nozzles and other standard *Flownex* components. The boundary conditions of the system were set as functions of generator load in order to represent typical values for use in case studies. The relationships between load and boundary conditions were based on large samples of data from the station's data capture system (DCS). A corresponding standby electric feed pump system was also modelled in *Flownex* for a comparative case study.

After model validation, a number of case studies were performed, demonstrating the functionality of the model and also providing specific results of value to the station in question. These results include the minimum generator load possible with different steam supplies; maximum condenser back pressure before plant availability is affected; the viability of changing the pump leak-off philosophy; and the effect of electric feed pump use on power consumption.

The main recommendations from the case studies were as follows:

i. to stroke the steam admission valves as per the design charts,
ii. to test the operation of the BFPT down to 40 % generator load,
iii. to keep the pump leak-off philosophy unchanged,
iv. to maintain the cooling water system and condensers sufficiently to avoid poor condenser vacuum,
v. to reconsider the decommissioning of the "cold reheat" steam supply,
vi. and, to favour use of the BFPT over the electric feed pumps at all generator loads.

Declaration

I, John Shaun Clark, hereby declare the work contained in this dissertation to be my own. All information which has been gained from various journal articles, text books or other sources has been referenced accordingly. I have not allowed, and will not allow, anyone to copy my work with the intention of passing it off as their own work or part thereof.

Signed by candidate

16/09/2019

John Shaun Clark

Date

Acknowledgements

The following individuals are gratefully acknowledged for their support.

General

- A/Prof. Wim Fuls – UCT academic supervisor and EPPEI lecturer
- Willem van der Westhuizen – Eskom industrial mentor and EPPEI lecturer
- Gary de Klerk – Eskom industrial mentor
- Wilson Kudiwa – Eskom line manager
- Prof. Pieter Rousseau –EPPEI lecturer
- Franz Woell – EPPEI lecturer
- Priyesh Gosai – EPPEI research manager

Low Load Tests

- Fulufhelo Makananise and Thabo Papo from Eskom Research, Testing and Development
- Merrill Quintrell from the Electric Power Research Institute (EPRI)
- Eric ten Siethoff and Amanda Card from MPR Associates (supporting EPRI)
- Ntombifuthi Ngcobo and Brenda Moeng – process engineering managers on site

Site Support

- Nicole Seumangal
- Muvhuso Ravele
- Tony Cattaert
- Nsizwa Mabena
- Johan Möller
- Daniel van Tonder
- Conrad Henning
- Lonke Nkunjana
- Nazier Allie

Fellow postgraduate students in the EPPEI *Energy Efficiency* specialisation centre and the *Applied Thermofluid Process Modelling* (ATProM) research group are gratefully acknowledged for their support.

Table of Contents

List of Figures vi
List of Tables xii
List of Nomenclature xiii
1. Introduction 1
1.1 Problem Statement 1
1.2 Objectives 1
1.3 Scope of this Study 2
1.4 Overall Report Structure 3
2. Theory and Literature Review 4
2.1 Eskom Literature and Site Observations 4
2.2 Centrifugal Pump Theory 24
2.3 Turbine Theory 34
2.4 Miscellaneous Considerations 65
3. Model Development 66
3.1 Visual Observations from Sites of Interest 66
3.2 Piping and Instrumentation Diagram / Process Diagram 71
3.3 Development of the Pump Curves 72
3.4 Heat Balance Diagram Summaries and Data Capture System Data 75
3.5 Turbine Drawings for Dimensional Considerations 78
3.6 Method to Determine Mass Flow Rate and Exhaust Enthalpy 81
3.7 Turbine Nozzle Throat Area Estimates 87
3.8 Turbine Nozzle Model Tuning in *Flownex* 90
3.9 Turbine Model Validation 95
3.10 High Level Turbine Representation 97
3.11 Steam Admission Valves 99
3.12 Reheat Attemperator Spraywater 107
3.13 Leak-Off Valves 108
3.14 BFPT Integrated Model 113
3.15 Model of Electric Feed Pump Train 115

4. Case Studies 123
4.1 Case Study 1: Effect of Steam Admission Valve Stroking, including the Presence of Cold Reheat Supply 123
4.2 Case Study 2: Effect of Changing Condenser Vacuum 130
4.3 Case Study 3: Effect of Changing the Leak-Off Valve Control Philosophy 136
4.4 Case Study 4: Electric Feed Pumps 137
4.5 Case Study 5: Blade Temperatures 139
5. Conclusions and Recommendations 141
5.1 Conclusion on Minimum Generation and Steam Supplies 141
5.2 Conclusion on Condenser Vacuum 141
5.3 Conclusion on Leak-Off Valves 142
5.4 Recommendations from Case Studies 142
5.5 Comments Concerning Use of the Model 143
5.6 Concluding Remarks 144
6. List of References 145
6.1 Document References 145
6.2 Image References 146
7. List of Appendices 149
Appendix A. Extract from Script for Boundary Conditions 150
Appendix B. Extract from Scripts for Steam Admission Valves 152
Appendix C. Equations for Signal Oil Pressures 154
Appendix D. Data from Heat Balance Diagrams for Station A1 155
Appendix E. Data from Heat Balance Diagrams for Station B1 157
Appendix F. Considerations of Optimum Turbine Blade Efficiency 159
Appendix G. Orifice Plate Theory and Modelling of Leak-Off Valves 167
Appendix H. Boundary Conditions – Pump Discharge Pressure 172
Appendix I. Flow Resistance Component – Linear Characteristic 175
Appendix J. Fleet Overview 177
Appendix K. Relevant AKZ Signals for Station A1 179
Appendix L. Lists of Reference Drawings 182
Appendix M. General *Flownex* and *Mathcad* Notes 183

List of Figures

Figure 2.1: Venn diagram illustrating selection of stations for this study 5

Figure 2.2: Drawing of Station A1/A2 BFPT (Eskom Station manuals, edited) 6

Figure 2.3: Diagram illustrating the BFPT steam control system at Station A1 (Eskom Station Manuals, edited) 7

Figure 2.4: Diagram illustrating the set pressures for the BFPT steam control system at Station A1 (Eskom station manuals, edited) 8

Figure 2.5: Siemens steam turbine SST-600 (Siemens AG, 2004) 10

Figure 2.6: Diagram illustrating the configuration of the BFPT at Station B1 11

Figure 2.7: Station B1 operational limits (station manuals, annotated) 11

Figure 2.8: Diagram illustrating a Voith variable speed coupling (Voith, 2017) 15

Figure 2.9: Diagram illustrating a Voith Vorecon variable speed coupling (UTK-EBPO, 2017, annotated) 15

Figure 2.10: Diagram of main steps in EPRI low load flexibility tests at Eskom (EPRI, 2017) 19

Figure 2.11: Operating snapshot from control room of BFPT at Station B1 20

Figure 2.12: Typical layout of a drum-type boiler (Rousseau and Fuls, 2017a, annotated) 21

Figure 2.13: Typical layout of a once-through boiler (Rousseau and Fuls, 2017b, annotated) 22

Figure 2.14: Boiler recirculation system at Station A1 (annotated mimic of operator control system interface) 23

Figure 2.15: Diagram summarising the different Unit control philosophies 23

Figure 2.16: Typical temperature rise in a pump at low flow (Sulzer, 2010) 27

Figure 2.17: Minimum flow rate guidelines for pumps exceeding 1 MW power input (Sulzer, 2010, annotated) 28

Figure 2.18: OEM-defined leak-off curve for Station A1 29

Figure 2.19: Diagram of a typical "Zikesch" throttle disc stack (station manuals) 30

Figure 2.20: Torque-speed curve for an induction motor showing three modes of operation (Wildi, 2006) 32

Figure 2.21: Typical power factor curve for an induction motor (Faizan, A., n.d.) 33

Figure 2.22: Typical turbine rotating blade and velocity triangles: impulse type (left), and 50% reaction type (right) 35

Figure 2.23: Different scenarios for the absolute exit velocities from a rotating blade 36

Figure 2.24: Repeating stages in a reaction turbine 36

Figure 2.25: Typical reaction ratios for steam turbines on coal-fired power stations (Cotton, 1998a) 38

Figure 2.26: Typical reaction ratios for steam turbines on nuclear power stations (Cotton, 1998b) 38

Figure 2.27: Excerpt from the turbine nozzle analogy paper. (a) Mollier diagram of the expansion process. (b) Velocity triangles. (c) Moving nozzle analogy. (Fuls, 2017a) 39

Figure 2.28: Mollier diagram for stator nozzle (Fuls, 2017a, annotated) 40

Figure 2.29: Mollier diagram for rotor nozzle (Fuls, 2017a, annotated) 41

Figure 2.30: Mollier diagram for work extraction (Fuls, 2017a, annotated) 42

Figure 2.31: Mollier diagram for carry-over (Fuls, 2017a, annotated) 43

Figure 2.32: Effect of steam dryness on critical pressure ratio 45

Figure 2.33: Diagram of a typical Pelton wheel (Fundacja na rzecz Czystej Energii, 2018a) 46

Figure 2.34: Photograph of a typical Pelton wheel (Fundacja na rzecz Czystej Energii, 2018b) 47

Figure 2.35: A replica of Heron of Alexandria's steam turbine (Bentley, 2007) 47

Figure 2.36: Condensed typical velocity triangles 48

Figure 2.37: Illustration of the design of a typical impulse blade (Christie, 1920, p. 615) 49

Figure 2.38: Illustration of the design of a typical reaction blade (Christie, 1920, p. 620) 50

Figure 2.39: Illustration of the design of a typical full-wing reaction blade (Christie, 1920, p. 621) 50

Figure 2.40: Diagram contrasting impulse and reaction turbines (Emoscopes, 2006) 51

Figure 2.41: Effect of changing reaction ratio on rotating blade angles 52

Figure 2.42: Typical turbine rotating blade and velocity triangles: impulse type (left), and 50% reaction type (right) 53

Figure 2.43: Illustration of turbine isentropic efficiency (Senanayake, 2016) 54

Figure 2.44: Stage losses in a typical impulse steam turbine (Frolov, n.d.) 55

Figure 2.45: Impulse stage custom Flownex component 57

Figure 2.46: Reaction stage custom Flownex component 57

Figure 2.47: Diagram summarising the methodology employed for the initial estimates of nozzle throat areas 58

Figure 2.48: Diagram summarising the methodology employed for the initial estimates of nozzle throat areas, with numbered points 61

Figure 2.49: Illustration of Stodola ellipse law (modified from Zajaczkowski, 2011) 64

Figure 3.1: A selection of photos of typical Eskom boiler feed pumps 66

Figure 3.2: Annotated photograph showing the feed pump configuration at Station A1 67

Figure 3.3: Last stage stationary row from Station A1 68

Figure 3.4: Photograph showing the BFPT rotor in-situ at Station B1 68

Figure 3.5: Annotated photograph showing the BFPT rotor blades at Station B1 (the numbers indicate the stages) 68

Figure 3.6: Rotating blades from Station A1 69

Figure 3.7: Approximate blade profile at tip of Stage 7 rotating blades at Station A1 70

Figure 3.8: Diagram of BFPT rotor from Station A1 (Eskom Station Manuals) 70

Figure 3.9: Consolidated diagram of BFPT / SFP system instrumentation for Station A1 71

Figure 3.10: Consolidated diagram of EFP system instrumentation for Station A1 71

Figure 3.11: Example of pump curve image used for digitisation 72

Figure 3.12: Station A1 pump curves as imported into Flownex 73

Figure 3.13: Confirmation of validity of OEM pump curves 74

Figure 3.14: Example of boundary condition projections from DCS values – IP bled steam pressure vs load 76

Figure 3.15: Example of boundary condition projections from DCS values – IP bled steam pressure vs load, low load tests 76

Figure 3.16: Naming convention for boundary conditions 77

Figure 3.17: Example of boundary condition projections from DCS values – condenser back-pressure vs load, demonstrating high variability due to sensitivity to ambient conditions 77

Figure 3.18: Feed pump discharge pressure vs generator load 78

Figure 3.19: Station A1 diagram for estimation of turbine blade diameters 79

Figure 3.20: Station B1 diagram for estimation of turbine blade diameters 79

Figure 3.21: Graph showing effect of relative blade length on mean diameter 80

Figure 3.22: Heat balance isentropic efficiencies 84

Figure 3.23: Turbine isentropic efficiencies from DCS and HBD 85

Figure 3.24: Estimated average loss coefficient 85

Figure 3.25: Layout of Station A1 system with reference to gearbox 86

Figure 3.26: Station A1 system configuration, with measurement points highlighted for turbine model 87

Figure 3.27: Expected change in reaction ratio over the shaft length, based on Cotton (1998) 88

Figure 3.28: Selection of carry-over efficiencies 91

Figure 3.29: Proposed grouping of turbine stages 92

Figure 3.30: Turbine model with 95 % load conditions 92

Figure 3.31: Effect of different partial arc inlet pressures 94

Figure 3.32: Turbine model corrected for partial arc admission 94

Figure 3.33: Model snapshot showing validation of 62 % case 95

Figure 3.34: Visual representation of different methods of determining mass flow rate 97

Figure 3.35: High level representation of turbine (Station A1) 98

Figure 3.36: Station A1 - chart showing steam admission valve displacement vs signal oil pressure 99

Figure 3.37: Station A1 - pressure drop over steam admission valves vs load 100

Figure 3.38: Pressure drop over first stage of Station A1 - per partial arc 100

Figure 3.39: Typical emergency stop valve and governor valve pair for an HP turbine (Woell, 2016, modified) 102

Figure 3.40: Diagram of Station A1 steam admission valves 1 and 2 (annotated; original drawings from station manuals) 103

Figure 3.41: Graphical representation of steam admission valve stroking; “V1” to “V4” represent valves 1 to 4 based on the DCS values, CRH represents the cold reheat valve stroking according to design, and V1 to V4 “design” curves represent the stroking of valves 1 to 4 based on station manual values 105

Figure 3.42: Graphical representation of steam admission valve opening (A_o) values 106

Figure 3.43: DCS trends showing fluctuating spraywater mass flow rates 107

Figure 3.44: Reheat spraywater flow rates from heat balance diagrams 107

Figure 3.45: Required feedwater mass flow rate vs load 108

Figure 3.46: Station A1 leak-off trends for BFPT being placed in service 109

Figure 3.47: Graph illustrating Q vs Δp for Station A1 leak-off orifice plate 110

Figure 3.48: Pressure drop vs mass flow rate for Station A1 leak-off valve 111

Figure 3.49: Trends of Station A1 BFPT on leak-off during low-load tests 112

Figure 3.50: Turbine model coupled to other components 114

Figure 3.51: Pump curves used for EFPs (main pumps), graphically representing inputs to Flownex 115

Figure 3.52: Configuration of feed pump trains at Station A1 116

Figure 3.53: Electric feed pump configuration at Station A1 with key values shown 117

Figure 3.54: Flownex model for a single EFP train at Station A1 – full generator load scenario 118

Figure 3.55: Process diagram for EFP train with instrumentation points used to determine hydraulic coupling efficiency 119

Figure 3.56: Diagram illustrating a Voith variable speed coupling (Voith, 2017) 119

Figure 3.57: Slip vs scoop position on both EFPs at Station A1 120

Figure 3.58: Efficiency vs (hydraulic) slip on both EFPs at Station A1 121

Figure 3.59: Scoop position vs generator load on EFP B at Station A1 121

Figure 3.60: EFP model at 100 % generator load, both pumps in service 122

Figure 4.1: Graphical representation of signal oil pressure values with respect to load: DCS stroking with cold reheat supply 124

Figure 4.2: Snapshot of predicted minimum load of plant at present 125

Figure 4.3: Graphical representation of signal oil pressure values with respect to load: design stroking with cold reheat supply 126

Figure 4.4: Snapshot of model at 90 % with valve stroking according to DCS values, showing choking on Stage 1 126

Figure 4.5: Snapshot of model at 23.7 % with valve stroking according to DCS values 127

Figure 4.6: Graphical representation of signal oil pressure values with respect to load for different scenarios 128

Figure 4.7: T-s diagram contrasting 100 % and 25 % load conditions, design valve configuration 129

Figure 4.8: Exhaust enthalpy and required steam mass flow rate at 100 % generator load for different condenser back pressures 132

Figure 4.9: Stage-by-stage power distribution at different condenser back pressures 133

Figure 4.10: Illustration of reverse-powering on the final stage 133

Figure 4.11: Stage-by-stage power distribution at 47 kPa, signal oil pressure maximum, 100 % generator load boundary conditions 134

Figure 4.12: Inlet and exhaust enthalpies with required steam mass flow rate at 100 % generator load for different condenser back pressures, cold reheat supply available and valves stroked according to design 134

Figure 4.13: Stage-by-stage power distribution at different condenser back pressures, with cold reheat and valve stroking according to design 135

Figure 4.14: Snapshot of current plant configuration with leak-off valve open at 37 % load, signal pressure at maximum, showing only the main feedpump 136

Figure 4.15: Snapshot of design plant configuration with leak-off valve open at 37 % load, signal pressure at maximum 137

Figure 4.16: Differences in power consumption between SFP and EFPs 138

Figure 4.17: Total temperatures at inlet to each row 140

Figure 7.1: Key to boundary conditions 150

Figure 7.2: Typical velocity triangles for the impulse turbine case 160

Figure 7.3: Typical velocity triangles for the 50 % reaction turbine case 162

Figure 7.4: Dimensionless descriptors for ideal stages with $\alpha = 20\ ^\circ$ 166

Figure 7.5: Empirical correlation for loss coefficient on orifices for 1.25'' < D < 3.00" (Holman, 2001) 168

Figure 7.6: Station A1 discharge coefficient vs diameter ratio for SFP leak-off 170

Figure 7.7: Graph illustrating Q vs Δp for Station A1 leak-off orifice plate 171

Figure 7.8: Chart of feed pump discharge pressure vs load during normal operation and low load tests 172

Figure 7.9: Boiler resistance curve from OEM 173

Figure 7.10: Feed pump discharge pressure vs generator load 174
Figure 7.11: Moody diagram (Beck and Collins, 2012) 175
Figure 7.12: List of Mathcad shortcuts 184
Figure 7.13: List of steam functions in Mathcad 185

List of Tables

Table 2.1: Different Feed Pump Drive Configurations 13
Table 2.2: Summary of Comparison between Configurations 13
Table 2.3: Effect of SFP Use on Net Heat Rate (based on an Eskom study) 18
Table 2.4: User Inputs for Custom Turbine Stage Components 56
Table 2.5: Critical Pressure Ratios for Steam Nozzles 59
Table 3.1: Estimated Blade Angles at Station B1 69
Table 3.2: Mean Blade Velocities for Rotating Stages at Stations A1, A2, B1 and B2 – Nominal Shaft Speeds 80
Table 3.3: RMS vs Mean Radius for an Example LP Turbine 81
Table 3.4: Turbine Nozzle Area Estimates for Station A1 90
Table 3.5: Targets and Boundary Conditions for Model Tuning and Validation in *Flownex* 90
Table 3.6: Validation of BFPT Model 96
Table 3.7: Mass Flow Rates by Different Methods 96
Table 3.8: Relative Steam Admission Valve Sizes for Station A1 103
Table 4.1: Descriptions of Modes for DCS Stroking with CRH 123
Table 4.2: Descriptions of Modes for Design Stroking with CRH 125
Table 4.3: Effect of Steam Admission Valve Configuration on Isentropic Efficiency 129
Table 4.4: Power Consumed in Different Feed Pump Train Configurations 138
Table 4.5: Predicted Blade Temperatures, Total Temperature Upstream of Row (°C) 139
Table 7.1: Equations for Estimating Signal Oil Pressure vs Load for Different Configurations 154
Table 7.2: Summary of Main Heat Balance Diagrams for Station A1 155

Table 7.3: Summary of Main Heat Balance Diagrams for Station B1 157
Table 7.4: Overview of Key Features of the Eskom Fleet 177
Table 7.5: Selection and Naming of Test Stations 178
Table 7.6: Key Characteristics of Stations Considered 178
Table 7.7: List of Relevant AKZ Numbers for DCS Signals for Station A1 179
Table 7.8: List of EtaPro Servers 181
Table 7.9: List of P&IDs for Station A1 182
Table 7.10: List of Rotor Drawings for Station A1/A2 182
Table 7.11: List of Pump Curves 182

List of Nomenclature

General Symbols

°C	Degrees Celsius; x °C = (273 + x) K
bar	1 bar = 100 kPa
h	Specific enthalpy
m’	Mass flow rate
p	Pressure
Q	Heat, volumetric flow rate
R	Reaction ratio
s	Specific entropy, (as subscript) isentropic
T	Temperature
W	Work
v	Absolute steam velocity
v_b	Blade velocity
v_r	Relative steam velocity

SI (Système International d' Unités) units of measurement will not be listed here.

Greek Symbols

α	Blade absolute velocity inlet angle (nozzle exit angle)
β	Blade relative velocity inlet angle (rotating blade inlet angle)
γ	Blade absolute velocity exit angle
Γ	Static enthalpy drop coefficient
Δ	Delta - difference / change
δ	Blade relative velocity exit angle
ϵ	Efficiency (of blades, nozzles, etc.)
η	Efficiency
ρ	Blade speed ratio
φ	Design flow coefficient
ψ	Stage loading coefficient

Acronyms and Abbreviations

ABB	ASEA Brown Boveri, an original equipment manufacturer
ACC	Air-Cooled Condenser
AKZ	Anlagenkennzeichnungssystem, a system for the unique identification of power station systems and components
BBC	Brown Boveri Company, original equipment manufacturer of turbines
BFP	Boiler Feed Pump
BFPT	Boiler Feed Pump Turbine
BP	Booster Pump
BS	Bled Steam
CRH	Cold Reheat
CV	Control Valve
CW	Cooling water
DCS	Data Capture System
DST	Deaerator Storage Tank
EFP	Electric Feed Pump
GB	Gearbox
GEC	General Electric Company, an original equipment manufacturer of turbines
HP	High Pressure
IP	Intermediate Pressure
IV	Isolating Valve
KKS	Kraftwerk Kennzeichen System, a system for the unique identification of power station systems and components
LH	Left-hand

LP	Low Pressure
MAN	Maschinenfabrik Augsburg-Nürnberg, an original equipment manufacturer of turbines
MCR	Maximum Continuous Rating
MP	Main Pump
MS	Main Steam
MTR	Motor
NPSH	Net Positive Suction Head
OCGT	Open Cycle Gas Turbine
OEM	Original Equipment Manufacturer
P&ID	Piping and Instrumentation Diagram
P/S	Power Station
PGIM	Power Generation Information System
RH	Right-hand, reheat
SFP	Steam Feed Pump
SV	Stop Valve
VSD	Variable Speed Drive

1. Introduction

1.1 Problem Statement

With the growth in the renewable sector of Eskom's energy mix, the need has grown for the coal-fired plants in the fleet to be able to run at minimum generation in a sustainable and efficient manner. A significant number of these power stations utilise boiler feed pump turbines (BFPTs), which use bled steam from the main turbine in order to drive the steam feed pump (SFP), which pumps feedwater to the boiler. Electric feed pumps (EFPs) serve as standby capacity for these SFPs but their use is generally undesirable as it results in increased auxiliary power consumption and reduced efficiency. These BFPTs are constrained with respect to the minimum loads at which they can remain in service, and there are implications for overall cycle efficiency and life cycle costing as to the best way in which to operate these BFPTs in response to changing system requirements. Some stations have been designed with only electric feed pumps, particularly those stations using dry cooling systems for their condensers, but a significant number still utilise BFPTs.

1.2 Objectives

The objective of this study is to develop a high fidelity model of a typical boiler feed pump system using the software *Flownex.* The model is to primarily focus on the boiler feed pump turbine together with its associated steam feed pump, but attention will also be given to the standby electric feed pumps, the boundary conditions affected by the rest of the process, and peripheral plant such as steam admission, spraywater and leak-off valves.

This model will be utilised to study several case studies, especially those involving the limits of low load operation of the boiler feed pump turbine under different conditions. These different conditions include different steam supplies and different valve-stroking philosophies. In addition to studying the limits of low load operation, the effect of condenser back pressure, possible changes to leak-off valve philosophies, and contrasts between the use of electric motor-driven pumps and turbine-driven pumps will all be studied. From these case studies, predictions and recommendations will be made.

1.3 Scope of this Study

Scope

The scope of the study is limited to detailed consideration of the boiler feed pump system on one typical unit of one typical coal-fired power station in Eskom's fleet. Case studies will be based on this system only. While the model created can be used for a wide range of case studies, it will be assumed that considerations of low load operation, condenser vacuum, leak-off philosophy and differences between electric motor-driven boiler feed pumps (EFPs) and turbine-driven boiler feed pumps (SFPs) will be of the greatest relevance with reference to the problem statement.

Assumptions

Various assumptions will be made in order to model the system of interest utilising the information that is available and these are stated in the text as they arise. Major assumptions include but are not necessarily limited to the following:

- There has been no significant deterioration in the turbine isentropic efficiency since commissioning as refurbishments are executed during outages as required.
- Similarly, there is no significant deterioration in pump efficiency since commissioning.
- In modelling boundary conditions as a function of load, a thousand samples per DCS signal at 10 minute intervals will be sufficient to describe the typical relationships.
- Boundary conditions may be extrapolated where loads are below the range for which there is useful data available.

Exclusions

The models built will be created using *Flownex* and as such, the focus will be on the thermofluid process under consideration. There are other factors affecting the successful operation of such systems, whether at low load or under normal operating conditions. The following factors will not be considered in this study:

- Shaft speeds and vibrational concerns.
- Controllability of the steam admission valves / detailed consideration of the hydraulic control system (it will be considered sufficient to model all valves as responding to one signal oil pressure as per the design).
- Variability of boundary conditions despite the generator load being fixed – for example, at a given load, reheat spraywater demand is modelled as a fixed, typical value; in reality, this demand varies even if the load does not change because process conditions may change within the boiler.

Some of these exclusions may have a significant bearing on the findings and recommendations of this study. For example, whereas the system may be capable of sustaining a certain minimum load thermodynamically, the plant operator may nevertheless find that the hydraulic control system for the steam admission valves cannot control in a stable manner at that load.

1.4 Overall Report Structure

This dissertation will focus on one specific typical station, designated *Station A1*, with some comparisons being made with similar stations within Eskom's fleet. A detailed discussion of this station and the underlying theory in Chapter 2 will lead into modelling of these systems using the *Flownex* software in Chapter 3, with validation using signals from the stations' data capture systems (DCS). Unless otherwise indicated, the station in question will be Station A1. Where DCS data is used, it will be from only one unit at this station. The unit was chosen because it was one of the better units in terms of available instrumentation for remote monitoring.

It is appreciated that any experimental data incorporates a degree of uncertainty. However, the accuracy of the data used is considered sufficient for this application, given that the instrumentation has been specified by reputable experts in Control and Instrumentation to a tolerance that is reasonably practicable for the application, and, furthermore, calibration is conducted at suitable intervals by SANAS-accredited laboratories.

The impact of low load operation on these feed pump systems will then be considered, along with other case studies of interest, in Chapter 4. Some of the principle questions considered are the minimum loads achievable with different steam supplies and valve configurations, the impact of condenser vacuum on the system, the use of leak-off valves at low loads, and the effect of operating electric feed pumps instead of the steam feed pump.

The results of these case studies will be used to make recommendations in Chapter 5. Chapter 6 contains references and Chapter 7 contains appendices.

2. Theory and Literature Review

This chapter includes a review of relevant external literature as well as an overview of information available through Eskom station manuals, databooks and site visits. For confidentiality reasons, station names have been replaced with numbers, and descriptions are given in a generic or summarized manner.

2.1 Eskom Literature and Site Observations

2.1.1 Overview of the Eskom Fleet

Eskom owns and operates a Generation fleet which includes fifteen coal-fired power stations and one nuclear power station. Each of these stations has between two and ten units, a unit being comprised of one set of turbines, a generator, a boiler and other associated equipment. A detailed comparison of these stations is beyond the scope of this study but some of the principal characteristics will be compared here in order to justify the choice of station for this study's focus.

Table 7.4 in Appendix J provides an overview of Eskom's fleet of coal-fired/nuclear power stations. Based on this, Table 7.5 in the same appendix provides a closer consideration of criteria affecting the stations' relevance to this study.

The Venn diagram appearing in Figure 2.1 presents this graphically. The number after each label is the number of applicable stations while the number in brackets is the number of applicable units. Nine of the sixteen stations have steam feed pumps. Of these nine, three stations have units of less than 500 MW output. The remaining stations have been assigned names A1, A2, B1, B2, C and D. Note that A1 and A2 are similar stations, as are B1 and B2. The focus of this study is Station A1 as it is the station from this set for which information was most readily available and for which site access was most readily obtained. However, the other five stations assigned names will be utilised for comparison and discussion as they are stations with BFPTs and a similar generated load per unit.

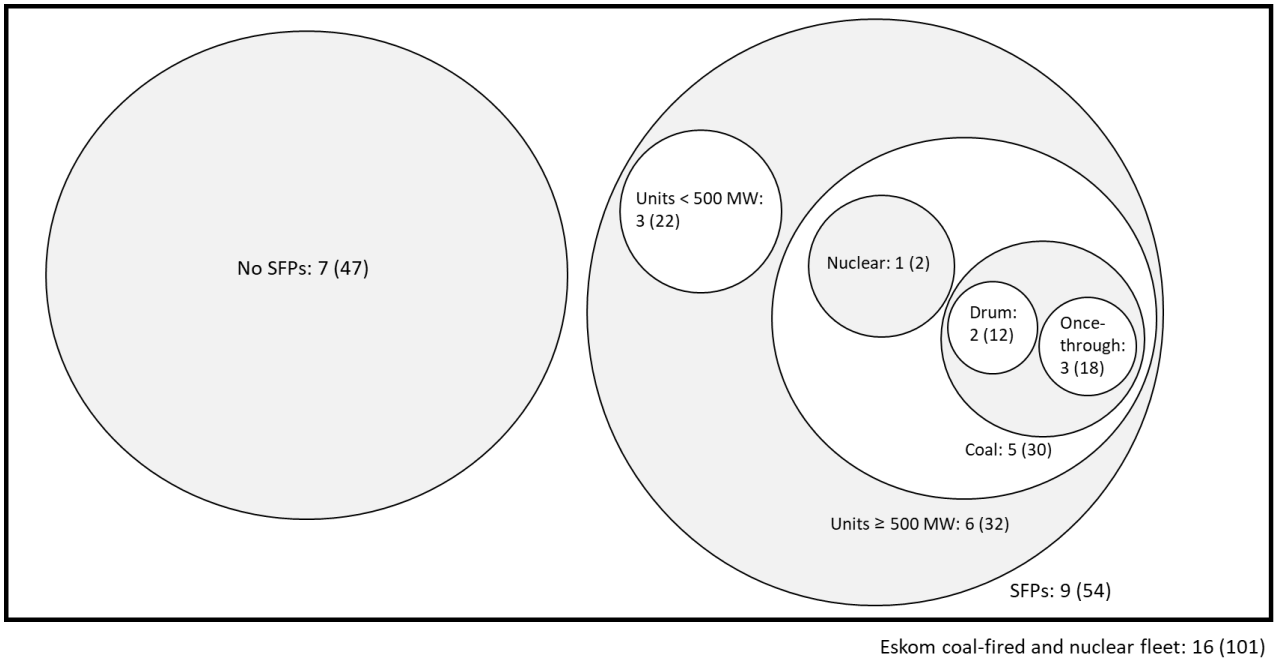

Figure 2.1: Venn diagram illustrating selection of stations for this study

Table 7.6 in Appendix J shows key characteristics of the six stations which have been assigned names for ease of comparison.

In particular, stations A1, A2, B1 and B2 will be discussed in more detail here. Stations A1 and A2 are very similar to each other, and stations B1 and B2 are very similar to each other, being of approximately the same design. Stations A1 and A2 both have once-through boilers whereas stations B1 and B2 have drum boilers. All have gross generation capacities in the region of 600 – 620 MW. All have boiler feed pump configurations of 1 x 100 % SFP with 2 x 50 % EFPs as standby. Station commissioning completion dates are in the range 1980 to 1990. All have main steam conditions of approximately 535 °C and 160 bar.

2.1.2 Power Station A1/A2

As noted above, stations A1 and A2 are nearly identical, with some relatively minor differences. Each of the units at A1/A2 has a feed pump system with one steam feed pump (SFP) powered by a boiler feed pump turbine (BFPT) and two electric feed pumps (EFPs). The BFPT receives steam bled from the main turbine while the EFPs are driven by electric motors, coupled to the pumps by means of *Voith* variable speed hydraulic fluid couplings. These couplings allow for the pump speed to be varied by means of adjusting the “scoop” which determines the amount of oil present within this coupling. The BFPT speed is controlled by means of limiting the amount of steam admitted to the turbine, through the use of “nozzle” steam admission valves and a Woodward governor. This

steam is tapped off from the Intermediate Pressure (IP) turbine or the Cold Reheat (CRH), which is the exhaust from the High Pressure (HP) turbine. The main turbine, or "centreline", is comprised of one HP turbine, one IP turbine and two LP turbines per unit. The two LP turbines exhaust into two condensers, designated "hot" and "cold". The "cold condenser", situated below LP turbine 1, has its steam space directly connected to that of the BFPT condenser. The BFPT turbine system is illustrated in Figure 2.2. Note that the steam path is from left to right and the block at the top left shows the positions of two of the four steam admission "nozzle" valves used for control during normal operation. The BFPT condenser steam space is situated below the turbine exhaust.

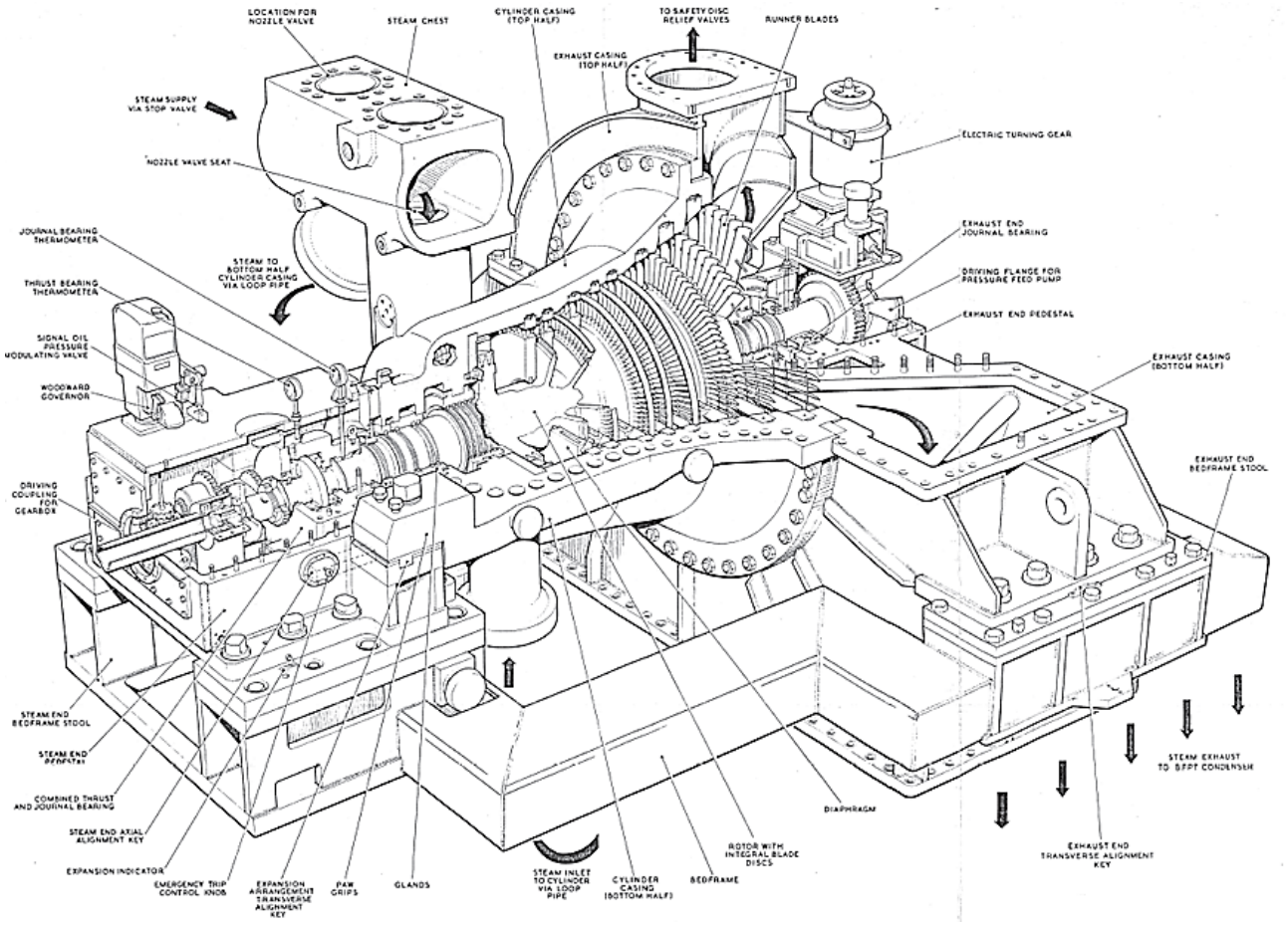

Figure 2.2: Drawing of Station A1/A2 BFPT (Eskom Station manuals, edited)

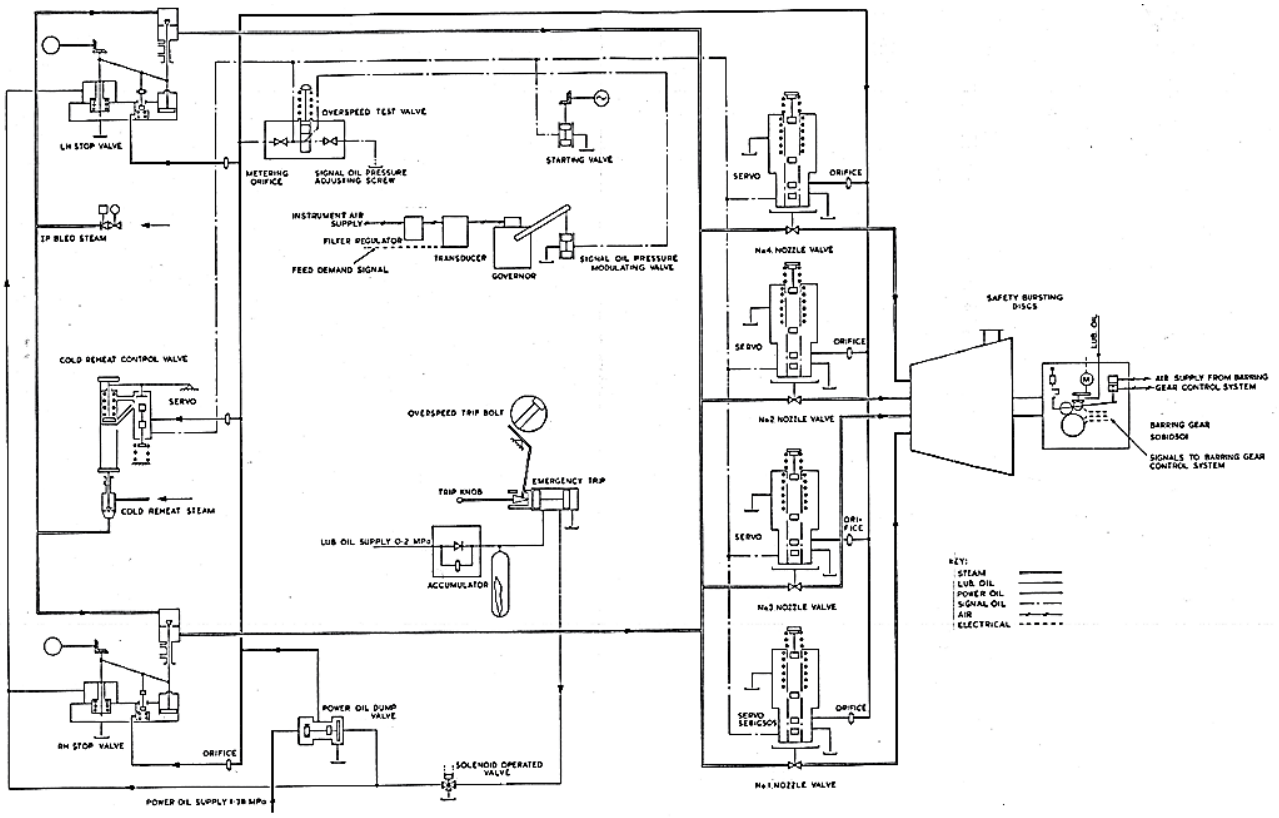

Figure 2.3: Diagram illustrating the BFPT steam control system at Station A1 (Eskom Station Manuals, edited)

The relationship between signal oil pressure and lifting height for the control valves is shown in Figure 2.3. There are four “nozzle valves” (which may be considered governor valves), and one cold reheat valve.

According to the manuals (Figure 2.4), the valves open in the following sequence as the signal oil pressure is increased:

1. Nozzle valves 1 and 2
2. Nozzle valves 3 and 4
3. Cold reheat valve

Whereas at full load, the nozzle valves will provide adequate steam to drive the BFPT using only IP bled steam, at lower loads, with lower extraction steam pressures, higher pressure steam from the cold reheat supply will also be required. In this instance, the signal pressure will keep increasing until the power demands of the BFPT are met.

At Station A1, the cold reheat supply was decommissioned some years ago, motivated by an apparent instability of the control system at low loads. As a result, operators report that the BFPT cannot remain in service below a load of about 320 MW (52.5 %) depending on the Unit in question.

At Station A2, modifications were made to this control system and the cold reheat supply is still utilised. Information is not as readily available for Station A2 as it is for Station A1, however.

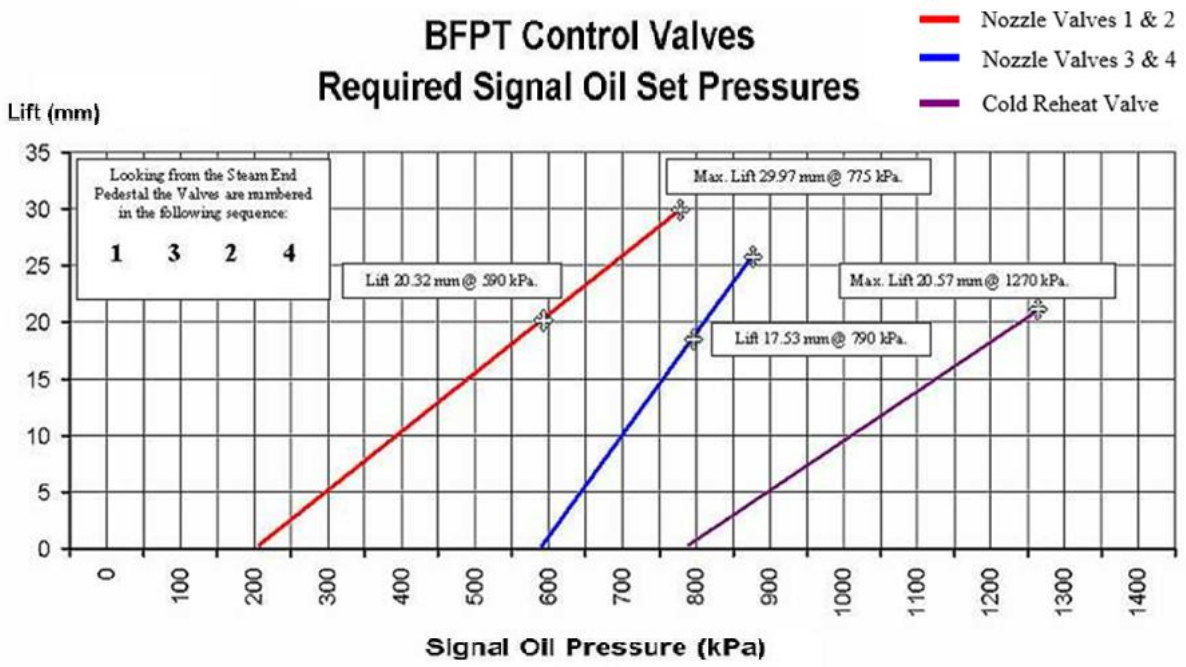

Figure 2.4: Diagram illustrating the set pressures for the BFPT steam control system at Station A1 (Eskom station manuals, edited)

The relevant P&IDs (Piping and Instrumentation Diagrams) for Station A1 are listed in the appendices. These provide a detailed view of the system layout as well as the location of instrumentation available. Eskom uses a KKS (Kraftwerk Kennzeichen System) or AKZ (Anlagenkennzeichnungssystem) system to provide unique identifiers to all the components of which the equipment at its power stations is comprised. Station A1 uses the AKZ system. The AKZ numbers of the instrumentation on these P&IDs were compared against signals on the station's Data Capture System (DCS), used as data sources in Chapter 3. The principal instrumentation from these various P&IDs is conveniently summarised in Chapter 3.

Heat balance diagrams for Station A1 were obtained for 45%, 60%, 80% and 100% load conditions. Dimensioned diagrams for the Station A2 BFPTs, identical to those of Station A1, were also obtained. Various pump curves were obtained for the fleet, in particular for the SFPs, EFPs and booster pumps of Stations A1, A2, B1 and B2.

In addition, the following salient points are noted from the station manuals for Station A1, regarding its BFPT and feed pumps:

- Turbine type: “impulse reaction” (elsewhere, only “impulse”)
- Number of expansion stages: 9
- Maximum turbine speed: 83 Hz (4 980 rpm)
- Overspeed governor trip speed: 87.5 Hz (5 250 rpm)
- Turbine steam inlet temperature and pressure (bled steam): 379 °C and 1.103 MPa
- Turbine steam inlet temperature and pressure (cold reheat steam): 332 °C and 3.69 MPa
- Steam pressure at exhaust on bled steam, main turbine 100 %, cooling water at 22 °C; 8.46 kPa
- Turbine critical speed (first): 50 Hz (3000 rpm)
- Booster pump (BFPT): Sulzer 302 HZB 580
- Main pump (BFPT): Sulzer HPT POK 43
- Booster pump (EFP): Sulzer 253 HZB 640
- Main pump (EFP): Sulzer HPT POK 32-25
- Hydrodynamic coupling minimum slip: 2.2 % / 2.4 % (at full load)

The contract data stipulates that the changeover to the cold reheat steam supply should occur at 40 % of generator load, with the supply steam at source being at 1.55 MPa (absolute) and the temperature being 310 °C at changeover.

Similar Turbines

Some research into similar turbines available commercially yielded the turbine shown in Figure 2.5 as the best match, the Siemens SST-600 (Siemens AG 2004). The geometrical similarities with Figure 2.2 can be readily observed. It has the following specifications (Siemens AG, 2015):

- Power output: up to 150 MW
- Speed: 3000 – 18 000 rpm
- Live steam inlet pressure: ≤ 16.5 MPa
- Live steam inlet temperature: ≤ 565 °C
- Exhaust conditions if condensing: ≤ 100 kPa

The steam path is customised for the customer’s needs, although the image shown below shows 15 stages. Variations of this model have been used since the 1970s, with applications including boiler feed water pumps.

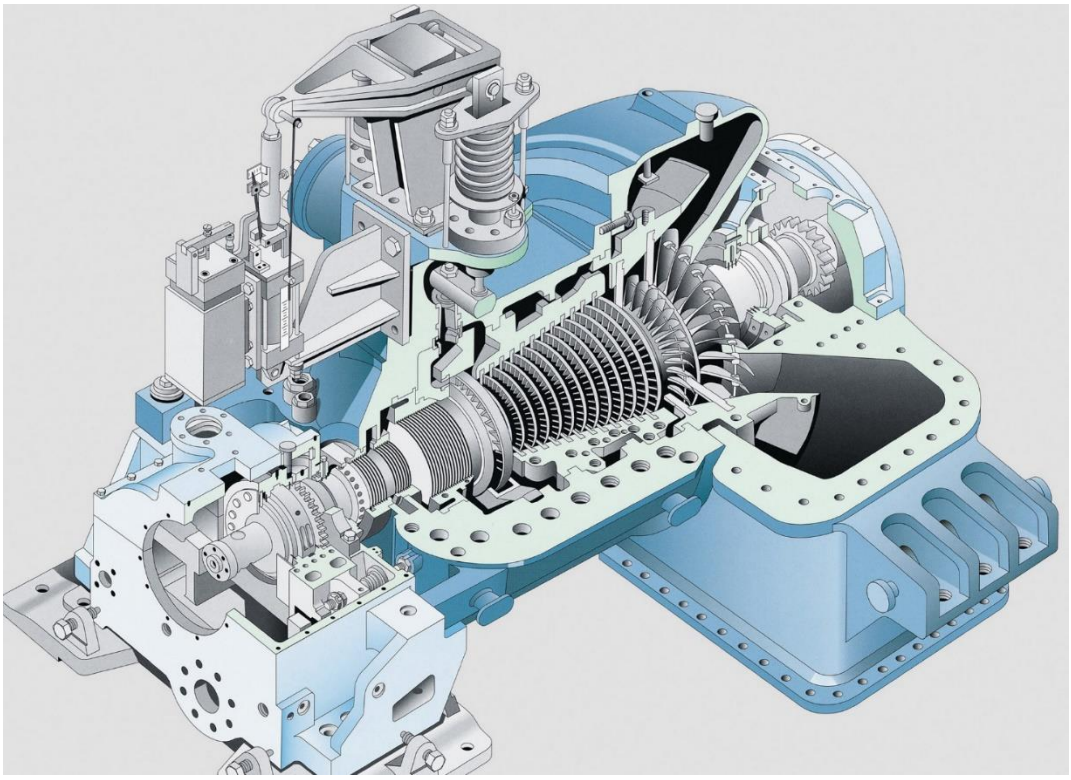

Figure 2.5: Siemens steam turbine SST-600 (Siemens AG, 2004)

2.1.3 Comparison with Power Station B1/B2

The overall configuration at these stations does not differ substantially from that of A1/A2. (This discussion will focus on Station B1, for which information was more readily available than for Station B2.)

The most notable difference between A1 and B1 is the BFPT itself which on B1 has four initial "High Pressure" ("HP") stages and then two sets of two "Low Pressure" ("LP") stages in parallel. This is represented in Figure 2.6 below. In addition to this, it is noted that the supply for Station B1 was from the cold reheat (that is, main HP turbine exhaust) and from the IP bled steam (that is, steam bled off the main IP turbine). Both of these supplies are still available for use, unlike in the case of A1. The turbine is nominally "impulse".

During normal operation, bled steam from the main IP turbine is supplied through one stop valve and two control valves. When the pressure from this steam turbine is insufficient – for example, at low generator loads or during tripping – steam from the reheater inlet ("cold reheat") is utilised.

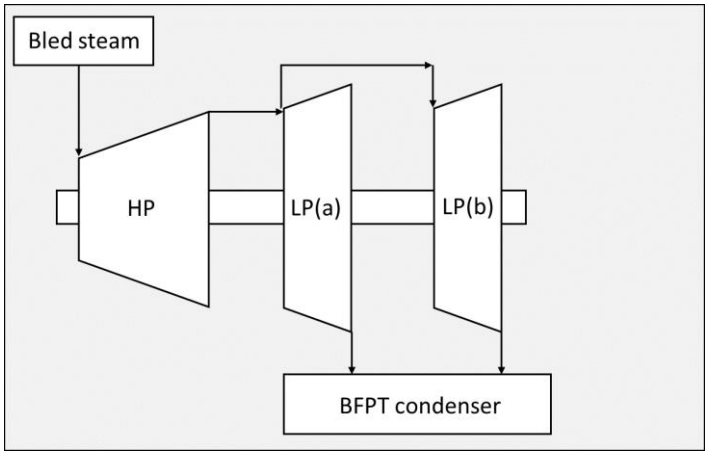

Figure 2.6: Diagram illustrating the configuration of the BFPT at Station B1

The limits of operation appear in Figure 2.7, from station manuals. The minimum load rating from the OEM is 30 % (of 600 MW). The nominal shaft power is 12.7 MW.

Rating		Peak Rating		Max. Rating	Nominal Rating	Minimum Rating
Main Turbine Load	MW %	133		121	600 100	180 30
Feed Pump Turbine Load at Coupling	MW	17.0		15.4	12.7	5.8
Live Steam Pressure Temperature	MPa (abs) °C	0.932 343	/ /	0.932 343	0.932 343	0.303 284
Auxiliary Steam Pressure Temperature	MPa (abs) °C	/ /	4.1 333	/ /	/ /	1.3 285
Steam Throughput	kg/s	25.49	24.61	22.86	12.15	10.89 (6.76 + 2.13)
FPT Speed	rpm	5 500	5 500	5 334	4 996	4 099
Outlet Pressure	kPa (abs)	8.50	8.50	7.75	6.07	4.55

Figure 2.7: Station B1 operational limits (station manuals, annotated)

2.1.4 Turbine-Driven or Electric-Driven Boiler Feed Pumps for New Build Stations

The "new build stations" considered below refer to Eskom's most recent build of supercritical coal-fired stations which are currently in the process of being commissioned.

Eskom pump specialists Willem van der Westhuizen and Tony Cattaert described in a paper the decision-making process whereby a configuration of three electric feed pumps using *Voith Vorecon* hydraulic couplings was selected as the chosen drive configuration for the new build stations (van der Westhuizen and Cattaert, 2010).

Two configurations were considered:

i. 100 % SFP and two 50 % EFPs
ii. Three 50 % EFPs

For the new build, EFPs were chosen over SFPs based on economic evaluations over a 50-year lifespan. Included in this evaluation were considerations of initial capital costs, redundancy, and spares-holding as well as the complexities of interfacing with a dry cooling system. The new build stations use ACCs (air-cooled condensers). OEMs (original equipment manufacturers) do not generally support using SFPs on units with ACCs. BFPTs are usually configured to have their own shell-and-tube condensers which utilise cooling water from the main cooling water circuit.

Having chosen to eliminate SFPs, four drive train configurations were considered for the EFPs:

1. High speed VSD (variable speed drive) motor with a speed reduction gearbox.
2. Low speed VSD motor with a speed increase gearbox.
3. *Voith Vorecon* variable-speed planetary gear fluid drive coupling.
4. *Voith* variable-speed fluid drive coupling.

These different configurations are summarised in Table 2.1. For the figures within this table, BP denotes booster pump; GB, gearbox; MTR, motor; MP, main pump and VSD, variable speed drive. *Voith* indicates an ordinary *Voith* hydrodynamic coupling while *Vorecon* indicates the *Vorecon* coupling discussed below.

Table 2.1: Different Feed Pump Drive Configurations

Configuration	Description	Diagram
1	High speed VSD (variable speed drive) motor with a speed reduction gearbox	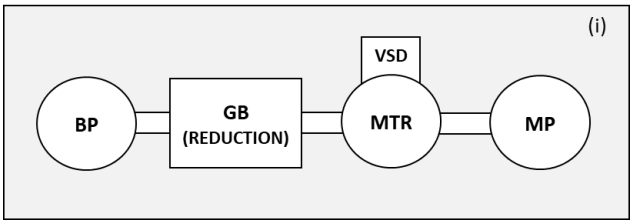
2	Low speed VSD motor with a speed increase gearbox	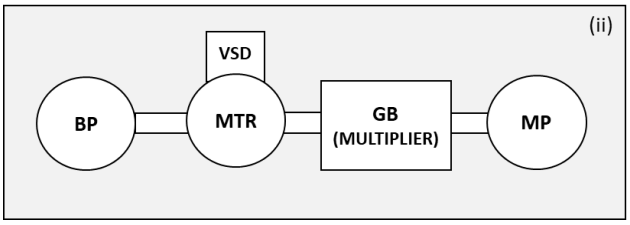
3	*Voith Vorecon* variable-speed planetary gear fluid drive coupling	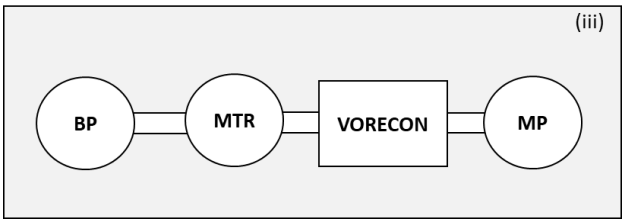
4	*Voith* variable-speed fluid drive coupling	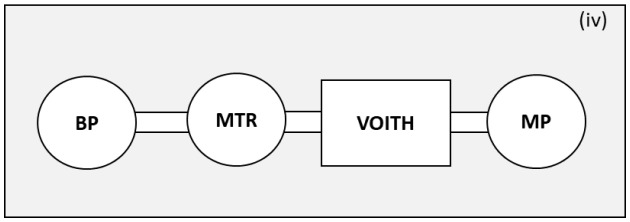

The results of the study are summarised in Table 2.2. The economic model was considered for an expected 50-year lifespan.

Table 2.2: Summary of Comparison between Configurations

	BFP set efficiency	Power consumed (MW)	Relative capital cost	Example stations	Economic model ranking
Configuration 1	81.2%	24.275	203%	Three other Eskom stations	4
Configuration 2	79.9%	24.685	161%	No Eskom experience	2
Configuration 3	77.2%	25.521	133%	No Eskom experience	1
Configuration 4	70.2%	28.103	100%	Stations A1, A2, B1 and B2 – for start-up, shutdown and standby	3

Further Consideration of the *Vorecon* Coupling

The hydrodynamic coupling selected for use on the new build stations is the *Voith Vorecon* RW16-145 F9. The motor's speed is 1480 rpm with a main pump speed ranging from 2 500 to 5 770 rpm, dependent on the *Vorecon's* control. Transition between the two *Vorecon* modes of operation is set to occur at 80 % of the maximum speed, or 4 616 rpm.

Mode 1 operates like an ordinary *Voith* coupling (Configuration 4) – a hydrodynamic variable speed coupling with an adjustable scoop tube. The drive shaft connected to the motor is connected to an impeller within the coupling while the driven shaft, connected to the main pump, is connected to a turbine within the coupling. Torque is transferred from the drive shaft to the driven shaft by means of oil circulating within the coupling, driven by the impeller and driving the turbine. By adjusting the scoop tube position, the amount of oil or oil level between impeller and turbine is adjusted. When the scoop is fully engaged, slip can be as low as 2.2 %, in the case of Station A1, while with the scoop fully retracted, slip is 100 %. This concept is illustrated in Figure 2.8 (Voith, 2017). During this time, the torque converter used during Mode 2 is drained of oil and the hydrodynamic brake is filled with oil, keeping the fixed planetary gear at low speed.

A *Vorecon* operates in this mode until the scoop is fully engaged, at which point a mechanical lock-up clutch engages and the *Vorecon* begins to operate in Mode 2. A torque converter with adjustable guide vanes adds additional speed to the output shaft by means of a planetary gear system. In this mode, the torque converter is filled with oil and the hydrodynamic brake is drained.

By splitting the operating range into two sections, corresponding to Mode 1 and Mode 2, an increased efficiency is obtained. The overlap between these two modes is at around 75-80 % of the maximum output speed. It is of some interest to note that during optimisation on one of the new build units, it was found that there was a dead band between 80 – 100 % scoop position. This setting was adjusted in order to make the system more responsive. The *Vorecon* configuration for the RW series, as used on the new build stations, is illustrated in Figure 2.9 (Voith, 2017).

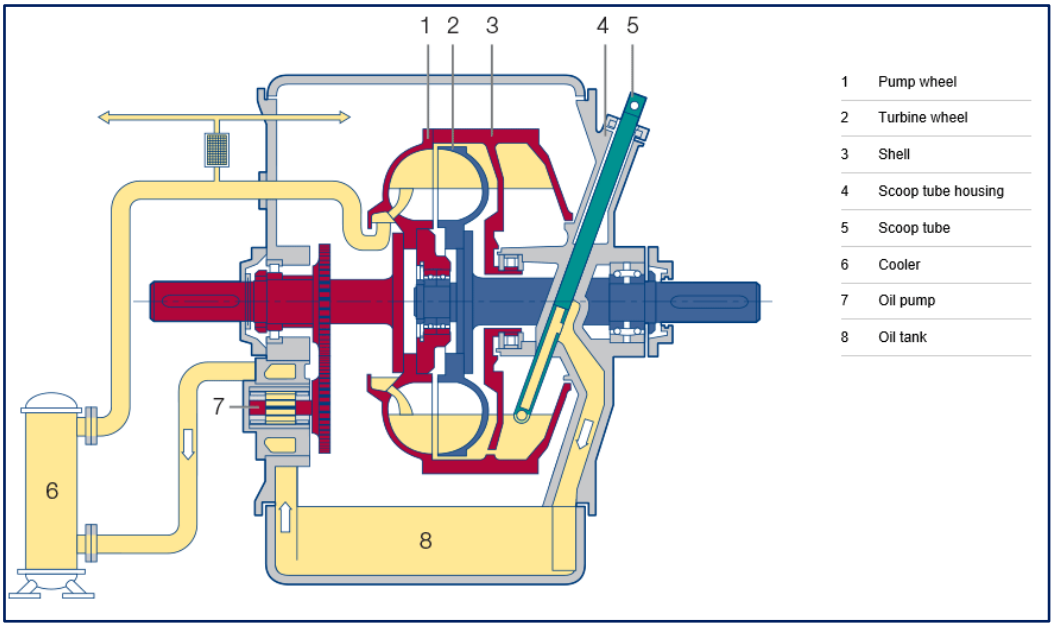

Figure 2.8: Diagram illustrating a Voith variable speed coupling (Voith, 2017)

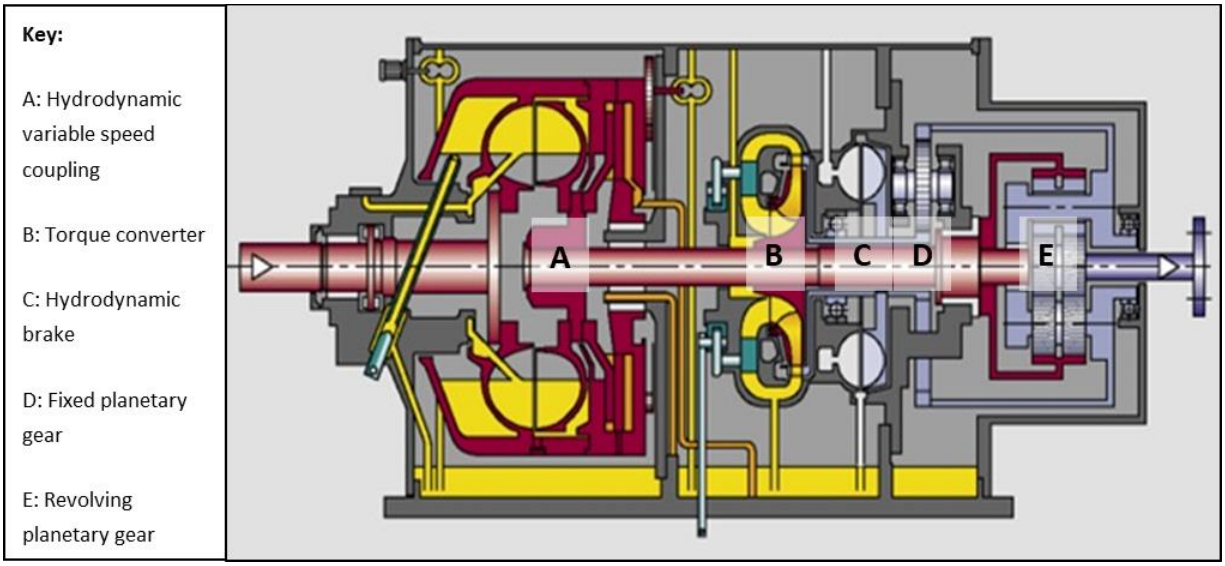

Figure 2.9: Diagram illustrating a Voith Vorecon variable speed coupling (UTK-EBPO, 2017, annotated)

2.1.5 Considerations of the Merits of BFPTs over EFPs

Availability Survey

For the period 2010 – 2013, an internal Eskom survey was conducted considering BFPT utilisation across the coal-fired fleet.

The unavailability of BFPTs across the fleet was calculated to have a cost in the order of R 100 million to R 200 million per annum in terms of auxiliary power consumption, based on the electricity prices at the time (in 2013), applicable for each power station. This represents a substantial amount of lost revenue for these stations.

Furthermore, the gross generator power output is limited for a given unit. As auxiliary power consumption increases, the net power output is reduced and in a scenario of short supply, this can contribute to the likelihood of load shedding[1] or influence the number of OCGTs (open cycle gas turbines) which must be run to avert load shedding.

The key contributing factors of interest are listed below per station considered in this dissertation. These provide motivation for the choice of case studies in Chapter 4.

When considering unavailability due to low unit loading, it is noted that this was in the period up to 2013 and since then the demand for lower loads has increased substantially.

Station A1

1. The overall BFPT utilisation – determined as the percentage of time for which the BFPT is in service while the unit is on load – was 83.81 %.
2. Condenser issues, including bursting of rupture discs[2], accounted for 25 % of unavailability.
3. Unit loading being too low to run the BFPT accounted for 4 % of unavailability.
4. Speed control system faults (including governor and hydraulics problems) accounted for 33 % of unavailability.

[1] Load shedding is the deliberate curtailment of demand when the national supply is severely constrained; it involves the disconnection of consumers based on rotating schedules in order to safeguard the grid.

[2] Sacrificial discs on the top of the condenser steam space which burst when the condenser exceeds a pressure of approximately 100 kPa absolute. This prevents over-pressurisation of the condenser.

Station A2

1. The overall BFPT utilisation was 81.38 %.
2. Condenser issues accounted for 9 % of unavailability.
3. Unit loading being too low to run the BFPT accounted for 15 % of unavailability. This was largely due to wet coal during the rainy season forcing partial load losses to be booked.
4. Speed control system faults (including governor and hydraulics problems) accounted for 17 % of unavailability.

Station B1

1. The overall BFPT utilisation was 95.06 %.
2. Condenser issues accounted for 0 % of unavailability.
3. Unit loading being too low to run the BFPT accounted for 0 % of unavailability.
4. Speed control system faults (including governor and hydraulics problems) accounted for 20 % of unavailability.

Station B2

1. The overall BFPT utilisation was 88.30 %.
2. Condenser issues accounted for 21 % of unavailability.
3. Unit loading being too low to run the BFPT accounted for 4 % of unavailability.
4. Speed control system faults (including governor and hydraulics problems) accounted for 17 % of unavailability.

Station C

1. The overall BFPT utilisation was 58.91 %.
2. Condenser issues accounted for 0 % of unavailability.
3. Unit loading being too low to run the BFPT accounted for 7 % of unavailability.
4. Speed control system faults (including governor and hydraulics problems) accounted for 4 % of unavailability.
5. BFPT turbine rotor failures – for example, blade failures – accounted for 30 % of unavailability with excessive vibration after return to service accounted for 22 % (this was specifically a problem on one unit).

(Station D does not fall within the coal-fired fleet and was therefore not considered in this study.)

Strategies

In 2014, Eskom identified a target of 90 % BFPT utilisation.

The key motivating arguments were:

- Plant redundancy to prevent a pump trip causing a partial load loss or unit trip.
- Savings on diesel consumption on OCGTs during peak periods.
- It costs less to produce steam than the equivalent amount of electricity.

Effect on Heat Rate

An exercise was conducted by Eskom specialists for Station A2 in 2012 utilising the software "Steam Master". There it was shown that by running the EFPs instead of the SFP at full load, the net heat rate would typically deteriorate from 8636.8 kJ/kWh to 8707.1 kJ/kWh, equivalent to a change of net efficiency from 41.682 % to 41.346 %. This provides an indication of the typical effect of SFP-use on overall heat rate. This is shown in Table 2.3.

Table 2.3: Effect of SFP Use on Net Heat Rate (based on an Eskom study)[3]

	W_{gross}	W_{net}	Q_{in}	η_{net}	HR_{net}
	MW	MW	MW	MW/MW	kJ/kWh
Case 1 (SFP, full load)	600	567.357	1361.150	41.682%	8636.8
Case 2 (EFPs, full load)	600	549.791	1329.738	41.346%	8707.1

2.1.6 Minimum Generation Tests at Stations A1 and B1

As noted in the problem statement, the addition of renewable generation capacity has made it necessary for Eskom's coal-fired fleet to operate units at lower loads than historically. Therefore, Eskom commissioned EPRI (Electric Power Research Institute) to conduct minimum generation tests at Stations A1 and B1. This section will consider the procedures and results of these tests, Tiers 1 – 3.

These tests were conducted according to the following schedule for both stations:

- Tier 1 in July 2017
- Tier 2/3 in November 2017

Figure 2.10 summarises the steps associated with these different tiers of testing.

[3] This table was produced from the heat balance in the study, with the assumption that the auxiliary power consumption due to EFPs at full load would be 18.210 MW in total.

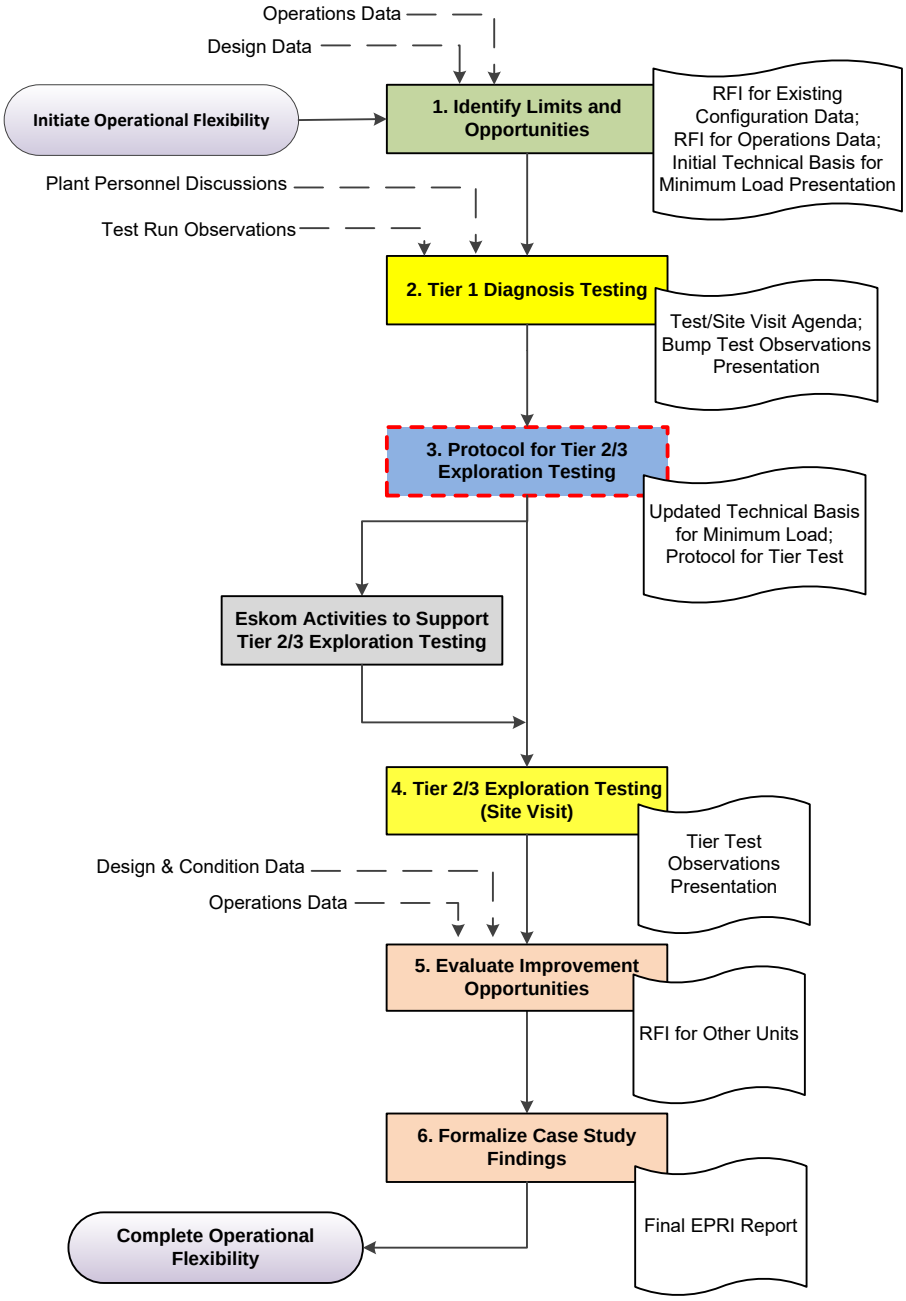

Figure 2.10: Diagram of main steps in EPRI low load flexibility tests at Eskom (EPRI, 2017)

All the above Tier 2/3 tests were witnessed on-site by the author in November 2017.

Some of the principal observations are noted below.

Station A1

This is a once-through boiler with a nominal gross generator load of 609 MW. A minimum generator load of approximately 240 MW was obtained with 2 mills in service, no fuel oil support, and negligible collecting vessel level (the limit of Benson mode). The BFPT should remain reliably in service down to about 320 – 350 MW, as shown during previous tests.

The Operator made the decision to place the BFPT on leak-off before the tests commenced and therefore the limits of operation on pumping duty could not be tested during the minimum generation test as the main feedwater supply was from the electric driven pumps. However, it was observed that the BFPT remained on leak-off down to the minimum generator load point of the test (about 200 MW). As noted previously, the cold reheat steam supply has been decommissioned. This demonstrated that the IP bled steam supply was adequate to sustain leak-off flow at these low loads.

Station B1

This is a drum-type boiler with a 600 MW capacity. A minimum generator load of 245 MW was obtained with no oil support, or 235 MW with 2 mills in service and oil support on one mill. The steam flow limit was reached at 235 MW (this limit is imposed by the Fossil Fuel Firing Regulations). The BFPT remained in service throughout with speed above 4000 rpm. The cold reheat supply opened as the generator load decreased.

This is shown in Figure 2.11, where CV 3 (Control Valve 3) begins to open as the load is reduced. The respective positions of CV 1, CV 2 and CV 3 are 101 %, 89 % and 12 %. “Extraction 4B” is the bled steam supply from the IP turbine while “Extraction 6” is the steam supply from the cold reheat.

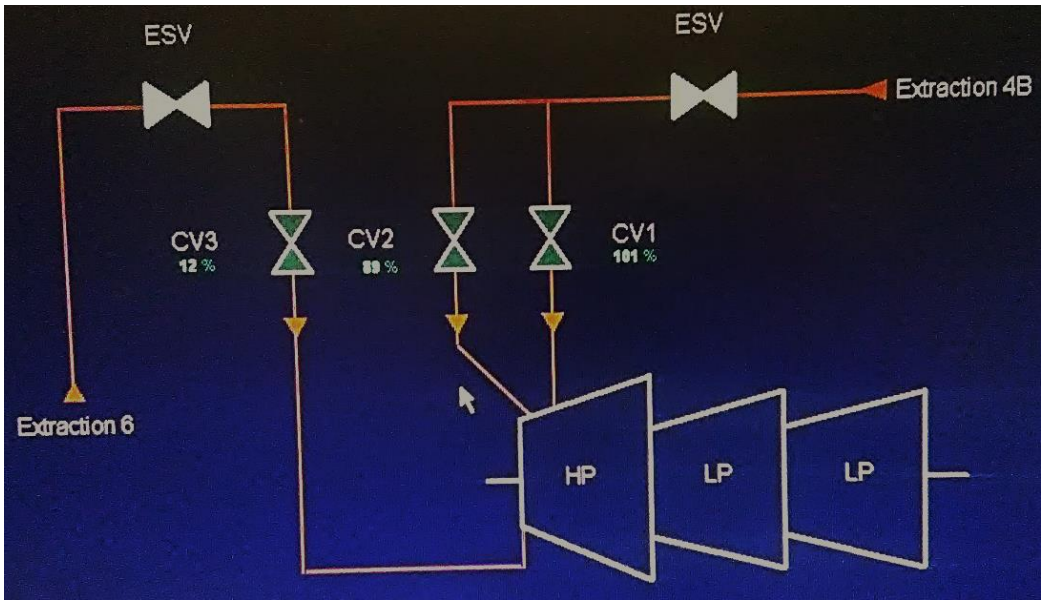

Figure 2.11: Operating snapshot from control room of BFPT at Station B1

Various other observations were made, especially relating to pulverised fuel (coal) mills, oil burners, boiler fans and flue gas measurements. However, these considerations are beyond the scope of this study.

Benson Mode and Recirculation, and Limits on Station A1

Typical drum and once-through boilers are shown in Figure 2.12 and Figure 2.13. When a once-through boiler is in recirculation mode, it functions in a similar way to a drum boiler. Its collecting vessel accumulates level and functions much like the drum in a drum-type boiler. The steam moves through the separating vessels to the superheaters while the condensate collects in the collecting vessel and is pumped back to the economiser inlet by the circulating pump. Above a certain load, referred to as the "Benson point", usually in the region of 40 % generator load, the unit moves from recirculating mode into "Benson" (or once-through) mode. In this mode, all fluid entering the separating vessels leaves to the superheaters as steam and no condensate collects in the collecting vessel (thus there is no recirculation).

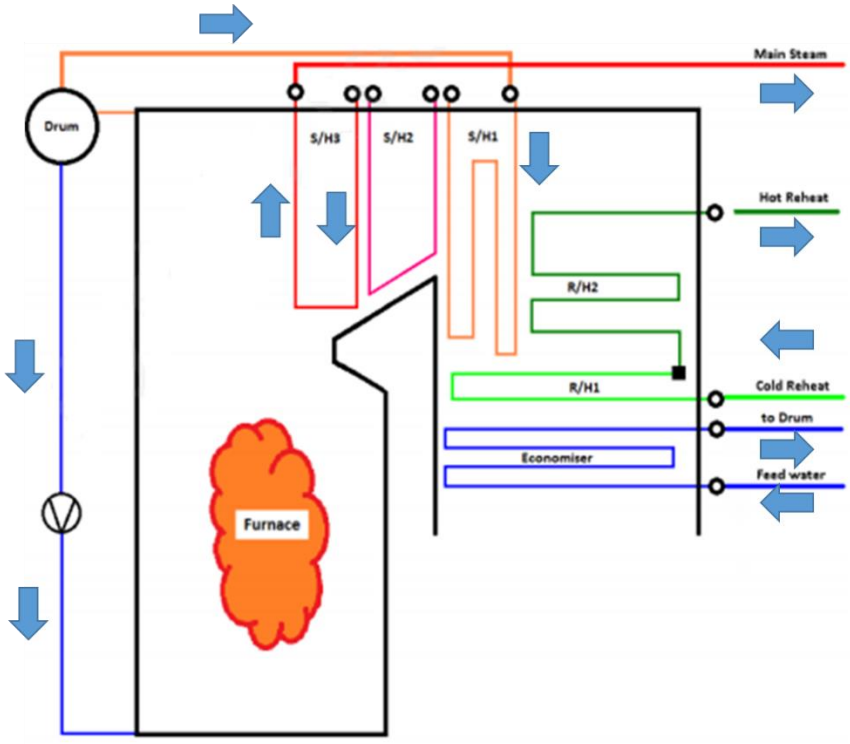

Figure 2.12: Typical layout of a drum-type boiler (Rousseau and Fuls, 2017a, annotated)

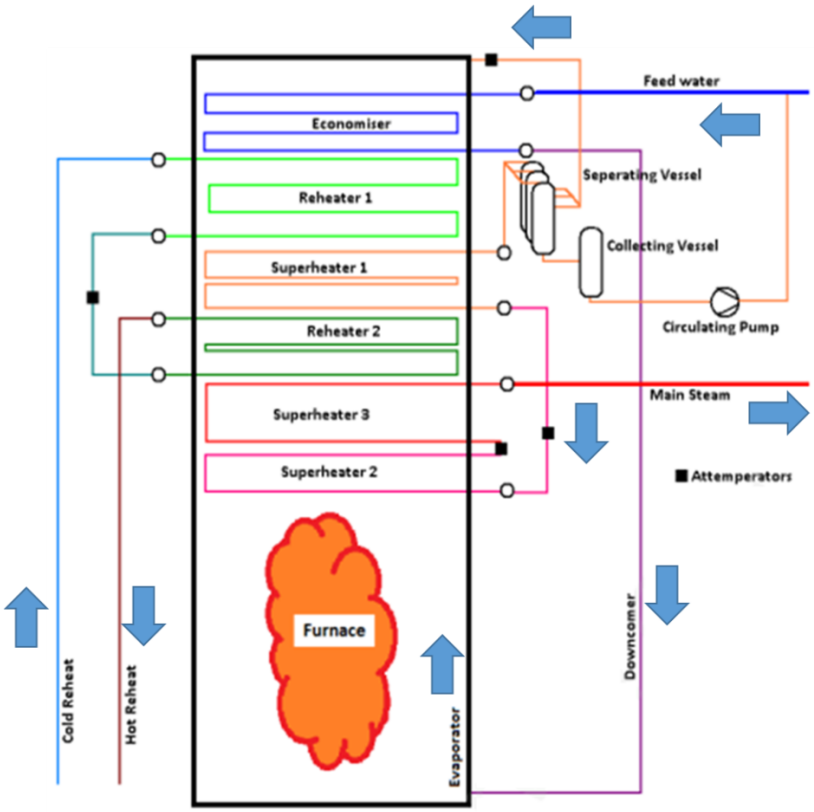

Figure 2.13: Typical layout of a once-through boiler (Rousseau and Fuls, 2017b, annotated)

At Station A1, the response of the boiler recirculating system was tested at low loads. This system is shown in Figure 2.14 below. It was found that the collecting vessel drain valves were able to keep the collecting vessel level below the maximum value; however, recirculation equilibrium could not be obtained using the existing equipment and controls. In particular, circulator pump flow measurement was not possible below about 10 kg/s, the circulator pump regulating valve was not capable of fine control within ±2 kg/s, and the EFP flow control was not capable of fine control (within ±2 kg/s). It was noted that a collecting vessel level below 0.8 m would result in an automatic trip of the circulator pump. For this reason, the decision was made to limit the load to the lowest load achievable without obtaining collecting vessel level, which is to say, the Benson point.

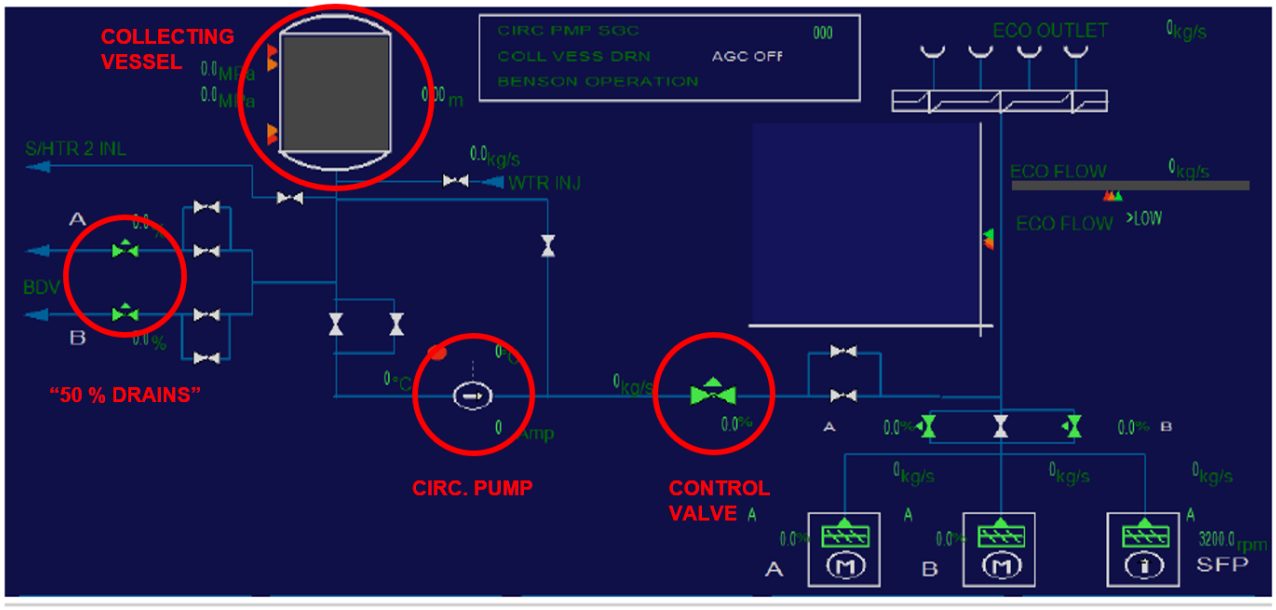

Figure 2.14: Boiler recirculation system at Station A1 (annotated mimic of operator control system interface)

These observations are of relevance here because the limitations discussed are partially due to the feed pump control system, and these should be kept in mind if future plant modifications are to be considered. Also, the limit of 40 % provides context for the case studies, when considering targets for low load operation.

Turbine-Follow and Boiler-Follow Mode

Figure 2.15 summarises the difference between boiler-follow and turbine-follow mode. These points are of relevance when different control philosophies are considered. Station B1 was able to remain in coordinated control down to minimum loads whereas Station A1 needed to change to turbine-follow modes at low loads.

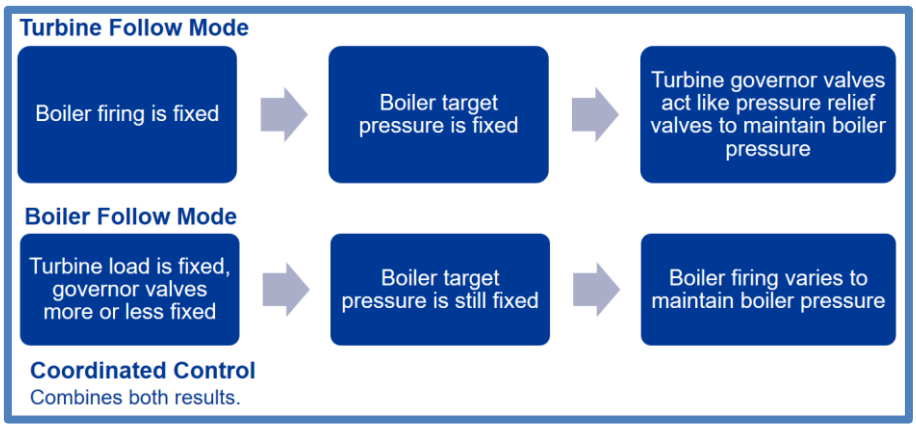

Figure 2.15: Diagram summarising the different Unit control philosophies

2.2 Centrifugal Pump Theory

2.2.1 Similarity Laws

From traditional centrifugal pump theory, the centrifugal pump similarity/scaling/affinity laws may be expressed with the following equations. Q, N, and D denote volumetric flow rate, impeller rotational speed and impeller diameter respectively. NPSH is net positive suction head and Ẇ is the power consumed by the pump (that is, the shaft power). The subscripts (1) and (2) denote any two similar pumps being compared.

$$\frac{Q_1}{Q_2} = \frac{N_1}{N_2} \cdot \left(\frac{D_1}{D_2} \right)^3 \quad (1)$$

$$\frac{H_1}{H_2} = \left(\frac{N_1}{N_2} \right)^2 \cdot \left(\frac{D_1}{D_2} \right)^2 \quad (2)$$

$$\frac{NPSH_1}{NPSH_2} = \left(\frac{N_1}{N_2} \right)^2 \cdot \left(\frac{D_1}{D_2} \right)^2 \quad (3)$$

$$\frac{\dot{W}_1}{\dot{W}_2} = \left(\frac{N_1}{N_2} \right)^3 \cdot \left(\frac{D_1}{D_2} \right)^5 \quad (4)$$

For the same pump running at different speeds, the ratio of diameters is one and so these equations simplify as shown:

$$\frac{Q_1}{Q_2} = \frac{N_1}{N_2} \quad (5)$$

$$\frac{H_1}{H_2} = \left(\frac{N_1}{N_2} \right)^2 \quad (6)$$

$$\frac{NPSH_1}{NPSH_2} = \left(\frac{N_1}{N_2} \right)^2 \quad (7)$$

$$\frac{\dot{W}_1}{\dot{W}_2} = \left(\frac{N_1}{N_2} \right)^3 \quad (8)$$

Consequently, if pump curves are obtained for a given speed, these may be scaled according to these equations when the pump is running at different speeds.

2.2.2 Pumps in Series and Parallel

Pumps in series – for example, a booster pump and a main pump – all experience the same mass flow rate, and thus for an approximately constant fluid density, approximately the same volumetric flow rate. The total head generated is the sum of the head produced per pump, which may be expressed as follows:

$$H_{Total} = \sum_{i=1}^{n} H_{Pump(i)} = H_{Pump(1)} + H_{Pump(2)} + \ldots \quad (9)$$

If a multistage pump is comprised of identical impellers per stage (which is commonly the case), then each stage can be assumed to contribute the same head increase (that is, the total head generated divided by the number of stages). A multistage pump curve may therefore readily be split into smaller single stage curves.

For pumps in parallel, the total head increase over each pump is the same while the flow may differ.

2.2.3 Net Positive Suction Head

This section is based on the discussion by Sulzer (2010).

The leading edge of a pump impeller is subject to localised points of high velocity and low pressure, where the fluid may evaporate if the pressure at that point falls below the vapour pressure of the fluid at that temperature. If this occurs, the resulting bubbles that form collapse where the fluid pressure again increases above the vapour pressure. It is this sudden collapse of the bubbles that causes cavitation damage to surfaces downstream. A net positive suction head (NPSH) is therefore defined in order to avoid this phenomenon. Different NPSH values may be obtained for a pump running at a given speed and with a constant flow rate, where the suction head is reduced in steps and the impeller eye is monitored with a stroboscope. These are:

1. $NPSH_i$: cavitation inception – the suction head at which bubbles are first observed,
2. $NPSH_0$: 0 % head drop – the suction head at which head output of the pump will start to reduce,
3. $NPSH_3$: 3 % head drop – the suction head at which 3 % drop in pump head output will occur, a widely used criterion as it is easier to measure than the other values,
4. $NPSH_{FC}$: full choking.

The available NPSH is defined as follows:

$$NPSH_A = \frac{p_s - p_v}{\rho \cdot g} + \frac{v_s^2}{2 \cdot g} \quad (10)$$

Where:

- p_s is the absolute suction pressure
- p_v is the absolute vapour pressure (that is, saturation pressure) at the fluid temperature
- v_s is the suction flow velocity

The NPSH margin is the difference between the available NPSH, $NPSH_A$, and the required NPSH, $NPSH_R$. $NPSH_R$ is required NPSH relative to defined conditions – for example, $NPSH_i$ to avoid cavitation inception. If no conditions are specified, then it is conventional to assume that the NPSH value is $NPSH_3$, 3 % NPSH.

2.2.4 Leak-Off Valves

Sulzer (2010) defines minimum flow rate as "the lowest pump delivery that can be maintained for extended periods of operation without excessive wear or even damage". This is determined by the following criteria:

1. Temperature rise due to internal energy loss
2. Increased vibration due to excessive flow separation and recirculation
3. Increased pressure fluctuation at part load
4. Increased axial thrust at low flow rates
5. Increased radial thrust (this is more applicable to single volute pumps)

Of these, the temperature rise and the poor hydraulic performance are usually the main limitations in setting minimum flow values.

Temperature Rise

Only part of the power consumed by a pump is converted into hydraulic energy. Most of the remaining energy is converted into heat due to friction within the pump. External energy losses due to factors such as the mechanical losses in bearings are relatively small and will be neglected in this discussion. As flow rate is reduced, hydraulic efficiency is reduced and internal losses increase. This leads to severely elevated fluid temperatures which increase the vapour pressure and make evaporation more likely, with associated dangers of cavitation damage. Figure 2.16 from Sulzer's Centrifugal Pump Handbook (2010) illustrates this conceptually.

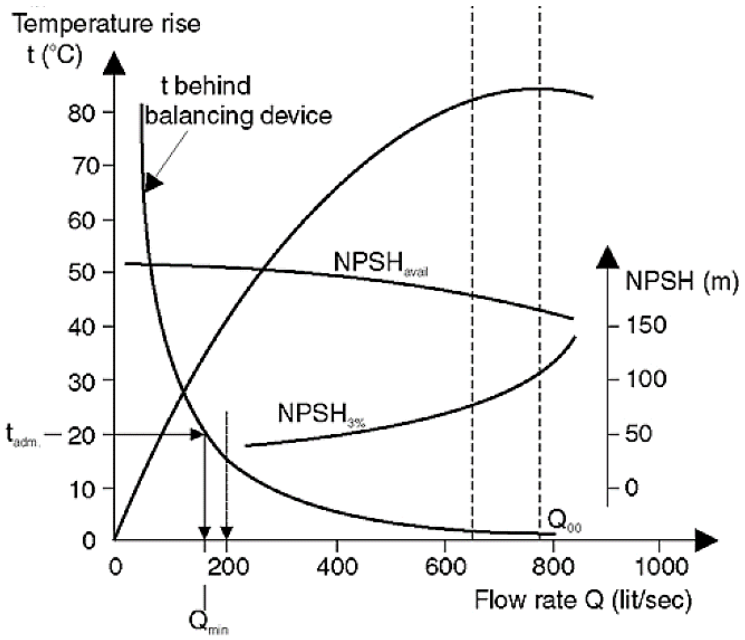

Figure 2.16: Typical temperature rise in a pump at low flow (Sulzer, 2010)

Poor Hydraulic Performance

For pumps with a power input exceeding about 1 MW and with high specific speed, a higher minimum flow rate may be required than that expected from temperature rise only. Forces due to flow recirculation at the impeller entry may cause excessive vibration in the pump and pipework, even at 25 % to 35 % of the flow at the best efficiency point. A diagram appears in Figure 2.17 providing guidelines in this respect (Sulzer, 2010).

This diagram is in terms of specific speed, defined as:

$$N_q = N \cdot \frac{\sqrt{Q}}{H_{st}^{3/4}} \qquad (11)$$

Where H_{st} is the stage head in m, Q is the flow rate in m^3/s and N is the pump speed in rpm.

For Station A1, the specific speed was calculated to be 27 and for Station B1, it was calculated to be 39. These were calculated at the MCR (maximum continuous rating) conditions. These points are illustrated in Figure 2.17. Q_{00} is flow at the best efficiency point. For stations A1 and B1, this value is 550 L/s. This indicates that to avoid hydraulic instability, the flow rate should exceed 25 % of Q_{00}. To remain within the stable working range, the flow rate should exceed 40 % of Q_{00}.

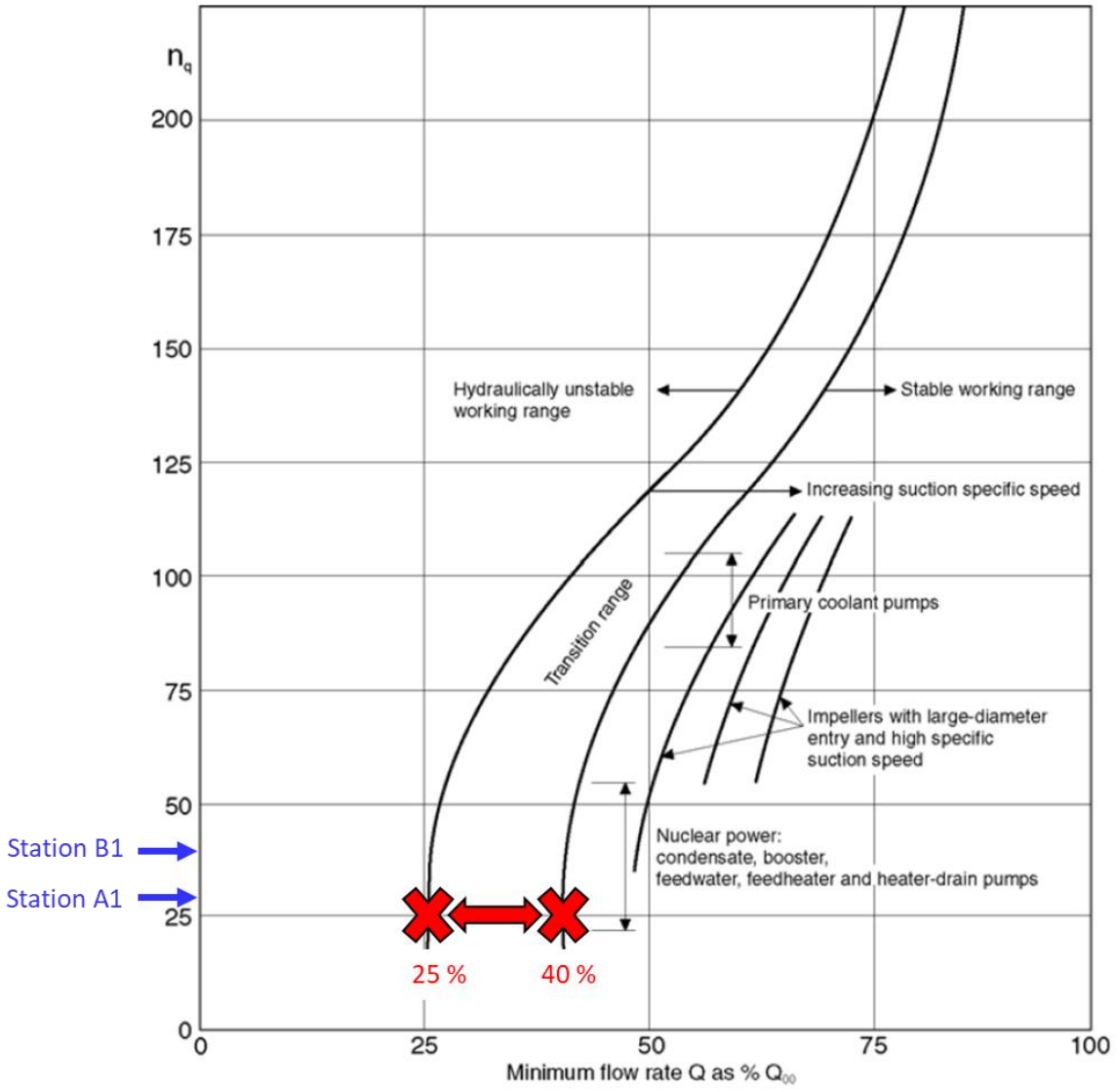

Figure 2.17: Minimum flow rate guidelines for pumps exceeding 1 MW power input (Sulzer, 2010, annotated)

Leak-Off Valves

To maintain the minimum flow condition, it is common for centrifugal pumps to have leak-off lines installed which recirculate fluid from the pump discharge back to the suction line or the supply tank. Because of the pressure difference, it is necessary for a large pressure drop to occur over the leak-off line, and leak-off valves are designed accordingly. Pumping to the supply tank is preferable to pumping directly to the suction because the warmer discharge water is then able to mix with the cooler water in the tank.

There are four main types of leak-off valves:

1. Fixed flow or orifice
2. ARC (automatic recirculation) type
3. Binary type
4. Modulating type

The first type is not used on feed pumps at Eskom. The second type is common only on the oldest stations in the fleet, working on a purely mechanical spring-loaded principle to cause the valve to open when the pump's NRV closes. The fourth type works with a stack of labyrinths which reduce the pressure and is only present on the newest stations. The remaining stations utilise the third type – the binary type. This binary type works on an open / closed principle and applies to stations A1, A2, B1 and B2 considered in this study.

Figure 2.18 illustrates the OEM-defined leak-off curve for Station A1. The pump curves used were for a speed of 4542 rpm, with the head being shown per stage. It can be observed that for the volumetric flow rate associated with the rated boiler MCR (Q_{00}), the leak-off valves are expected to open at 14.5 % of Q_{00}. This differs from the recommended limits in Figure 2.17. The different limits will be explored in Chapter 4.

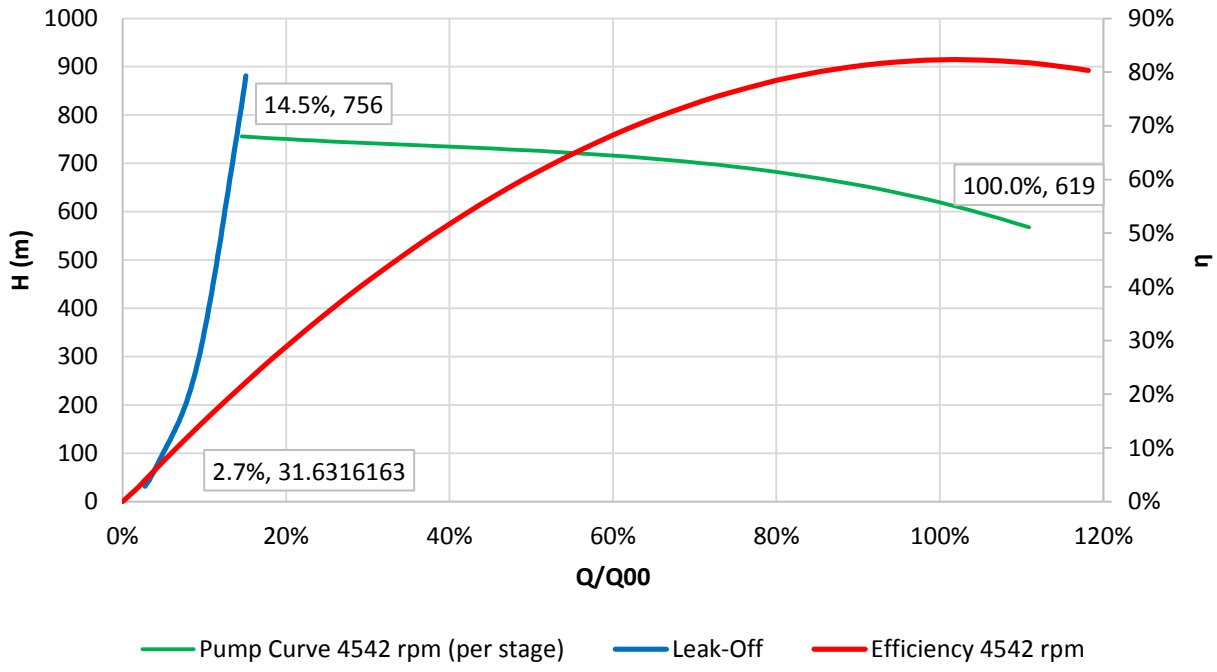

Figure 2.18: OEM-defined leak-off curve for Station A1

In a similar way, the OEM pump curves for Station B1 indicate the leak-off valves are to open at about 15 % of Q_{00}.

At Station A1 and A2, each SFP train has an integrated isolating and pressure reduction valve, whereas originally the isolating valves were parallel slide valves separate from the pressure reduction vessels. This modification was motivated by poor performance and life span of the parallel slide valves as cavitation erosion occurred due to the very high velocities encountered in the valve throats.

An example of a *Zikesch*-type pressure reduction stack is shown in Figure 2.19. The feedwater from the pump discharge enters from the bottom of the diagram and each throttle disc reduces the pressure until the feedwater exits at the right of the diagram.

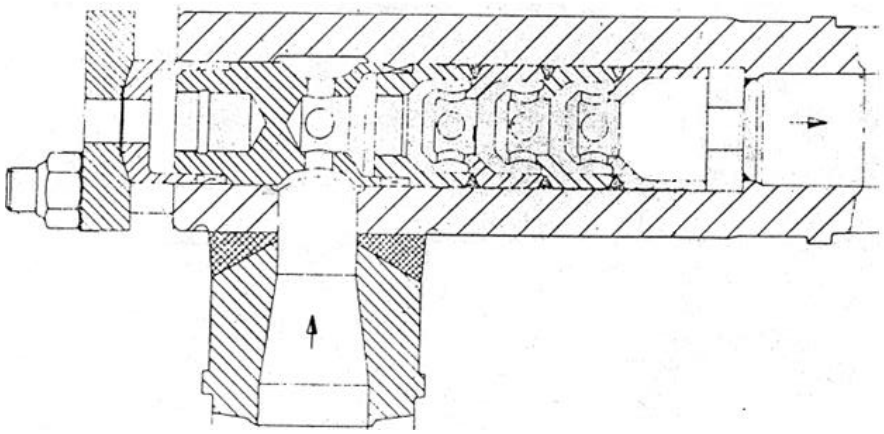

Figure 2.19: Diagram of a typical "Zikesch" throttle disc stack (station manuals)

At Station A2, each EFP train has a separate parallel slide valve and pressure reduction stack but a modification is in progress to change these to integrated valves. At Station A1, these have already been changed to integrated valves, motivated by wear experienced on the parallel slide valves and obsolescence of this valve model.

Regardless of whether the pressure reduction stack is integral to the isolating valve or not, all of these valves will be treated as binary control, that is, either open or closed.

2.2.5 Flow Measurement with Orifice Plates

Orifice plates are commonly used as flow measurement devices, particularly on feedwater flow. In some instances, for example on the SFP leak-off on Station A1, the DCS for a station only measures and records differential pressures without converting this into a flow rate. It is therefore relevant to review the theory. A more detailed discussion is included in Appendix G. This discussion is based on the text "Experimental Methods for Engineers" by Holman (2001) and Standard BS EN ISO 5167, Part 2 (2003), "Measurement of fluid flow by means of pressure differential devices".

Based on this discussion, the pressure drop over an orifice, Δp, may be converted into a volumetric flow rate using the following relationship:

$$Q = \frac{C \cdot \pi}{4} \frac{d^2}{\sqrt{1-\beta^4}} \cdot \sqrt{2 \cdot \Delta p \cdot \rho} \qquad (12)$$

Where:

- Q is the volumetric flow rate
- C is the discharge coefficient, approximately 0.6 for the application of leak-off valves being considered
- d is the orifice diameter
- β is the ratio of orifice diameter to pipe diameter (d/D, which was 0.578 in the leak-off orifice example in Appendix G).
- Δp is the pressure drop over the orifice
- ρ is the fluid density before the orifice
  (All units S.I.)

2.2.6 Electric Motor Theory

This section will revise some elementary theory of electrical machines for use in the electric feed pump consideration in Section 3.15.

The running speed N of an induction motor is always less than the synchronous speed, N_S, which is determined by the frequency of the electrical power supply, f, and the number of poles, p (always a multiple of two). The difference between these two speeds is expressed in the form of a ratio termed slip. Synchronous speed (N_s) in rpm and slip (S) are defined as follows:

$$N_s = \frac{f \cdot 120}{p} \qquad (13)$$

$$S = \frac{N_s - N}{N_s} \tag{14}$$

It follows that:

$$N = N_s \cdot (1 - S) \tag{15}$$

An induction motor has a characteristic torque-speed curve. When expanded, this curve has three sections or modes of operation – motoring, generating and braking, as shown in Figure 2.20 (Wildi, 2006). It is observed that as the machine is operating in the "motor" mode and approaches synchronous speed, the curve becomes almost vertical, such that a significant change in torque may be achieved with very little change in speed. Graphically, as slip tends to zero, the speed tends to N_s, the synchronous speed, and torque tends to zero. A synchronous motor, in comparison, operates at the synchronous speed regardless of the operating condition (provided that this operating condition is within the operating envelope).

In the absence of more detailed information, the electric feed pump motors at Station A1 will be assumed to run at a constant slip on their operating range, this slip being the slip observed at full load.

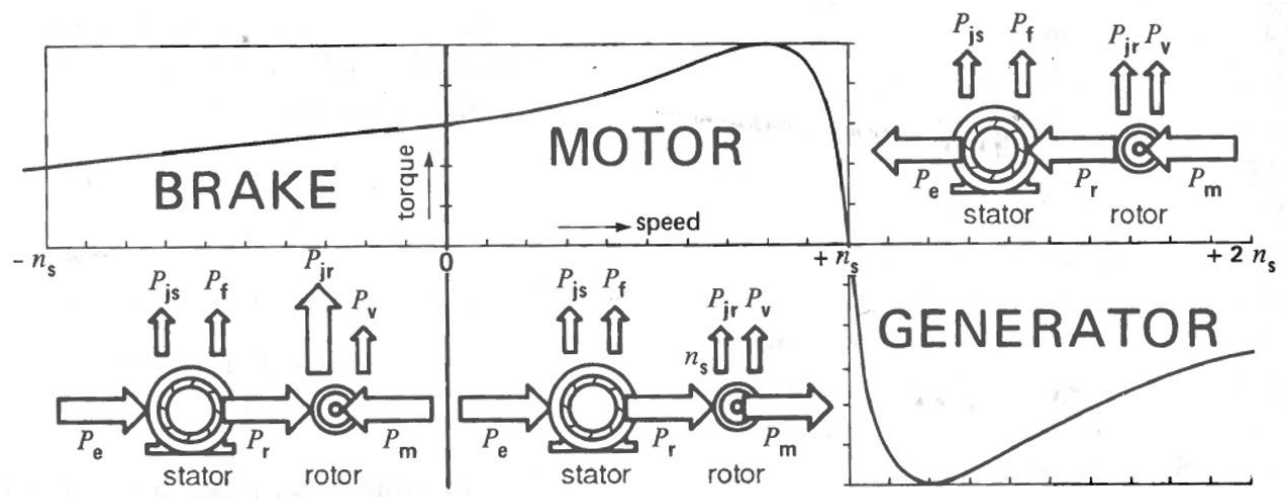

Figure 2.20: Torque-speed curve for an induction motor showing three modes of operation (Wildi, 2006)

Power Consumption and Power Factor

The power consumption of an induction motor may be stated as follows.

Per phase,

$$\dot{W}_{elec,phase} = I_{phase} \cdot V_{phase-neutral} \cdot PF \quad (16)$$

In total,

$$\dot{W}_{elec,3-phase} = 3 \cdot I_{phase} \cdot V_{phase-neutral} \cdot PF \quad (17)$$

Since it is most common for nameplates of induction motors to state the phase-to-phase voltage (that is, the line voltage), it is convenient to rewrite the voltages as follows:

$$V_{phase-neutral} = \frac{V_{phase-phase}}{\sqrt{3}} \quad (18)$$

Thus,

$$\dot{W}_{elec,3-phase} = \sqrt{3} \cdot I_{phase} \cdot V_{phase-phase} \cdot PF \quad (19)$$

The power factor is the ratio of active (real) power [P, kW] to the apparent power [S, kVA]. The apparent power takes into account the reactive or imaginary power. This is expressed in the following equation.

$$PF = \frac{P}{S} \quad (20)$$

Figure 2.21 illustrates typical generic curves for an induction motor (Faizan, A., n.d.). It is observed that at higher loads, the power factor curve is significantly flattened.

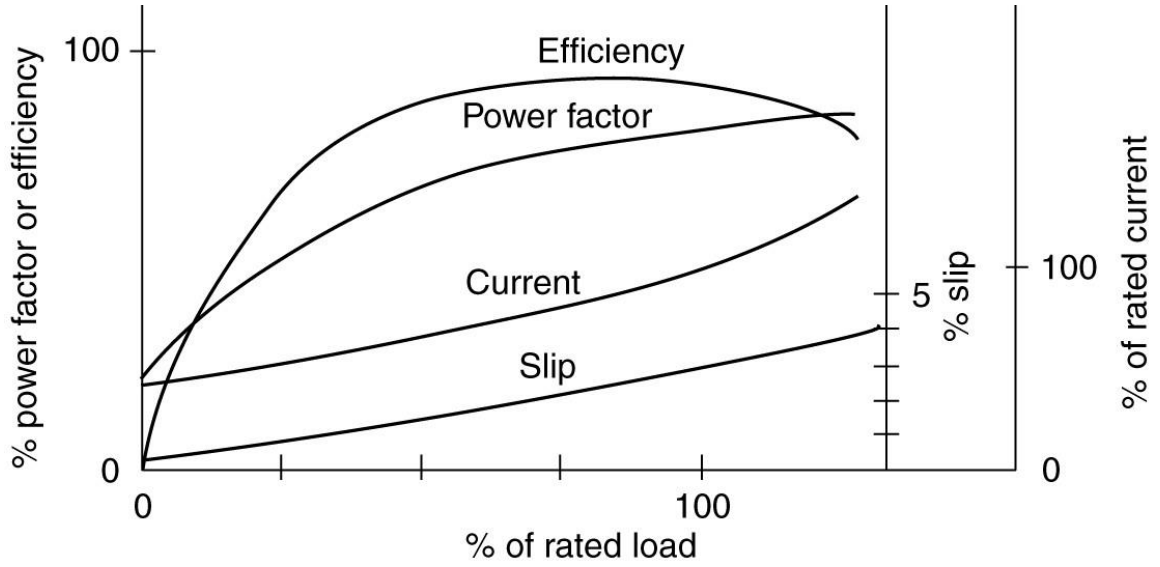

Figure 2.21: Typical power factor curve for an induction motor (Faizan, A., n.d.)

The nominal power factor for the electric feed pump motors at Station A1 is 0.885, based on Eskom reports, and the phase-to-phase voltage (line voltage) is 11 kV. The only DCS plant data available on the motor is the current drawn. At sufficiently high loads, the power factor may be assumed to be relatively constant, and the power consumed may therefore be approximated by the following equation:

$$\dot{W}_{EFP}[kW] = \left(\sqrt{3} \cdot 11 \cdot 0.885\right) \cdot I_{phase}[A] \qquad (21)$$

It is appreciated that as the motor load reduces, the power factor is expected to reduce. This means that applying the above equation with its assumptions, the motor will appear to absorb more real power than it actually does. However, this is the best approximation possible with the available information.

2.3 Turbine Theory

2.3.1 General Considerations

Velocity Triangles

This consideration is limited to axial flow steam turbines as these are the only turbines encountered in the systems of interest. Christie (1910), Church (1928), Cotton (1998), Nag (2008), Dixon and Hall (2014), and Fuls (2017a) were studied. Based on these, Figure 2.22 shows the naming convention for velocity triangles which will be used in this dissertation, noting that different authors show different preferences[4]. Subscript r denotes relative velocity. Subscript b denotes blade. Point 2 for a given stage is taken as the entrance to the rotating row while Point 3 is taken as the exit from the rotating row. Point 1 is taken to be the inlet to the stationary row. For the turbines considered here, every turbine stage is comprised of a stationary row of blades and a rotating row of blades. Subscripts S and R will therefore denote stationary and rotating rows respectively.

[4] It is not uncommon for the symbols c, w and u to be used for absolute steam velocity, relative steam velocity and blade velocity respectively. Some sources also measure angles from the shaft's axial vector instead of measuring from the shaft's tangential vector. Consequently, all angles then become the complements of those expected, and so caution is advisable when equations are used from different sources.

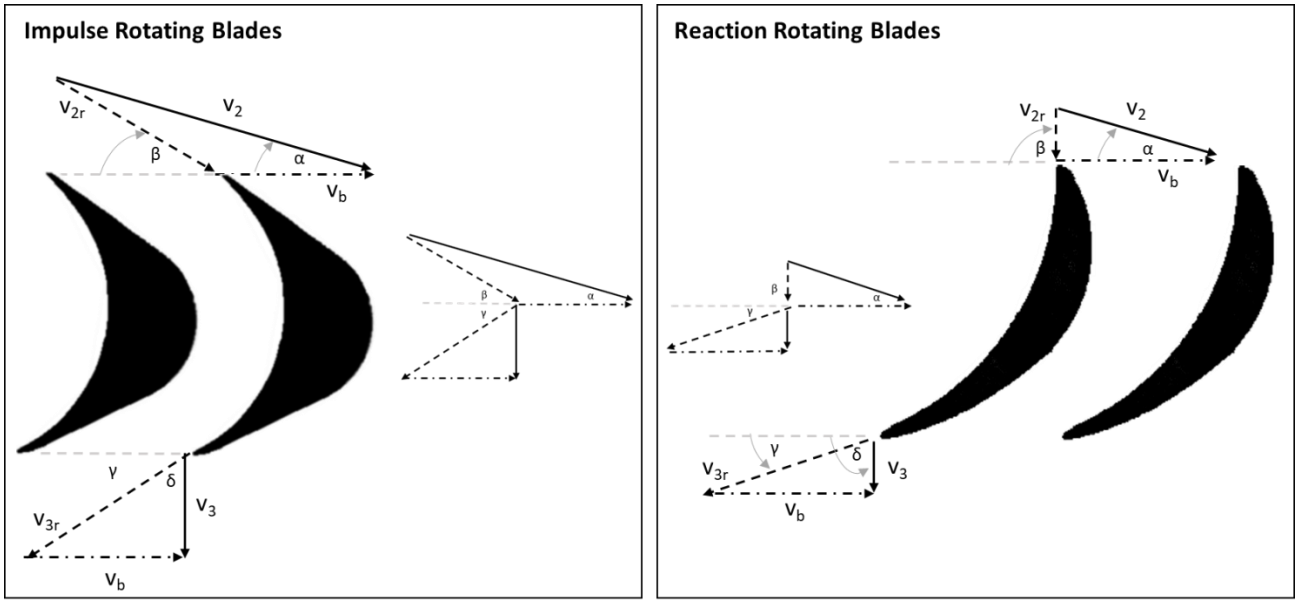

Figure 2.22: Typical turbine rotating blade and velocity triangles: impulse type (left), and 50% reaction type (right)

Figure 2.22 shows the two typical blade types, being impulse and reaction-type. The profiles used in producing these diagrams were obtained from Christie (1910). While advances have been made in optimising blade profiles, these profiles provide a reasonable illustration for this discussion.

Some symmetry and equality assumptions can normally be made and these are illustrated in Figure 2.22. For the impulse case, $v_{2r} \approx v_{3r}$ and $\beta \approx \gamma$, making the rotating blades symmetric. For the 50 % reaction case, $v_2 \approx v_{3r}$, $\alpha \approx \gamma$, $v_{2r} \approx v_3$, and $\beta \approx \delta$. Consequently, for 50 % reaction turbines, the stationary and rotating blades mirror each other. In both cases, $\delta \approx 90°$ for optimum stage efficiency, while Nag (2008) reports that α is typically in the range 16° to 22°. Figure 2.23 illustrates the scenarios possible for the absolute exit velocities from a rotating blade. When δ is acute (scenario (i)), the turbine is braked and when δ is obtuse (scenario (iii)), energy is wasted. This applies to impulse blades (left) and reaction blades (right).

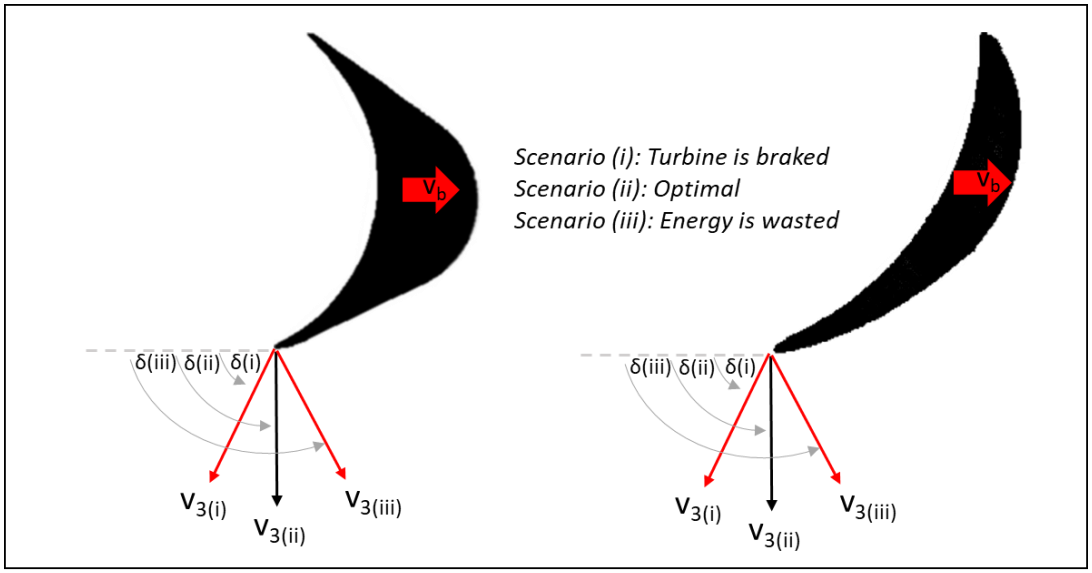

Figure 2.23: Different scenarios for the absolute exit velocities from a rotating blade

It follows from Figure 2.22 that repeating stages in a reaction turbine will appear similar to those in Figure 2.24, allowing for the same blades to be used for stationary and rotating rows.

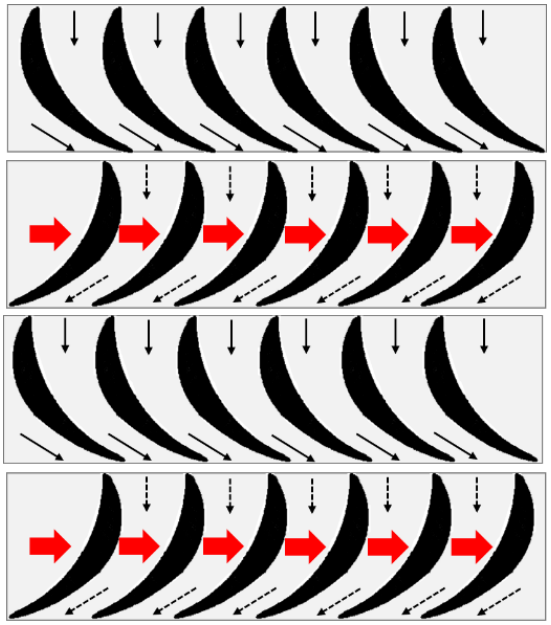

Figure 2.24: Repeating stages in a reaction turbine

Dimensionless Parameters R and Γ

The reaction ratio is defined as follows:

$$R = \frac{\Delta h_{row,rotating}}{\Delta h_{stage}} = \frac{h_2 - h_3}{h_1 - h_3} \qquad (22)$$

A variable Γ may be defined such that:

$$\Delta h_{stage} = \Gamma \cdot \frac{v_b^{\,2}}{\cos^2 \alpha} \qquad (23)$$

It can be shown using the velocity triangles above that for optimal efficiency, an impulse stage has Γ = 2 and a 50 % reaction stage has Γ = 1. More generally, it can be shown that for optimal blade efficiency:

$$\Gamma = 2 \cdot (1 - R) \qquad (24)$$

This relationship is derived in detail in Appendix F. See also the work of Dixon and Hall (2014) for further discussion.

Changing Reaction Ratios

This above equation can be used to estimate the enthalpy drop per stage for different reaction ratios. In practice, R typically ranges from 0 (impulse turbines) to 0.5 (50 % reaction turbines). Whereas texts commonly consider only R=0 or R=0.5, Cotton (1998) shows that coal-fired power stations typically display a significant increase in reaction ratio along the turbine steam path, regardless of whether the turbine is nominally impulse or reaction. Typical industry values for steam turbines on coal-fired power stations are shown in Figure 2.25. For comparison, the corresponding diagram from Cotton for nuclear turbines is shown in Figure 2.26. The trends for LP turbines in Figure 2.26 bear some similarities to those of Figure 2.25. Because the BFPTs under consideration are all condensing turbines, the LP (low pressure) turbines will be considered suitable approximations for BFPTs.

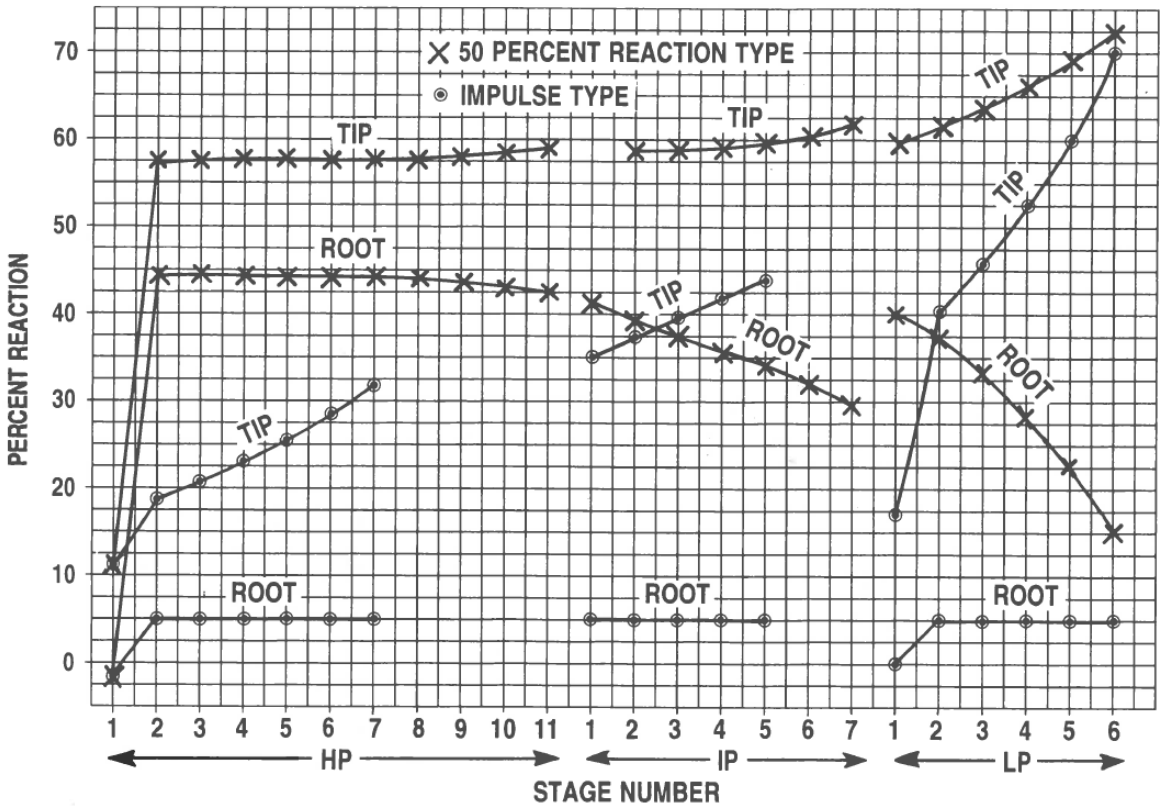

Figure 2.25: Typical reaction ratios for steam turbines on coal-fired power stations (Cotton, 1998a)

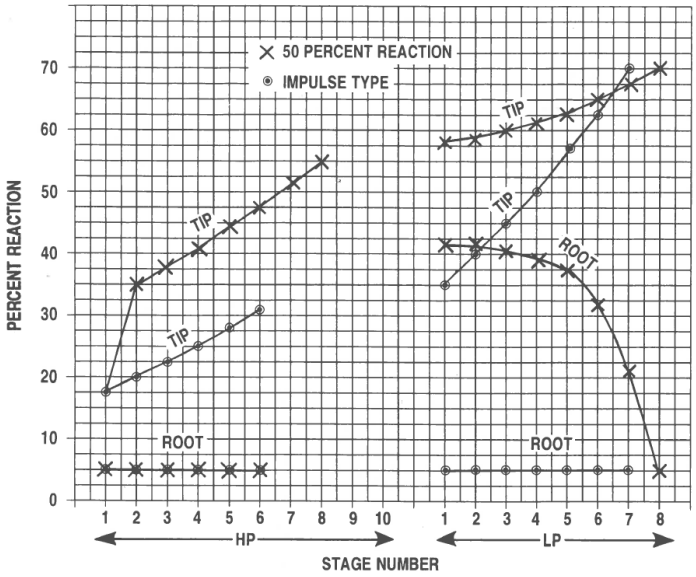

Figure 2.26: Typical reaction ratios for steam turbines on nuclear power stations (Cotton, 1998b)

2.3.2 Turbine Modelling using the Nozzle Model

The stage-by-stage turbine nozzle model developed by Fuls (2017a) forms the basis for the turbine modelling methodology used here. This is summarised visually in Figure 2.27 as an excerpt from the paper introducing this methodology, "Accurate stage-by-stage modelling of axial turbines using an appropriate nozzle analogy with minimal geometric data". In the paper, it is shown that any axial flow steam turbine may be represented in the form of a stator nozzle to represent the acceleration of the fluid through the stationary blades, a rotor nozzle to represent the acceleration of the fluid through the rotating blades, a work extraction point to represent the removal of energy from the fluid as work is done, and a carry-over diffuser component which represents the carry-over efficiency between stages – that is, the extent to which kinetic energy is dissipated before reaching the next stage. These nozzles must have defined throat areas A_S and A_R as well as loss coefficients, ζ_S and ζ_R. The diffuser is assigned a carry-over efficiency, η_{CO}.

It is noted that in Figure 2.27 the velocity triangle naming conventions generally align with those of Figure 2.22 but the rotor exit velocities are manipulated so that the nozzle effect and the work extraction may be separated in the model. *For this reason, point 4 in Figure 2.27 corresponds to point 3 in Figure 2.22.*

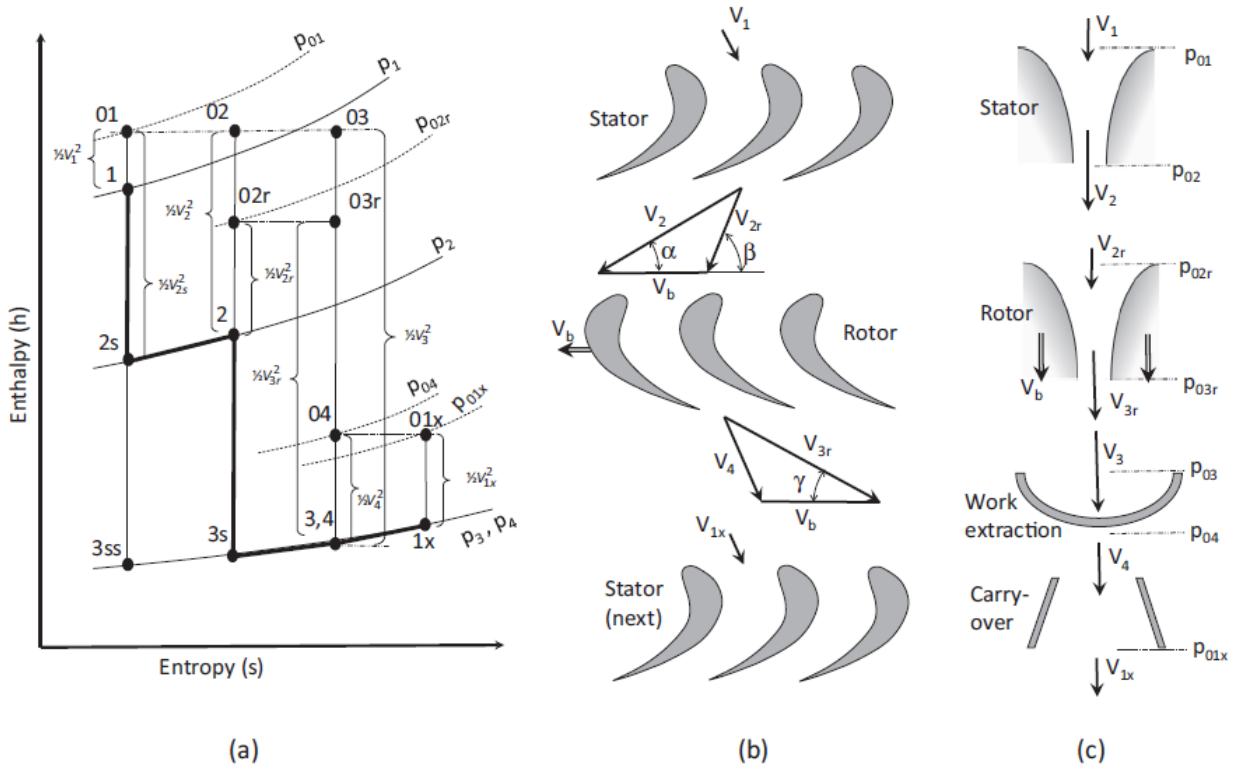

Figure 2.27: Excerpt from the turbine nozzle analogy paper. (a) Mollier diagram of the expansion process. (b) Velocity triangles. (c) Moving nozzle analogy. (Fuls, 2017a)

These four elements will be considered in more detail with relevant equations– stator nozzle, rotor nozzle, work extraction and carry-over diffuser, as these must be understood in order to apply the methodology to the systems of interest. Note that for these discussions, it is assumed that the nozzles are subsonic and not choked. All subscripts should be read with reference to Figure 2.27.

Stator Nozzle

The absolute exit velocity after the stator nozzle, v_2, can be expressed in terms of the inlet total enthalpy h_{01} , isentropic exit static enthalpy h_{2s} and the stator nozzle loss coefficient ζ_S as follows:

$$v_2 = \sqrt{\frac{1}{1+\zeta_S}} \cdot \sqrt{2 \cdot (h_{01} - h_{2s})} \tag{25}$$

The actual exit static enthalpy is then

$$h_2 = h_{01} - \frac{1}{2} \cdot v_2{}^2 \tag{26}$$

This is illustrated in on a Mollier diagram in Figure 2.28, an annotated version of the figure from Fuls, 2017a.

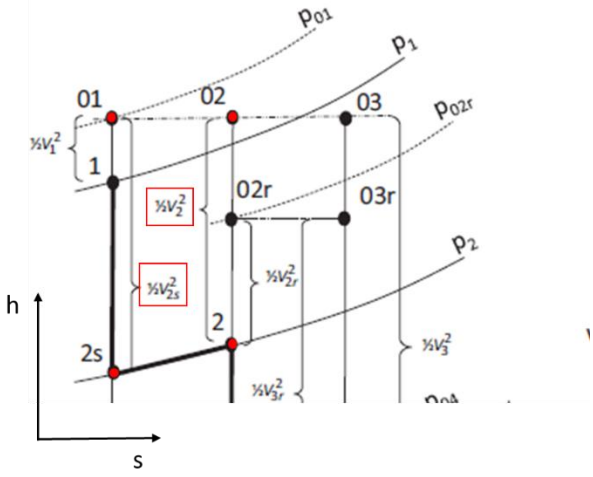

Figure 2.28: Mollier diagram for stator nozzle (Fuls, 2017a, annotated)

Rotor Nozzle

Applying the cosine rule to the velocity triangle at Point 2, the relative velocity entering the rotor may be expressed as follows:

$$v_{2r} = \sqrt{v_b^2 + v_2^2 - 2 \cdot v_b \cdot v_2 \cdot \cos\alpha} \tag{27}$$

The **relative** total enthalpy remains constant as it is assumed that no work is being extracted yet:

$$h_{02r} = h_2 + \frac{1}{2} \cdot v_{2r}{}^2 \tag{28}$$

As for the stator nozzle, the relative exit velocity can be calculated as:

$$v_{3r} = \sqrt{\frac{1}{1-\zeta_R}} \cdot \sqrt{2 \cdot (h_{02r} - h_{3s})} \tag{29}$$

And the exit static enthalpy is:

$$h_3 = h_{02r} - \frac{1}{2} \cdot v_{3r}{}^2 \tag{30}$$

This is illustrated in on a Mollier diagram in Figure 2.29, an annotated version of the figure from Fuls, 2017a. The enthalpy drop from point (2) to point (3) is all converted to (relative) velocity.

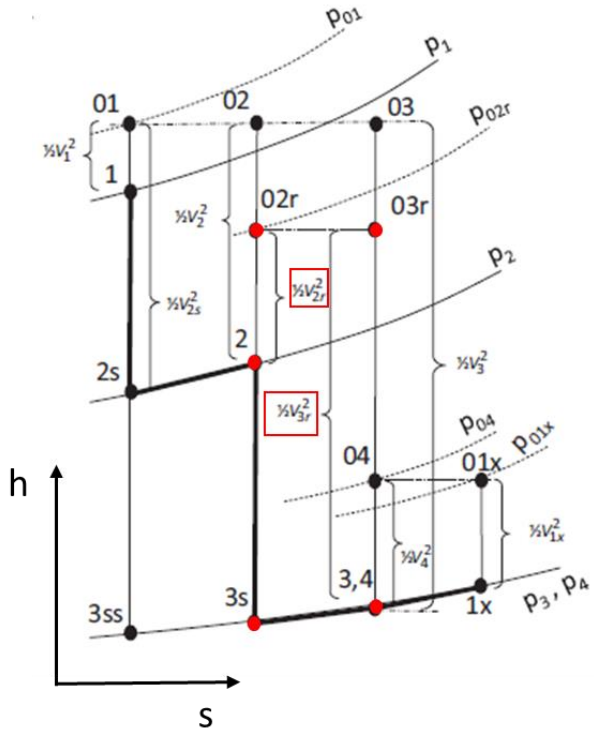

Figure 2.29: Mollier diagram for rotor nozzle (Fuls, 2017a, annotated)

Work Extraction

One can consider a fictitious kinetic energy component, v_3 after the rotor as if no work was extracted from the fluid up to this point. (In practice, over the rotating row, work is extracted even as the flow is accelerated by the nozzle.) This velocity is defined as:

$$v_3 = \sqrt{2 \cdot (h_{01} - h_3)} \tag{31}$$

This is not to be confused with the exit velocity v_3 shown in Figure 2.22. A blade efficiency, η_b, is defined to represent the portion of the fictitious kinetic energy which is converted into shaft work. This cannot be 100 % as this would imply completely stagnant exit conditions. The work is then expressed as:

$$w = \eta_b \cdot \tfrac{1}{2} v_3^{\,2} \tag{32}$$

One can also calculate the work extraction using velocity triangles, and considering Euler's turbomachinery equation, resulting in an efficiency of:

$$\eta_b = \frac{v_b(v_2 \cos\alpha + v_{3r} \cos\gamma - v_b)}{\tfrac{1}{2} v_3^{\,2}} \tag{33}$$

The numerator is the Euler work done while the denominator is the maximum work that could be extracted: $h_{01} - h_4$. In order to calculate the blade efficiency, an assumption must be made about γ, the rotor blade exit angle. For the impulse stage component implemented in *Flownex*, the assumption is that $\gamma \approx \beta$. For the reaction stage, the assumption is that $\gamma = \alpha$. This is based on the usual assumptions made with respect to the symmetry of velocity triangles (refer to Section 2.3.1).

The kinetic energy remaining after the stage (exit velocity) can then be calculated as:

$$v_4 = \sqrt{1-\eta_b} \cdot v_3 \tag{34}$$

Note that:

$$h_{04} = h_{01} - w \tag{35}$$

This is illustrated on a Mollier diagram in Figure 2.28.

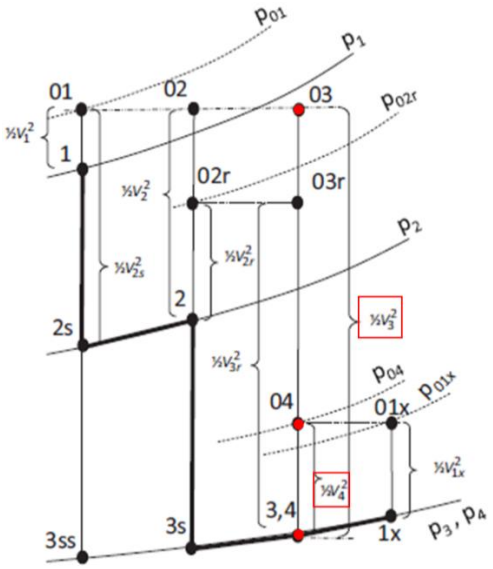

Figure 2.30: Mollier diagram for work extraction (Fuls, 2017a, annotated)

Carry-over

Not all of this kinetic energy is carried through to the next stage. Turbulence and sudden expansion cause some of this kinetic energy to return to heat. By defining a carry-over efficiency, $\eta_{CO,}$ the velocity reaching the next stage can be expressed as:

$$v_{1x} = \sqrt{\eta_{CO}} \cdot v_4 \tag{36}$$

Because no work is done in the carry-over section, the total enthalpy remains unchanged:

$$h_{01x} = h_{04} \tag{37}$$

The static inlet pressure p_{1x} to the following stage is the same as the static exit pressure of the stage before it, p_4 (assuming no choking in the rotor). The total pressure will however decrease over this gap due to the loss of kinetic energy. Carry-over losses are often termed “reheat losses” in steam turbines. This is illustrated on a Mollier diagram in Figure 2.31.

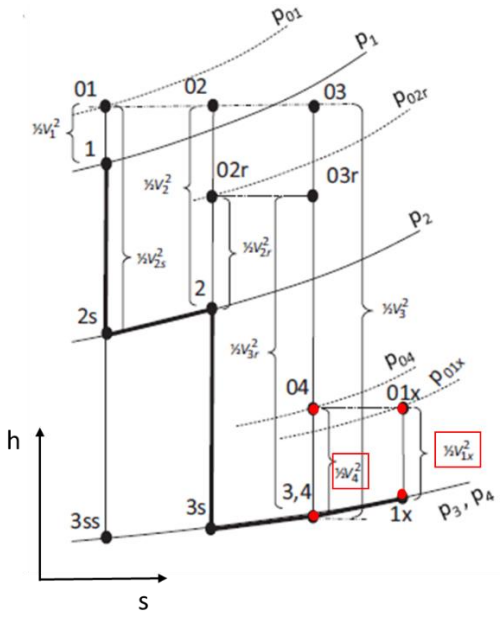

Figure 2.31: Mollier diagram for carry-over (Fuls, 2017a, annotated)

2.3.3 Choking and Sonic Flow

As noted in Section 2.3.2, the turbine nozzle model assumes no choking. A nozzle is said to be choked when the Mach number at its throat is 1, that is, the velocity has reached the speed of sound in that medium. The discharge (mass flow per unit area) is then at its maximum and more discharge cannot be achieved, even with reduced outlet pressures.

Classical nozzle theory defines a critical pressure ratio, r^*, above which choking will not occur. For an ideal gas it is defined as follows:

$$r^* = \frac{p^*}{p_0} = \left(\frac{2}{\gamma+1}\right)^{\frac{\gamma}{\gamma-1}} \tag{38}$$

Where p_0 is the total pressure at the nozzle inlet, p* is the static pressure at the throat when the flow is choked and γ is the specific heat ratio, c_p/c_v.

It may be assumed that steam expands isentropically through the nozzle according to the following relationship:

$$\left(\frac{p_1}{\rho_1}\right)^{k_1} = \left(\frac{p_2}{\rho_2}\right)^{k_2} \tag{39}$$

Where (1) and (2) are any two points along the length of the nozzle.

Thus the equation becomes:

$$r^* = \frac{p^*}{p_0} = \left(\frac{2}{k+1}\right)^{\frac{k}{k-1}} \tag{40}$$

k is termed the isentropic index. For initially dry saturated steam, k=1.135 and therefore r*=0.577. For initially superheated steam, k=1.3 and therefore r*=0.546. For wet steam, Zeuner's relation is used, shown below where x is the steam quality, or dryness (Nag, 2008).

$$k = 1.035 + 0.1x \tag{41}$$

The actual pressure ratio over the nozzle must be kept above this critical pressure ratio, in order to prevent choking from occurring. Figure 2.32 illustrates this graphically.

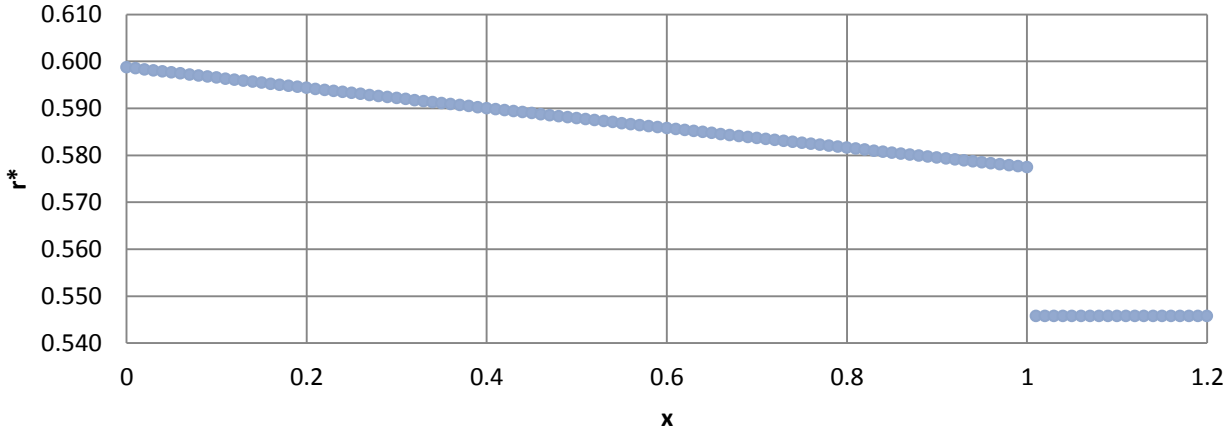

Figure 2.32: Effect of steam dryness on critical pressure ratio

Sonic Flow in Last Stages of LP Turbines

Cotton (1998) notes that LP turbines typically experience sonic conditions in the last stage at design conditions, with the critical pressure ratio being exceeded on the stationary and rotating blades. Once a choked flow condition is reached, decreasing the condenser pressure has no effect on the stages upstream and so there is no gain in power output.

2.3.4 Other Dimensionless Descriptors

Dixon and Hall (2014) identify three common dimensionless descriptors used to describe a turbine: design flow coefficient (φ), stage loading coefficient (ψ) and stage reaction (R). Reaction was already discussed in Section 2.3.1 but the other two descriptors will be introduced here.

Blade speed ratio (ρ) will also be considered with reference to Church (1928) and Nag (2008). The coefficient Γ, discussed by Fuls (2017a) which could be termed the static enthalpy drop coefficient, was already introduced in Section 2.3.1.

Design Flow Coefficient (and Blade Speed Ratio)

The design flow coefficient is defined as follows, with reference to Figure 2.22:

$$\phi = \frac{v_2 \cdot \sin\alpha}{v_b} \tag{42}$$

The blade speed ratio, ρ, is defined as follows:

$$\rho = \frac{v_b}{v_2} \tag{43}$$

That is, the ratio of the blade speed to the absolute velocity of the steam jet as it reaches this rotating blade.

ρ and φ are therefore related as follows:

$$\phi = \frac{\sin \alpha}{\rho} \tag{44}$$

Stage Loading Coefficient

This is defined as:

$$\psi = \frac{h_{02} - h_{03}}{{v_b}^2} = \frac{w}{{v_b}^2} \tag{45}$$

Applying Euler's turbomachinery equation, this becomes:

$$\psi = \frac{v_2 \cdot \cos \alpha + v_3 \cdot \cos \delta}{v_b} \tag{46}$$

For a turbine running at optimum efficiency, δ=0 °, and the stage loading becomes the same as the static enthalpy drop coefficient Γ, as shown in Appendix F.

2.3.5 Discussion of Impulse and Reaction Turbines

Typical velocity diagrams for impulse and reaction blades were discussed in Figure 2.22. This section will briefly contrast these two types of blading, as well as pressure versus velocity staging.

A Pelton wheel is a typical impulse turbine which is relatively easy to visualise. One is shown in Figure 2.33 and Figure 2.34 below. It is readily observed that it is the impulse of the water jet striking the buckets that drives the buckets around. This is contrasted with the oldest known turbine, that of Heron of Alexandria, shown in Figure 2.35. This is a reaction turbine and while this configuration is not common for practical use, it does serve to illustrate the concept. All of the driving force on the turbine is imparted as a reaction to the steam escaping through the nozzles, in much the same way as a rocket functions.

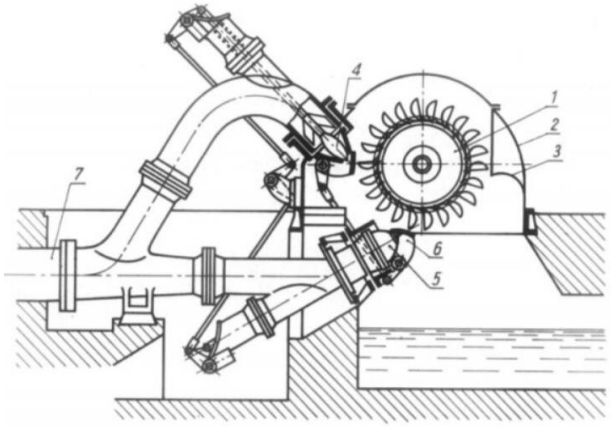

Figure 2.33: Diagram of a typical Pelton wheel (Fundacja na rzecz Czystej Energii, 2018a)

Figure 2.34: Photograph of a typical Pelton wheel (Fundacja na rzecz Czystej Energii, 2018b)

Figure 2.35: A replica of Heron of Alexandria's steam turbine (Bentley, 2007)

Impulse steam turbines are sometimes referred to as De Laval turbines, particularly in the case of a single stage turbine. Neglecting friction, there is no static pressure drop over the rotating blades of an impulse turbine. All of the work done on the rotating blades is due to the action of the jet as it strikes the blade and is then deflected. There is no nozzle behaviour over the rotating blades and no associated reaction force. The cross section reduces over the nozzles/fixed blades (assuming pressure staging) but remains constant over the moving blades.

50 % reaction steam turbines are sometimes referred to as Parsons turbines. "Reaction turbine" is typically taken to mean "50 % reaction turbine" unless otherwise specified. Unlike the impulse turbine, where all of the static pressure drop occurs over the stationary blades/nozzles, in a reaction turbine, this pressure drop, and corresponding enthalpy drop, occurs over both stationary and rotating blades. For a 50 % reaction turbine, the static enthalpy drop is split 50 % between

moving and stationary blades. Some of the work done on the blades is due to the impulse of the jet of steam striking the rotating blades and being deflected and some of the work is due to the reaction of the steam on the blades as the flow is accelerated by the nozzle action of the converging rotating blades.

Symmetry assumptions were considered in Figure 2.22; the condensed versions of these velocity triangles are shown in Figure 2.36. In both diagrams, δ = 90 °.

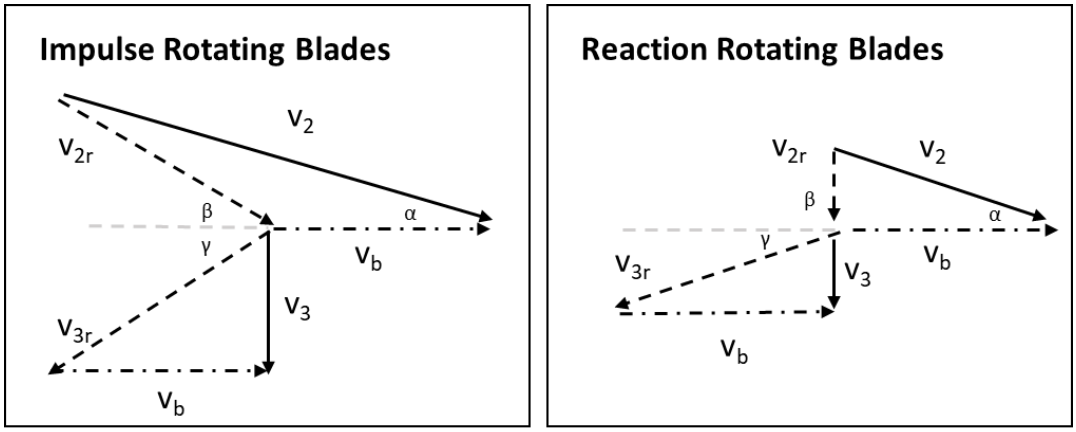

Figure 2.36: Condensed typical velocity triangles

Blade Shapes

According to Church (1928), impulse rotating blades are typically formed by connecting the arcs of two concentric circles with tangents, such that the tips on both ends are very sharp. These blades are usually approximately symmetric. These shapes can be adjusted further to accommodate real effects – for example, by increasing β and by decreasing γ.

For the steam to enter the blading without shock, the following relationship should hold, which is evident from the velocity triangles:

$$\tan\beta = \frac{\sin\alpha}{\cos\alpha - \rho} \qquad (47)$$

Church notes that in practice, the blade angle β tends to be slightly larger than the value obtained above. The exit blade angle, γ, is in practice often made smaller than β in order to improve efficiency but this is limited by considerations of friction. Typical values at high and intermediate pressures are in the region of 15 ° to 30 ° and in the region 30 ° to 40 ° at the turbine's low-pressure end (Church, 1928).

Christie, 1920, in the Marine Engineer's Handbook, comments that outlet blade angles vary from 16 ° to 35 °, being larger in Curtis stages and in the last stages of a turbine under vacuum. The inlet blade angle is typically larger than that dictated by the relative velocity inlet angle, some designers choosing to add 5 ° to this value. A typical blade design is illustrated in cross-section in Figure 2.37. The axial flow is from left to right.

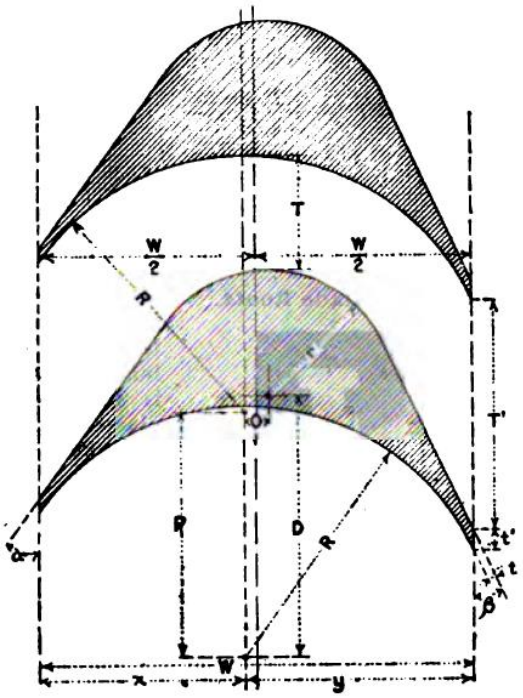

Figure 2.37: Illustration of the design of a typical impulse blade (Christie, 1920, p. 615)

Unlike impulse rotating blades which base their shape on arcs of concentric circles, reaction blading does not have such a well-defined geometric form. The following points generally apply, however (Church, 1928):

i. The entrance blade angle approximately aligns with the relative velocity of the steam from the stationary row before it
ii. The concave face is an arc of a single radius (as far as possible)
iii. The exit has a well-defined convergent nozzle which does not become divergent on the longest allowable blade (whether at the tip or the root)

In practice, blade entrance angles are typically 5 ° to 15 ° larger than the angle of the relative velocity vector, resulting in an inlet blade angle of about 85 ° being common (Church, 1928). Christie (1920) also provides a figure of about 85 ° but suggests that the tangent of the curve at entrance approximately aligns with the relative velocity vector. The exit angles are typically stated indirectly in the form of "gaging". Church considers gaging in the range 20 % to 75 %, which corresponds to approximately 11.5 ° to 48.6 °.

Christie (1920) states that the outlet angle is usually 18 ° to 22 °, averaging 20 °. In the case of "wing blades", the last stages, outlet angles of up to 50 ° are encountered, with outlet angles of about 35 ° being encountered on semi-wing blades (the blades upstream of wing blades). Typical designs are illustrated in Figure 2.38 and Figure 2.39. Axial flow is directed down and blade motion is to the left in both diagrams.

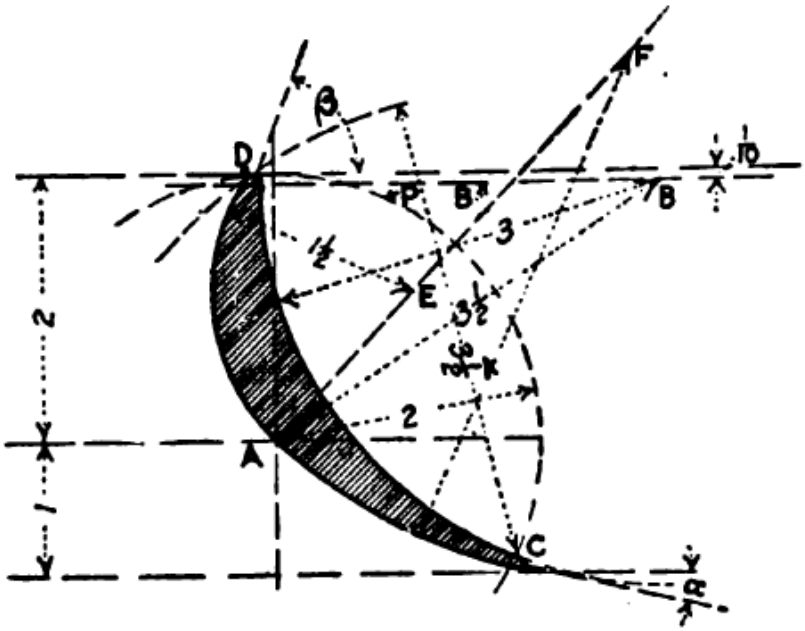

Figure 2.38: Illustration of the design of a typical reaction blade (Christie, 1920, p. 620)

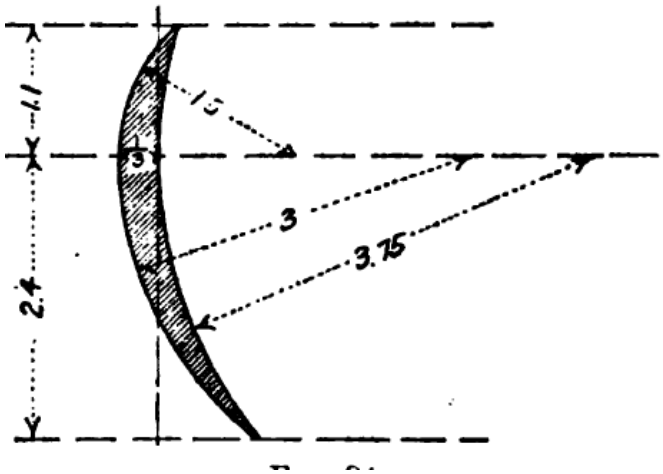

Figure 2.39: Illustration of the design of a typical full-wing reaction blade (Christie, 1920, p. 621)

Figure 2.40 from Wikipedia's Emoscopes (2006) conveniently summarises some of the major differences between impulse and reaction turbines.

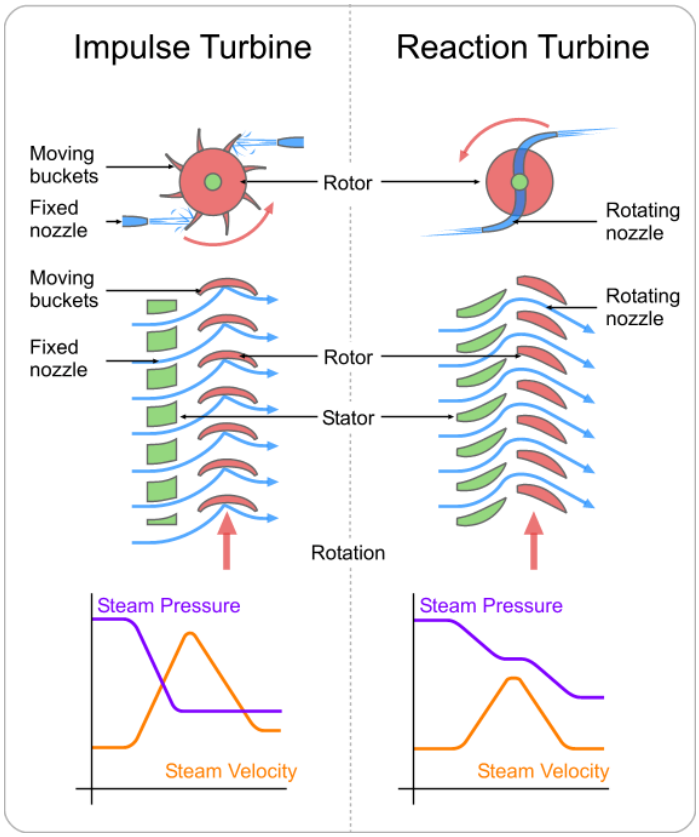

Figure 2.40: Diagram contrasting impulse and reaction turbines (Emoscopes, 2006)

Velocity vs Pressure Staging

In a pressure stage, there is a drop in static pressure over the stationary blades / nozzles. The cross-sectional area reduces and there is an associated velocity increase. This corresponds to a decrease in the static enthalpy. The stages considered so far have all been pressure stages. Pressure staging turbines are sometimes referred to as Rateau turbines. This is the assumed configuration unless otherwise specified.

In a velocity stage, the stationary row serves only to redirect the flow to the next moving row. The cross-sectional area is effectively constant and the static pressure and velocity therefore remain approximately constant over the stationary row (neglecting losses due to friction). In other words, there is no nozzle effect associated with the stationary rows and the stage has a reaction ratio, R, of 1. Multiple velocity stages are uncommon; the limit in practice is usually two, sometimes three stages. A major reason for this is that as more stages are added, the percentage work extracted by later stages reduces substantially. With an idealised three-stage scenario, the work extraction ratio is approximately 5:3:1. With four, 7:5:3:1 (Church, 1928).

Velocity staging is usually only seen in the first stages of a HP turbine, and is then referred to as a Curtis stage, or a two-row governing stage. A single-row governing stage is simply an impulse stage. The turbines considered in this dissertation are comprised exclusively of pressure stages.

Example Velocity Triangles

Applying the equations introduced for ρ as a function of R, summarised in the equation below, and enforcing the requirement that δ = 90 ° (axial exit), the diagrams in Figure 2.41 were generated. (This relationship is discussed in more detail in Section Figure 2.31.) Blade velocity was kept constant at 320 m/s and α was kept constant at 20 ° for ease of comparison. The solid lines represent the absolute velocity vectors and the dashed lines represent the relative velocity vectors. The blade efficiency was the same for all cases: $\cos^2 \alpha = 88.3\%$.

$$\rho = \frac{\cos \alpha}{2(1-R)} \qquad (48)$$

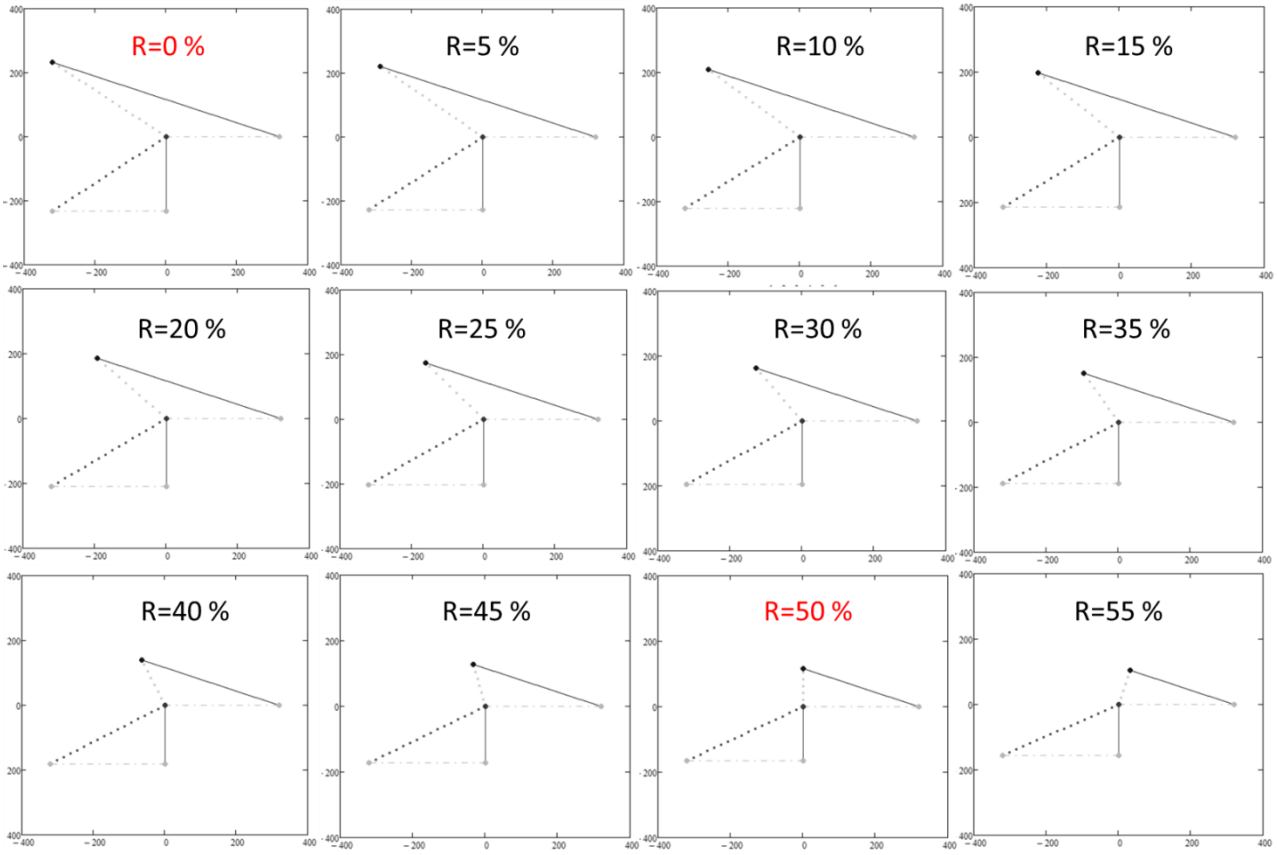

Figure 2.41: Effect of changing reaction ratio on rotating blade angles

Figure 2.42 is a reproduction of the figure used in Section 2.3.1. The symmetry of the 0 % and 50 % can readily be compared.

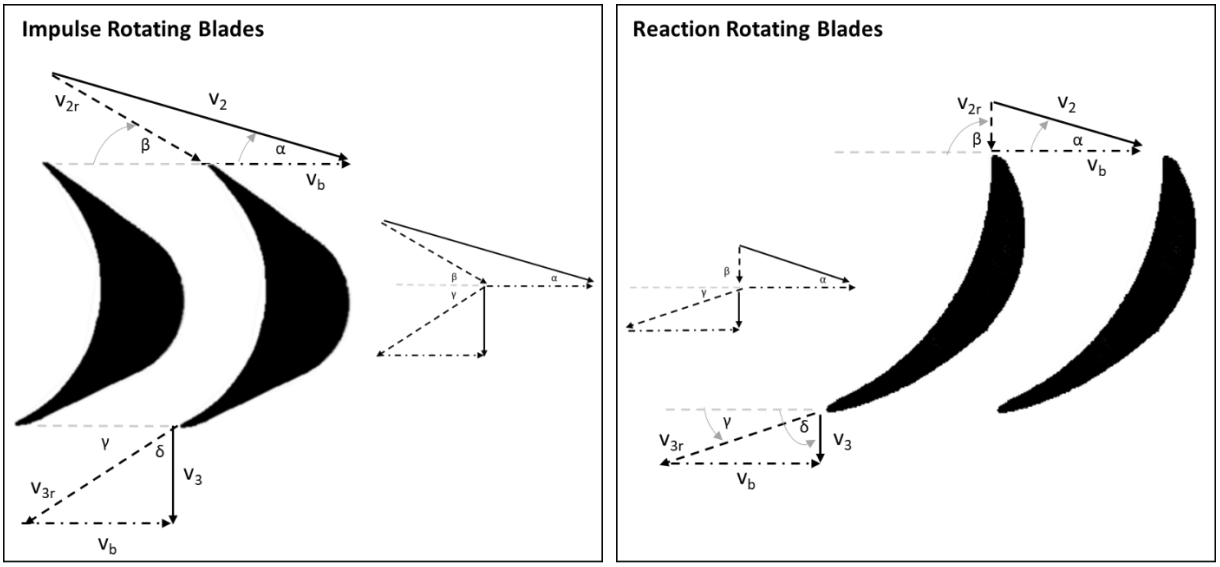

Figure 2.42: Typical turbine rotating blade and velocity triangles: impulse type (left), and 50% reaction type (right)

2.3.6 Isentropic Efficiencies and Losses

The isentropic efficiency of a turbine is defined as follows:

$$\eta_T = \frac{h_{0i} - h_{0e}}{h_{0i} - h_{0e,s}} \tag{49}$$

Where $h_{0e,s}$ is the isentropic exit enthalpy, evaluated at the exit pressure (and inlet entropy),"i" denotes "inlet", "e" denotes "exhaust", "0" denotes total properties and "s" denotes isentropic.

From the definition of stagnation or total enthalpy, $h_0 = h + \frac{v^2}{2}$, where h is the static enthalpy and v is the absolute velocity of the fluid. In general, the inlet and outlet velocities are assumed to be negligible and so $h_{0i} = h_i$ and $h_{0e} = h_e$. (Note that the inlet here is to the first stage of the turbine.) The equation therefore becomes:

$$\eta_T = \frac{h_i - h_e}{h_i - h_{e,s}} \tag{50}$$

This can then be represented on an h-s or T-s diagram. An example appears on an h-s (Mollier) diagram in Figure 2.43.

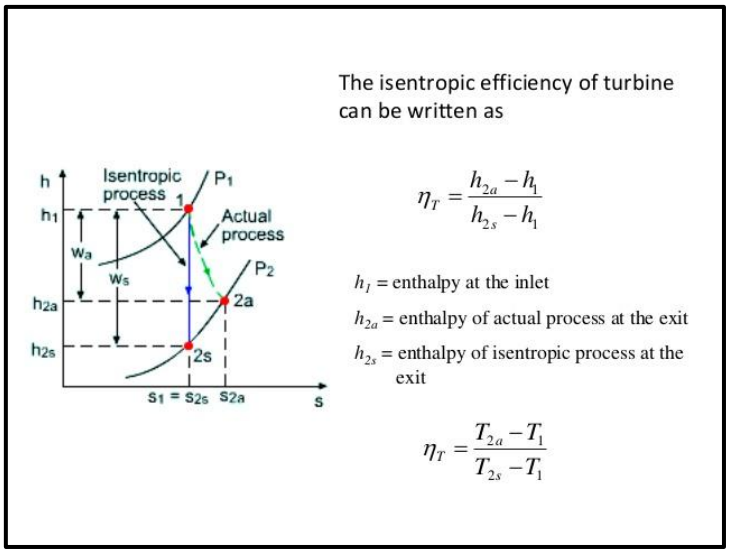

Figure 2.43: Illustration of turbine isentropic efficiency (Senanayake, 2016)

This assumption is generally valid except for the exhaust of a low-pressure turbine, where velocities can commonly reach 350 m/s (Rousseau and Fuls, 2017). In this case, two enthalpy end points are defined, the Expansion Line End Point ($h_{ELEP} = h_e$) and the Used Energy End Point (($h_{UEEP} = h_{0e} = h_e + \Delta h_{loss}$). Considering the used energy end point, the efficiency can be re-expressed as follows:

$$\eta_T \approx \frac{h_i - \left(h_e + \Delta h_{loss}\right)}{h_i - \left(h_{e,s} + \Delta h_{loss}\right)} \tag{51}$$

With

$$\Delta h_{loss} = \frac{1}{2} \cdot v_{ex}{}^2 \tag{52}$$

Where v_{ex} is the absolute exhaust velocity from the final stage.

Specific work provided by the turbine can be expressed as follows:

$$w_T = h_i - h_{UEEP} \tag{53}$$

Relating this to the concept of carry-over efficiency introduced previously, the enthalpy after the final stage will be h_{UEEP} if all if the carry-over efficiency for the last stage is set to zero – in other words, all of the velocity is converted into heat (hence the term “reheat”). It is sensible to set this value to zero (or effectively zero) for the last stage of a condensing turbine, as there is no following stage to receive the velocity and all of this kinetic energy must be brought to stagnation conditions in the condenser.

Sources of Loss (ζ)

Cotton (1998) identifies several noteworthy sources of inefficiency in a turbine stage (which will affect the loss coefficients, ζ, introduced previously). These include:

1. Friction losses in the stationary and rotating blades (affected by blade profiles and roughness; this is sometimes considered as "profile loss").
2. Tip leakage losses – losses due to steam bypassing the rotor blades (affected by the effectiveness of blade shrouding, for example).
3. Interstage packing leakage losses – losses due to steam bypassing the stationary blades, by passing between the stationary blade ring and the rotor.
4. End wall losses – on the inner and outer end walls (of the rotor hub and stator cylinder respectively), the no-slip boundary condition results in vortices forming which are not useful to the next stage (the effect is less significant as the blades' aspect ratio increases (radial height over throat width)).

Some of these losses are illustrated in Figure 2.44 for an impulse stage (Frolov, n.d.).

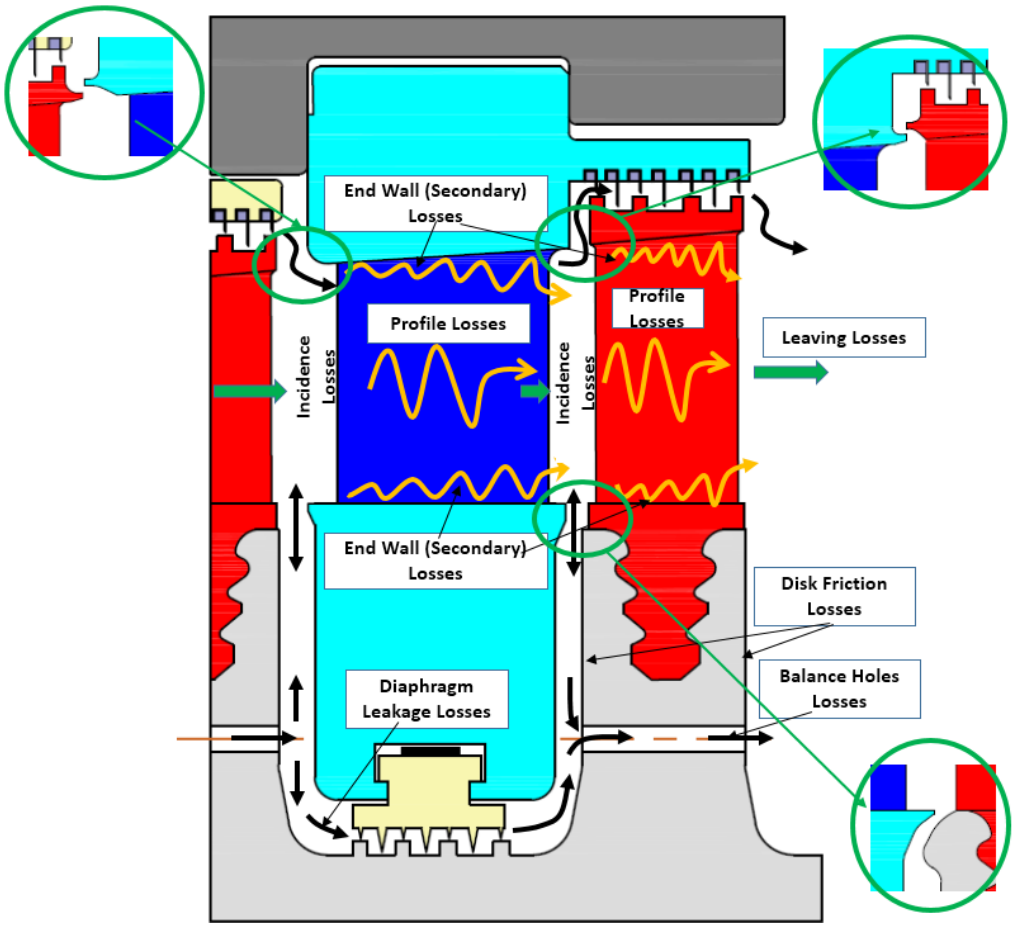

Figure 2.44: Stage losses in a typical impulse steam turbine (Frolov, n.d.)

In addition to this, incidence loss, resulting from the distortion of ideal velocity triangles through changing steam flow and rotor speed, has an impact on ζ.

Quantifying the impact of these different losses is beyond the scope of this dissertation given that the turbine is being modelled with minimal geometric inputs. Instead, the ζ-values in this study were tuned/calibrated during the model development.

2.3.7 *Flownex* Custom Stage Components for the Turbine Model

Flownex is a one-dimensional thermofluid process modelling software package which solves the conservation equations of mass, energy and momentum. It allows for components to be assembled in complex networks with boundary conditions, component characteristics and fluid characteristics being set by the user. The components may be standard or custom-made. Custom components were created by Fuls based on the theory presented in his paper (Fuls, 2017a) to represent an impulse stage (reaction of zero) and a reaction stage (non-zero reaction). More information may be obtained about *Flownex* on their website, https://www.flownex.com.

The principle user inputs for these components are listed in Table 2.4, separated into groups for convenience. Boundary conditions will not be considered here.

Table 2.4: User Inputs for Custom Turbine Stage Components

Group 1	From drawings / manuals / data capture system	Mean blade diameter, D
		Rotor speed, N
Group 2	Estimated based on enthalpy and pressure drops and tuned in *Flownex*	Stator throat area, A_s
		Stator blade exit angle, α
		Rotor throat area, A_R (*only required for reaction stages*)
Group 3	Estimated based on visual clues and tuned in *Flownex*	Stator loss coefficient, ζ_S
		Rotor loss coefficient, ζ_R
		Carry-over efficiency, η_{co}

Figure 2.45 and Figure 2.46 illustrate these custom *Flownex* components with labels for subcomponents. These can be compared against part (c) of Figure 2.27. Note that "Nozzle(s)" denotes the nozzle for the stationary stage, "Nozzle(r)" denotes the nozzle for the rotating stage, "Node" denotes the node at which work is extracted and the "Diffuser" subcomponent models velocity carry-over to the next stage. The script subcomponent contains the code that executes the equations discussed previously (for example, calculating the work to be extracted at the node).

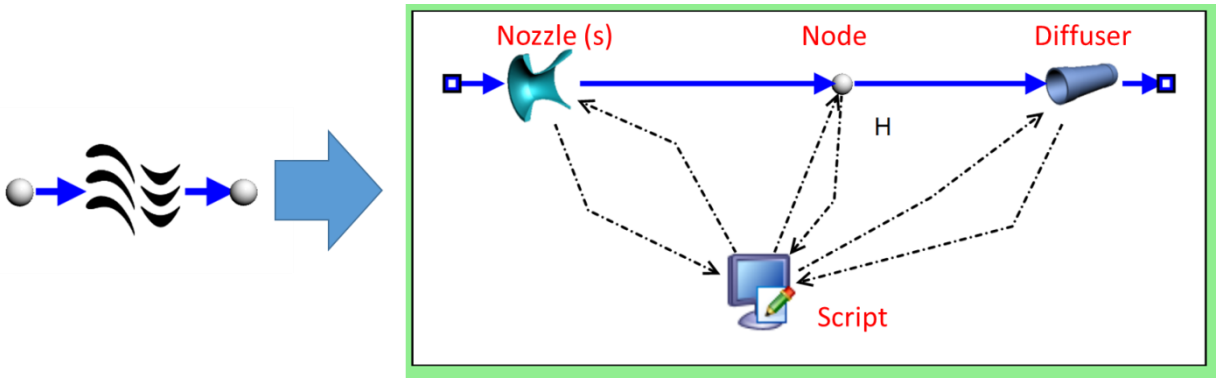

Figure 2.45: Impulse stage custom Flownex *component*

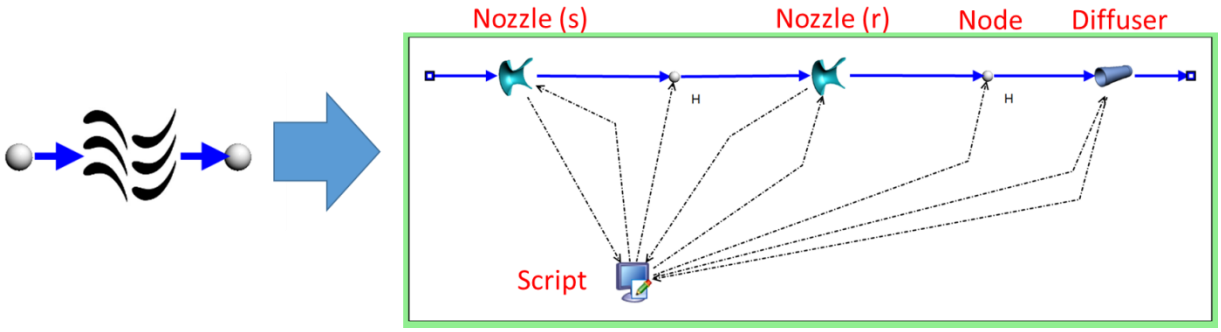

Figure 2.46: Reaction stage custom Flownex *component*

2.3.8 Methodology for Nozzle Throat Area Estimates

The process followed in order to estimate nozzle throat areas is summarised in Figure 2.47.

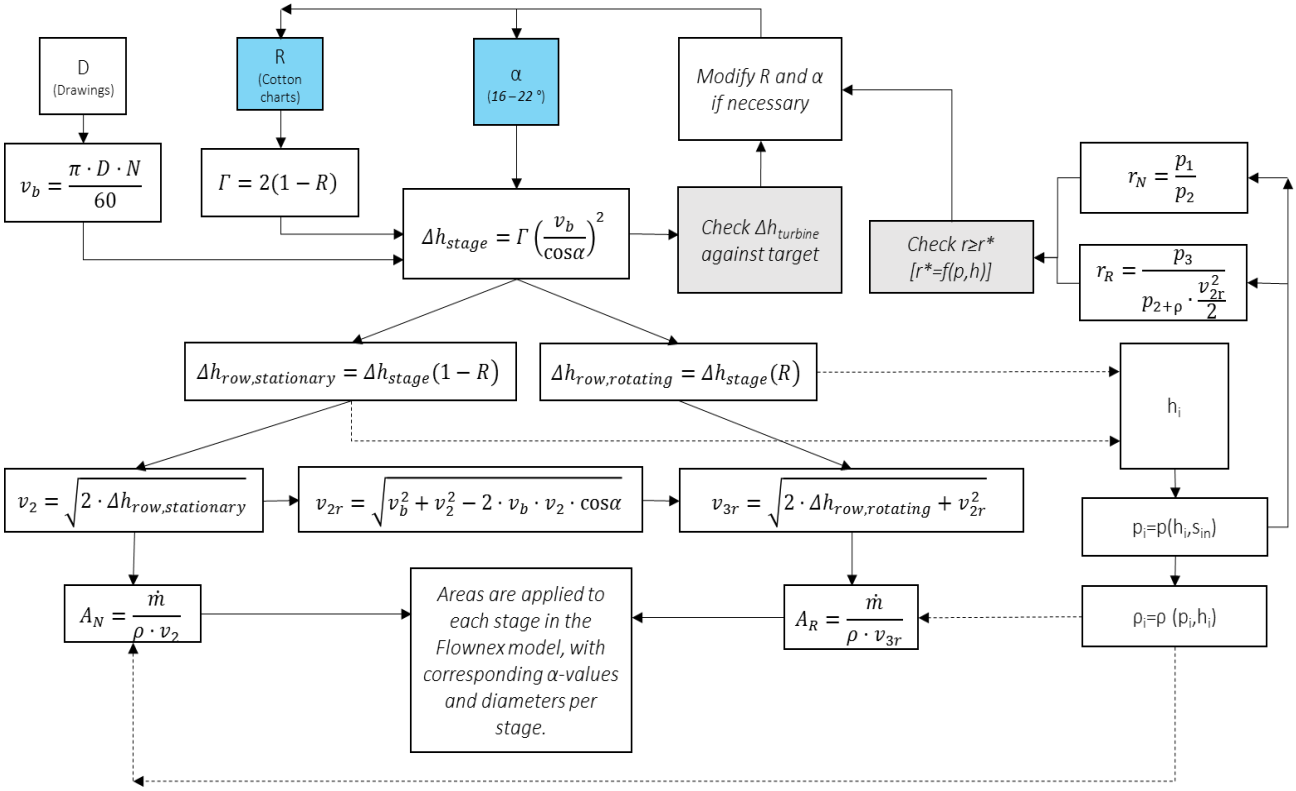

Figure 2.47: Diagram summarising the methodology employed for the initial estimates of nozzle throat areas

Importance of Estimating Enthalpy Drops

To calculate initial nozzle throat areas, it was required to know expected throat velocities, mass flow rate and density at the exit of each row. It was assumed that all nozzles would be converging so that the narrowest section, the throat, would be at the exit of each row.

The mass flow rate was determined based on expected total enthalpy drop and power required from the turbine, as will be discussed in Section 3.6. The density was calculated using steam tables from the estimated pressure and enthalpy after each stage, while the velocities were calculated from the expected enthalpy drops.

For these estimates, an isentropic process was considered. Knowing the enthalpy after each row and maintaining the same entropy, inter-row pressures could be calculated.

Once the isentropic enthalpy drops per row are known, it is evident that the required nozzle throat areas can readily be calculated.

Obtaining Enthalpy Drops

The correct total isentropic enthalpy drop is obtained by assuming certain reaction ratios and nozzle angles (based on typical values) and adjusting these accordingly. Using these values, the pressure ratios are checked across the stationary and rotating rows in order to avoid choking across any rows. In the event that there is choking, the reaction ratios and/or nozzle angles may then be adjusted further such that choking is avoided while still obtaining the correct enthalpy drop.

This is an iterative process of adjusting α-values and reaction ratios until the correct total isentropic enthalpy drop is obtained without choking.

If additional boundary values are known for setting up the model, then these may be introduced as additional targets. For example, in the following chapter it will be seen that Station A1 had an intermediate pressure measurement available which allowed for the first stage to be considered separately from the other stages.

Critical Pressure Ratios

Based on Section 2.3.3, Table 2.5 provides critical pressure ratios for different steam conditions.

Table 2.5: Critical Pressure Ratios for Steam Nozzles

	k	p*/p0
Superheated steam	1.300	0.546
Dry saturated steam	1.135	0.577
90 % dry steam	1.125	0.579
80 % dry steam	1.115	0.582
50 % dry steam	1.085	0.588
Wet saturated steam (liquid)	1.035	0.599

From this table, it is evident that the critical pressure ratio for the first stage of the turbines under consideration will be 0.546. From the heat balance diagram for Station B1, a minimum exhaust dryness fraction of 0.938 is expected, occurring at full load. In order to avoid choking, it should therefore suffice to keep the pressure ratio over each blade / nozzle row above the range 0.546 to 0.579 (depending on the stage). A preliminary target was therefore set for **r ≥ 0.58**, where r is the ratio of inlet to outlet pressure for a row.

Since the stationary blades / nozzles in the turbines under consideration can be considered to be converging nozzles and the reaction moving blades can also be considered to be converging nozzles, the exit pressure from each row can be considered to be the throat pressure.

Considering a stationary row,

$$r = \frac{p_2}{p_1 + \rho \cdot \frac{v_1^2}{2}} \tag{54}$$

And if v_1 is taken to be negligible, which is the case for zero carry-over, then:

$$r \approx \frac{p_2}{p_1} \tag{55}$$

Considering a rotating row,

$$r = \frac{p_3}{p_2 + \rho \cdot \frac{v_{2r}^2}{2}} \tag{56}$$

However, v_{2r} cannot be taken to be zero as this is the velocity which is transferred from the stationary nozzle to the rotating nozzle. The stationary nozzle exists to generate this velocity.

As shown in Figure 2.47, by applying velocity triangles, this relative velocity is calculated as follows:

$$v_{2r} = \sqrt{v_b^2 + v_2^2 - 2 \cdot v_b \cdot v_2 \cdot \cos\alpha} \tag{57}$$

And:

$$v_2 = \sqrt{2 \cdot \Delta h_{row,stationary}} \tag{58}$$

The required minimum pressure ratio was calculated from the dryness factor as discussed in Section 2.3.3, *Choking*.

Following the Flow Diagram

With the above discussion in mind, the aforementioned flow diagram should be applied as follows, following the numbered points in Figure 2.48:

1. Set estimated α and R values.
2. Calculate the isentropic enthalpy drop per stage.
3. Split this enthalpy drop between the rows of each stage according to the reaction ratio.
4. From these enthalpy drops per row, calculate the nozzle velocities.
5. Knowing the enthalpy drops per row, determine the enthalpy between rows (h_i) along with the associated pressure and density, assuming isentropic expansion.
6. Calculate the required nozzle areas, having calculated nozzle velocities and densities.

7. *Check:* Determine the pressure ratio over each stage and confirm it is acceptable with respect to the critical pressure.
8. *Check:* Add the enthalpy drops per row and check that the total is correct with respect to the target value.

This process is best implemented in the form of a spreadsheet. The reaction ratios and nozzle angles can then be modified per stage until by trial-and-error the correct total isentropic enthalpy drop is obtained without choking any of the nozzles. The output is a set of nozzle areas.

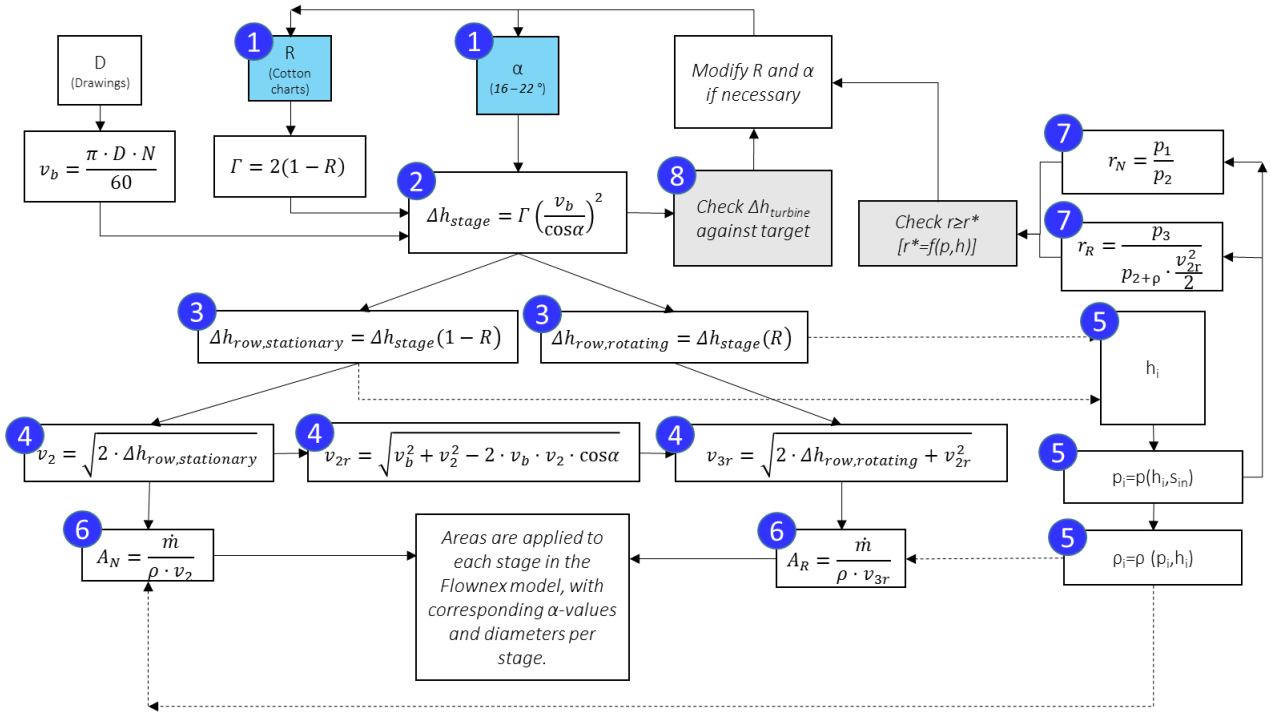

Figure 2.48: Diagram summarising the methodology employed for the initial estimates of nozzle throat areas, with numbered points

2.3.9 *Flownex* Flow Resistance Components for the Steam Admission Valves

In order to keep the steam admission valve components as simple as possible while still accurately representing their behaviour in the steady state model, and in view of scarcity of information around the specifics of these valves, the decision was made to utilise generic flow resistance components to represent these valves. This section therefore considers the standard components available in *Flownex*.

A pressure drop through a pipe or other fitting can in general be expressed as follows (neglecting height differences):

$$\Delta p_{0L} = K \cdot \frac{1}{2} \cdot \rho \cdot \bar{v}^2 \quad (59)$$

Noting that $\dot{m} = \rho \cdot \bar{v} \cdot A$, this can be rewritten in scalar form as follows:

$$\Delta p_{0L} = \frac{1}{2} \cdot \left(\frac{K}{\rho \cdot A^2} \right) \cdot |\dot{m}| \cdot \dot{m} \quad (60)$$

Quadratic Resistance, varying density

Considering a pipe with Darcy friction factor f,

$$K = f \cdot \left(\frac{L}{D} \right) \quad (61)$$

Which gives

$$\Delta p_{0L} = \left[\frac{1}{2} \cdot (f) \cdot \left(\frac{L}{D} \right) \cdot \left(\frac{1}{A^2} \right) \right] \cdot \left[\frac{1}{\rho} \cdot |\dot{m}| \cdot \dot{m} \right] \quad (62)$$

This is the form of the equation used by the *Flownex* component when a quadratic resistance is chosen, and when the "include density variation effects" input is selected.

Flownex utilises three factors to represent the constant (left) portion of this expression:

- A_f: flow admittance
- A_{sf}: scaling factor
- A_o: opening

These are taken as inputs to describe the component characteristics and *Flownex* then utilises the following equation to solve:

$$\Delta p_{0L} = \left[\frac{1}{A_f \cdot A_{sf} \cdot A_o} \right] \cdot \left[\frac{1}{\rho} \cdot |\dot{m}| \cdot \dot{m} \right] \quad (63)$$

In using this component to represent a valve, the scaling factor was set to 1, the flow admittance was taken as a representation of the valve's behaviour when fully open, and opening was varied in order to represent the effects of changing the valve position.

Thus:

$$A_f \cdot A_o = \left[\frac{2 \cdot A^2}{K} \right] \quad (64)$$

Quadratic Resistance (constant density)

When density is taken as constant ("include density variation effects" input is deselected), the above equations take the following form:

$$\Delta p_{0L} = \left[\frac{1}{2}\cdot(f)\cdot\left(\frac{L}{D}\right)\cdot\left(\frac{1}{A^2}\right)\cdot\left(\frac{1}{\rho}\right)\right]\cdot\left[|\dot{m}|\cdot\dot{m}\right] \quad (65)$$

$$\Delta p_{0L} = \left[\frac{1}{A_f\cdot A_{sf}\cdot A_o}\right]\cdot\left[|\dot{m}|\cdot\dot{m}\right] \quad (66)$$

$$A_f\cdot A_o = \left[\frac{2\cdot A^2}{\rho\cdot K}\right] \quad (67)$$

It is worth noting here that the unit for the product $A_f \cdot A_o$ is no longer m^4 due to the incorporation of density into the definition.

Linear and Square root resistance

The linear resistance option for the component is applicable for laminar flow but since the valves being modelled are highly turbulent in behaviour, it will not be considered further here. A discussion is included in Appendix I should the reader wish to compare this with the quadratic option.

A square root resistance behaviour is also available in *Flownex* but this is only applicable to very specific cases and will not be utilised here.

2.3.10 Other Turbine Models

There are several common means of representing turbines in a one-dimensional model. Some of the common methods are described here, with acknowledgement to Rousseau and Fuls (2017) for summarising the works of Stodola and others. Some of these methods will be used for comparison with the nozzle model when turbine model validation is considered.

Constant Flow Coefficient Method

$$\dot{m} = C_f\sqrt{p_{0i}\cdot\rho_i} \quad (68)$$

$$C_f = \frac{\dot{m}_D}{\sqrt{p_{0i,D}\cdot\rho_{i,D}}} \quad (69)$$

$\dot{m}_D$, $p_{0i,D}$ and $\rho_{i,D}$ are the design mass flow rate, the design total inlet pressure and the design inlet density respectively. p_{0i} and ρ_i are then the total inlet pressure and inlet density at other conditions.

Expressed another way,

$$\dot{m} = \dot{m}_D \sqrt{\frac{p_{0i} \cdot \rho_i}{p_{0i,D} \cdot \rho_{i,D}}} \tag{70}$$

It is clear that this method does not take into account changing outlet conditions.

Stodola Ellipse Law

$$\dot{m} = \dot{m}_D \sqrt{\left(\frac{p_{0i} \cdot \rho_i}{p_{0i,D} \cdot \rho_{i,D}} \right) \cdot \left(\frac{1 - \left(\frac{p_{0e}}{p_{0i}} \right)^2}{1 - \left(\frac{p_{0e,D}}{p_{0i,D}} \right)^2} \right)} \tag{71}$$

$\dot{m}_D$, $p_{0i,D}$, $\rho_{i,D}$, $p_{0e,D}$, and $\rho_{e,D}$ are the design mass flow rate, the design total inlet pressure, the design inlet density, the design total exhaust pressure and the design exhaust density respectively. p_{0i} , ρ_i, p_{0e} , and ρ_e are the total inlet pressure, inlet density, total exhaust pressure and exhaust density at other conditions.

Although this model takes into account changing outlet conditions, it ignores the effect of choking which occurs at suitably low pressure ratios. This is illustrated graphically in Figure 2.49, where mass flow rate is on the vertical axis, exhaust pressure is on the horizontal axis and inlet pressure is on the axis going into the page. It is clear that mass flow rate will increase as the inlet pressure is increased or as the exhaust pressure is reduced, regardless of the choking limit.

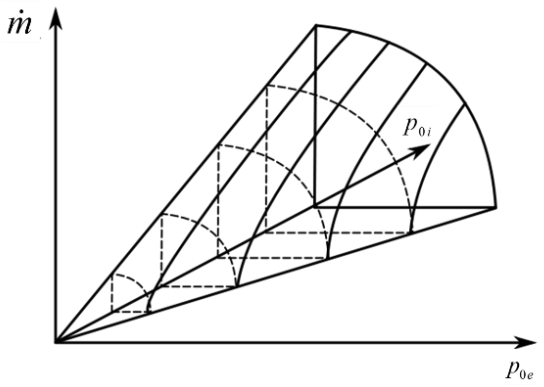

Figure 2.49: Illustration of Stodola ellipse law (modified from Zajaczkowski, 2011)

Fuls' Semi-Ellipse Model

$$\dot{m} = \dot{m}_D \sqrt{\left(\frac{p_{0i} \cdot \rho_i}{p_{0i,D} \cdot \rho_{i,D}} \right) \cdot \left(\frac{1 - \left(\frac{r - r^*}{1 - r^*} \right)^{\alpha}}{1 - \left(\frac{r_D - r^*}{1 - r} \right)^{\alpha}} \right)} \qquad (72)$$

Where:

- $r = \left(\frac{p_{0e}}{p_{0i}} \right)$ is the pressure ratio, and r^* the ratio at which the turbine will choke
- α is typically about 2, dependent on the number of turbine stages and the stage areas

This model considers the effects of choking and is based on a modified version of Stodola's equation.

Fuls (2017b) introduced this model in his paper, "Enhancement to the Traditional Ellipse Law for More Accurate Modelling of a Turbine with a Finite Number of Stages". In this paper, it is presented as the most accurate way in which to model a turbine without conducting a stage-by-stage analysis.

Existing *Flownex* Turbine Components

Flownex has standard turbine components, "Turbine" and "Simple Turbine". The former requires detailed information including turbine performance curves while the latter allows for options with a loss coefficient or an option utilising the Stodola ellipse law. However, these do not allow for a stage-by-stage analysis of the turbine. The simple turbine is utilised for the high level representation of the overall turbine in 3.10, using the "restrictor with a discharge coefficient" option for the internal pressure drop model.

2.4 Miscellaneous Considerations

Unless otherwise indicated, all "steam tables" used in this document will be the IF97 formulations, which is to say, the International Association for the Properties of Water and Steam (IAPWS) Industrial Formulation 1997 for the Thermodynamic Properties of Water and Steam (abbreviated to IAPWS-IF97). Note that IAPWS-IF97 supersedes IFC-67, the 1967 IFC Formulation for Industrial Use. IAPWS-IF97 is referenced under Wagner et al., 2000. Many of the Eskom power stations were designed using IFC-67, therefore some differences in the reported enthalpy values can be observed in the heat balance data.

3. Model Development

This chapter describes the development of a model in Flownex *which represents the complete boiler feed pump turbine system, including the turbine, steam admission valves, pump stages and relevant boundary conditions. Unless otherwise stated, the station under consideration is Station A1.*

3.1 Visual Observations from Sites of Interest

Figure 3.1 shows a selection of photographs of typical Eskom boiler feed pumps during witnessed reconditioning. Clockwise from the top left corner: a shaft with impellers fitted, a pull-out or cartridge with barrel casing, and the assembled pump. Note that the impellers are typically identical for each stage of a given boiler feed pump. Each impeller and diffuser is assembled on the shaft per stage and in this way the "cartridge" is built up. This cartridge is then inserted into the barrel casing.

Figure 3.1: A selection of photos of typical Eskom boiler feed pumps

Figure 3.2 shows photographs of the feed pump configuration from Station A1. There are two EFP trains and one BFPT train. Only one EFP train is labelled in the photograph. Figure 3.3 shows the open BFPT at Station B1. The annotations show the labelling convention. Figure 3.4 shows the change in rotor blading over the length of the BFPT shaft at Station B1.

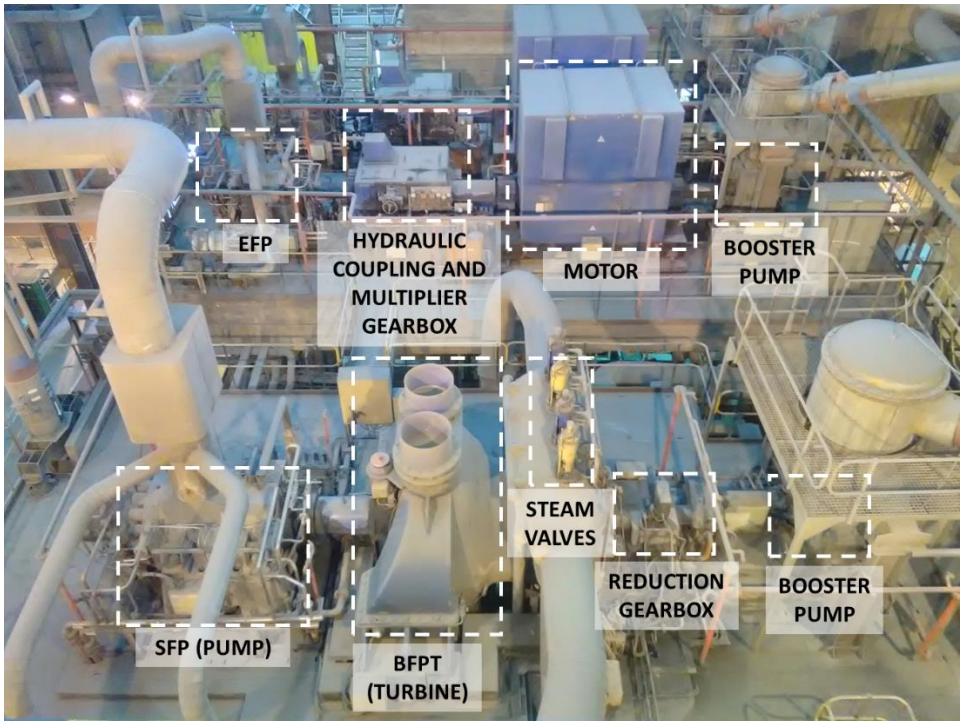

Figure 3.2: Annotated photograph showing the feed pump configuration at Station A1

In addition to studying available drawings, several observations were made regarding the turbines on site. For example, Figure 3.3 shows that the last stage stationary row at Station A1 has steam entering approximately axially (i.e. $\delta \approx 90$ ° from the previous stage) and departing at an angle close to the tangential, consistent with estimates of 16 ° to 22 ° for α. Figure 3.4 and Figure 3.5 show how on Station B1, a similar BFPT demonstrates an increasing reaction ratio along its length, based on the changing profile, consistent with the expectations from Cotton, and Figure 3.6 shows a typical rotating blade profile at Station A1.

Figure 3.3: Last stage stationary row from Station A1

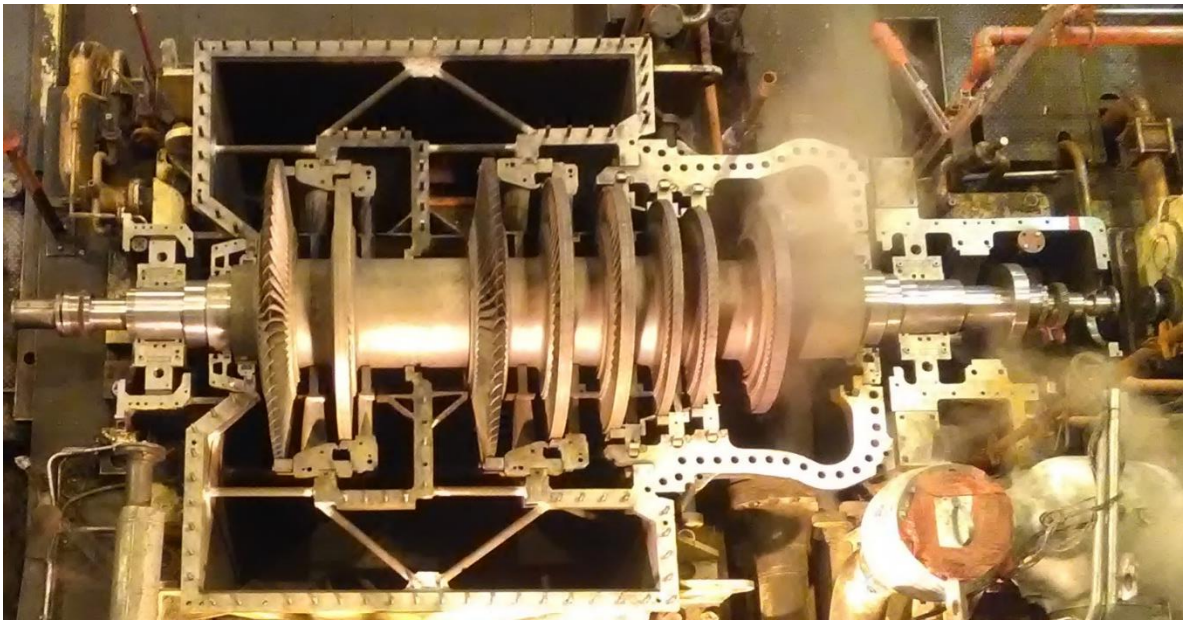

Figure 3.4: Photograph showing the BFPT rotor in-situ at Station B1

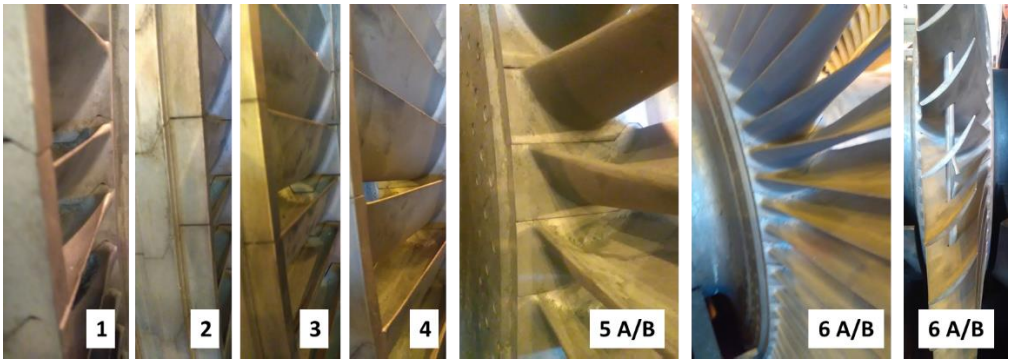

Figure 3.5: Annotated photograph showing the BFPT rotor blades at Station B1 (the numbers indicate the stages)

Figure 3.6: Rotating blades from Station A1

Referring to Figure 3.5, the rotating blade angles were estimated from the photographs and recorded in Table 3.1. Note that for the first four stages, the blades were approximately symmetrical and of approximately constant cross-sectional profile over the blade length. The initial symmetry is indicative of impulse blading. Stage 5 (A/B) exhibited a marked asymmetry but remained approximately constant in profile over the blade length. Stage 6 (A/B) exhibited an approximately symmetric profile at the blade root, twisting along the blade length to become severely asymmetric as the tip, with a noticeable reduction in cross-sectional fluid flow area. Evidently the blades increase in degree of reaction over the length of the steam path. Note that these angles are very rough visual estimates owing to the perspective of the photographs, and are only intended to provide an indication of the blade characteristics.

Table 3.1: Estimated Blade Angles at Station B1

	Blade entrance angle (°) - β	Blade exit angle (°) - γ	Angle of deviation (β +γ, °)
Stage 1	40	40	80
Stage 2	22	22	44
Stage 3	26	26	52
Stage 4	48	48	96
Stage 5A/5B	28	38	66
Stage 6A/6B - root	50	50	120
Stage 6A/6B -tip	129	25	154

Similar estimates could not be made for multiple stages at Station A1 due to poor availability of information and units not being on outage at the time of site visits. However, from Figure 3.6, a profile could be estimated for Stage 7, appearing in Figure 3.7.

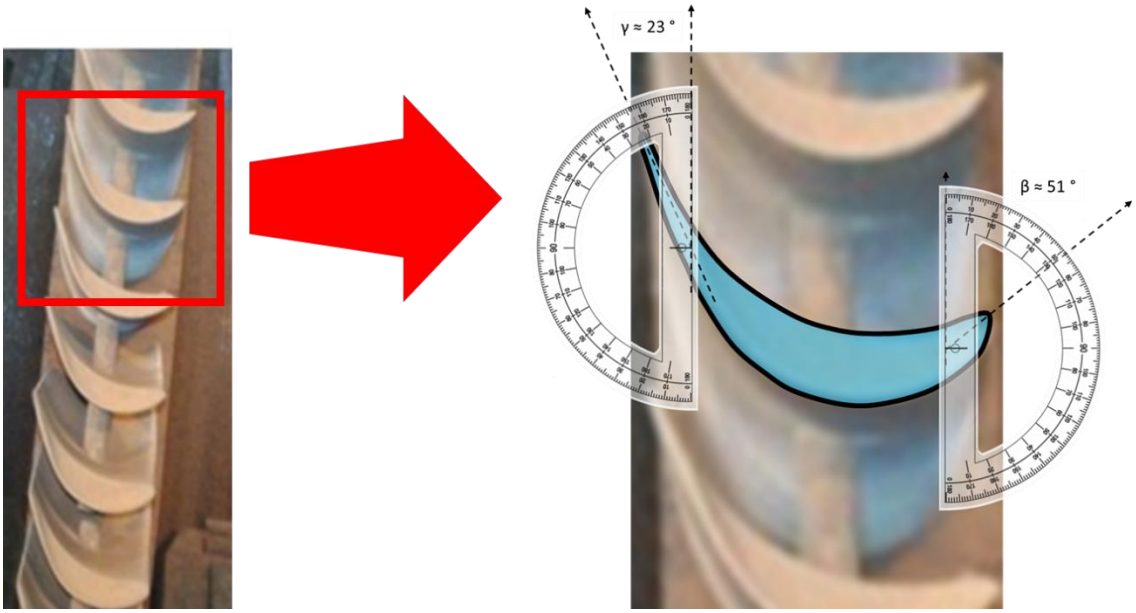

Figure 3.7: Approximate blade profile at tip of Stage 7 rotating blades at Station A1

A diagram of the Station A1 rotor appears as Figure 3.8 and although it is not possible to estimate blade angles from this, there is evidently a transition from impulse towards reaction in the shape of the blading over the length. Note that the direction of axial flow is from left to right.

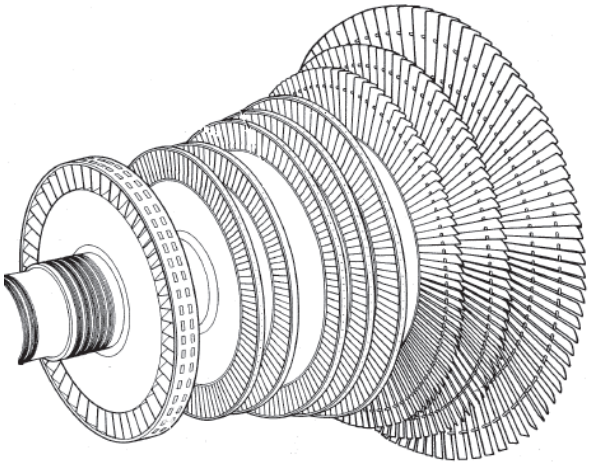

Figure 3.8: Diagram of BFPT rotor from Station A1 (Eskom Station Manuals)

3.2 Piping and Instrumentation Diagram / Process Diagram

The various piping and instrumentation diagrams available for Station A1 were considered and consolidated into Figure 3.9, which summarises all available measurements for ease of reference when model tuning and validation is considered. Figure 3.10 shows the corresponding diagram for the EFP system.

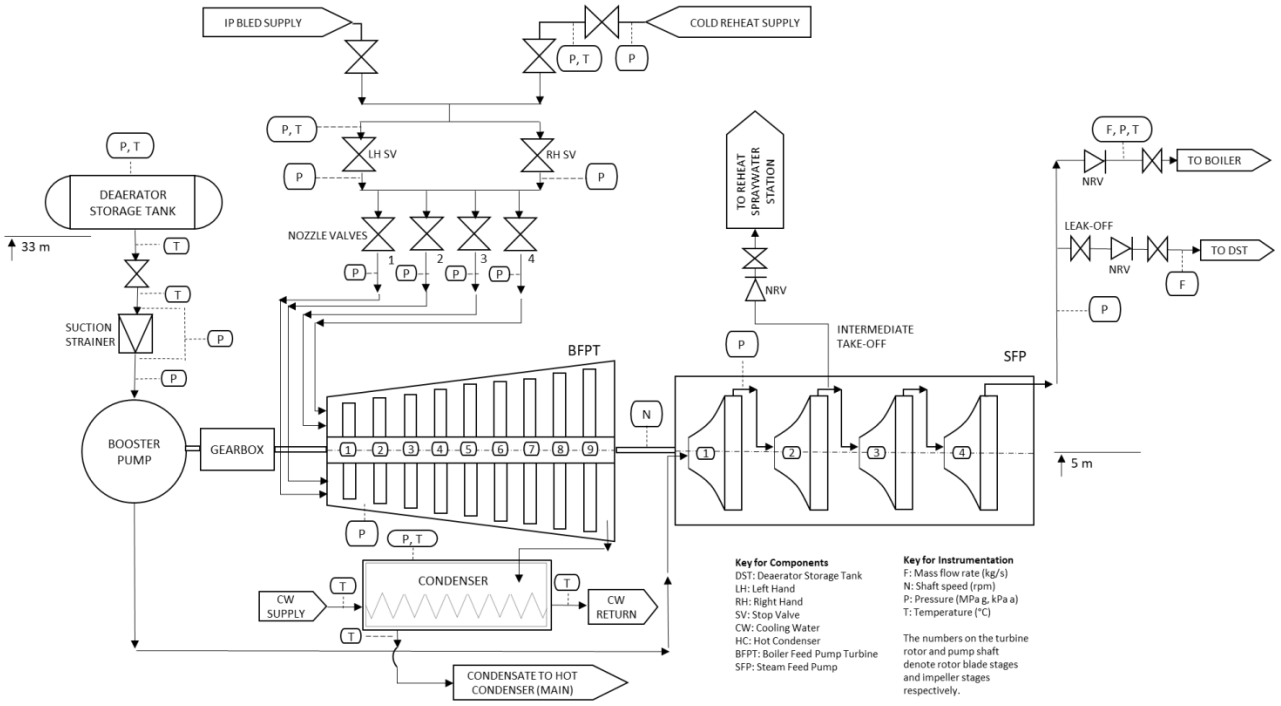

Figure 3.9: Consolidated diagram of BFPT / SFP system instrumentation for Station A1

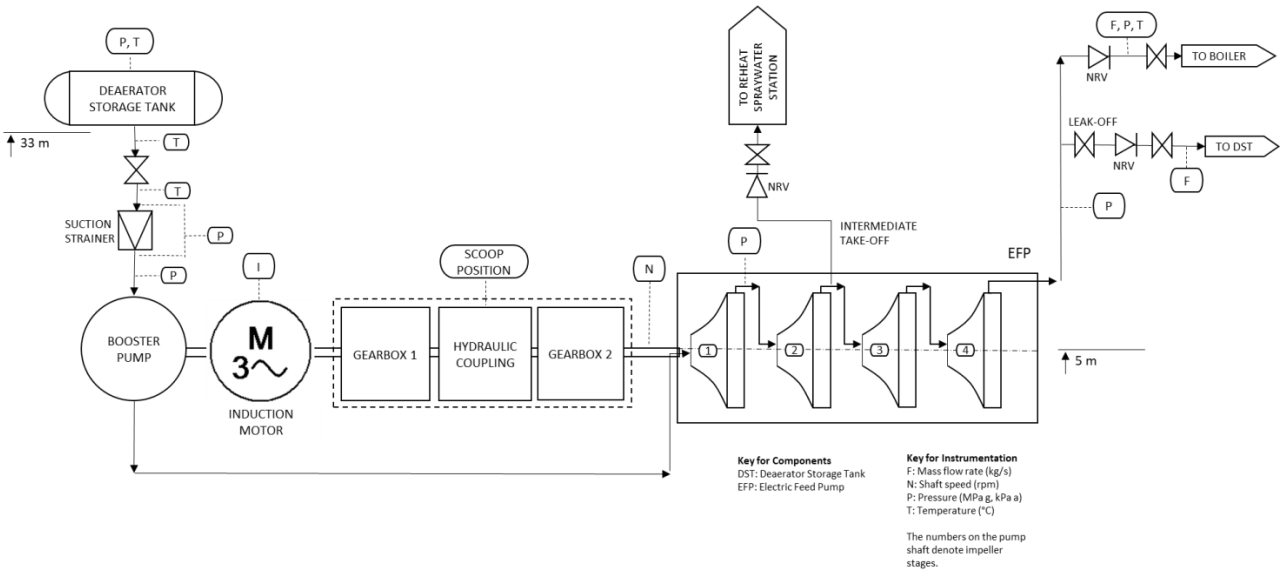

Figure 3.10: Consolidated diagram of EFP system instrumentation for Station A1

3.3 Development of the Pump Curves

Figure 3.11 illustrates a set of pump curves for the SFP at Station A1. Note that this image only shows the pump curves (head vs flow) at different speeds, although hydraulic efficiency curves, power curves and NPSH (net positive suction head) curves were also utilised. Documents such as these were used as the initial inputs after having been scanned as images.

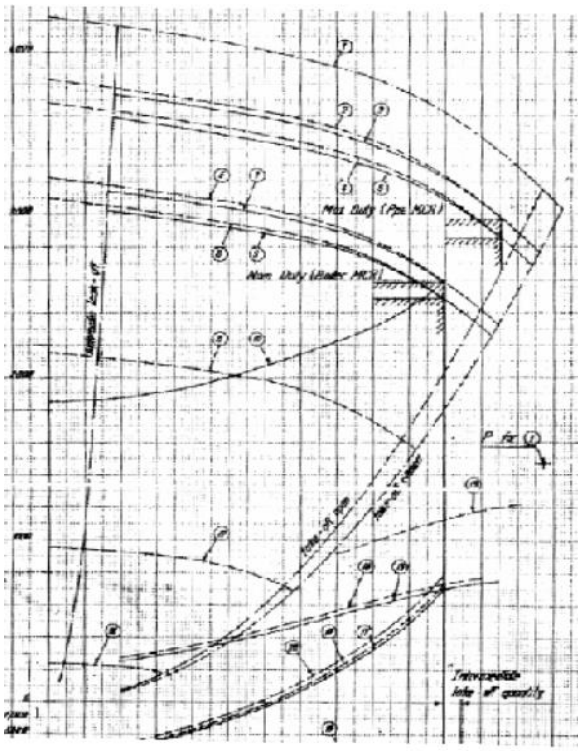

Figure 3.11: Example of pump curve image used for digitisation

Each of these curves was digitized using software *Digitize*, or alternatively using *Mathcad*. The sets of coordinates obtained, describing each curve, were then stored in an Excel spreadsheet. The data was checked for quality and consistency, and smoothed where necessary.

These curves were assigned lines-of-best-fit or regression lines of polynomials up to the sixth order using Excel's "trendline" function. The equations for these curves were applied to the existing set of x-values and the resulting y-values (y') were compared against the measured y-values. The acceptance criterion applied was that the absolute difference between y and y' should not exceed 10 m. (This was chosen based on the resolution of the pump curve drawings with consideration for how accurately points along the curves could be selected.) Based on this, the pump curves were represented as third order polynomials, the efficiencies were represented with quadratic equations and the NPSH curves were represented as sixth order polynomials.

Some of the pump curves represented the main pump alone. Most of the SFP and EFP curves for Station A1 included the booster pumps, with the main pump speed and sometimes the booster pump speed being stated. The gearbox ratios for the SFP trains were calculated using these stated speeds. These were found to be 3.06 and 4.25 respectively for Stations A1 and B1. Knowing the main pump speed for one of these combined curves, the booster pump speed could then be determined and the booster pump curve equation could be scaled accordingly using pump similarity laws, as discussed in Section 2.2.1.

Once scaled, the booster pump curve could be subtracted from the main pump curve noting that these are pumps in series, or curves with only the main pump could be used. Curves were used for which the intermediate take-off was closed in order that all pump stages would experience the same mass flow rate (and approximately the same volumetric flow rate). The total head provided by the main pump was divided by the number of impellers so that curves could be imported into *Flownex* for the booster pump and each individual stage of the main pump. The head, efficiency and NPSH curves were digitised and imported into *Flownex*. The leak-off line was also digitised and incorporated into a script to check that minimum flow requirements were met. An example of these curves appears in Figure 3.12.

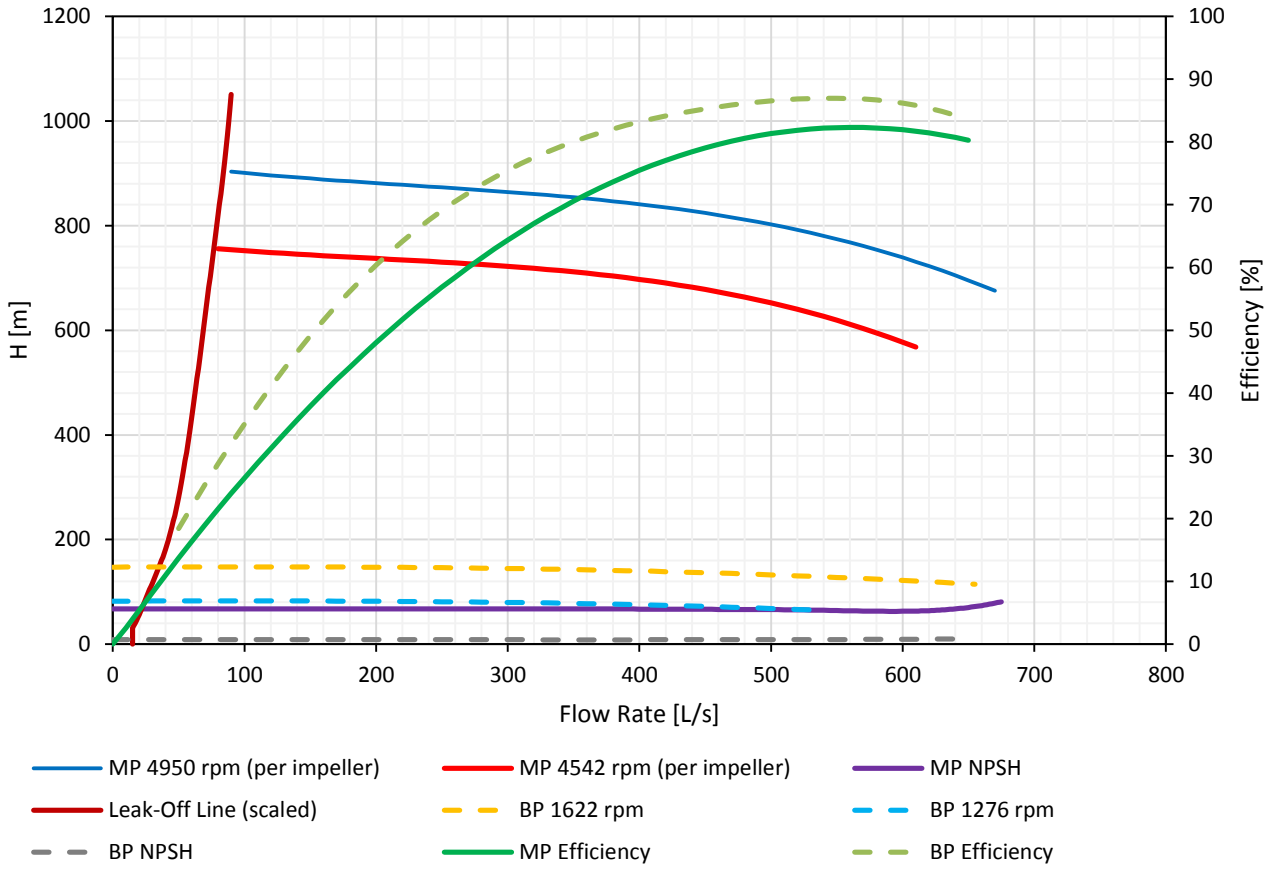

Figure 3.12: Station A1 pump curves as imported into Flownex

Confirmation with DCS Values

These curves are based on the pump curves provided by the OEM. In order to confirm their validity, DCS values were checked for the same period as used for the DCS boundary conditions - sampled at intervals of 10 minutes from 29/04/2016 00:00 to 06/05/2016 00:00. The speed is varied to meet the required feedwater flow rate at the boiler's operating pressure.

They are plotted in Figure 3.13. For each speed cluster, all points within a tolerance of ±5 rpm to the speed stated were plotted. These stated speeds were chosen at intervals of 100 rpm in order to allow for visibility. The volumetric flow rate was calculated from measured mass flow rate and density at the suction temperature. The head difference was calculated from the static pressure difference over the booster pump and main pump, using the density calculated at suction.

The combined curves were plotted based on the OEM pump curves. These were calculated as the sum of main and booster pump heads scaled from the reference speeds of 4542 rpm and 1622 rpm respectively. It was observed that these points were approximately located along the lines from the OEM pump curves.

This confirms the applicability of the theoretical curves to represent the physical system.

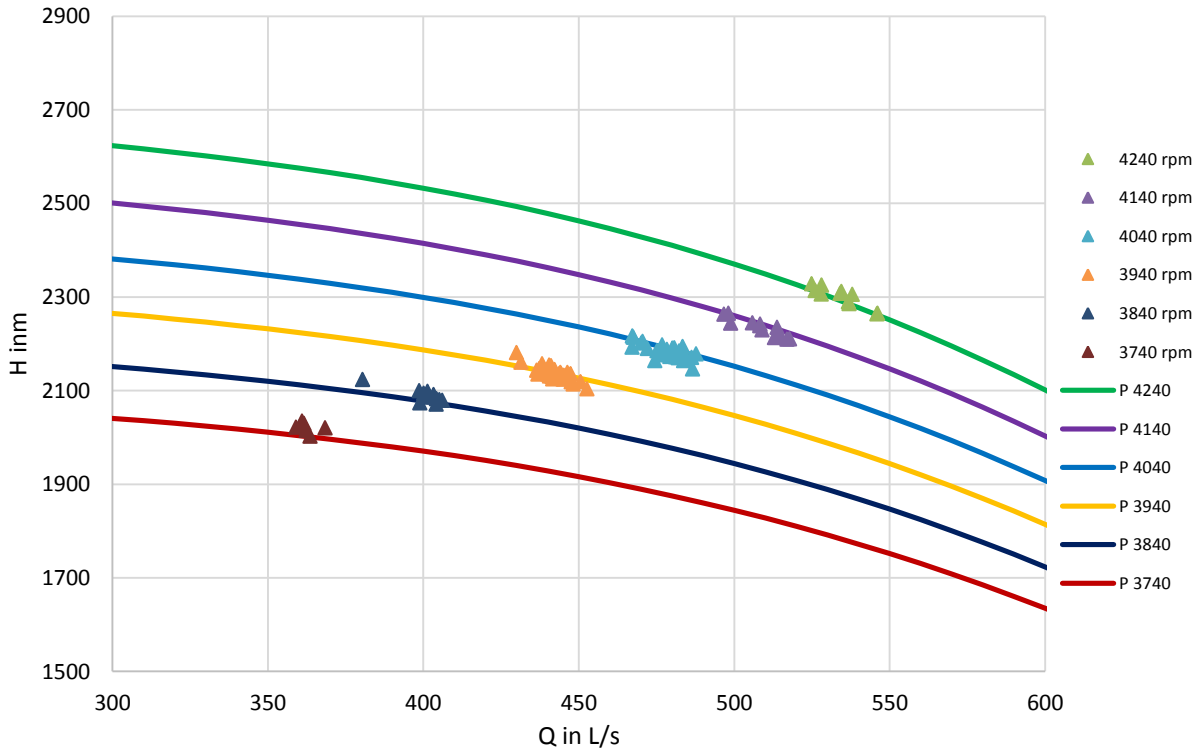

Figure 3.13: Confirmation of validity of OEM pump curves

3.4 Heat Balance Diagram Summaries and Data Capture System Data

The relevant values from the OEM heat balance diagrams for Stations A1 and B1 are summarised in Appendices D and E, with assumptions. These serve to describe the process under consideration and they are used for boundary conditions. These provide a useful indication of design values. Station B1 serves as a comparison for Station A1.

General Boundary Conditions from DCS Trends

In addition to the heat balance data from station manuals, data was accessed from the data capture system (DCS) of Station A1 for the purposes of model tuning, model validation and integrated model development. For this last point, each of the boundary conditions of interest was sampled from the data capture system and averaged against generator load at intervals of 10 minutes for one week. From this, lines of best fit were obtained allowing for typical boundary conditions to be determined for different generator load inputs. The correlations obtained for different boundary conditions with respect to generator load were utilised in a script, so that a generator load input would set all relevant boundary conditions to typical values for that load.

An example of this is shown in Figure 3.14, where a good linear correlation is seen between IP bled steam pressure and generator load. The load is limited to the range of approximately 60 % – 95 % as this is the range on which the Unit typically operates.

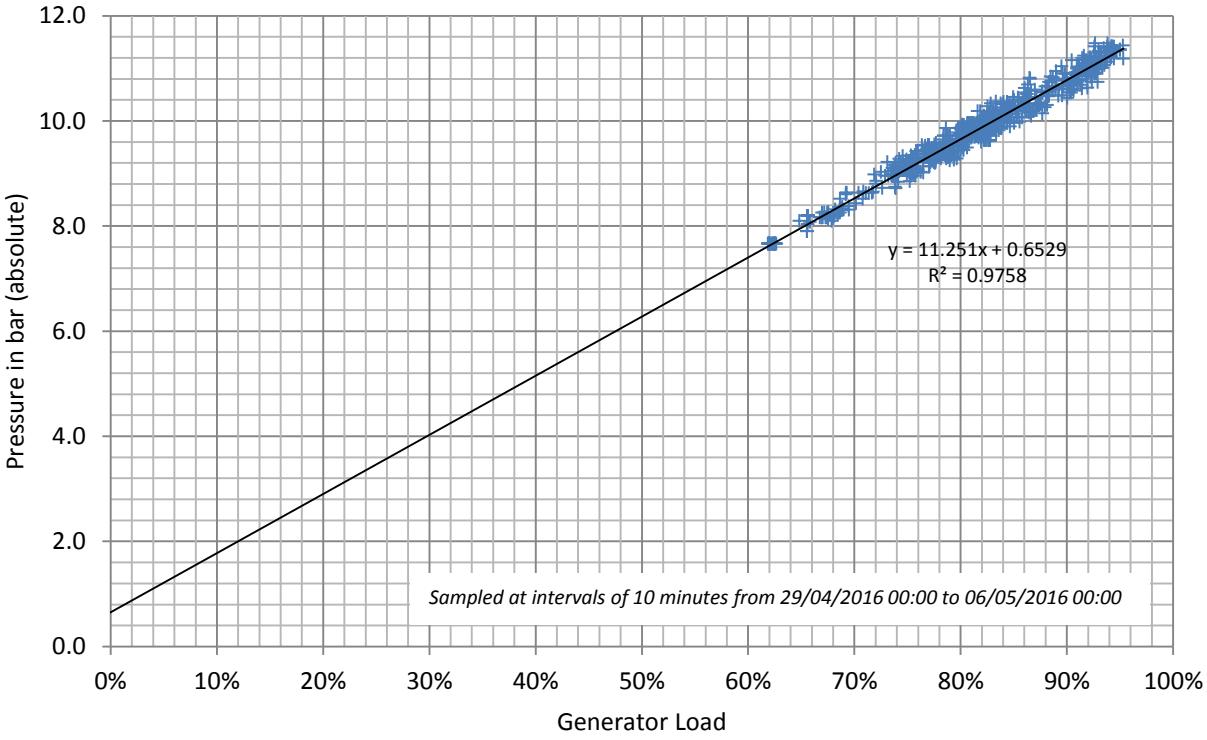

Figure 3.14: Example of boundary condition projections from DCS values – IP bled steam pressure vs load

During the minimum generation tests discussed in Section 3.12, additional data was obtained for these boundary conditions outside of the normal range, sampled at intervals of five minutes. An example is shown in Figure 3.15. Although the BFPT was not in service during these tests, the boundary condition (IP bled steam pressure in this case) can be seen to follow a linear trend down to 40 % load where useful data is available, justifying the linear extrapolation outside of the normal operating range.

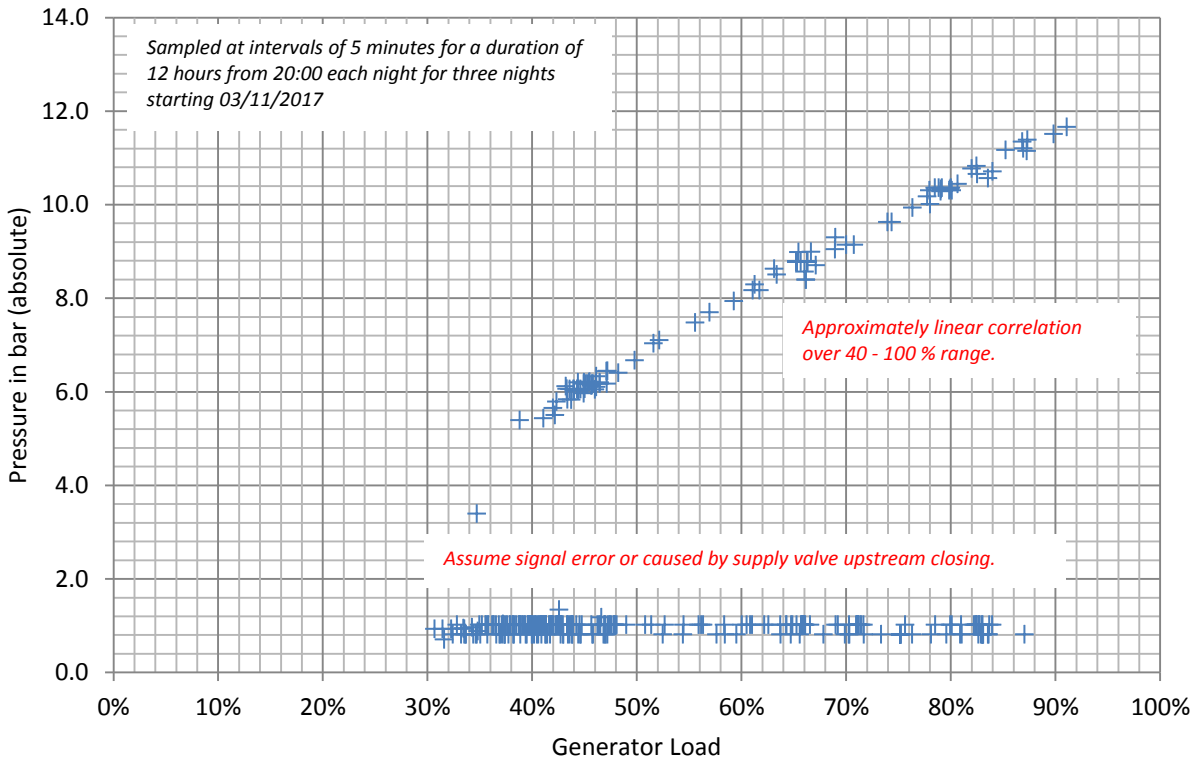

Figure 3.15: Example of boundary condition projections from DCS values – IP bled steam pressure vs load, low load tests

With the exception of condenser pressures, all pressure measurements available from the DCS were gauge values. In order to obtain absolute values, an atmospheric pressure of 84 kPa was assumed, based on typical weather measurements.

Figure 3.16 illustrates the naming convention used for the different boundary conditions. Shown in red are the assumed relationships with respect to generator load. Most are linear. Condenser vacuum is exponential to reflect the expected relationship but this is highly variable depending on ambient conditions and so the exponential curve reflects typical values with respect to load, , as shown in Figure 3.17. The question of poor condenser back pressure and its variability is discussed under Case Studies. Pump discharge pressure was also assigned a non-linear correlation, as discussed in the following section.

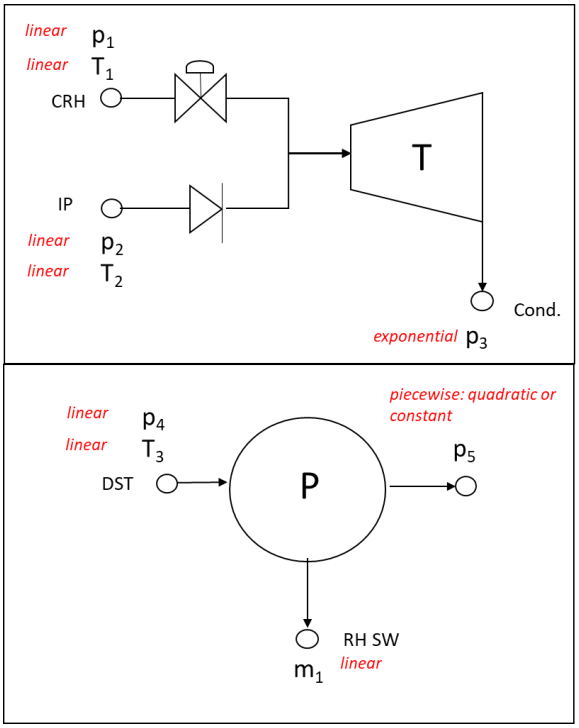

Figure 3.16: Naming convention for boundary conditions

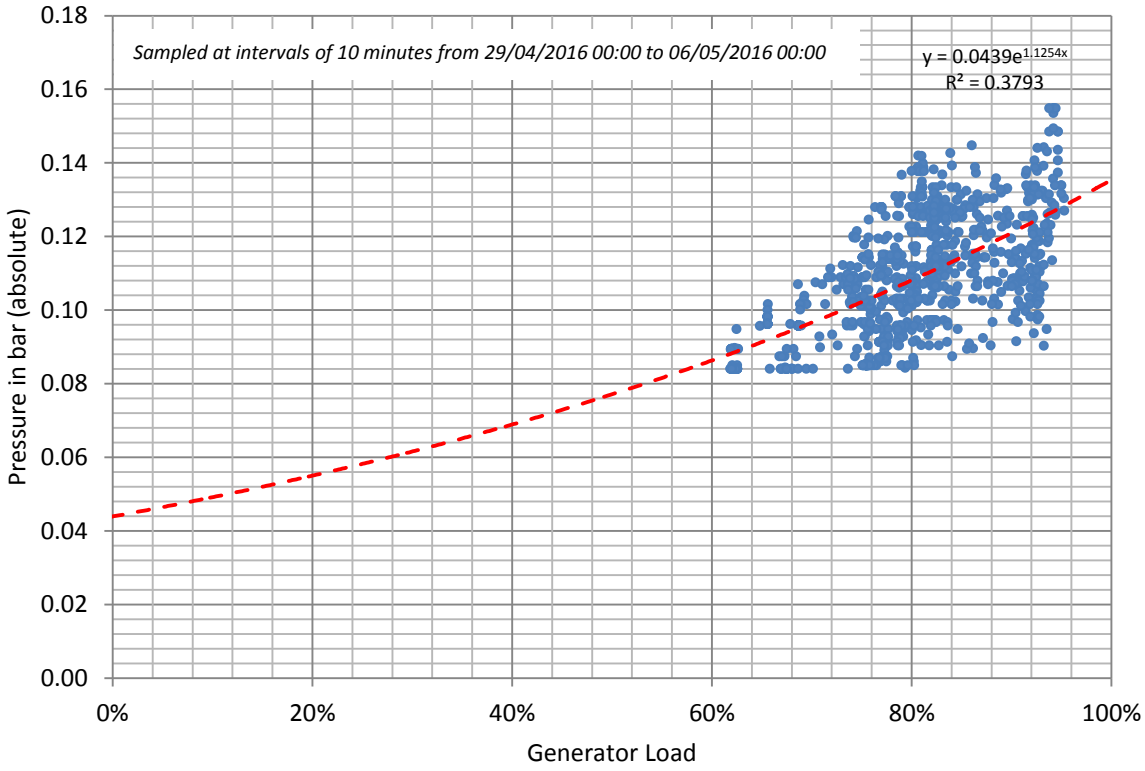

Figure 3.17: Example of boundary condition projections from DCS values – condenser back-pressure vs load, demonstrating high variability due to sensitivity to ambient conditions

Pump Discharge Pressure

Based on the discussion contained in Appendix H, the decision was made to model the pump discharge pressure as a static back pressure solely dependent on generator load. The boundary condition as a function of generator load is illustrated in Figure 3.18.

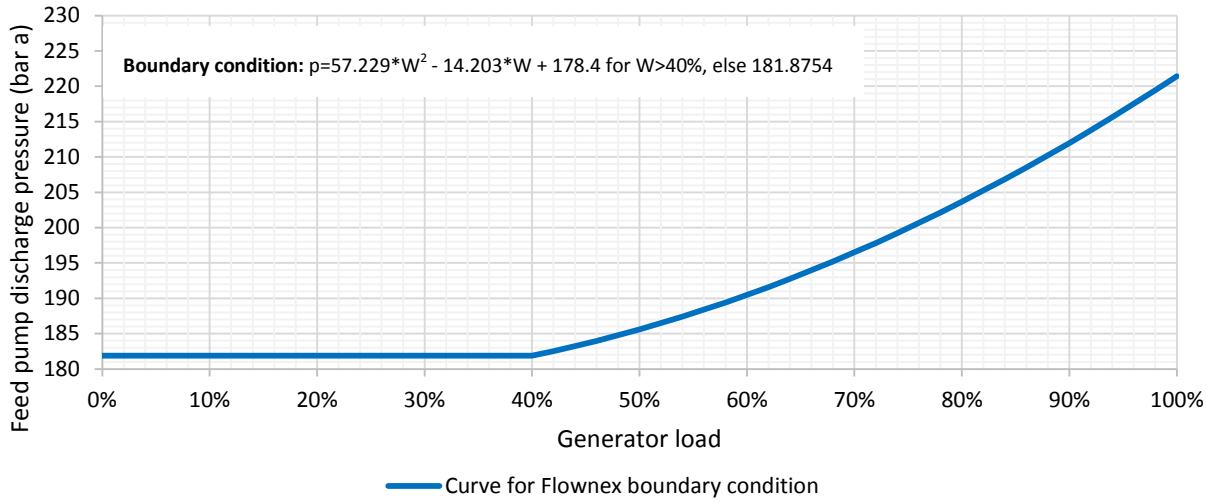

Figure 3.18: Feed pump discharge pressure vs generator load

All boundary condition correlations are expressed in the excerpt from the *Flownex* script appearing in Appendix A.

3.5 Turbine Drawings for Dimensional Considerations

Suitable drawings were obtained of the relevant turbines, allowing for the mean blade diameters to be measured. As the blade diameters were not dimensioned on these drawings, they were measured and then scaled with reference to a component of known size.

Figure 3.19 shows this diagram for Station A1. The rotating rows are indicated in yellow and numbered one to nine. Figure 3.20 shows this diagram for Station B1 with the rotating rows again indicated in yellow and numbered in order to allow for comparison between stations.

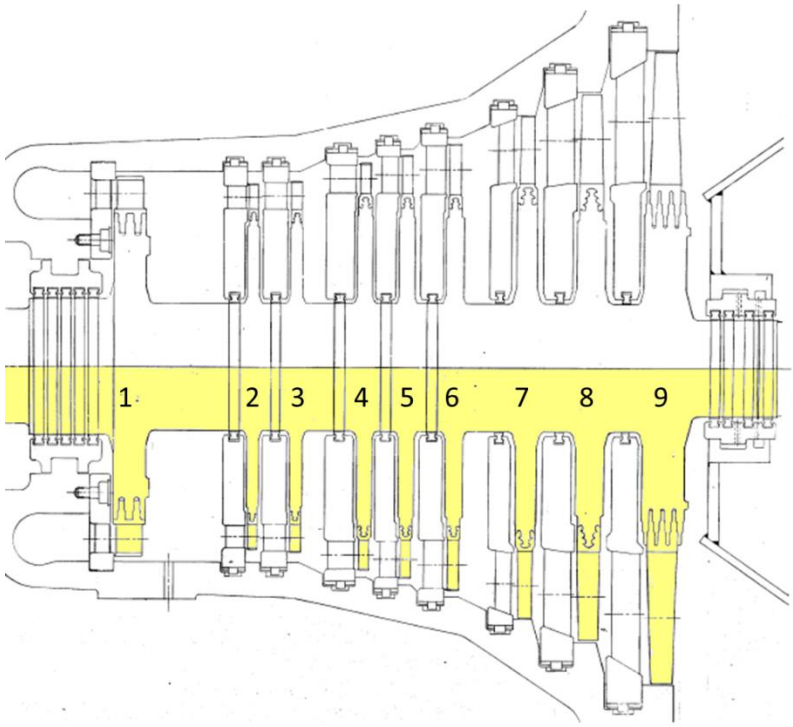

Figure 3.19: Station A1 diagram for estimation of turbine blade diameters

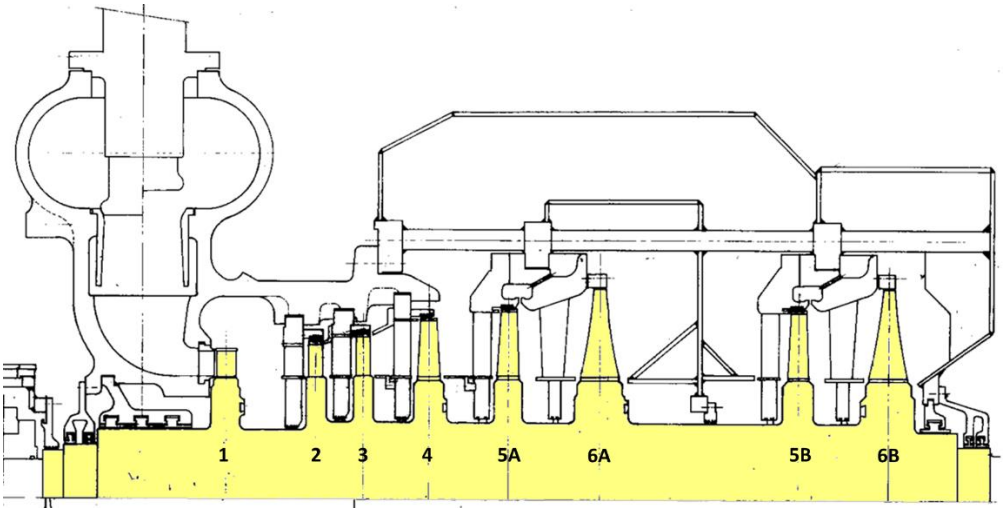

Figure 3.20: Station B1 diagram for estimation of turbine blade diameters

The nominal rotor speed at full load was determined from the pump curves. The shaft speeds at boiler maximum continuous rating (MCR) are 4542 rpm for Station A1/A2 and 5276 rpm for Station B1/B2. Knowing the blade mean diameters and speeds, the mean blade velocities for each stage was calculated for MCR conditions and used in the model calibration. Mean blade diameters are shown in Table 3.2, together with blade velocities at the nominal shaft speeds. Stations B1/B2 are also included for comparison purposes.

Table 3.2: Mean Blade Velocities for Rotating Stages at Stations A1, A2, B1 and B2 – Nominal Shaft Speeds

	Station A1/A2		Station B1/B2	
Stage	Mean diameter (mm)	Mean blade velocity (m/s)	Mean diameter (mm)	Mean blade velocity (m/s)
1	837.4	199.145	975.0	269.344
2	821.4	195.351	1 005.0	277.632
3	829.4	197.248	1 035.0	285.919
4	909.2	216.214	1 095.0	302.495
5	933.1	221.904	1 140.0	314.926
6	957.0	227.594	1 200.0	331.501
7	1 052.7	250.353	N/A	N/A
8	1 108.5	263.630	N/A	N/A
9	1 204.2	286.389	N/A	N/A
	Nominal shaft speed (rpm)	4542	Nominal shaft speed (rpm)	5276

The mean diameters were used here but consideration was given to the possibility of using root-mean-square (RMS) diameters instead in order to more accurately represent the turbine. These diameters are calculated as follows:

$$D_{mean} = \frac{D_{inner} + D_{outer}}{2} \tag{73}$$

$$D_{RMS} = \sqrt{\frac{D_{inner}^{\ 2} + D_{outer}^{\ 2}}{2}} \tag{74}$$

Figure 3.21 illustrates the effect of relative blade length on the ratio of mean radius to RMS radius. The red portion represents the range occupied by condensing main LP turbines on 970 MW units running at 1500 rpm – considered to be the extreme case of relative blade length. Throughout this range, the ratio of mean diameter to RMS diameter is 95 % or higher, making the use of the mean diameter justifiable.

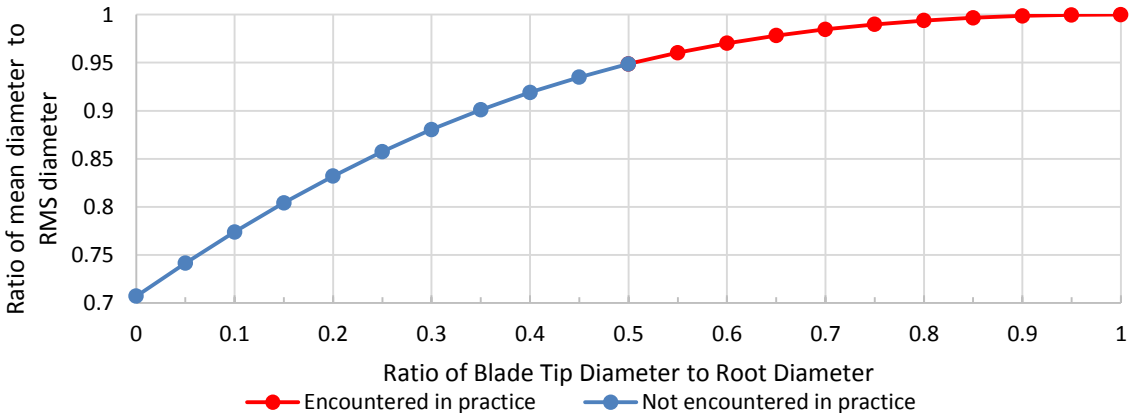

Figure 3.21: Graph showing effect of relative blade length on mean diameter

The blade dimensions of interest for the low pressure turbine discussed above are shown in Table 3.3. Root-tip ratio reduces along the length of the turbine, reaching a minimum of 0.529 on the last stage.

Table 3.3: RMS vs Mean Radius for an Example LP Turbine

Stage no.	Base diameter (m)	Blade length (m)	Root radius (m)	Tip radius	Root radius / tip radius	RMS radius / mean radius
1	2.900	0.066	1.450	1.516	0.956	1.000
2	2.900	0.098	1.450	1.548	0.937	0.999
3	2.900	0.148	1.450	1.598	0.907	0.999
4	2.940	0.239	1.470	1.709	0.860	0.997
5	2.950	0.423	1.475	1.898	0.777	0.992
6	2.880	0.756	1.440	2.196	0.656	0.979
7	2.780	1.240	1.390	2.630	0.529	0.956

From the above one can conclude that using the mean radius for modelling the turbine is adequate.

3.6 Method to Determine Mass Flow Rate and Exhaust Enthalpy

Whereas some DCS values were directly available for nozzle area estimates and the tuning of the *Flownex* model, the steam mass flow rate and real exhaust enthalpy used for model tuning in Section 3.8 and model validation in Section 3.9 had to be determined from other values.

The assumptions which had to be made will be clarified here before the resulting values are used in setting up the model.

3.6.1 Mechanical Efficiency

The feedwater mass flow rate is measured in the plant but the bled steam mass flow rate is not and this value must be inferred by calculating a mechanical efficiency.

The feedwater mass flow rates are stated on the heat balance diagrams. The density before and after the pump can be determined from pressure and temperature, and from this an average density can be obtained. This was used to convert the mass flow rate into a volumetric flow rate. The isentropic work done by the pump is then expressed as follows:

$$W_{P,s} = \Delta p_{FW} \cdot Q_{FW} \tag{75}$$

This is the useful hydraulic work done on the fluid.

Alternatively, the isentropic work can be expressed as:

$$W_{P,s} = \Delta h_{FW,s} \cdot \dot{m}_{FW} \quad (76)$$

Where the discharge enthalpy is evaluated at suction entropy and discharge pressure, and the suction enthalpy is taken from the heat balance diagram.

The real work consumed by the fluid can be expressed as follows, using the heat balance suction and discharge enthalpies, and feedwater mass flow rate:

$$W_P = \Delta h_{FW} \cdot \dot{m}_{FW} \quad (77)$$

The pump isentropic efficiency (or hydraulic efficiency) is then:

$$\eta_P = \frac{W_{P,s}}{W_P} \quad (78)$$

The hydraulic efficiency is also provided on the pump curves as a function of volumetric flow rate for a nominal speed of 4542 rpm. Neglecting a change in running speed, and using this curve to determine each of the heat balance η_p values (as a function of volumetric flow rate), these values agreed with the calculated η_p values within 1 to 3 hydraulic efficiency percentage points.

The real work done by the turbine, the useful work output, can be expressed as follows, with the enthalpy and mass flow rate values being read off the heat balance diagram:

$$W_T = \Delta h_{stm} \cdot \dot{m}_{stm} \quad (79)$$

This is approximately the same value as the “turbine coupling power” quoted on the heat balance diagrams.

A mechanical efficiency, η_{mech}, may be defined as follows:

$$\eta_{mech} = \frac{W_{P,s}}{W_T} \quad (80)$$

If there were no mechanical losses along the shaft, then the real work done by the turbine would equal the isentropic work consumed by the pump (which exceeds the real work of the pump, as only a portion of the ideal work is done on the fluid).

Utilising the 100 % heat balance diagram without reheat spraywater, a mechanical efficiency of 98.968 % was obtained. The gearbox efficiency accounts for part of this. It will be shown in a subsequent section that the gearbox efficiency is substantially poorer than this total mechanical efficiency.

This total mechanical efficiency value could then be used to determine the required steam mass flow rate for a given feedwater mass flow rate required for given boundary conditions. The assumption was made that η_{mech} was constant over generator load.

Steam mass flow rate can be expressed as follows:

$$\dot{m}_{stm} = \frac{\dot{W}_P}{\eta_{mech} \cdot \Delta h_{stm}} = \frac{\dot{m}_{FW} \cdot \left(\frac{\Delta p_{FW}}{\rho_{FW}} \right)}{\eta_{mech} \cdot \Delta h_{stm}} \quad (81)$$

Subscripts “FW”, “stm” and “T” denote feedwater, steam and turbine respectively.

3.6.2 Turbine Isentropic Efficiency

The exhaust enthalpy cannot be directly measured as this turbine is condensing and the exhaust steam is wet (that is, having a dryness factor between 0 and 1). If the turbine under consideration was, for example, the HP turbine, the exhaust steam, being superheated, could have its enthalpy determined by measuring the exhaust temperature and pressure and the actual isentropic efficiency would then be known.

The exhaust enthalpy at different load conditions must therefore be inferred for the BFPT by considering heat balance data. For this reason, it is necessary to calculate the predicted turbine isentropic efficiency.

For each heat balance diagram available, the isentropic efficiency was determined over the turbine and steam valves as follows:

$$\eta_s = \frac{h_{bled\_steam} - h_{exhaust,real}}{h_{bled\_steam} - h_{exhaust,isentropic}} = \frac{h_{bled\_steam} - h_{exhaust,real}}{h_{bled\_steam} - h(p_{condenser}, s_{bled\_steam})} \quad (82)$$

h, p and s have the usual meanings of enthalpy, pressure and entropy respectively. Where h was calculated as a function of pressure and temperature, steam tables were used.

It was necessary to calculate this efficiency over the steam admission valves and the turbine together as pressures were not measured between the valves and the turbine. On the range 45 % to 100 %, this efficiency ranged from 71 % to 77 %, as illustrated in Figure 3.22. A quadratic trendline was utilised which had a correlation coefficient of 0.995. Extrapolating, this line meets the zero load axis at an efficiency of about 60 % and the turning point of the parabola occurs around 100 % load, as expected. This curve was used to infer the efficiencies at different loads when utilising DCS data.

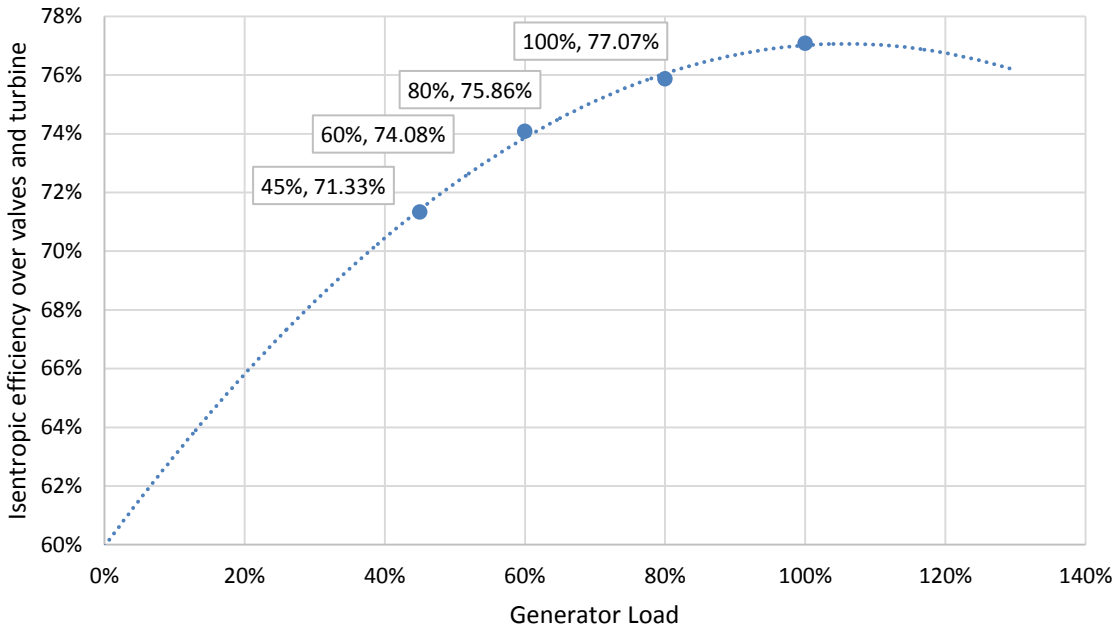

Figure 3.22: Heat balance isentropic efficiencies

Considering the four cases utilised – 62 %, 69 %, 83 % and 95 % - all during periods of load stability during May 2016 – it was noted that none of the turbine exhaust temperatures or condenser hotwell temperatures exceeded the saturation temperature associated with the condenser back pressure, in other words, the steam quality was between 0 and 1. In order to determine a reasonable exhaust enthalpy, the curve shown in Figure 3.22 was applied.

The bled steam enthalpy and entropy were calculated from steam tables as a function of the measured pressure and temperature upstream of the steam admission valves. Isenthalpic throttling was assumed, so that the enthalpy before and after the steam admission valves remained constant. The average pressure after the steam admission valves was calculated, noting that the pressure after each valve was different because of partial arc admission. This is considered a reasonable approximation given the available data. The entropy could then be evaluated at this pressure and enthalpy downstream of the valves.

Evaluating with respect to the condenser pressure and the inlet entropies, the exhaust enthalpies could be calculated assuming an isentropic process over valves and turbine. Applying the isentropic efficiency over valves and turbine, the actual exhaust enthalpy could be calculated.

The turbine isentropic efficiency could then be evaluated at these different conditions. This is illustrated below.

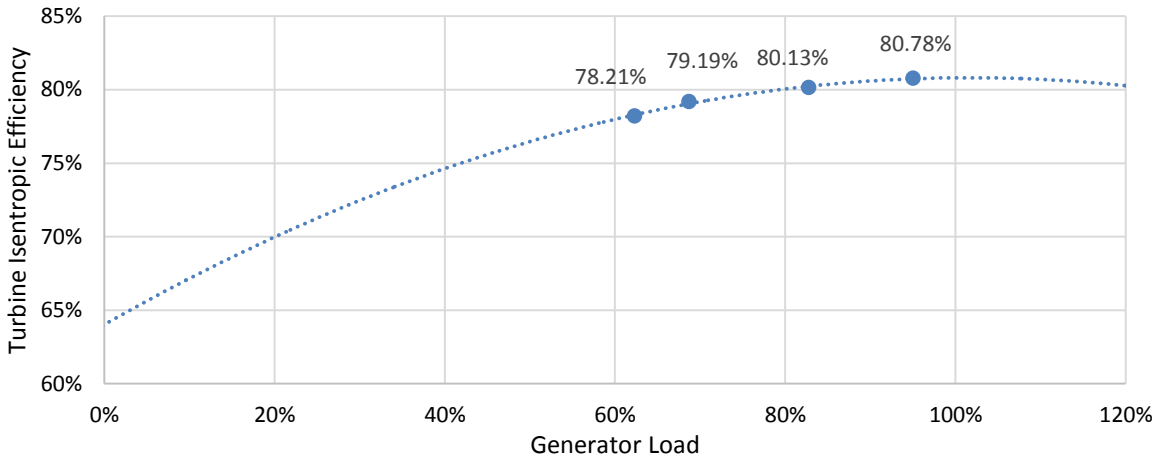

Figure 3.23: Turbine isentropic efficiencies from DCS and HBD

It is noted that once the effect of the valves is accounted for, the turbine efficiency is substantially higher than when the turbine and valves are considered together. Here an efficiency of about 81 % is encountered at 95 % load.

Relating to the Turbine Nozzle Model

The isentropic efficiency of each turbine nozzle can be related to the loss coefficient ζ as follows:

$$\zeta = \frac{1}{\eta} - 1 \qquad (83)$$

If there are no carry-over or exhaust losses, then the complete turbine's in-efficiency is simply due to the nozzle losses. Applying this to the total turbine efficiency, an average ζ value may be estimated to be used as an initial model input. This is plotted in Figure 3.24. For the 95 % case, this value is 0.2380.

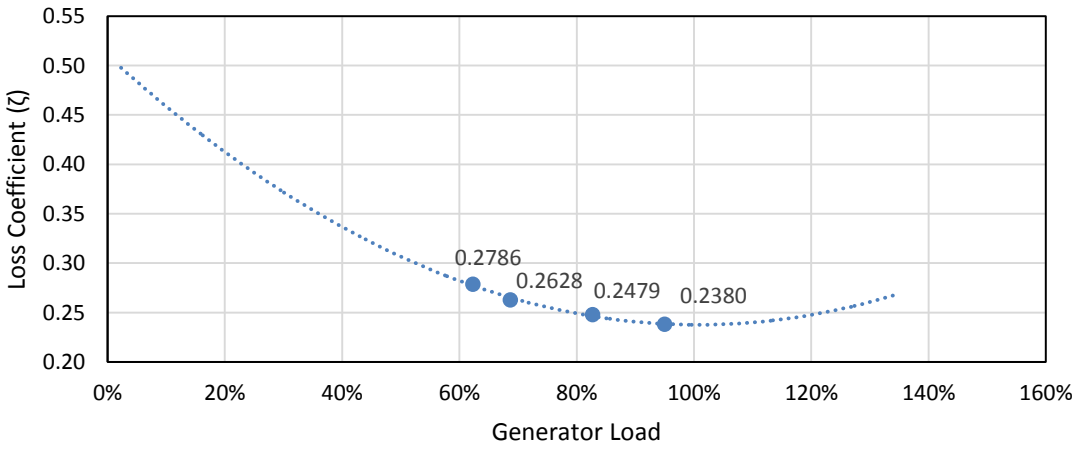

Figure 3.24: Estimated average loss coefficient

3.6.3 Gearbox Efficiency

The turbine and main pump shafts are directly coupled to each other whereas the turbine shaft is connected to the booster pump via a mechanical gearbox. It will be assumed that all of the mechanical loss associated with η_{mech} can be assigned to the gearbox for the purpose of modelling in Flownex.

While the mechanical loss is almost negligible relative to the total power transferred, the booster pump consumes a fraction of the power of the main pump and so the gearbox efficiency is much lower than the total mechanical efficiency.

The system layout is shown in Figure 3.25.

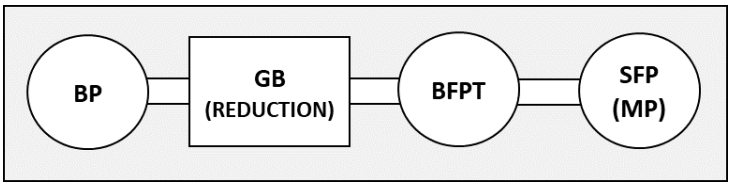

Figure 3.25: Layout of Station A1 system with reference to gearbox

Calculation of the Gearbox Efficiency

The gearbox reduction ratio used was 3.06 based on DCS measurements between the two speeds.

The head increases, H, for the main and booster pumps, were expressed as functions of volumetric flow rate Q for nominal speeds of 4542 rpm and 1622 rpm respectively. These functions were multiplied by $\left(\frac{N}{N_{reference}}\right)^2$ in order to scale the curves with reference to speed. The equations for H(Q) at reference speeds were obtained when the pump curves were digitised (see Section 3.3).

Assuming a constant density and volumetric flow rate over the pump based on the 100 % heat balance values, the hydraulic (real) power of each pump could be expressed in terms of shaft speed and summed together for the total power. The shaft speed is not stated on the heat balance diagrams. In order to determine the shaft speed corresponding to the expected power consumption at full load, an iterative solve loop was used. This yielded a speed of 4097 rpm at full load, considerably lower than the expected MCR speed of 4542 rpm obtained from pump curves.

Hydraulic efficiencies were expressed as functions of Q for the reference speeds of 1622 rpm and 4542 rpm. Since the pump similarity laws assume dynamic similarity (that is, the same Reynolds number), the efficiency is independent of scale. The effect of speed was therefore neglected. The total power consumed by each pump was then determined, and the mechanical efficiency, η_{mech}, calculated in 3.6.2 was applied to determine the total power consumed.

The lost power could then be calculated as the difference between these two and assigned to the gearbox, resulting in a gearbox efficiency of 70.243 %. This was later adjusted in the *Flownex* integrated model in order to achieve the expected shaft speed for the 95 % DCS case, with a final efficiency of 62.08 % being used.

3.7 Turbine Nozzle Throat Area Estimates

In estimating nozzle areas and tuning the model, the DCS snapshot for the 95 % scenario was used instead of the 100 % heat balance values as there is a substantial drop over the steam admission valves which is not represented when the heat balance supply pressure is used, and the intermediate pressure on the turbine is not provided on the heat balance diagrams. Accordingly, DCS values were also used for model validation. The measuring points used are highlighted in the following diagram – yellow for boundary conditions and turquoise for targets.

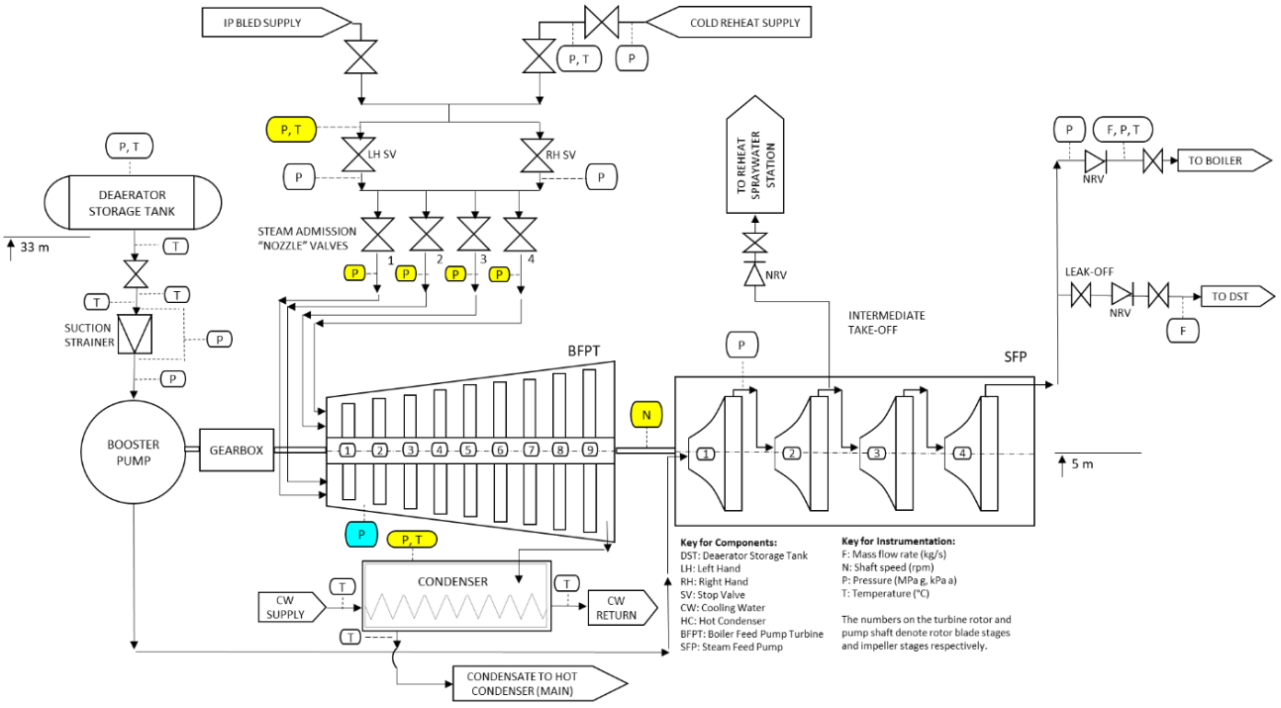

Figure 3.26: Station A1 system configuration, with measurement points highlighted for turbine model

The nozzle throat areas were estimated following the methodology discussed in Section 2.3.8 and illustrated in Figure 2.47. In calculating the nozzle areas, it is important to remember to use the *relative* exit velocity (v_{3r}) for the throat velocity in the moving rows. The throat velocity at the exit of the stationary rows is the absolute exit velocity, v_2. Note that because this turbine uses partial arc admission, the first stage was split into four identical parallel stages with quarter areas. The average pressure after the steam admission control valves was initially used as the inlet pressure to all four quarter-stages to facilitate model tuning.

Reaction Ratios

The enthalpy drops were estimated using the equations introduced in Section 2.3.1. In order to establish reasonable estimates for the reaction ratio, the chart by Cotton was considered (Figure 2.25). Based on this, Figure 3.27 displays typical reaction ratios for the system of interest. Because the turbine in question is nominally "impulse-type" in the manuals, the impulse charts were used. LP turbine charts were used because this is also a condensing turbine. Because these charts assume six stages and the turbine in question has nine stages, some modifications were made where the same reaction ratio value was used more than once. Care was taken to avoid choking on each row by maintaining pressure ratios above those required to theoretically avoid choking. As a result, all pressure ratios were ultimately above 0.6.

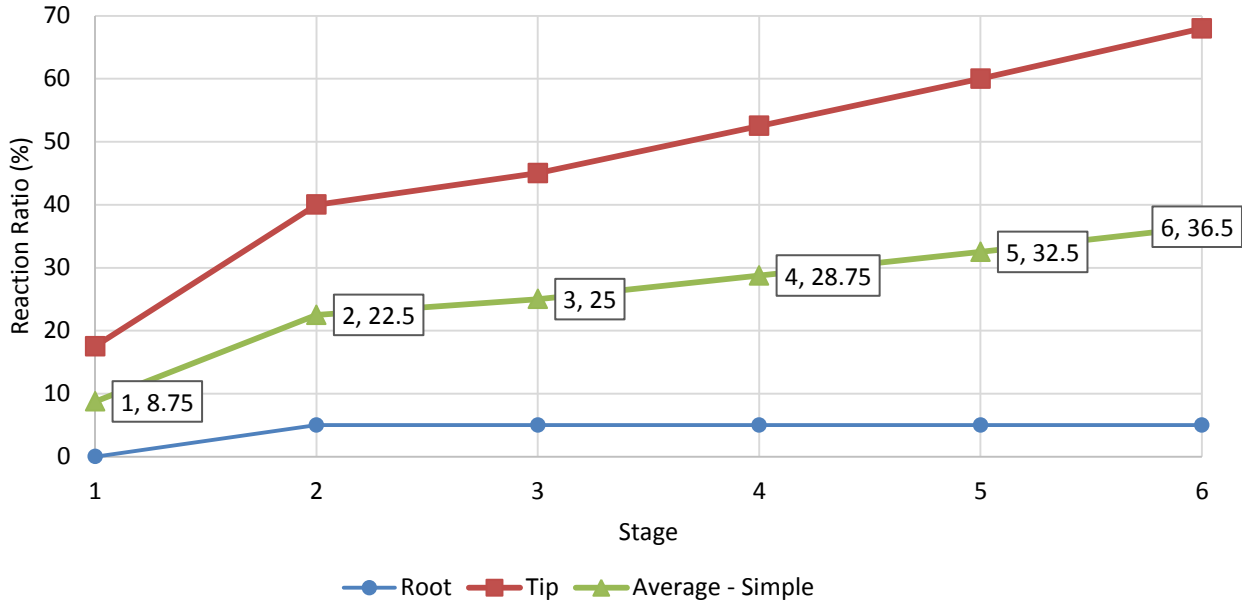

Figure 3.27: Expected change in reaction ratio over the shaft length, based on Cotton (1998)

Other Attempts with Reaction Ratios

Initially, all stages were chosen as impulse and this led to choking on a number of stages, justifying the use of non-zero R-values. After that, the assumption was made that the stage loading coefficients were the same for all stages. Two problems were apparent with this assumption: the expected pressure after the turbine's first stage was substantially higher than the target and the pressure ratios expected over the last three stages predicted choking. This was reflected in the performance of the model in *Flownex*. This necessitated the use of increasing R-values, supported by the observations of Cotton.

Critical Pressure Ratios

The required minimum and the actual pressure ratio per row were calculated as explained in Section 2.3.8 and adjustments were made by trial-and-error to the nozzle angles and the reaction ratios until the correct enthalpy drops were obtained without choking.

Nozzle Angles

Nozzle angles were modified in order to obtain the correct total (isentropic) enthalpy drop over the turbine while obtaining an approximately correct intermediate pressure after Stage 1. Because of the limited information available, Stage 1 was given one nozzle angle (37 °) while the rest of the stages were assumed to have the same angle (22 °).

Table 3.4 displays the major results of the initial area and nozzle angle estimates for Station A1. As the reaction ratio is increased, the portion of the pressure and enthalpy drops over the rotating rows increase, as expected.

In calculating these initial area estimates, the following assumptions were made:

1. The inlet velocity to each stage's stationary blades (the stationary nozzles) is negligible.
2. There is perfect carry-over of velocity from the stationary blade (stationary nozzle) exit to the rotating blade (rotating nozzle) inlet within each stage.
3. The process is isentropic.

In the *Flownex* model, carry-over efficiency will determine the inlet velocity to the stationary nozzle, making the first assumption no longer valid. The second assumption remains valid. The process will of course not be isentropic, with losses being driven by the nozzle ζ-values. It is therefore necessary to make some further scaling and adjustments to the *Flownex* model after calculating initial area estimates.

Table 3.4: Turbine Nozzle Area Estimates for Station A1

Group	Stage	S/R	α	R	Γ	Δh_{row}	r	Stationary nozzle velocity (v2)	Rotating nozzle velocity (v3r)	Nozzle area
			°			kJ/kg		m/s	m/s	m^2
A	1	S	37	0.00%	2.000	110.5	0.679	470.1		0.0056
		R				0.0	0.826		339.5	0.0078
B	2	S	22	0.00%	2.000	78.9	0.742	397.2		0.0335
		R				0.0	0.901		236.7	0.0562
	3	S	22	0.00%	2.000	80.4	0.721	401.1		0.0426
		R				0.0	0.892		239.0	0.0715
C	4	S	22	8.75%	1.825	80.5	0.701	401.1		0.0559
		R				7.7	0.864		257.5	0.0896
	5	S	22	22.50%	1.550	61.1	0.745	349.7		0.0825
		R				17.7	0.850		256.7	0.1203
	6	S	22	25.00%	1.500	60.2	0.728	347.1		0.1133
		R				20.1	0.830		261.8	0.1635
D	7	S	22	28.75%	1.425	65.8	0.679	362.7		0.1605
		R				26.5	0.781		285.6	0.2355
	8	S	22	32.50%	1.350	65.5	0.659	361.8		0.2691
		R				31.5	0.749		298.3	0.3928
	9	S	22	36.50%	1.270	68.4	0.626	369.8		0.4813
		R				39.3	0.695		321.1	0.7124
					Actual Σ	814.1				
					Expected Σ	816.3				

3.8 Turbine Nozzle Model Tuning in *Flownex*

Table 3.5 details the targets and boundary conditions used for model tuning and validation in *Flownex*. The first case, 95.01 %, was used for tuning. These were all extracted/calculated from DCS data.

Table 3.5: Targets and Boundary Conditions for Model Tuning and Validation in *Flownex*

Case	Generator load		95.01%	82.74%	68.67%	62.31%
Boundary Conditions	Supply steam pressure after valves	bar (a)	8.585	7.259	6.083	5.669
	Supply steam enthalpy	kJ/kg	3225.7	3221.8	3208.1	3209.2
	Condenser back pressure	bar (a)	0.1338	0.1128	0.0957	0.0894
	Shaft speed	rpm	4281.250	4066.600	3845.632	3758.625
Targets	Steam mass flow rate	kg/s	22.557	19.902	17.144	15.721
	Pressure after Stage 1	bar (a)	5.838	4.949	4.155	3.836
	Real exhaust enthalpy	kJ/kg	2566.9	2572.1	2573.3	2580.8

The carry-over efficiencies were chosen for Station A1 as follows: 0.01 for the final stage, 0.2 for the first stage, 0.4 for stages 3 and 6, and 0.9 for the remaining stages. These values were chosen based on the spacing between stages, as shown in Figure 3.28. The larger the spacing, the poorer the carry-over.

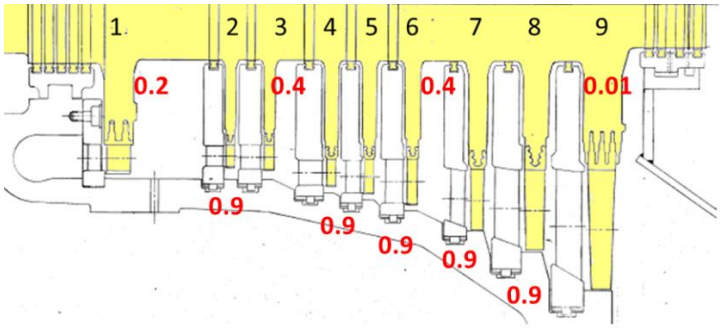

Figure 3.28: Selection of carry-over efficiencies

The nozzle angles (α) were kept as initially calculated.

Through a process of trial-and-error, the nozzle loss coefficients (ζ) were altered in order to achieve the correct exhaust enthalpy and the correct intermediate pressure after Stage 1. All of the nozzles for Stage 1 were set to loss coefficients of 0.2699 while the remaining nozzles were set to loss coefficients of 0.2337. It is noted that the anticipated average ζ-value was 0.2380 from Section 3.6.2 and so these values are not unexpected.

The ζ- and α-values could have been calculated per group noting that certain stages are similar to each other but with the limited information there were insufficient constraints to guide decision-making in this respect. (For example, no further intermediate pressure measuring points were available.) A logical grouping is shown in Figure 3.29. It would be practical to consider similar characteristics for each group and then tune to a known intermediate parameter such as pressure, if this was available. With the ζ values set, the real behaviour of the turbine results in steam mass flow rates less than that expected (because the initial nozzle areas assumed isentropic nozzles, and any nozzle loss acts like a contraction to the nozzle area). All nozzle areas were therefore scaled by the ratio of desired mass flow to mass flow obtained, until the correct mass flow was obtained.

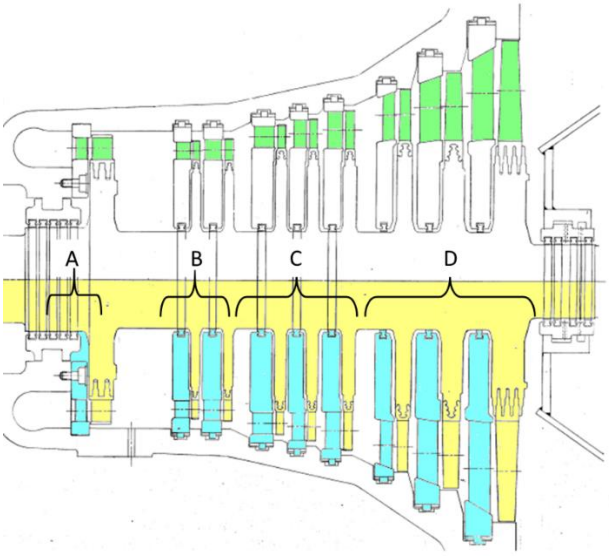

Figure 3.29: Proposed grouping of turbine stages

The resulting *Flownex* turbine model is shown with 95 % generator load boundary conditions in Figure 3.30. The blade efficiency is high because of the assumptions made about Γ, and the degree of reaction is seen to increase along the length, as expected.

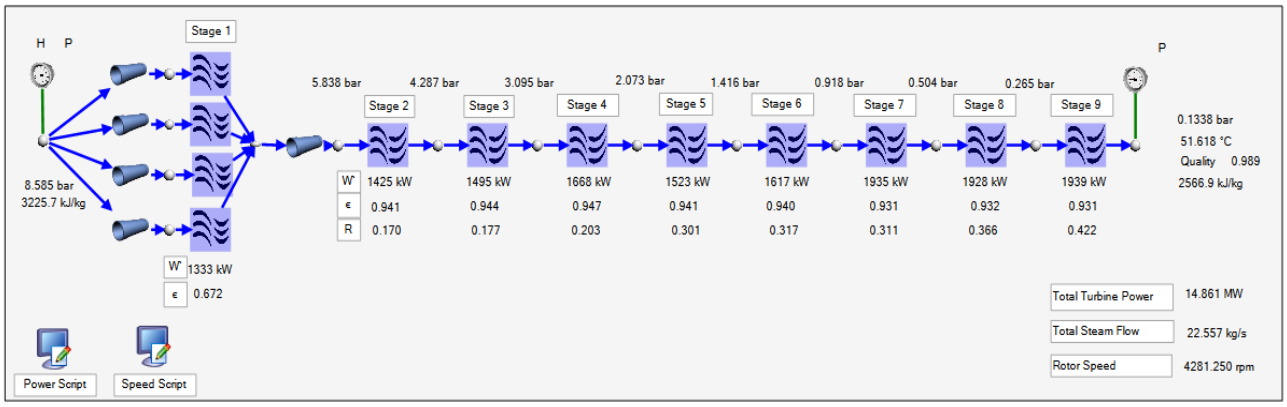

Figure 3.30: Turbine model with 95 % load conditions

Symmetry Assumptions

As noted in Section 2.3.2, in order to calculate the blade efficiency, an assumption must be made about γ, the rotor blade exit angle. For the impulse stage component implemented in *Flownex*, the assumption is that γ ≈ β. For the reaction stage, the assumption is that γ = α. This is based on the usual assumptions made with respect to the symmetry of velocity triangles (refer to Section 2.3.1). This means that stages 2 to 9 assume γ = α, based on the usual symmetry assumption for 50 % reaction turbines.

An alternative approach could have been to have assumed δ = 90 ° (purely axial exhaust from each stage) at full load conditions and then to calculate the γ values. This is a modification that might be considered in future.[5]

If this assumption was made, the following would apply:

$$w = v_b(v_2 \cos\alpha + v_{3r} \cos\gamma - v_b) = v_b(v_2 \cos\alpha + v_3 \cos\delta) = v_b(v_2 \cos\alpha) \qquad (84)$$

And

$$\gamma = \cos^{-1}\left(\frac{v_b}{v_{3r}}\right) \qquad (85)$$

Flow Solver

Difficulties were experienced in model stability and in convergence on pressure with certain pressure relaxation parameters for the flow solver. It was found through a process of trial-and-error that a pressure relaxation value of 0.05 was optimal, although 0.1 was also effective in some cases. The pressure relaxation factor is an expression of the pressure step size taken when the flow solver resolves the network. The number of main iterations could also be varied. This was set between 200 to 1000, depending on how quickly the model was converging.

Challenges with Partial Arc Admission

The first stage was initially considered as four identical stages all experiencing an average inlet pressure. However, in practice, each portion of the first stage has its own valve and therefore a different inlet pressure. Applying the 95 % inlet pressures per section, the turbine was observed to be underpowered. This is illustrated in Figure 3.31. In particular, it can be observed that the power generated decreased from 14.861 MW to 14.697 MW, the steam mass flow decreased from 22.557 kg/s to 22.309 kg/s, and the pressure after Stage 1 decreased from 5.838 bar to 5.767 bar when the inlet boundary conditions were applied per quarter-stage.

[5] Care would need to be taken to ensure that γ was only calculated for the design condition and then fixed for other conditions. If the script were allowed to recalculate at other load conditions, this would represent a modifiable blade exit angle, which is unrealistic.

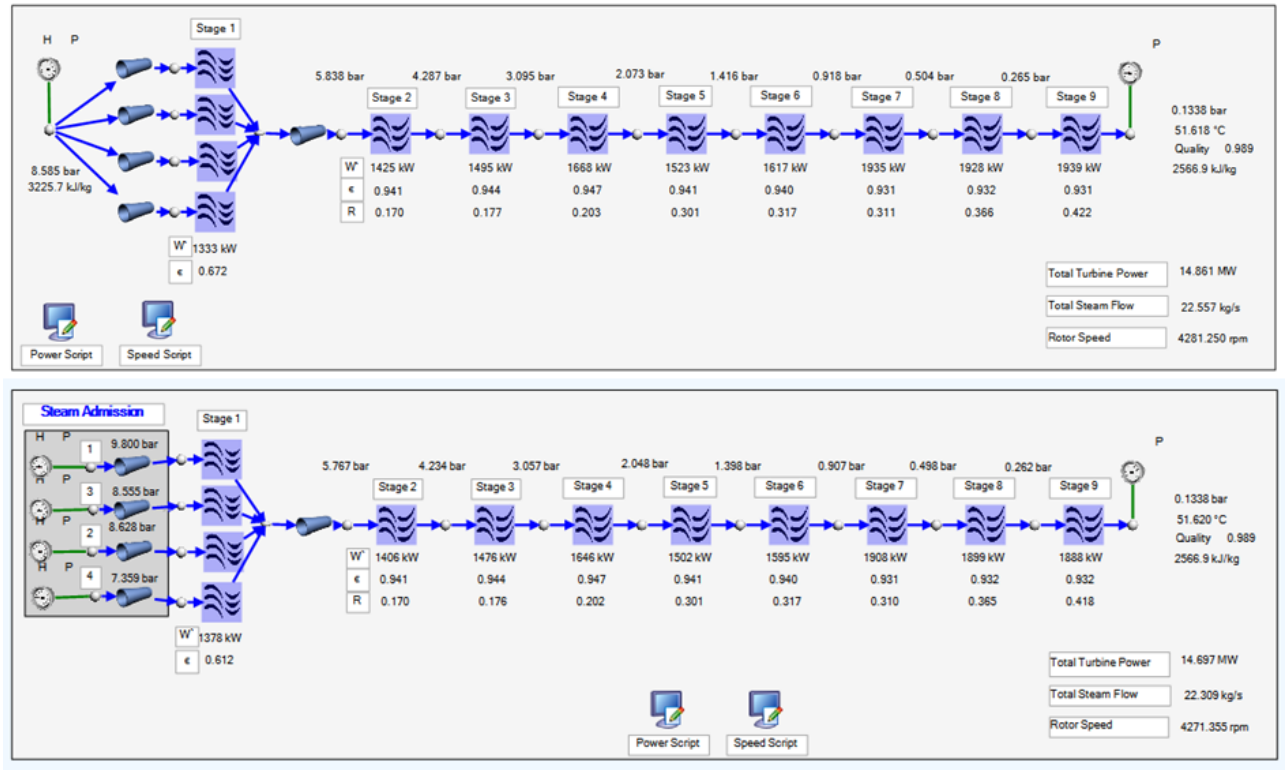

Figure 3.31: Effect of different partial arc inlet pressures

The nozzle characteristics were therefore refined further. The new loss coefficients were ζ_1 =0.2500 and $\zeta_{2...9}$ =0.2360. The areas also needed to be reduced slightly to correct the mass flow rate and this was achieved by applying a constant scaling factor. The new areas and loss coefficients were used in all subsequent applications. The turbine at 95 % load after corrections is shown in Figure 3.32.

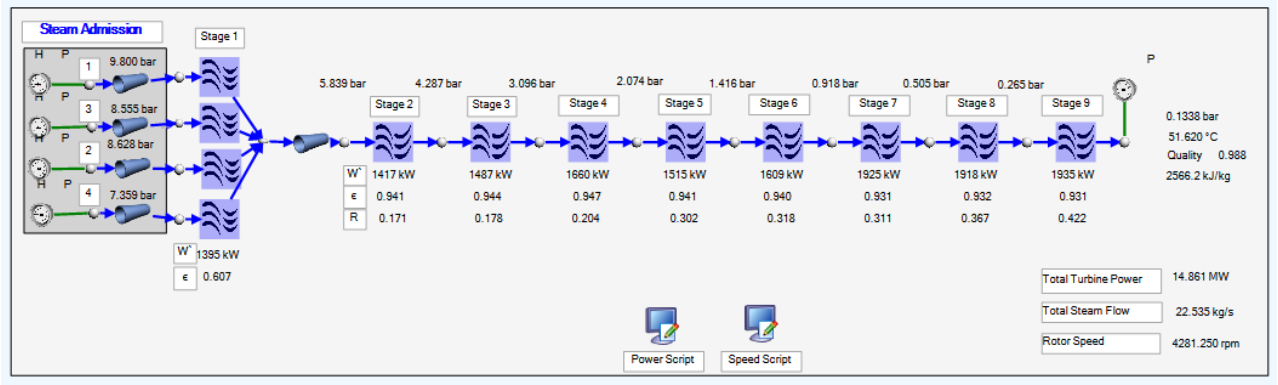

Figure 3.32: Turbine model corrected for partial arc admission

3.9 Turbine Model Validation

The turbine model for Station A1 was tuned for the 95 % load scenario and then the boundary conditions were adjusted to reflect other scenarios. These data snapshots were accessed from the station's data capture system during periods of relative stability – load approximately constant over a duration of at least an hour. Three parameters were considered: intermediate pressure after the first stage, steam mass flow rate and exhaust enthalpy. Power was also considered for illustrative purposes; it is appreciated that the error here reflects the combined errors of mass flow rate and enthalpy. While the intermediate pressure was obtained directly from the DCS, the required mass flow rate and exhaust enthalpy were calculated by applying pump hydraulic efficiencies, a gearbox efficiency and heat balance turbine isentropic efficiencies as introduced in sections 3.6.1 to 3.6.3. As a result, the mass flow target values incorporate a level of uncertainty from the outset.

The results are shown in Table 3.6. The most significant errors were encountered on mass flow rate and turbine power as the load was reduced. This turbine is typically only operated in the range of about 60 % to 100 % generator load and so data was not available outside of this range. Within the range considered, errors were in most cases quite low. In view of typical tolerances in measurement equipment used, this error is considered acceptable for general applications of the model.

Note that Table 3.6 uses the final values as used in the integrated model, and partial arc setup (that is, four different inlet pressure boundary conditions). A snapshot of the model showing validation of the 62 % case appears in Figure 3.33. Note that red highlighting indicates a stage is choked, blue indicates that it is not choked. One quarter-arc of the first stage is choked in this case, but steam is still free to flow through the remaining arcs and so the stage is not considered choked overall.

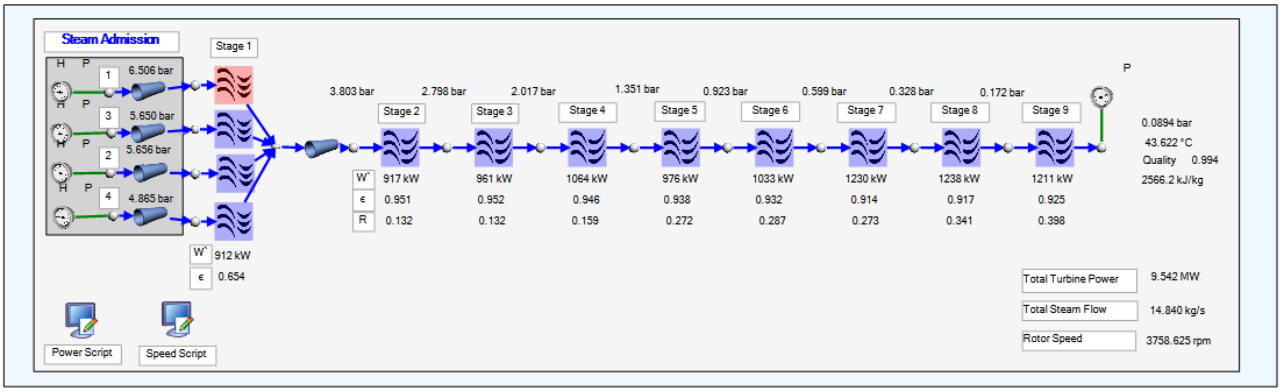

Figure 3.33: Model snapshot showing validation of 62 % case

Table 3.6: Validation of BFPT Model

Case[6]	Parameter	Unit	Expected value	Model result	Difference (absolute)	Percentage error (absolute)
95%	Pressure after Stage 1	bar a	5.838	5.839	0.001	0.01%
	Real enthalpy after Stage 9	kJ/kg	2566.9	2566.2	0.7	0.03%
	Real enthalpy drop over turbine	kJ/kg	658.8	659.5	0.7	0.10%
	Steam mass flow rate required	kg/s	22.444	22.443	0.001	0.00%
	Total turbine power	MW	14.786	14.801	0.014	0.10%
83%	Pressure after Stage 1	bar a	4.949	4.904	0.044	0.90%
	Real enthalpy after Stage 9	kJ/kg	2572.1	2566.5	5.6	0.22%
	Real enthalpy drop over turbine	kJ/kg	649.7	655.3	5.6	0.86%
	Steam mass flow rate required	kg/s	19.812	18.936	0.876	4.42%
	Total turbine power	MW	12.872	12.409	0.463	3.60%
69%	Pressure after Stage 1	bar a	4.155	4.087	0.068	1.64%
	Real enthalpy after Stage 9	kJ/kg	2573.3	2564.1	9.2	0.36%
	Real enthalpy drop over turbine	kJ/kg	634.7	644.0	9.2	1.45%
	Steam mass flow rate required	kg/s	17.069	15.922	1.147	6.72%
	Total turbine power	MW	10.834	10.253	0.581	5.36%
62%	Pressure after Stage 1	bar a	3.836	3.803	0.034	0.88%
	Real enthalpy after Stage 9	kJ/kg	2580.8	2566.2	14.6	0.56%
	Real enthalpy drop over turbine	kJ/kg	628.4	643.0	14.6	2.32%
	Steam mass flow rate required	kg/s	15.657	14.840	0.818	5.22%
	Total turbine power	MW	9.839	9.542	0.297	3.02%

Comparison with Other Methods

In view of the error being greatest on the steam mass flow rate, the constant flow coefficient method and the Stodola ellipse law, as introduced in Section 2.3.10, were applied to the boundary conditions in order to compare these results. Note that in both cases the 95 % case conditions were used as design values as using the 100 % heat balance bled steam values would not account for the effect of the throttling of the steam admission valves. The modified Stodola method was not applied here as turbine stage choking was not considered a concern on this operating range.

Table 3.7: Mass Flow Rates by Different Methods

	Case 1 - 95%	Case 2- 83%	Case 3 - 69 %	Case 4 - 62%
Nozzle model	22.443	18.936	15.922	14.840
Constant flow coefficient method	22.444	19.053	16.530	15.240
Stodola ellipse law	22.444	19.053	16.530	15.240
Required	22.444	19.812	17.069	15.657

[6] 579 MW, 504 MW, 418 MW, 379 MW respectively

This is illustrated graphically in Figure 3.29. The three models are in general closer to each other than to the required mass flow rate. This further points to the uncertainty in the calculation of the required mass flow. Since some of the first stage nozzles do choke at lower load, the estimates by the constant flow and ellipse law is expected to report larger mass flows as compared to the detail nozzle model.

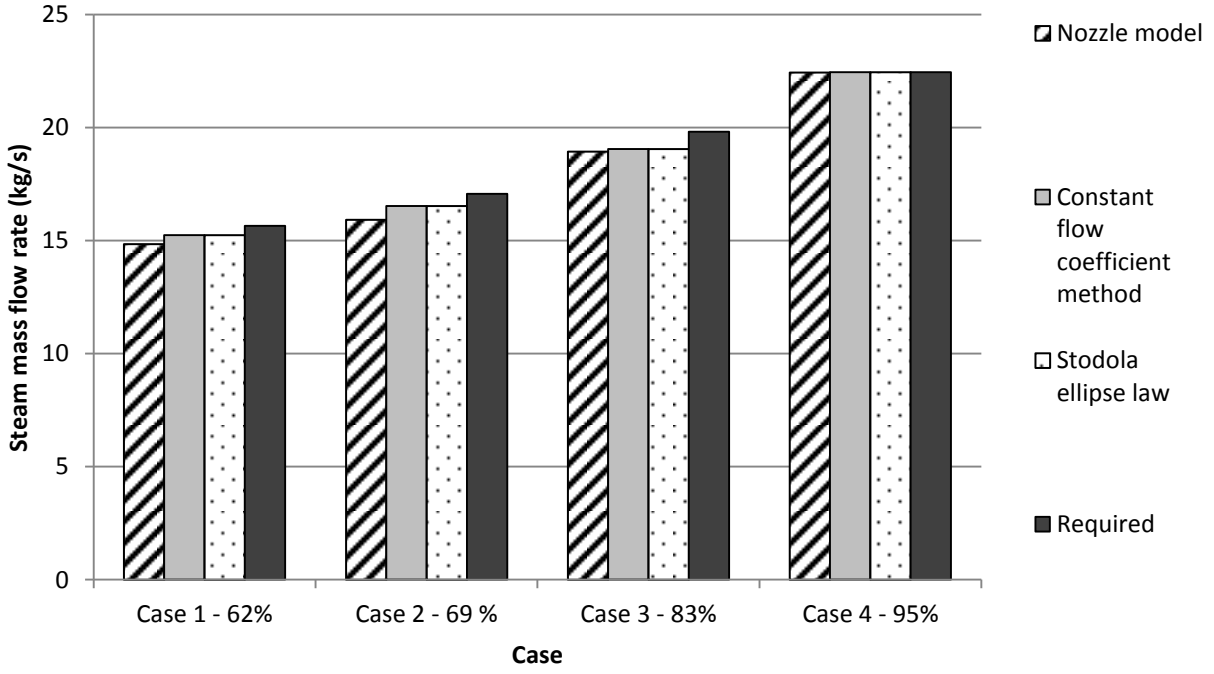

Figure 3.34: Visual representation of different methods of determining mass flow rate

3.10 High Level Turbine Representation

In order to couple the turbine to the pump via a gearbox in *Flownex,* it was necessary to represent the stage-by-stage turbine model with an equivalent high level representation which would have the same power output and speed for given operating conditions. This is because the stage-by-stage model does not have the ability to connect to a shaft and enable power matching.

The simple turbine is utilised for the high level representation of the overall turbine, using a restrictor with a discharge coefficient as the pressure drop description. This component has a characteristic equation as follows:

$$\Delta p_0 = \frac{\rho \cdot Q^2}{2 \cdot C_d{}^2 \cdot A^2} \qquad (86)$$

Where C_d is the discharge coefficient and A is the physical throat area. The other symbols have the usual meanings.

A simple turbine was modelled with a modified water as the fluid – density being fixed to 1000 kg/m^3. The area was set to 1 m^2, and the isentropic efficiency was set to 100 %. The discharge static pressure was fixed at 1 bar. The inlet temperature was fixed at 20 °C. Defining pressure in bar for convenience, the above equation becomes:

$$\Delta p \cdot 10^5 = \frac{1000 \cdot Q^2}{2 \cdot C_d{}^2 \cdot 1^2} \Rightarrow Q = C_d \sqrt{200 \cdot \Delta p} \tag{87}$$

The hydraulic work is equal to the product of the pressure change and the volumetric flow. Defining work in kilowatts for convenience, and keeping pressure in bar, the hydraulic work may be expressed as follows:

$$\begin{aligned} \dot{W} \cdot 10^3 &= \Delta p \cdot 10^5 \cdot Q = \Delta p \cdot 10^5 \cdot C_d \sqrt{200 \cdot \Delta p} \\ \therefore \dot{W} &= 1000 \cdot C_d \sqrt{2(\Delta p)^3} \end{aligned} \tag{88}$$

If p_{in} is set to 20 bar then C_d = 0.005 will yield Ẇ = 19 850 kW, which exceeds the full load power output required. Therefore by modifying p_{in} from 1 bar to 20 bar, the full power range may be represented. With C_d = 0.005, and p_{in} =1 bar, the previous equation becomes:

$$\dot{W} = 1000 \cdot 0.005 \sqrt{2(p_{in} - 1)^3} = \sqrt{50(p_{in} - 1)^3} \tag{89}$$

Re-arranging so that p_{in} is the subject, this becomes:

$$p_{in} = \sqrt[3]{\frac{\dot{W}^2}{50}} + 1 \tag{90}$$

In the above equation, it is important to note that p_{in} is in bar and Ẇ is in kW, for convenience.

This was implemented by means of a script which took the power produced by the stage-by-stage turbine as an input and determined the inlet pressure to the high level turbine. This ensured that the high level representation produced the same power as the stage-by-stage turbine. This simple turbine was connected to a shaft which was connected to the pump via a gearbox component. This is illustrated in Figure 3.35. The shaft speed was linked to the stage-by-stage model.

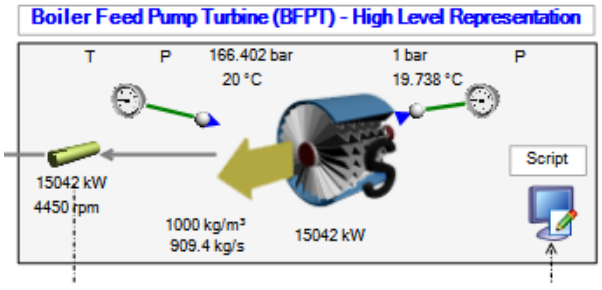

Figure 3.35: High level representation of turbine (Station A1)

3.11 Steam Admission Valves

3.11.1 Observed Valve Behaviour

Figure 2.4 illustrated the expected valve opening curves for Station A1, where all four steam admission valves responded to the same signal oil pressure. These are reproduced in Figure 3.36 below, with valve displacement having been converted to a percentage opening. It was noted from station manuals that whereas valves 1 and 2 had a fully open displacement of 29.7 mm, valves 3 and 4 had a fully open displacement of 25.9 mm and the cold reheat valve had a fully open displacement of 20.57 mm.

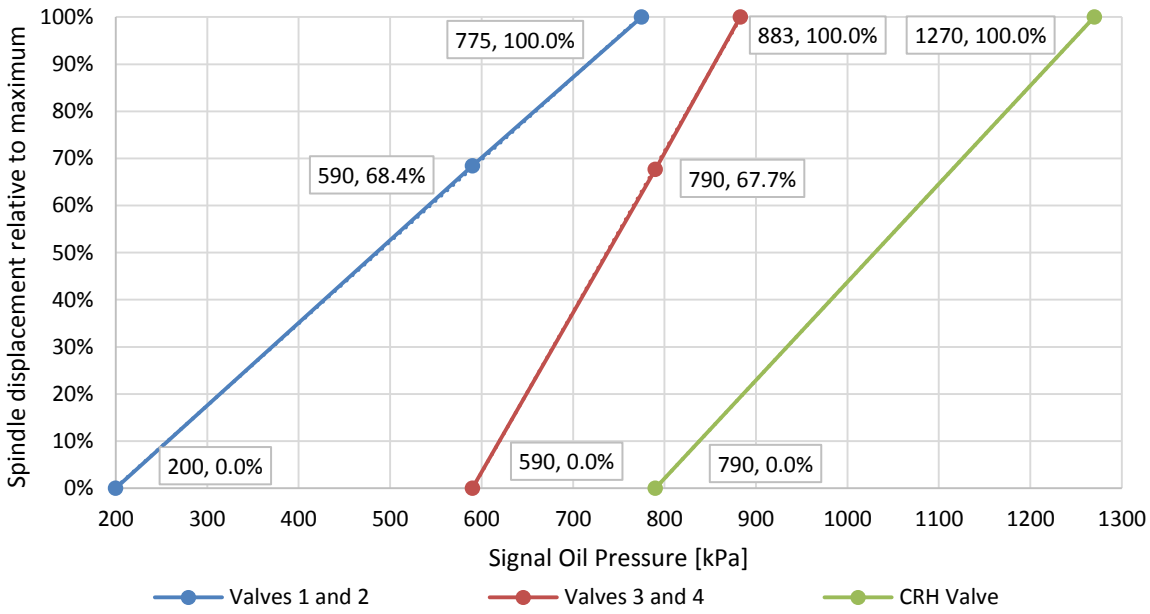

Figure 3.36: Station A1 - chart showing steam admission valve displacement vs signal oil pressure

However, in studying DCS data from the Unit studied at Station A1, it was observed that the valves were not stroked according to the above chart. It was noted that the pressure after valve 1 was greatest, then valves 2 and 3 (approximately equal), then valve 4. In other words, the valves were opening in the sequence 1-(2&3)-4. The pressure drop over each valve is illustrated in Figure 3.37. Signals were sampled at 10-minute intervals from the DCS over the period 29/04/2016 00:00 to 06/05/2016 00:00 (sample size 1008). The BFPT was in service for this full duration.

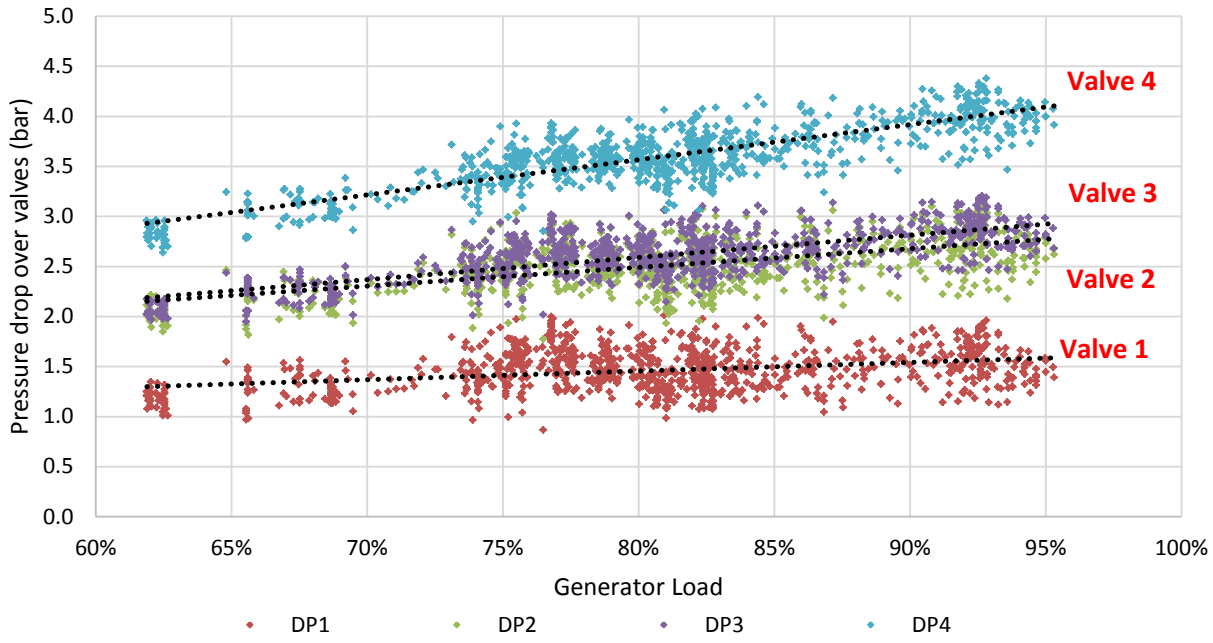

Figure 3.37: Station A1 - pressure drop over steam admission valves vs load

To establish whether any of the valves might in fact be closed but appear open, the pressures before and after the first stage of Station A1 were sampled at intervals of 10 minutes from 29/04/2016 00:00 to 06/05/2016 00:00. This is shown in Figure 3.38. If the valve for one segment was actually closed, there would not be a significant pressure drop over the stage for that segment, as there is no flow through the nozzle ring partial arc. However, there is a pressure drop of at least 1 bar over all stage segments, demonstrating that no valve is shut on this operating range.

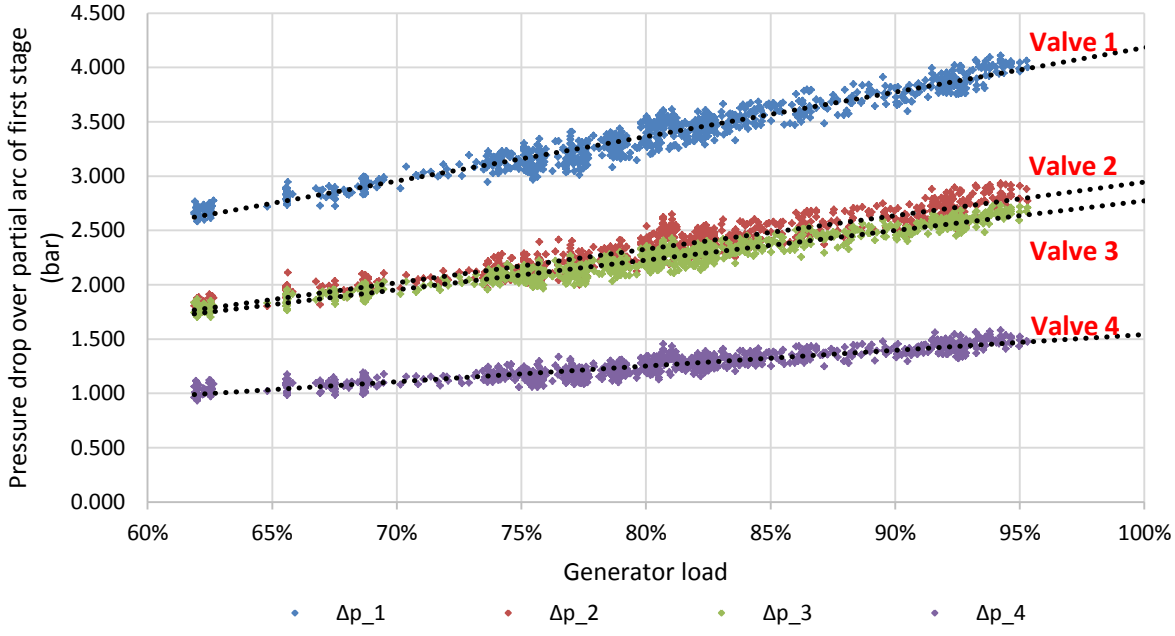

Figure 3.38: Pressure drop over first stage of Station A1 - per partial arc

Station manuals state that valves 1 and 2 have holes drilled through their valve heads to allow for the continuous admission of steam at all turbine loads, in order to maintain steam chest temperature. Thus it is expected that even when these two valves are "shut", there should still be a pressure drop observed over the partial arc, but it is expected to be relatively small. This flow will be modelled as part of the flow due to the displacement of the valve spindle.

3.11.2 Selection of Flow Resistance Component Type

The steam admission valves were modelled using the *Flownex* custom losses component "Flow Resistance Component". This component is discussed in more detail in Section 2.3.9.

Typical Reynolds numbers and density changes were considered in order to select a suitable flow resistance behaviour.

Reynolds Number

The Reynolds number for this case is expressed as follows:

$$\mathrm{Re} = \frac{\rho \cdot \bar{v} \cdot D}{\mu} = \frac{4 \cdot \dot{m}}{\mu \cdot \pi \cdot D} \qquad (91)$$

Valve 1 has a throat diameter of 0.1524 m. The steam mass flow rate (no reheat spraywater) from the 100 % heat balance diagram is 16.668 kg/s. The dynamic viscosity evaluated at the inlet conditions for the same heat balance diagram is μ(12.13b, 377.7 °C)=2.349x10^{-5} kg/(m*s). If it is assumed that Valve 1 admits ¼ of the total mass flow, the Reynolds number is 1.483 x 10^6 (≫ 2.3 x 10^3), thus a laminar regime is not applicable, and it will generally be assumed that turbulent behaviour will be observed throughout the operational ranges.

Density

For the 95 % detailed DCS case, the density was calculated from steam tables based on pressures measured upstream and downstream of the valves, and applying inlet enthalpy. The density in this case dropped from 3.8 kg/m^3 to 2.5 kg/m^3, demonstrating that density effects are significant. As load changes and the boundary conditions change, there is also a significant steam pressure variation which will further affect density.

Conclusion

Laminar behaviour cannot be assumed nor can density effects be ignored. The flow is typically highly turbulent and therefore the loss coefficient "K" may be taken as relatively constant. *A quadratic resistance behaviour including density effects is therefore considered most relevant to this model.*

3.11.3 Sizing of Valves - Admittance Factor

For the component type chosen, let A_{sf} =1 and A_o = 1. (Please refer to the relevant theory in Section 2.3.9 for a discussion of admittance factors.)

Then:

$$A_f = \left[\frac{2 \cdot A^2}{K} \right] \tag{92}$$

The throat diameters and maximum axial displacement of the valves are known from station manuals. These are shown in Table 3.8 together with the resulting ratios of admittance values, assuming identical K-values when fully open. Since these are similar valves and the flow is highly turbulent, this assumption is considered reasonable.

Figure 3.39 shows a typical emergency stop valve and governor valve pair for an HP turbine (based on Woell, 2016). Figure 3.40 shows the steam admission valves 1 and 2 for Station A1. From this it is apparent that the maximum flow admittance area may be approximated as follows:

$$A_{flow} \approx \Delta s_{\max} \cdot \pi \cdot d_{throat} \tag{93}$$

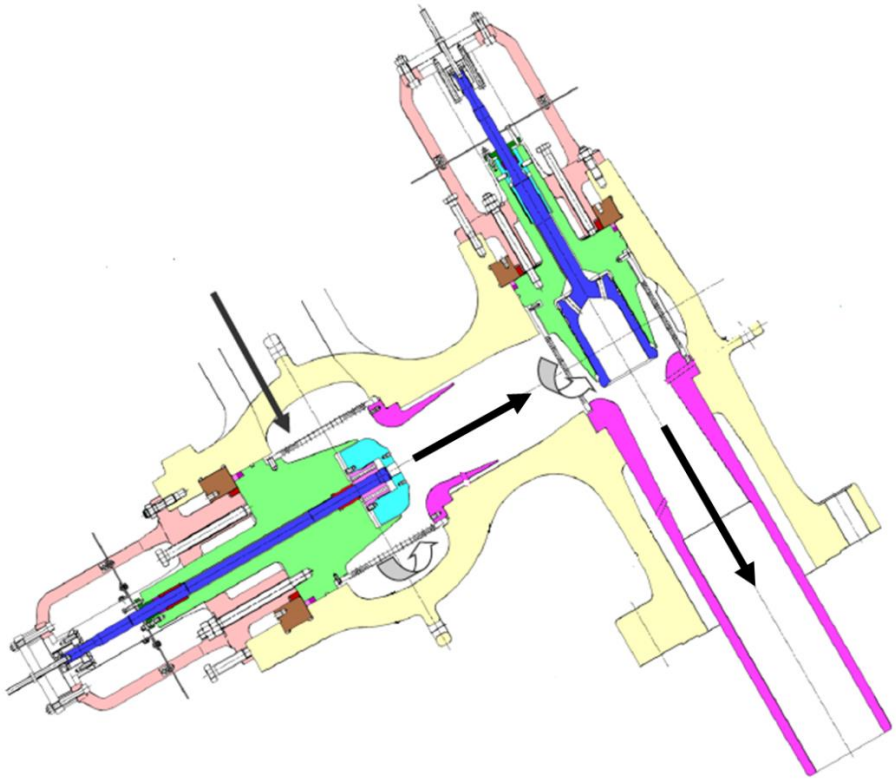

Figure 3.39: Typical emergency stop valve and governor valve pair for an HP turbine (Woell, 2016, modified)

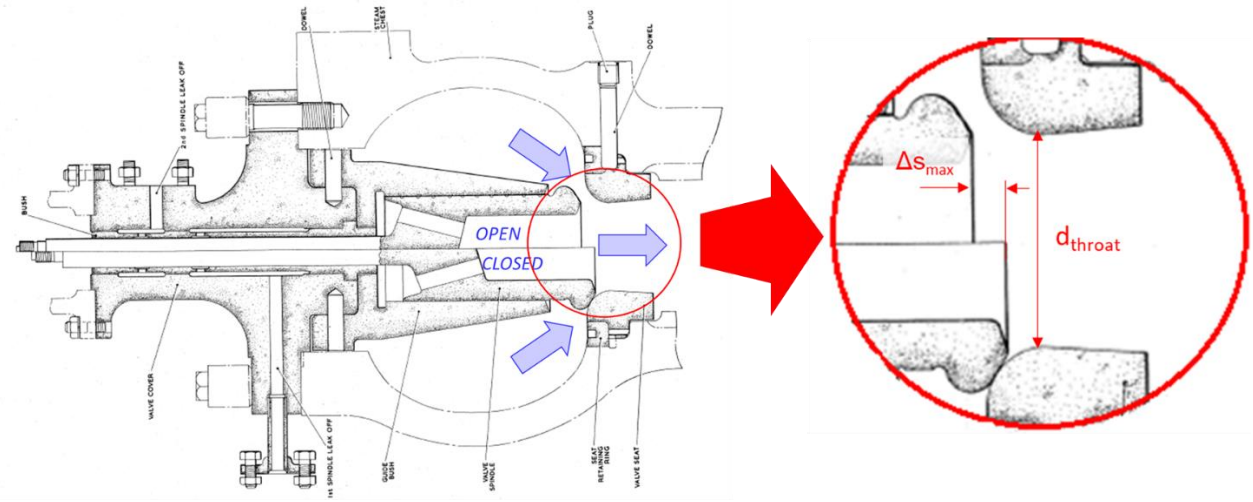

Figure 3.40: Diagram of Station A1 steam admission valves 1 and 2 (annotated; original drawings from station manuals)

Knowing the throat diameter and the maximum displacement for each valve, the minimum area may be determined and by relating these to each other, the admittances may be scaled by the ratio of the square of these areas. This step is important because the valves have different sizes. *Flownex* has a built-in designer function where a target value is associated with a certain property (in this case, the downstream pressure) and another property is assigned as the independent variable (in this case, the reference valve admittance). The designer iteratively adjusts the independent variable until the dependent variable reaches the target value. This functionality was used using the 95 % detailed DCS case in order to obtain the correct reference valve admittance so that the correct pressure would result after Valve 1 with all valves being open. The results are shown in Table 3.8.

Table 3.8: Relative Steam Admission Valve Sizes for Station A1

	Throat diameter	Maximum displacement (lift)	Flow area	Admittance with reference to valve 1	Valve admittance from designer
	mm	mm	mm^2		
Valve 1	152.4	29.7	143.5	1.0000	7.6367E-05
Valve 2	152.4	29.9	143.5	1.0000	7.6367E-05
Valve 3	139.7	25.9	113.7	0.7994	6.1047E-05
Valve 4	139.7	25.9	113.7	0.7994	6.1047E-05
CRH	114.3	20.57	73.9	0.5194	3.9669E-05

3.11.4 Valve Opening Factor

As shown in the equation below, for the component characteristics chosen, valve opening is proportional to A^2/K (this is based on the discussion in Section 2.3.9):

$$A_o = \left(\frac{2}{A_f}\right) \cdot \left(\frac{A^2}{K}\right) \tag{94}$$

Equivalently:

$$A_o = \left(\frac{K_{open}}{K}\right) \cdot \left(\frac{A^2}{A_{open}{}^2}\right) \tag{95}$$

If K is assumed to be constant for a given valve, then:

$$A_o = \left(\frac{A}{A_{open}}\right)^2 \tag{96}$$

It was noted in the previous section that:

$$A_{flow} \approx \Delta s_{\max} \cdot \pi \cdot d_{throat} \tag{97}$$

Therefore,

$$A_o = \left(\frac{\Delta s}{\Delta s_{\max}}\right)^2 \tag{98}$$

This approximation will be used to map charts of valve displacement vs signal oil pressure to A_o vs signal oil pressure.

With the valve admittance values, A_f, set for the five valves, the Designer feature was used in *Flownex* for the 60 %, 70 %, 80 %, 90 % and 100 % cases in order to obtain the target pressures downstream of each valve while applying the generated boundary conditions. Generated boundary conditions were obtained as per Section 3.4 and downstream pressures were expressed as a function of generator load based on linear trendlines.

The required valve spindle displacement was then obtained for each valve for each of these five load cases as the square root of the A_o values and these values were plotted against signal pressure. The generator load was translated to a signal oil pressure by using the linear trendline relating these two quantities.

Linear trendlines were utilised for displacement vs signal pressure and extrapolated given that the design curves in this respect are linear. The equations for valve displacement as a function of signal oil pressure are shown in Appendix B for the measured values (DCS) and as per the station

manuals. These are represented graphically in Figure 3.41. One can clearly see the difference between the design and actual valve stroking.

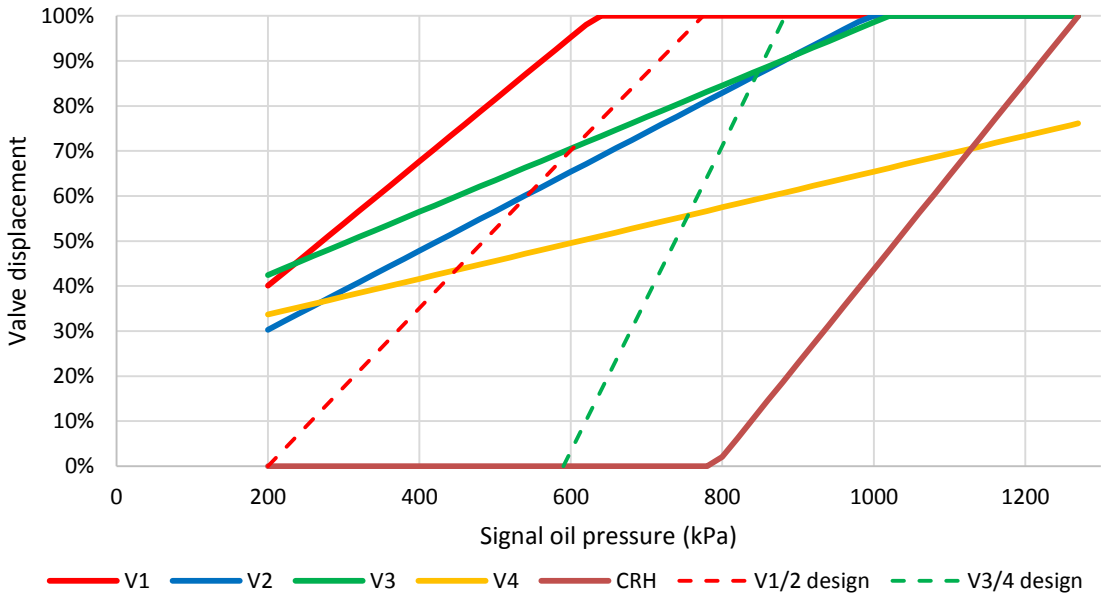

Figure 3.41: Graphical representation of steam admission valve stroking; "V1" to "V4" represent valves 1 to 4 based on the DCS values, CRH represents the cold reheat valve stroking according to design, and V1 to V4 "design" curves represent the stroking of valves 1 to 4 based on station manual values

In order to obtain A_o, these displacement values must be squared. For a given signal pressure input, a script was created in *Flownex* such that the percentage displacement would be calculated from the above equations (with conditional statements to ensure that results remained in the range 0 to 1). The corresponding A_o values were then calculated as the squares of the displacement values. These corresponding A_o curves are shown in Figure 3.42 with the required A_o values for the four load cases considered, superimposed in black. These values are shown on the range 200 to 1270 kPa as this is the signal oil pressure range from station manuals. The content of the script for valve opening can be viewed in Appendix B.

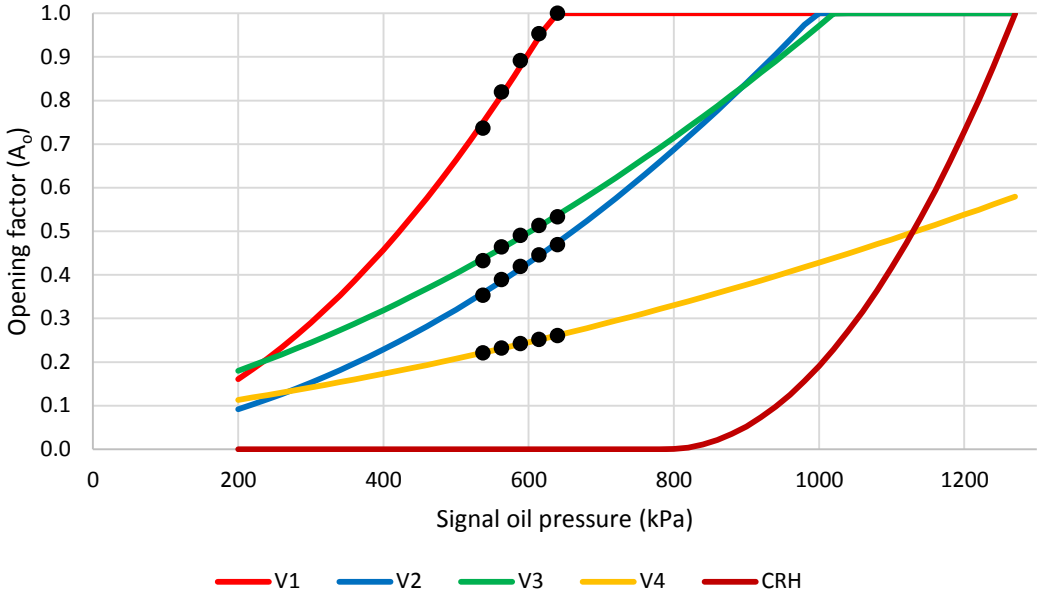

Figure 3.42: Graphical representation of steam admission valve opening (A_o) values

3.11.5 Signal Oil Pressure Curves

On the actual plant, the feedwater flow rate demand is set by the plant controller in order to achieve the desired plant load. A controller would then adjust the signal oil pressure such that this feedwater demand is met. In principle, it should be possible to set up such a controller in Flownex. This was briefly attempted, but several convergence difficulties were encountered. Since this project is not focussed on modelling the dynamic control behaviour, it was decided to implement a "lookup" function for signal oil pressure vs. load demand.

The signal oil pressure was manually adjusted until the target feedwater mass flow rate was obtained, for a range of generator loads. This was determined accurate to the nearest 1 kPa of pressure or 1 kg/s of feedwater mass flow rate. The resulting required signal oil pressures with respect to load for different scenarios is discussed in detail in Chapter 4.

The cold reheat supply was enabled at this point in order to test the model. In enabling the cold reheat supply by opening the cold reheat valve, the solver encountered problems if a guess value was not prescribed for the node downstream of this valve. The guess value was set to 5 bar and this was found to be effective.

3.12 Reheat Attemperator Spraywater

A survey of DCS data revealed that the reheat attemperator spraywater signal was not available at the Unit studied at Station A until the Unit returned from its outage in March 2017. Once measurements were again available, Figure 3.43 illustrates how the flow rates fluctuated from 0 to 25 kg/s without a convenient correlation with generator load. This is because the spraywater valves open in response to process conditions on the boiler side which may vary independently of load. Figure 3.44 illustrates the design values at four points from the heat balance diagrams. For the purposes of modelling this as a boundary condition, the decision was made to assume that the mass flow rate would follow the straight lines in Figure 3.44, that is, increasing linearly from 69 % to 100 % load. This was implemented in a script to set the mass flow rate extracted after the second stage of the pump based on the generator load.

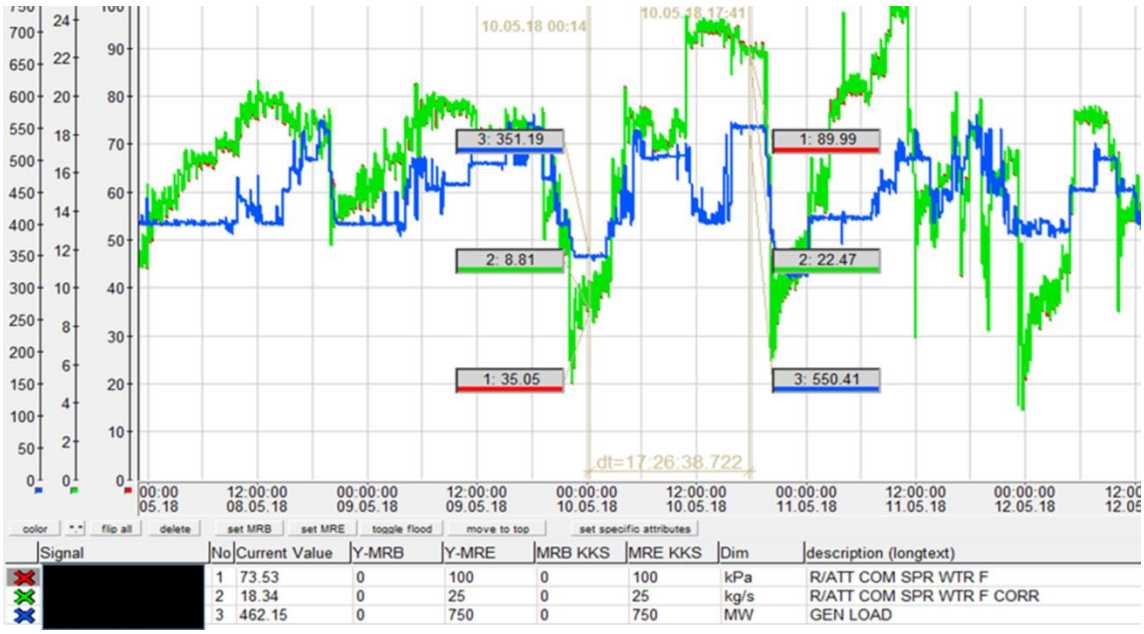

Figure 3.43: DCS trends showing fluctuating spraywater mass flow rates

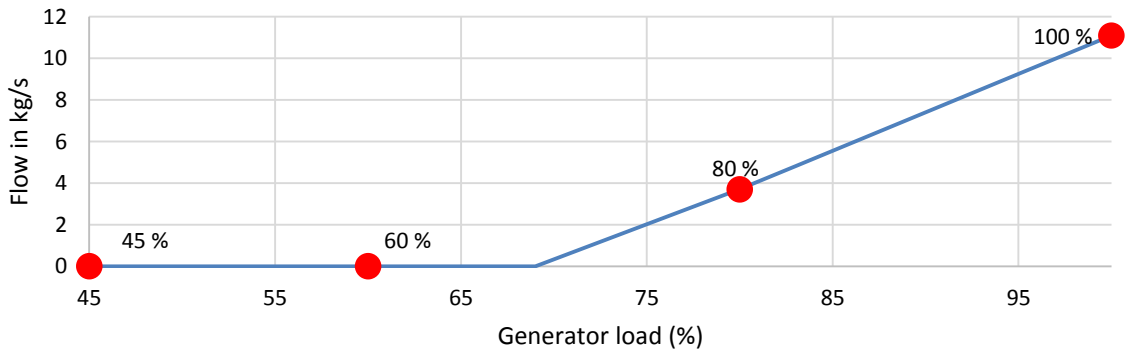

Figure 3.44: Reheat spraywater flow rates from heat balance diagrams

3.13 Leak-Off Valves

Figure 3.45 shows different scenarios for minimum flow superimposed on a graph of feedwater mass flow rate vs generator load based on the samples used previously. Staff at Station A1 reported that the transition to leak-off typically occurs around 80 – 100 L/s (14.6 % to 18.2 % of Q_{00}); this is generally taken to be nominally 15 %; whereas Sulzer, 2010, advises that flow rates should be kept above 40 % of Q_{00} for stable operation and not allowed to go below 25 % of Q_{00}. Assuming the reference density of 923.5 kg/m^3 may be applied here for a reasonable approximation, it is found that conservatively the leak-off valve should open at a load of 38 %. The crosses on the diagram indicate the expected loads at which the leak-off valve would need to open for these three different scenarios.

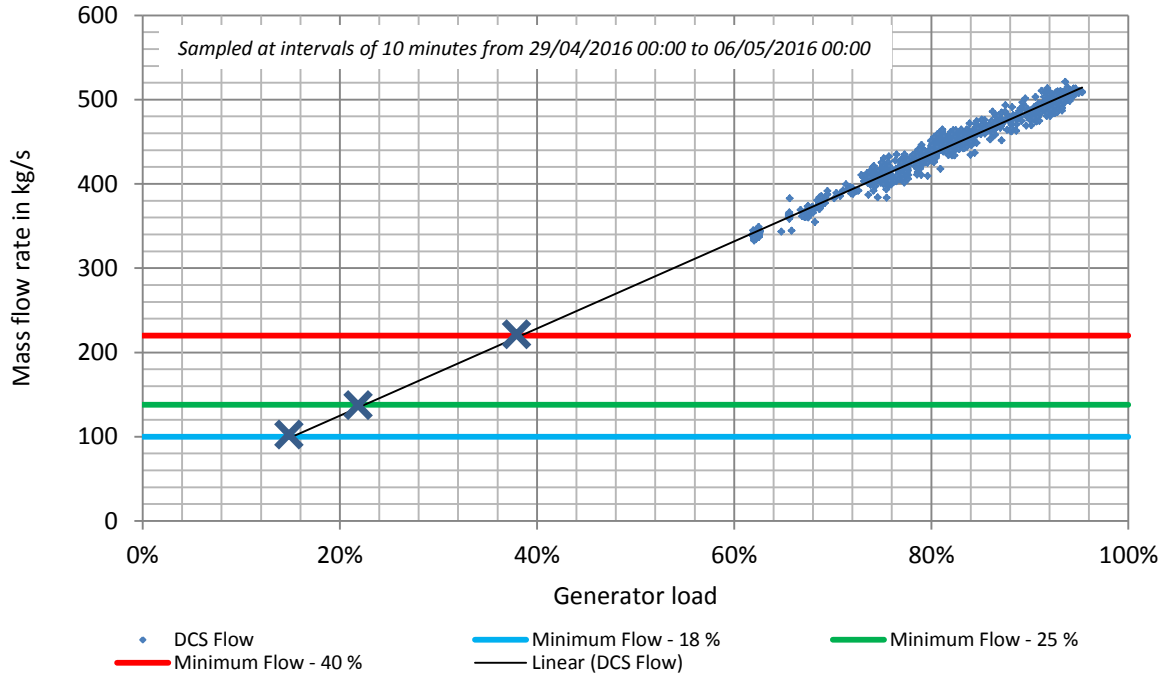

Figure 3.45: Required feedwater mass flow rate vs load

DCS trends were produced for a typical Unit start-up, shown in Figure 3.46 in order to better understand the operation of the leak-off valves. The Unit is on load for the whole duration. The DST shell pressure remains relatively constant during this time.

The following sequence of events is observed:

A. Both EFPs are on load. Run-up of the BFPT commences.
B. Shaft speed (Signal 5) increases and consequently leak-off flow (Signal 1) and discharge pressure (Signal 6) both increase.
C. The leak-off flow (Signal 1) plateaus with a maximum differential pressure of 206 kPa being recorded. Further increases in shaft speed do not increase this differential pressure but they do result in an increased discharge pressure (Signal 6).
D. The discharge pressure becomes sufficient to lift the SFP discharge NRV and the SFP begins to feed forward.
E. Shaft speed is increased until the SFP takes over from the EFPs. The EFPs stop feeding forward and the SFP leak-off valve closes.

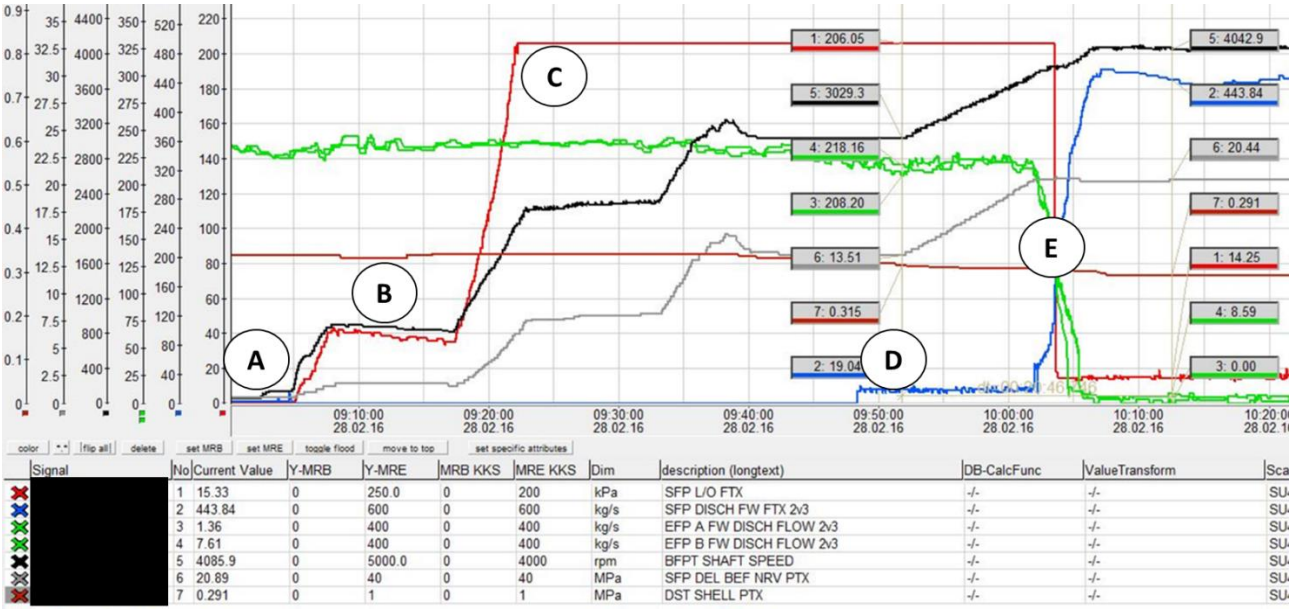

Signal	No	Current Value	Y-MRB	Y-MRE	MRB KKS	MRE KKS	Dim	description (longtext)	DB-CalcFunc	ValueTransform	Sca
	1	15.33	0	250.0	0	200	kPa	SFP L/O FTX	-/-	-/-	SU
	2	443.84	0	600	0	600	kg/s	SFP DISCH FW FTX 2v3	-/-	-/-	SU
	3	1.36	0	400	0	400	kg/s	EFP A FW DISCH FLOW 2v3	-/-	-/-	SU
	4	7.61	0	400	0	400	kg/s	EFP B FW DISCH FLOW 2v3	-/-	-/-	SU
	5	4085.9	0	5000.0	0	4000	rpm	BFPT SHAFT SPEED	-/-	-/-	SU
	6	20.89	0	40	0	40	MPa	SFP DEL BEF NRV PTX	-/-	-/-	SU
	7	0.291	0	1	0	1	MPa	DST SHELL PTX	-/-	-/-	SU

Figure 3.46: Station A1 leak-off trends for BFPT being placed in service

From this data it may be inferred that the maximum differential pressure recorded over the orifice is 206 kPa, which is expected to correspond to a flow rate of 82.5 L/s (15 % of Q_{00}, approximately 76.2 kg/s).

3.13.1 Flow Measurement

The pipe in which the orifice plate is located is known to have the following characteristics:

1. Outer diameter: 168.3 mm (nominal bore of 150 mm).
2. Thickness: 7.11 mm

However, information about the orifice plate was not available and so an orifice diameter of 89.03 mm was inferred from available data. This is discussed in Appendix G.

Applying this value, the following curve in Figure 3.47, is obtained, relating volumetric flow rate to differential pressure measured.

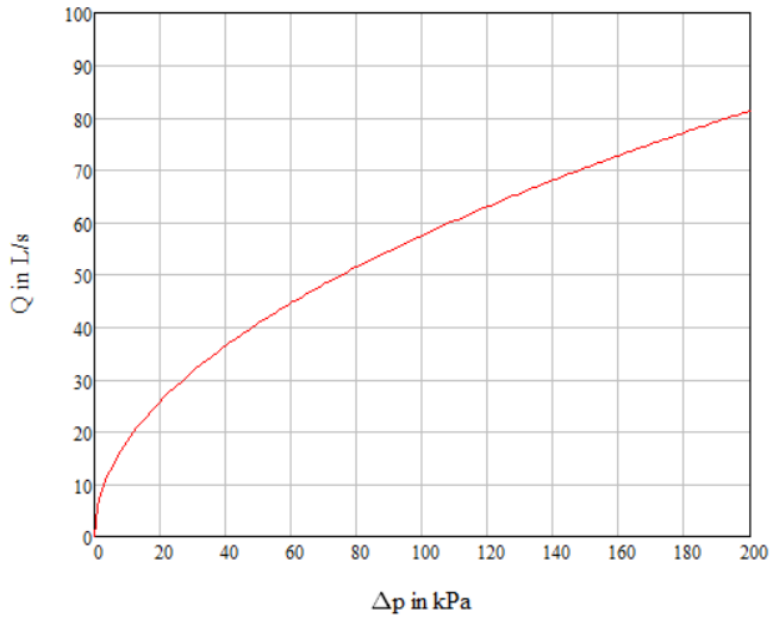

Figure 3.47: Graph illustrating Q vs Δp for Station A1 leak-off orifice plate

3.13.2 Leak-Off Valve Characterisation

Figure 3.46 demonstrates that with the leak-off valve open, the differential pressure rises approximately linearly as the upstream pressure rises linearly (the downstream pressure at the DST is constant during this time). It is assumed that the pressure immediately downstream of the leak-off valve is equal to the pressure at the booster pump suction, as these points are at similar heights (bearing in mind that the DST is located about 35 m above the feed pump train). Applying the orifice characteristics assumed in 3.13.1 to this DCS data, a characteristic curve may be obtained as shown in Figure 3.48, displaying a quadratic relationship between pressure difference over the valve and mass flow rate.

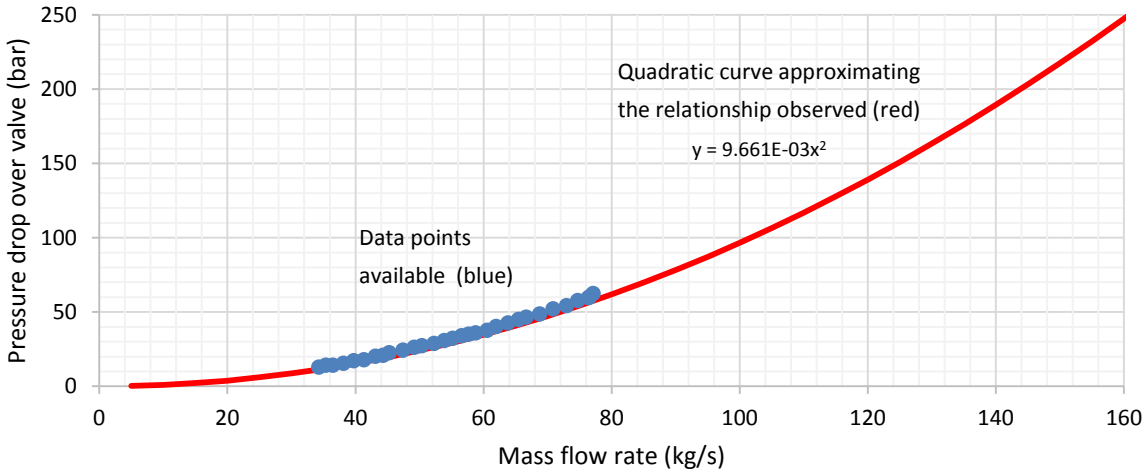

Figure 3.48: Pressure drop vs mass flow rate for Station A1 leak-off valve

If a quadratic flow resistance characteristic is used (see discussion in Section 3.11), assuming constant density:

$$\Delta p_{0L} = \frac{1}{2}\cdot\left(\frac{K}{\rho\cdot A^2}\right)(\dot{m})^2 = \left[\frac{1}{A_f\cdot A_{sf}\cdot A_o}\right]\cdot(\dot{m})^2 \qquad (99)$$

The graph shown in Figure 3.48 takes a quadratic form, supporting the above assumption. If the first order and zeroth order terms are deleted so that the curve matches the above equation, then the resulting curve, shown in red in Figure 3.49, allows for the admittance to be estimated. Setting $A_o = A_{sf} = 1$, and converting pressure from bar to pascals:

$$\Delta p_{0L} = 9.661\times10^{-3}\times10^{5}\cdot(\dot{m})^2 = A_f{}^{-1}\cdot(\dot{m})^2 \therefore A_f \approx 1.0351\times10^{-3} \qquad (100)$$

This admittance value is used in the *Flownex* to represent the leak-off valve. Because the valve at Station A1 is binary – either open or closed, with no controllability, the opening factor, A_o, will be set to either 0 or 1 depending on the scenario under consideration.

3.13.3 Discussion of Leak-Off Valve Behaviour

This discussion is to better understand the leak-off behaviour for later case studies.

Using the boundary conditions generated for the 100 % load case, the maximum differential pressure over the leak-off valve is 213.3 bar. However, above a pressure difference over the valve of about 62 bar, the orifice's measured pressure plateaus at the maximum value (due to the limitations of the sensor's range of measurement[7]) and so the maximum flow rate must be estimated through extrapolation. At a differential pressure of 213.3 bar over the leak-off valve, a maximum mass flow rate of 148.6 kg/s is expected.

However, from the discussion in Section 3.4, DCS values for the discharge pressure are observed to remain above 180 bar, even down to 30 % of generator load. This corresponds to a predicted mass flow rate of approximately 136.5 kg/s.

Figure 3.50 illustrates what occurred with the Station A1 SFP during the low-load tests of November 2017. During the time that the BFPT was on leak-off, the SFP was not feeding forward. In this "idling" state, the control system maintained a speed of about 3100 rpm with a discharge pressure of about 140 bar. This corresponds to a predicted mass flow rate of approximately 120.4 kg/s.

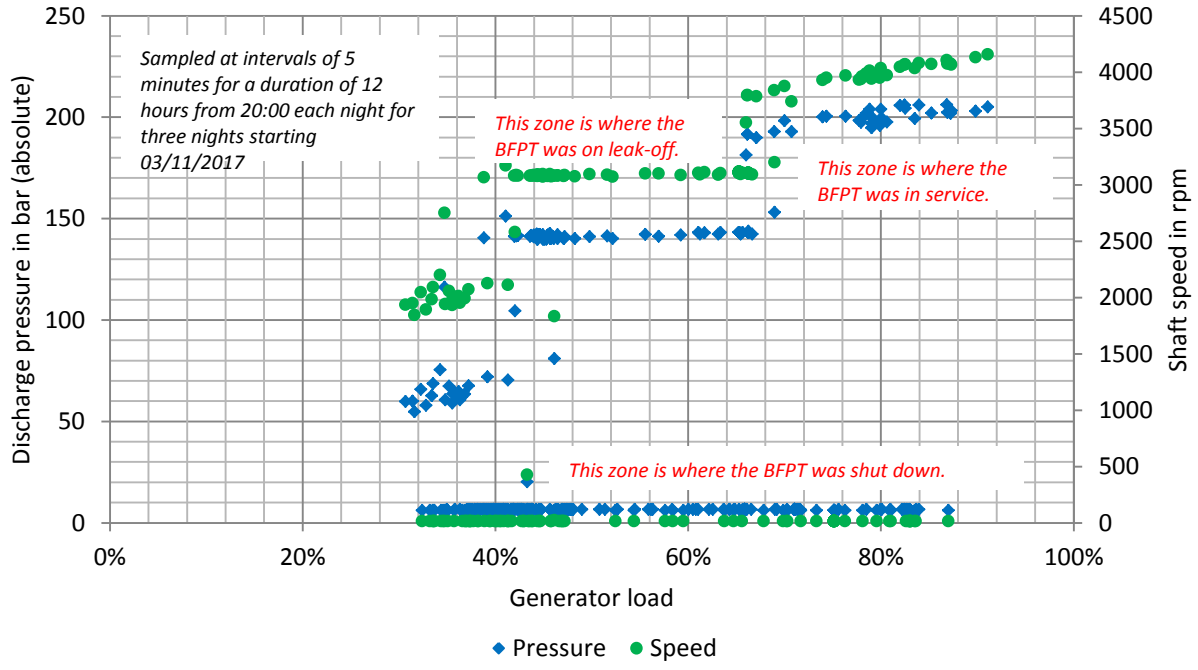

Figure 3.49: Trends of Station A1 BFPT on leak-off during low-load tests

[7] This is not a flaw in the instrumentation; the pressure transmitter is configured to measure leak-off flow on the usual range and the consideration here is beyond the usual limits of operation.

3.14 BFPT Integrated Model

The turbine model for Station A1 was linked to the pump stages. An image of the integrated model appears in Figure 3.50. This integrated model is used for case studies in Chapter 4. In order to achieve this integration, a number of factors were taken into account, which have already been given some consideration in this chapter. These include:

1. High level representation of the turbine (see section 3.10)
2. Gearbox efficiency (see section 3.6)
3. Reheat attemperator spraywater (see section 3.12)
4. Boundary conditions as a function of generator load (see section 3.3)
5. Minimum flow and NPSH checks (see sections 2.2.3 and 2.2.4)
6. Leak-off valves (see section 3.13)
7. Steam admission valves 1 to 4 with signal oil pressure (see section 3.11)
8. Cold reheat supply valve with signal oil pressure (see section 3.11)

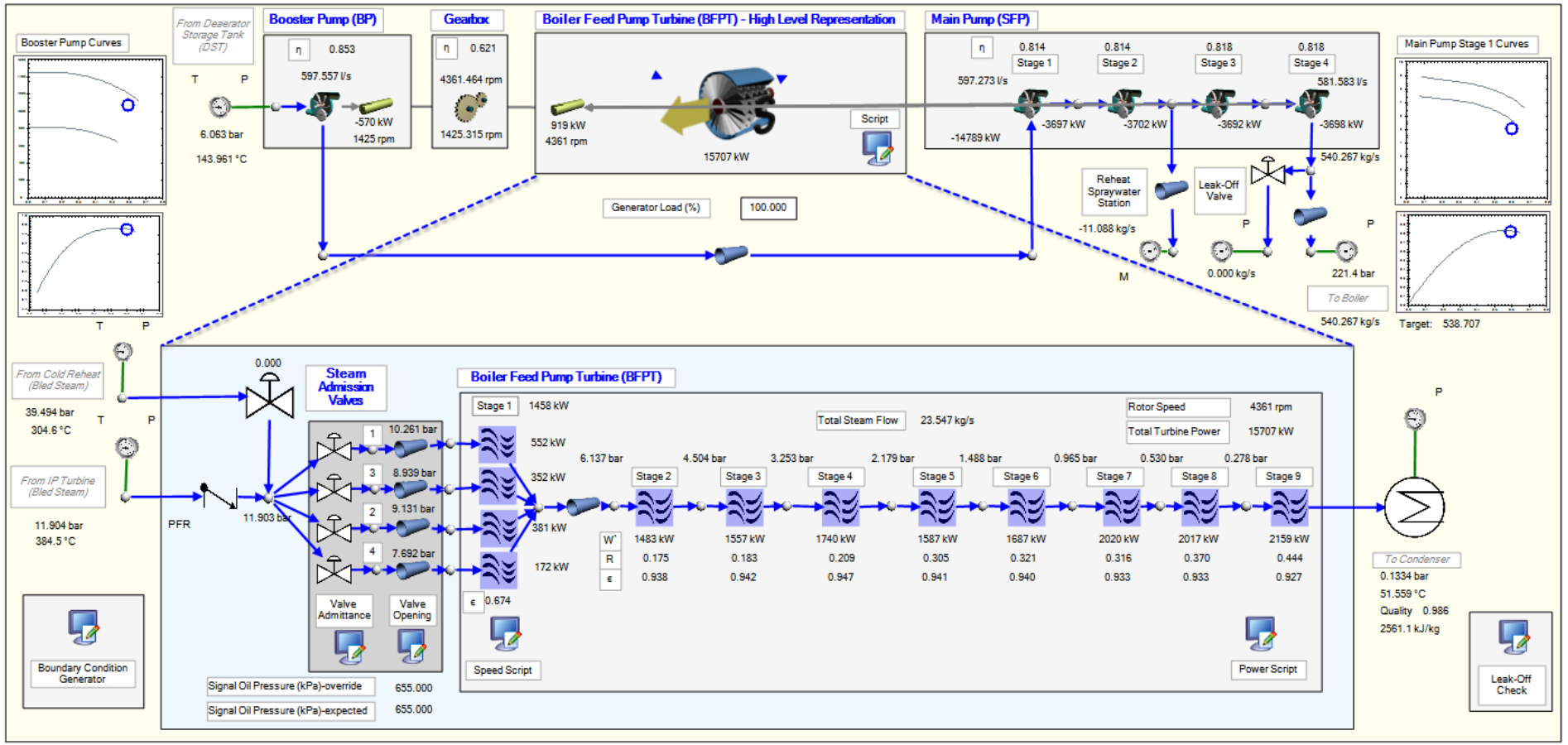

Figure 3.50: Turbine model coupled to other components

3.15 Model of Electric Feed Pump Train

In a similar process to that followed for the steam feed pump, relevant pump curves were digitised and trendlines were applied in order to smooth these curves. Each EFP is comprised of four pump stages, like the SFPs. The applicable curves for a single stage are shown in Figure 3.51. The pump curves used third order polynomials, the efficiency used a quadratic equation and the NPSH used a sixth order polynomial. These did not differ from the digitised values by more than ±5 m, 1 % and ± 1m respectively, which is considered acceptable in view of the resolution of the source curves. The reference suction temperature and density of the curves were 143 °C and 923.5 kg/m^3 respectively. The NPSH curve did not extend below a flow rate of 200 L/s and so it was assumed that the value at 200 L/s could be applied as constant on the range 0 L/s – 200 L/s.

3.15.1 Booster Pump

It was established that the booster pump for the SFP differed from the booster pump for each EFP. However, no pump curves were available for the EFP booster pump. The pump curve was therefore inferred from the main pump curves, some of which featured the total effect of booster pump and main pump, and some of which featured only the effect of the main pump. By subtracting these curves from each other, a pump curve for only the booster pump could be approximated. The booster pump runs at a fixed speed of 1489 rpm, being directly coupled to the motor.

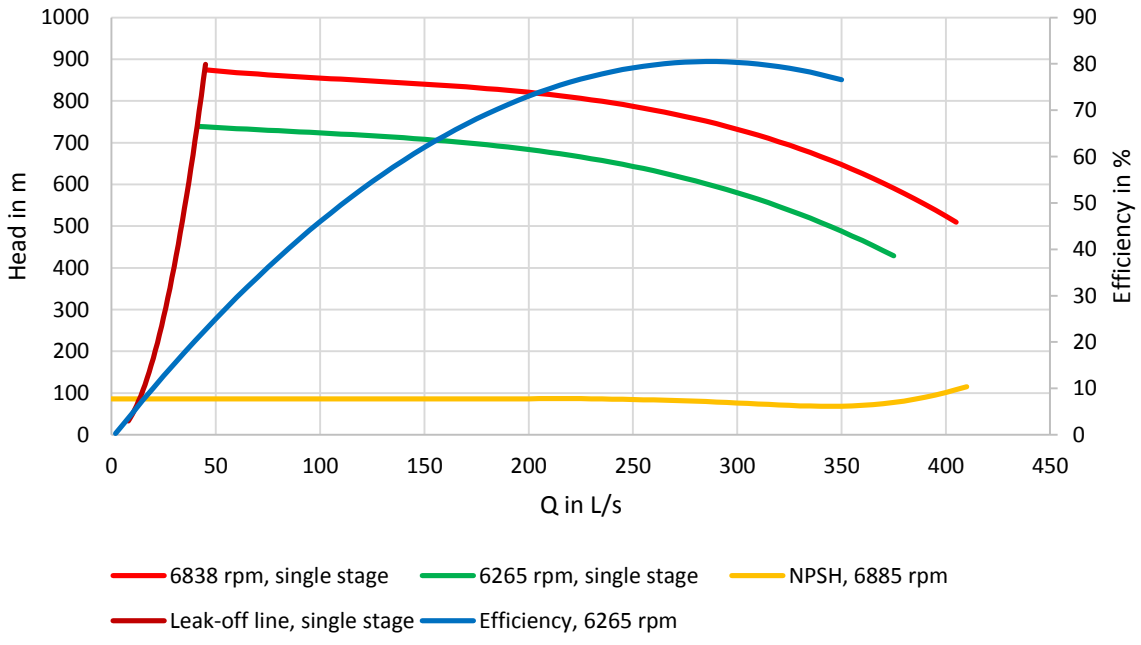

Figure 3.51: Pump curves used for EFPs (main pumps), graphically representing inputs to Flownex

The configuration of the feed pump trains is as shown in Figure 3.52.

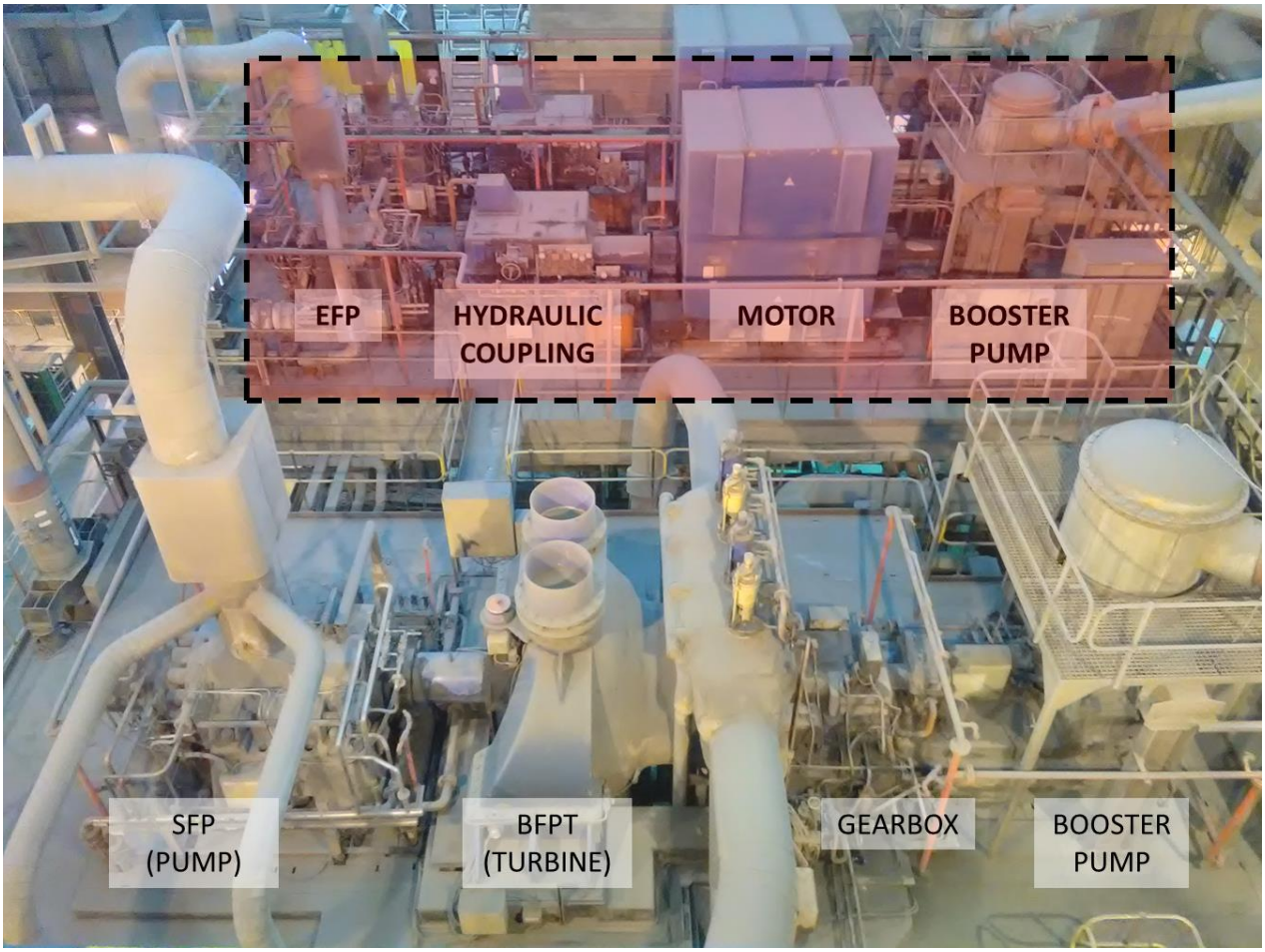

Figure 3.52: Configuration of feed pump trains at Station A1

3.15.2 Motor

The motor is a four-pole induction motor with a normal power output of 13 000 kW and a peak output of 20 800 kW. The guaranteed EFP performance in the station manual states that losses in the gearbox and the fluid coupling are 1360 kW at normal duty and 638 kW at maximum duty, with the pump input power being 8108 kW and 10 634 kW respectively. This results in a combined gearbox and fluid coupling efficiency of 85.64 % and 94.34 % respectively. The pump speed at normal duty is 6290 rpm and 6865 rpm at maximum.

3.15.3 Hydraulic Coupling

The hydraulic coupling has a slip of 2.2 % to 2.4 % at full load and for this case study the value will be assumed to be 2.2 % as this is the value considered as typical by van der Westhuizen and Cattaert, 2010. Applying this slip value to a maximum main pump speed of 6 865 rpm, a gearbox ratio of 1:4.714 is expected. These values are summarised in Figure 3.53 for the maximum load and normal conditions. The slip of the (variable) hydraulic coupling is adjusted by changing the scoop position (see Section 2.1.4). The lowest speed plotted on the EFP pump curves is 1716 rpm; this corresponds to a slip of approximately 75.6 %.

For the purposes of the case study in question, it was *initially* assumed that electrical losses may be ignored as being relatively insignificant, given that large induction motors typically have very high electrical efficiencies.

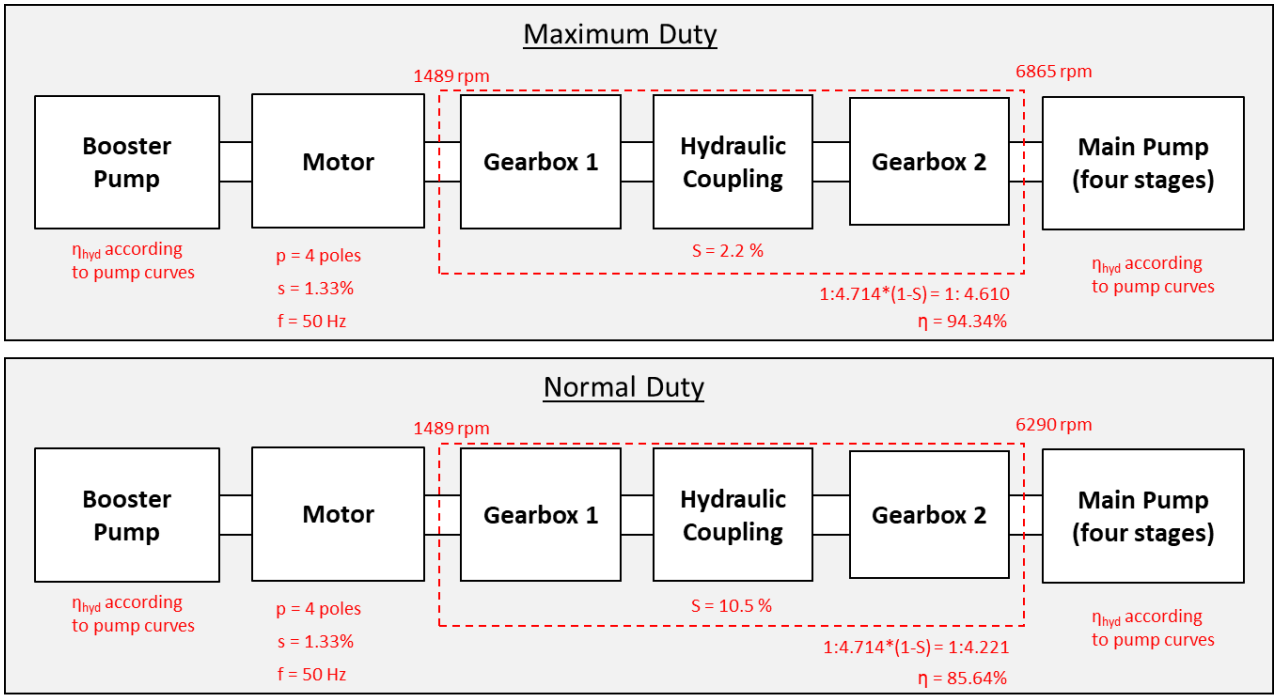

Figure 3.53: Electric feed pump configuration at Station A1 with key values shown

The pump curves and the other component characteristics as shown in the above figures were used in order to build a *Flownex* model of one EFP train. The boundary conditions on the feedwater side – inlet pressure and temperature, and outlet pressure – were expressed as a function of generator load the same as for the SFP. The reheat spraywater requirements were expected to be the same with respect to load, although split equally between the two pumps when both are in service. The feedwater mass flow rate demand was based on load using the same equations for typical values as in the SFP case.

The hydraulic turbine analogue used to represent the stage-by-stage turbine at a high level was used to model the electric motor by using the Designer feature to calculate the required power output in order to balance power around the gearbox. It was assumed that the motor speed would remain constant – that is, having constant slip – at all loads.

The hydraulic coupling and the gearbox were represented with a single gearbox component having a gearbox ratio defined by a script with a hydraulic coupling slip input, such that the gearbox ratio R was defined as follows:

$$R_{GB} = 4.714 \cdot (1 - S) \qquad (101)$$

The gearbox was initially assigned a fixed efficiency of 85.64 % to reflect normal operation.

The *Flownex* model is shown in Figure 3.54 for a single EFP train at Station A1, at full load conditions. It was assumed that the two EFP trains are identical and will share the feedwater mass flow rate and the reheater mass flow rate equally.

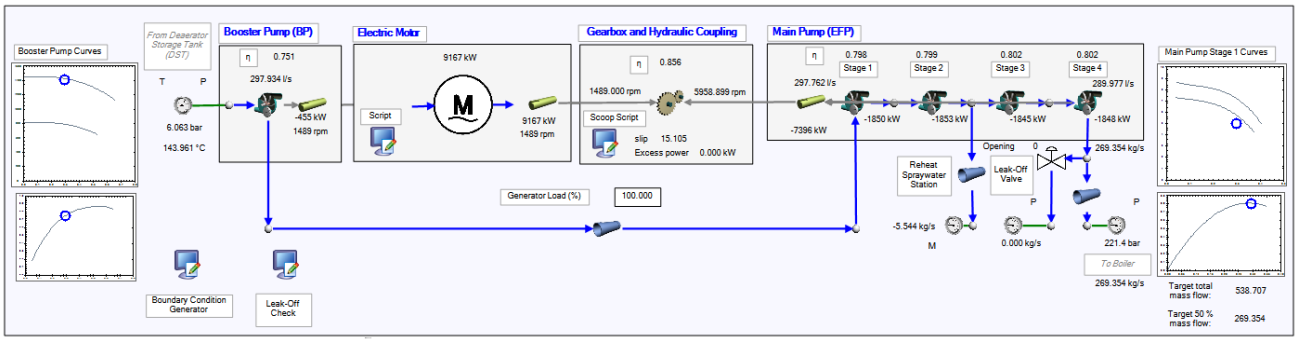

Figure 3.54: Flownex *model for a single EFP train at Station A1 – full generator load scenario*

The effect of scoop position on the mechanical efficiency was not quantified in the station manuals. This is a limitation of this model, so it was decided to consider plant data from the DCS.

3.15.4 Efficiency as a Function of Scoop Position

Figure 3.55 is a reproduction of the P&ID for the EFP trains, with relevant instrumentation highlighted. Yellow indicates that the measurement was used to calculate efficiency while the turquoise instrumentation was used to relate this efficiency to plant conditions.

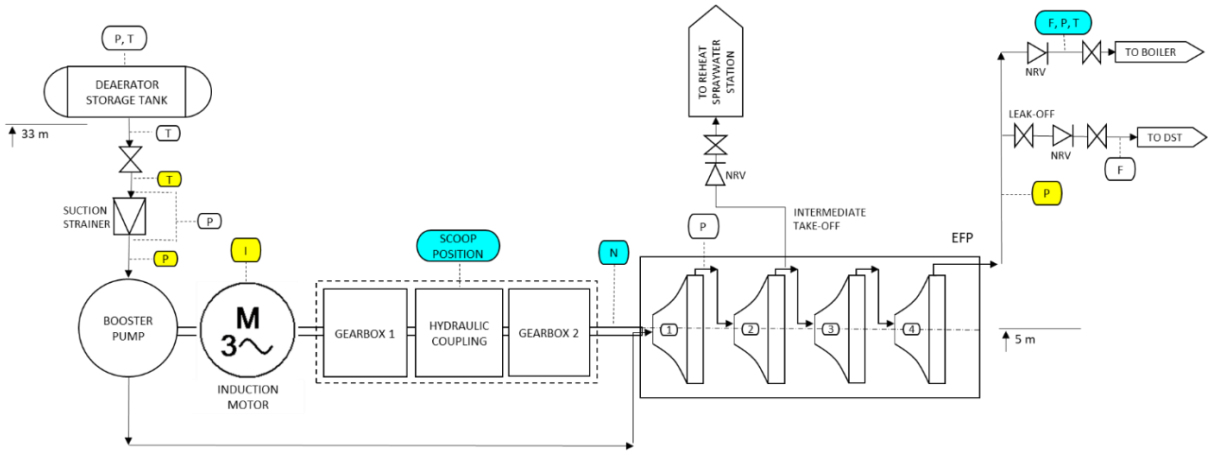

Figure 3.55: Process diagram for EFP train with instrumentation points used to determine hydraulic coupling efficiency

Section 2.1.4 discussed the type of hydraulic coupling used at this station. In Figure 3.56 the scoop tube is highlighted. By adjusting the scoop position, the amount of oil available to transfer the torque is altered and thus the slip is altered.

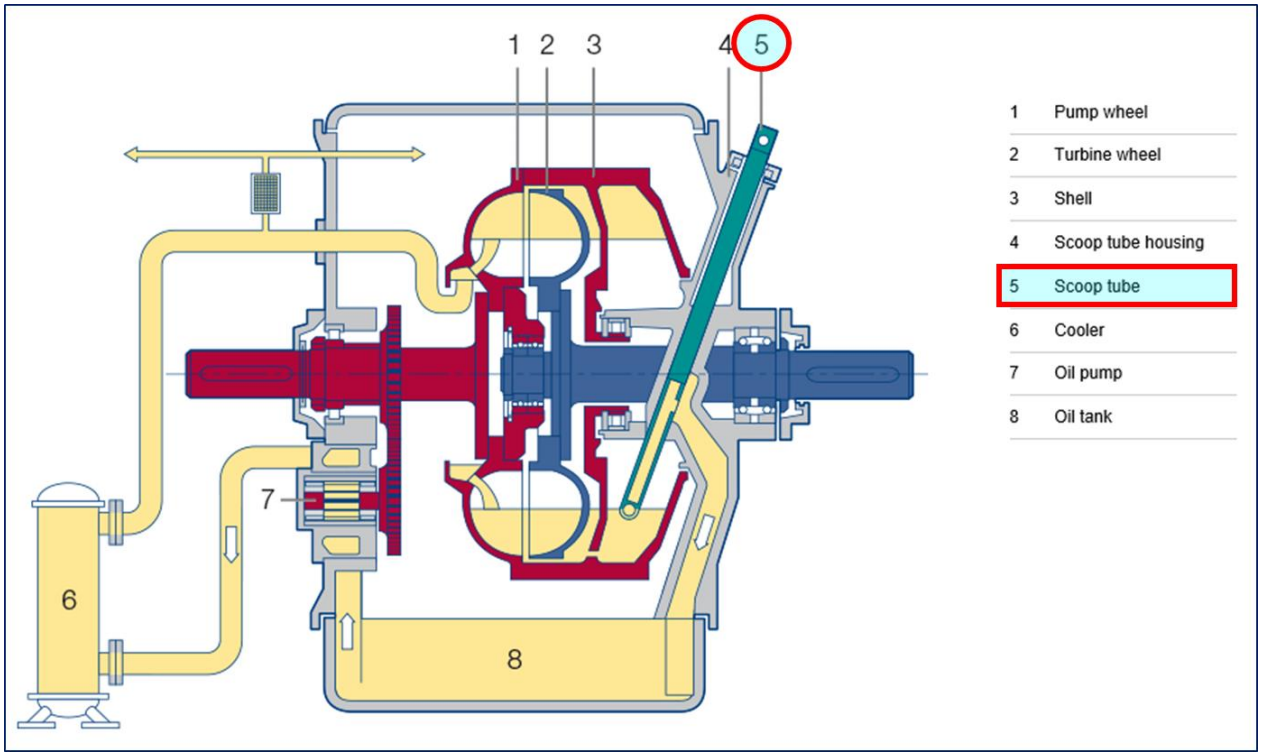

Figure 3.56: Diagram illustrating a Voith variable speed coupling (Voith, 2017)

Figure 3.57 illustrates the relationship between scoop position and slip for each of the two pumps, on a generator load range of 31.4 % to 99.5 %. It is observed that the relationship is approximately linear. However, the two pumps have different curves, suggesting that the two scoop positioners might be stroked differently. Therefore care must be taken in relating efficiency to scoop position, because the reported scoop position is not a reliable indicator of slip.

Note that for the following graphs in this section, some of the outliers were removed, most notably at points of major transition.

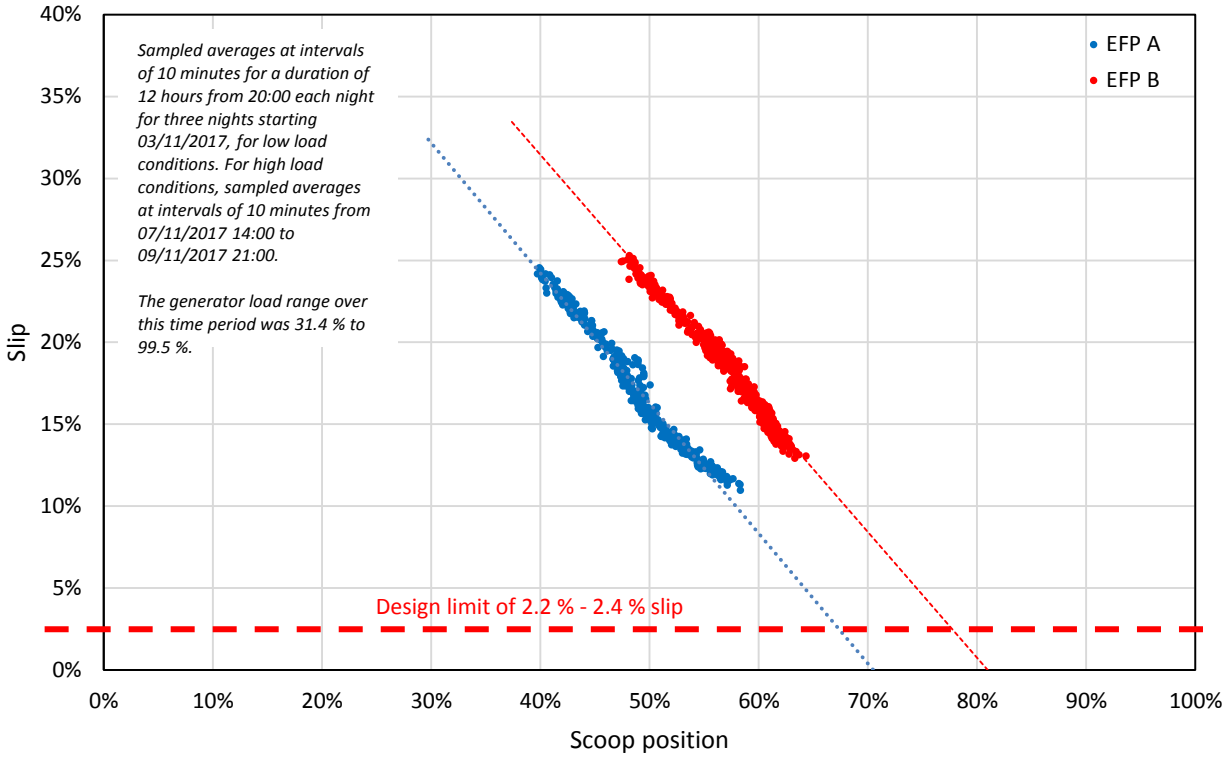

Figure 3.57: Slip vs scoop position on both EFPs at Station A1

There was no discharge temperature measurement available in order to calculate the real work consumed by the pump, and so the efficiency quoted is relative to the isentropic pump work (that is, the hydraulic work done on the fluid). Thus the total efficiency is calculated as shown below.

$$\eta = \frac{\dot{W}_{hyd}}{\dot{W}_{elec}} = \frac{\dot{m}_{FW} \cdot \left(h_{d,s} - h_s\right)}{\sqrt{3} \cdot I_{phase} \cdot V_{phase-phase} \cdot PF} \tag{102}$$

The suction enthalpy h_s is evaluated at the suction pressure and temperature while the isentropic discharge enthalpy $h_{d,s}$ is evaluated at the discharge pressure and suction entropy.

$$h_s = h(p_s, T_s) \tag{103}$$

$$h_{d,s} = h(p_d, s_s) = h\left[p_d, s(p_s, T_s)\right] \tag{104}$$

Figure 3.58 shows that mechanical efficiency is inversely proportional to slip and so efficiency can be expressed as a linear function of slip in *Flownex*.

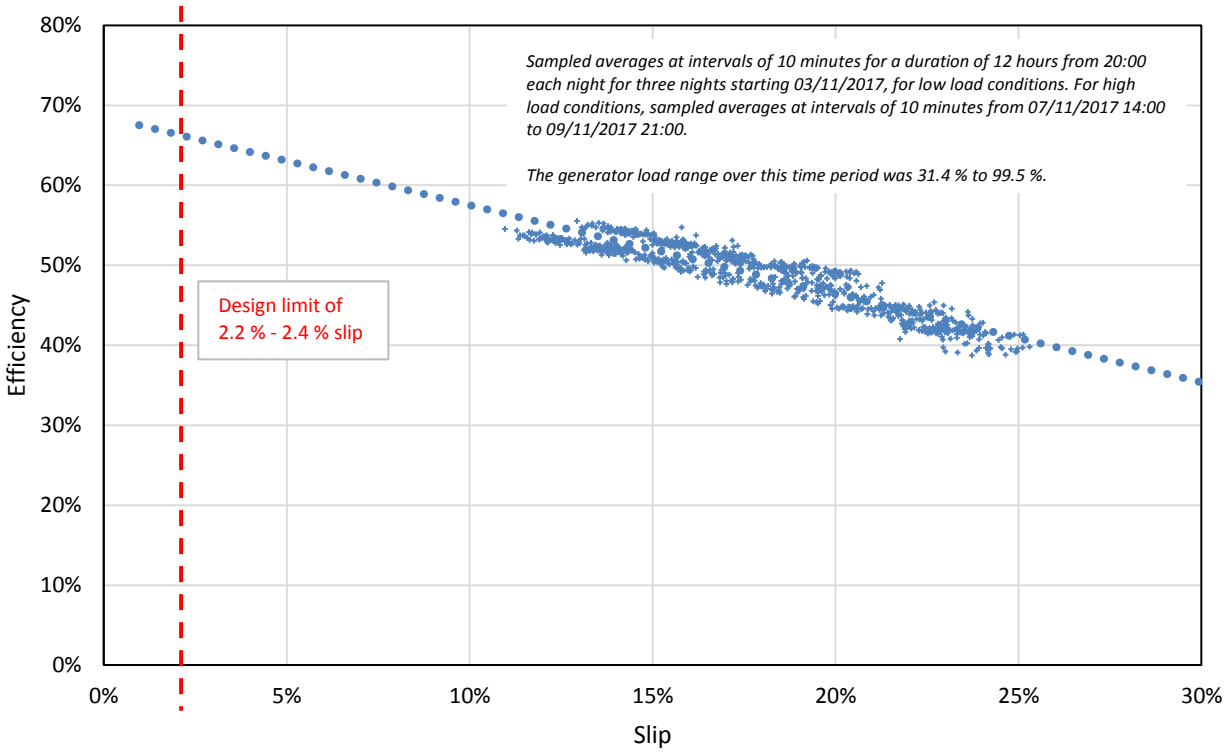

Figure 3.58: Efficiency vs (hydraulic) slip on both EFPs at Station A1

Figure 3.59 illustrates the transition from one pump to two pumps in the region of 60 % load, with the associated change in scoop position. This is viewed from the perspective of the "B" pump but a similar pattern is observed with the other pump.

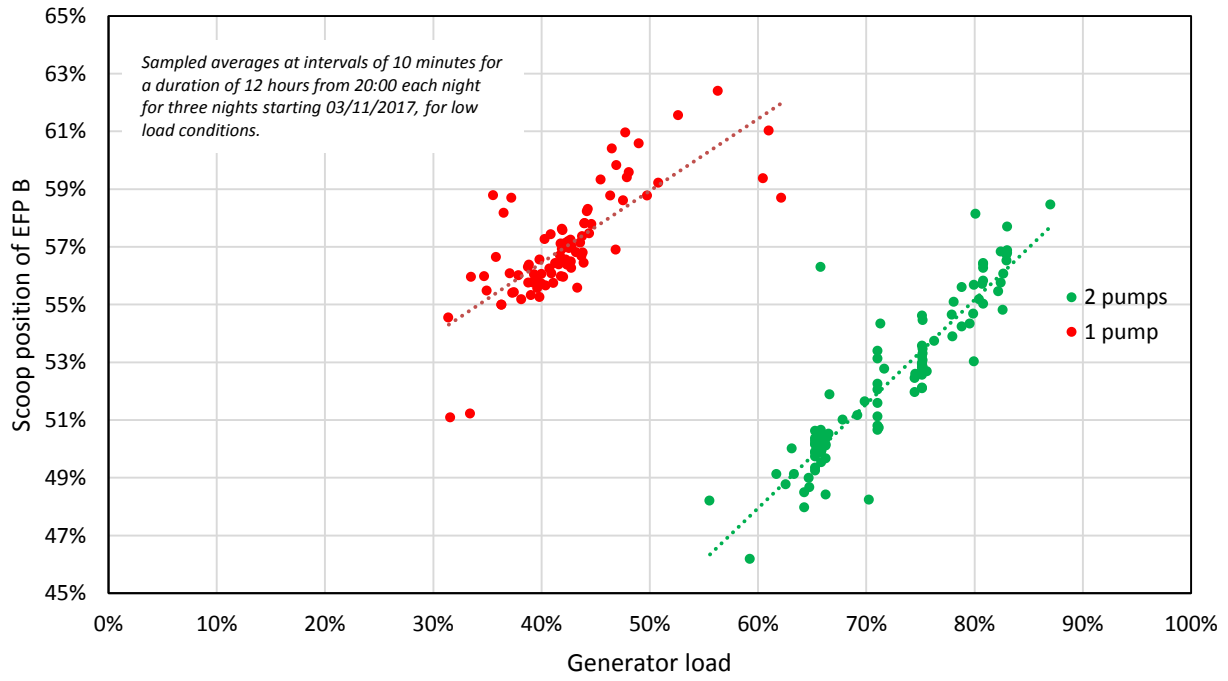

Figure 3.59: Scoop position vs generator load on EFP B at Station A1

3.15.5 Assumptions

As discussed in Section 2.2.6, the phase-to-phase voltage (line voltage) for the motor was taken as constant at 11 kV and the power factor was assumed to be constant at 0.885, based on values used in Eskom reports estimating the cost of EFPs running at full load. Furthermore, the motor slip was taken as constant over the operating range of the EFPs, meaning that all speed variability is attributed to the hydraulic coupling. These are the best approximations possible with the available information.

3.15.6 Revised EFP Model

Because the efficiency obtained from these considerations of DCS values is a total efficiency (that is, incorporating the hydraulic efficiency of the pump as well as the mechanical efficiency of the system transmitting the torque from the motor to the pump shaft), for the purposes of the EFP case study, the hydraulic efficiencies of all pump stages were artificially set to 100 % and the total efficiency was applied to the gearbox representing the hydraulic efficiency. The hydraulic coupling slip was then adjusted using a designer in *Flownex* in order to obtain the correct feedwater mass flow rate for the load condition. The assumption was made that one pump would be in service up to 60 % generator load and that two pumps would be in service above 60 % generator load, based on Figure 3.59. When two pumps ran, the assumption was made that these would each contribute exactly half of the total feedwater mass flow. A designer was then used to obtain the correct motor power consumption in order to balance power around the gearbox. This revised EFP model is represented in Figure 3.60.

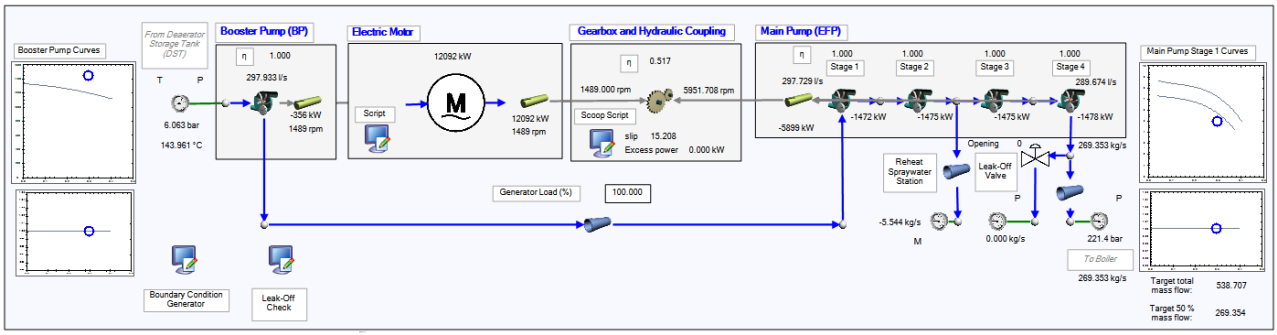

Figure 3.60: EFP model at 100 % generator load, both pumps in service

4. Case Studies

This chapter considers several case studies that were investigated utilising the integrated model built in the preceding chapter. Each case study is separately introduced, quantified and discussed.

4.1 Case Study 1: Effect of Steam Admission Valve Stroking, including the Presence of Cold Reheat Supply

4.1.1 Case Study Background and Objective

As was discovered during the model development, the steam admission valves of station A1 were stroked differently to the design philosophy. In addition, it has been noted that the cold reheat supply has been disabled in the plant. This case study investigates the limits of operation with and without cold reheat steam, and with different valve stroking configurations. This is of value given that the cold reheat supply cannot be tested with the current plant configuration, and given that operators are in general reluctant to test limits of operation as it is commonly seen as introducing unnecessary risks.

It is expected that lower minimum generator loads could be achieved with the SFP in service when the cold reheat supply is utilised.

4.1.2 Valve Stroking as per DCS, with Cold Reheat

Section 3.11.5 considered the predicted signal oil pressure curves in order to open the steam admission valves sufficiently for the feedwater mass flow rate demand to be met at different load conditions, assuming the cold reheat supply was available. The charts are shown in Figure 4.1. Recalling the charts for valve stroking, valves reach fully closed/fully open positions at signal oil pressures of 1270 kPa, 1000 kPa, 780 kPa and 640 kPa. The resulting chart was therefore treated piecewise with up to four different “modes” of operation, each having its own quadratic trendline. These modes are described in Table 4.1 and the trendline equations are provided in Appendix C.

Table 4.1: Descriptions of Modes for DCS Stroking with CRH

Mode 1	V4, CRH controlling	$1270 \geq p > 1000$
Mode 2	V2, V3, V4, CRH controlling	$1000 \geq p > 780$
Mode 3	V2,V3,V4 controlling	$780 \geq p > 640$
Mode 4	V1,V2,V3,V4 controlling	$640 \geq p$

The model predicted that required feedwater mass flow rates could be met with cold reheat steam down to a generator load of 24 % (146 MW). Signal oil pressure reached its minimum value – i.e. valves were most closed – between 60 and 70 % load. The cold reheat valve opened between 37 % and 36 % load (225 MW – 219 MW).

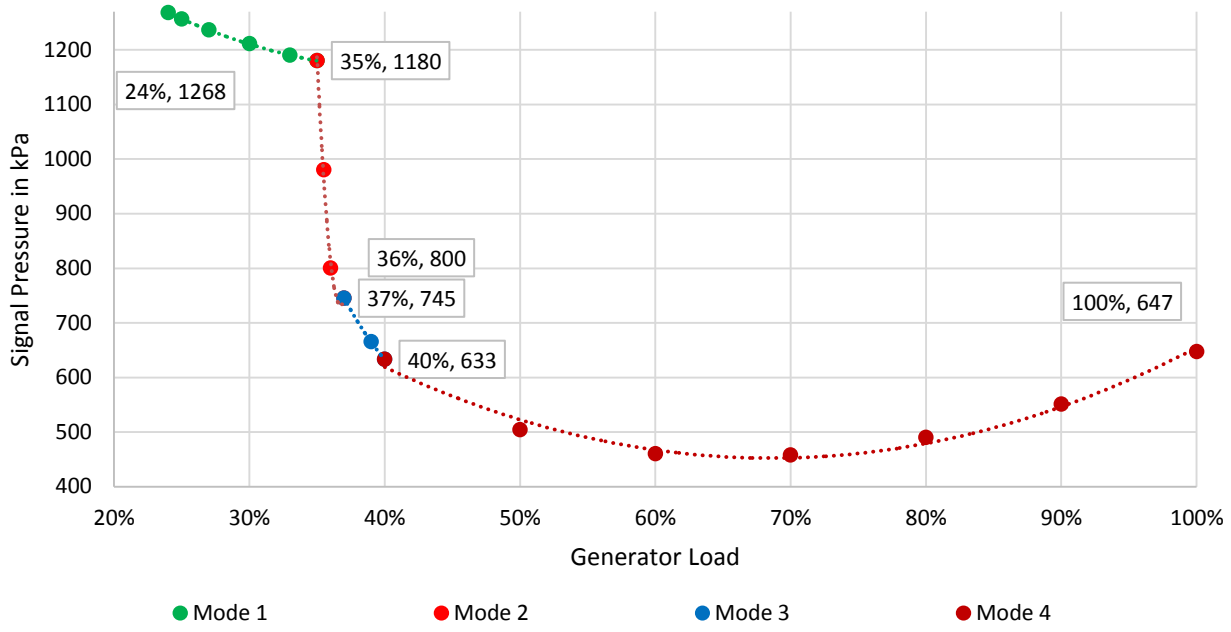

Figure 4.1: Graphical representation of signal oil pressure values with respect to load: DCS stroking with cold reheat supply

4.1.3 Valve Stroking as per DCS, with Cold Reheat Decommissioned

The previous section considered the behaviour of the system with the cold reheat steam supply commissioned. As noted previously, this steam supply is not currently available for use, although it is a possibility that this supply could be made functional in future. This section therefore considers limits of operation with only the IP bled steam supply.

The above exercise was repeated, manually obtaining the signal oil pressures for different loads with CRH decommissioned. To the nearest ±0.05 % generator load, the minimum load achievable with actual valve stroking and no cold reheat was 31.65 % (193 MW), shown in the snapshot in Figure 4.2. Signal oil pressure again reached its minimum value – i.e. valves were most closed – between 60 and 70 % load.

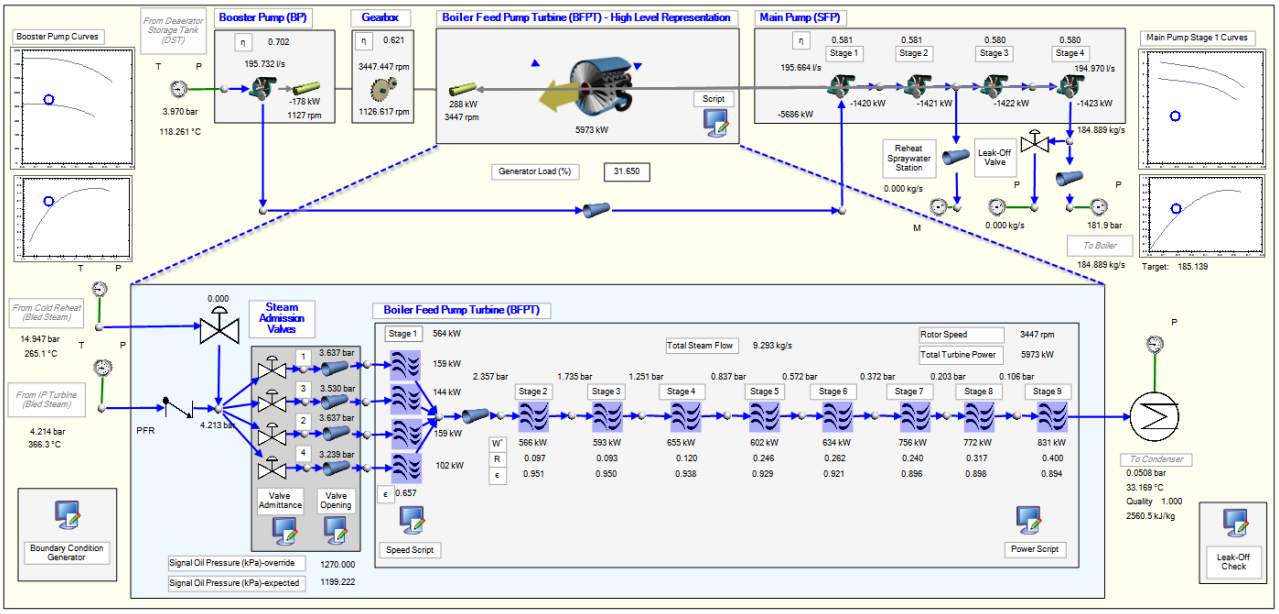

Figure 4.2: Snapshot of predicted minimum load of plant at present

Trendline equations for this scenario are provided in Appendix C.

4.1.4 Stroking the Valves According to Design, Cold Reheat Available

Figure 3.41 illustrates the difference in valve stroking between actual and design graphically. The relevant equations are available in Appendix B. This section will consider the implications of stroking the valves according to the design philosophy.

The script describing valve displacement in terms of an input signal oil pressure was modified so that the stroking reflected the manuals (also available in Appendix B). The valve admittance was again calculated as the square of the percentage displacement. New signal oil pressures were obtained for the different load cases with cold reheat supply available. The resulting curves for the case with cold reheat are shown in Figure 4.3.

The modes are described in Table 4.2 and the trendline equations are provided in Appendix C.

Table 4.2: Descriptions of Modes for Design Stroking with CRH

Mode 1	CRH controlling	1270 ≥ p > 883
Mode 2	V3,V4,CRH controlling	883 ≥ p > 780
Mode 3	V1,V2,V3,V4 controlling	780 ≥ p > 590
Mode 4	V1,V2 controlling	590 ≥ p > 200

To a tolerance of ±0.05 % of full generator load, the minimum load achievable with station manual valve stroking cold reheat was 23.7 % (144 MW). The cold reheat supply valve began to open between 36 % and 35 % (219 MW – 213 MW). The minimum signal oil pressure occurred in the region of 70 % load.

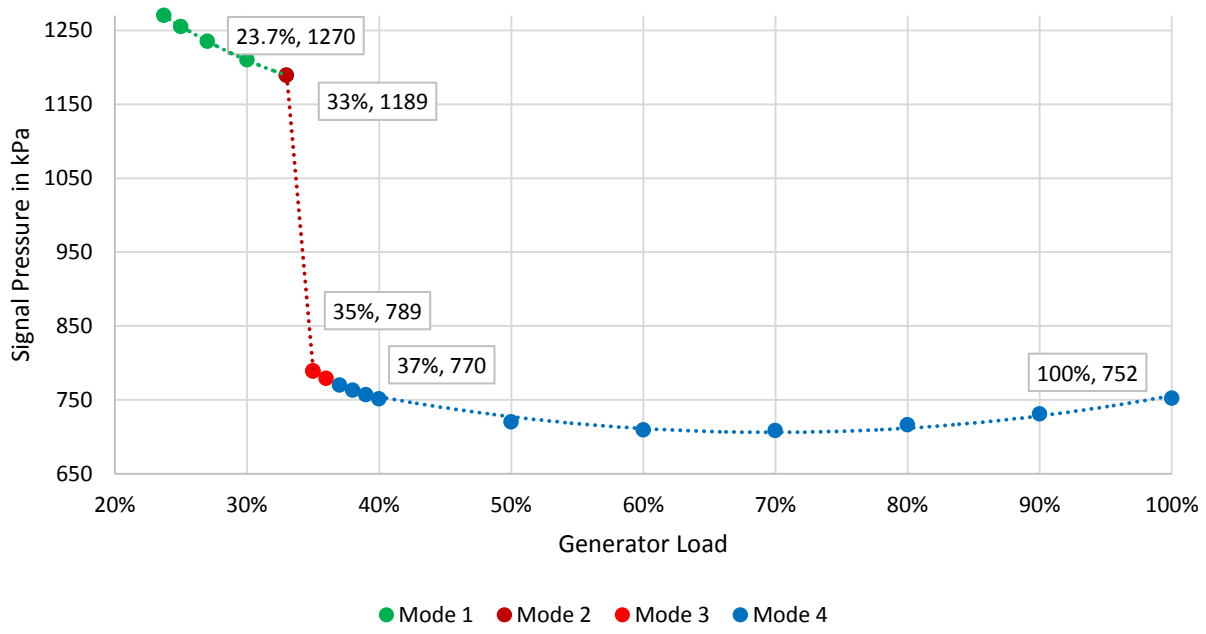

Figure 4.3: Graphical representation of signal oil pressure values with respect to load: design stroking with cold reheat supply

It was observed that choking was evident on the partial arcs associated with steam admission valves 1 and 2 on much of the load range, whereas with DCS stroking this had occurred only on the arc of valve 1. This is illustrated in the snapshot of the model at 90 %, shown in Figure 4.4

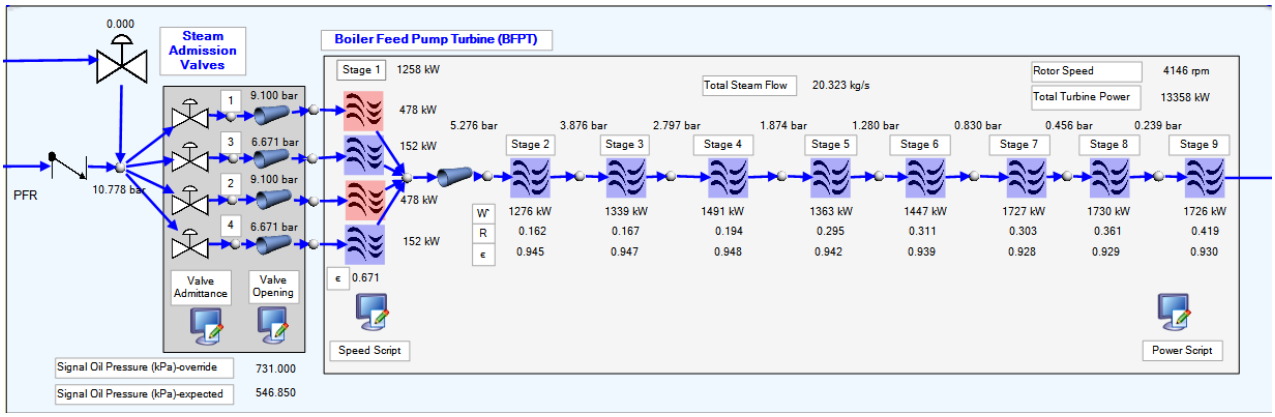

Figure 4.4: Snapshot of model at 90 % with valve stroking according to DCS values, showing choking on Stage 1

A snapshot of the model at the minimum load of 23.7 % is shown in Figure 4.5. At these lower loads with the cold reheat supply open, choking is observed on the final stage.

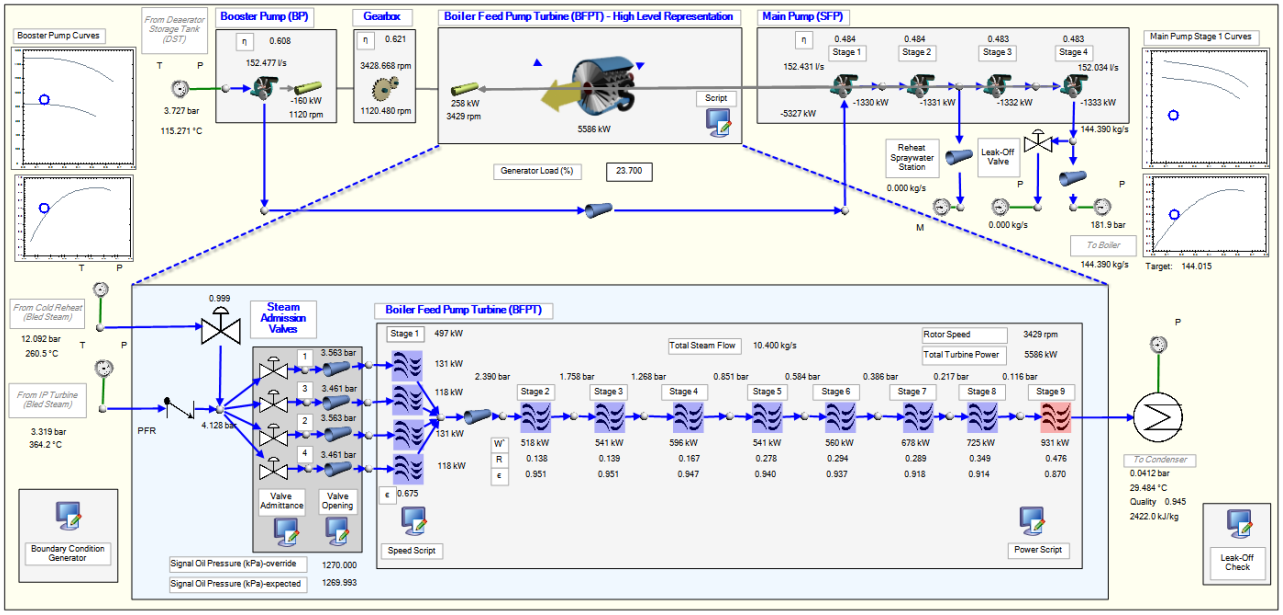

Figure 4.5: Snapshot of model at 23.7 % with valve stroking according to DCS values

4.1.5 Stroking the Valves According to Design, Cold Reheat Decommissioned

The process was repeated for the scenario with the cold reheat supply unavailable. This is the actual condition on the station. The minimum load achievable was 30.25 %. The minimum signal oil pressure occurred at about 70 % load. Note that the maximum signal oil pressure is 883 kPa because at this point all available valves are fully open. Trendline equations are provided in Appendix C.

4.1.6 Summary

The four different cases are plotted together in Figure 4.6, with the minimum loads and the points at which cold reheat supply is utilised being highlighted in red and yellow respectively for convenient comparison.

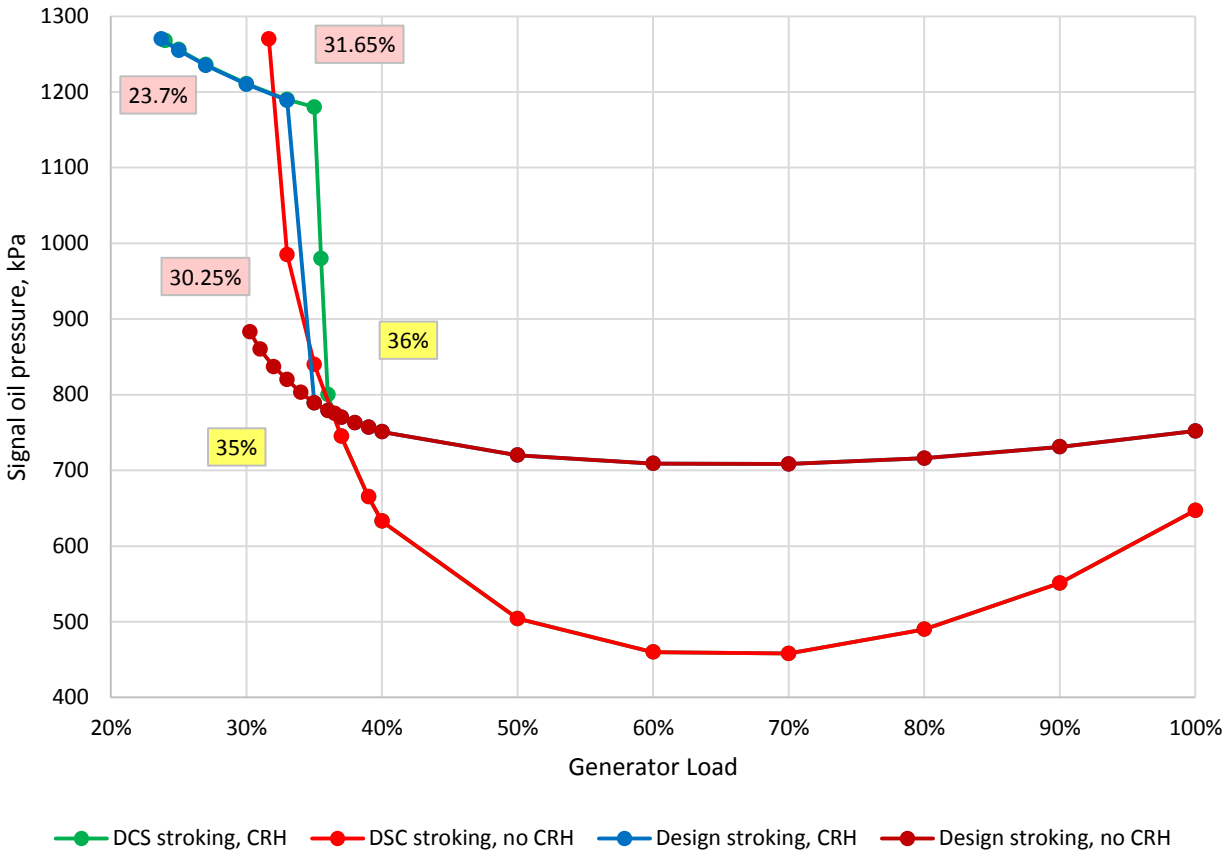

Figure 4.6: Graphical representation of signal oil pressure values with respect to load for different scenarios

4.1.7 Effect of Different Valve Configurations on Overall Isentropic Efficiency

The effect of valve configuration was considered with respect to overall isentropic efficiency of the turbine and valves. It was suspected that because throttling is a highly non-isentropic process, the different valve stroking arrangements could result in different degrees of throttling at different loads, thus affecting overall isentropic efficiency.

Table 4.3 shows the isentropic efficiency of the turbine, taken from the bled steam extraction point to the exhaust to the condenser, at 25 %, 40 % and 100 % generator load conditions. It is observed that there is a negligible difference between the two configurations when considering the accuracy of instrumentation and other factors.

Table 4.3: Effect of Steam Admission Valve Configuration on Isentropic Efficiency

Generator load	Steam supply	Isentropic efficiency	
		Actual stroking (DCS)	Design stroking (station manuals)
100%	IP bled steam	76.97%	77.03%
40%	IP bled steam	75.89%	75.91%
25%	CRH steam	60.63%	60.59%

The 25 % scenario demonstrates a marked reduction in efficiency from the 100 % case, attributed to the use of the cold reheat bled steam supply, which is at a much lower enthalpy than the corresponding IP bled steam supply. This difference is illustrated in a T-s (temperature-entropy) diagram in Figure 4.7, with an insert showing the equivalent Mollier (h-s, or enthalpy-entropy) diagram. Note that only the first partial arc-governor valve set is shown in each case.

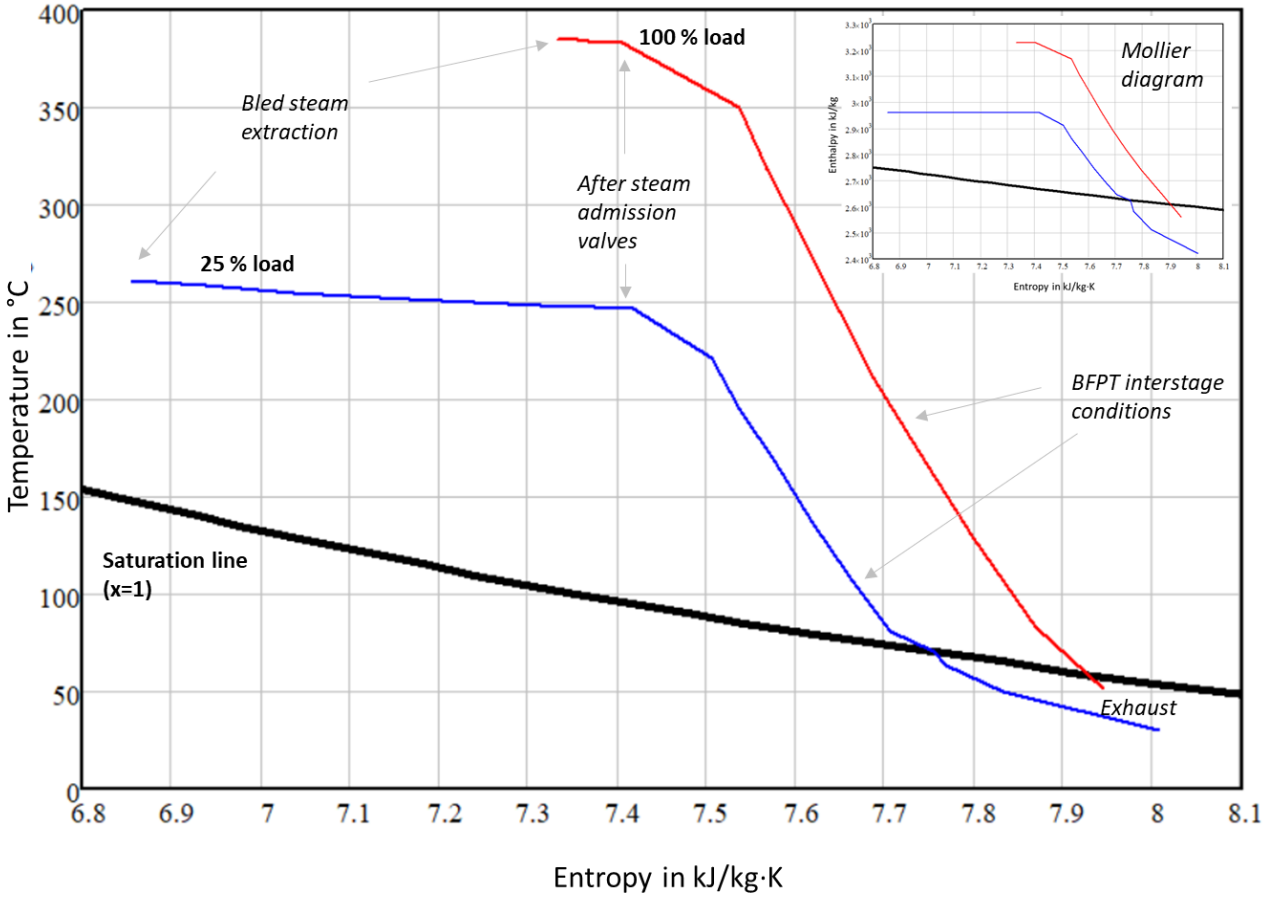

Figure 4.7: T-s diagram contrasting 100 % and 25 % load conditions, design valve configuration

4.2 Case Study 2: Effect of Changing Condenser Vacuum

Condenser vacuum is dependent on a number of factors. At Station A1 the principal causes of poor condenser vacuum are condenser fouling (for example, calcium carbonate scale) and poor cooling water inlet temperatures. The poor cooling water inlet temperatures result from poor cooling tower performance (blocked fill, blocked spray nozzles, and other defects) as well as from poor ambient conditions, most notably high wet bulb temperatures. This is a significant problem. At this station it has been the case in the past that the BFPT could not be placed into service as it would trip on poor condenser vacuum protections. At times, BFPTs have been operated in the range 25 kPa - 30 kPa backpressure for extended durations. The BFPT condensers have frequently been acid cleaned or cleaned through high pressure water jetting in order to address scaling. A better understanding of what occurs on the BFPT during poor vacuum operation is therefore of value. It is also of benefit to consider the impact of improved vacuum.

The following operating points are noted:

- 8.46 kPa: expected condenser pressure at 100 % load with cooling water inlet temperature of 22 °C as per design data.
- 17 kPa: alarm on BFPT condenser / automatic de-loading on main condenser.
- 22 kPa: automatic trip on main condenser.
- 34 kPa: automatic trip on BFPT condenser.

It is possible to have substantially different pressures in the BFPT condenser and the cold condenser because the interconnector valve connecting the two steam spaces can be closed, and also because the narrow pipe connecting these two steam spaces can cause a large pressure difference.

As the condenser back pressure deteriorates, the exhaust enthalpy will increase and the bled steam mass flow rate requirements will also increase. There may be a point where the BFPT is unable to supply required power to the pumps to maintain the feedwater demand. Also, the power output from the final stage will reduce to the point that reverse powering eventually occurs and some stages run in the mode of a fan. Operating in such a mode is likely to cause damage to the turbine, particularly if “fluttering” occurs on the last stage blades.

As the back pressure improves, the opposite effect is expected, with choking likely on the final stages.

4.2.1 Current DSC valve stroking without Cold Reheat

This case study will consider the 100 % load case with the valves stroked according to the DCS system and without cold reheat supply available. With a back pressure of 13.34 kPa, this will form the base case as this is the current plant arrangement.

The model was run with deteriorating back pressure, noting the effects on required mass flow rate and stage power distribution. Noting that the BFPT has an automatic trip at 34 kPa and an alarm at 17 kPa, the model was run at approximately 1 kPa intervals from 13 kPa to the point at which the valves are at their open limit.

The model was then run at reduced back pressure from 13 kPa to 1 kPa, with a special consideration of 2.20 kPa as this is the saturation pressure corresponding to the design inlet temperature of 19 °C. It is appreciated that the condenser back pressure can only approach this limit owing to it having an effectiveness of less than one.

For this case study it was assumed that the other boundary conditions and the feedwater mass flow rate target will remain unaffected by the change in back pressure.

The turbine model, decoupled from the feedwater portion of the model, was utilised with the shaft speed being fixed to correspond to the shaft speed from the integrated model (4357.411 rpm) and the designer feature was used to adjust the signal oil pressure until the correct power output was achieved (15 655.9 kW). Where the designer was unable to determine a solution, the signal oil pressure was varied manually until the correct power output was obtained, to the nearest 1 kW. A report was generated, considering the relative power distribution over the different stages, the mass flow rate required, the signal oil pressure required (i.e. extent of valve opening), the exhaust enthalpy and incidence of choking. The steam supply was only sufficient up to a back pressure of 25.85 kPa. Above this back pressure, the steam admission valves could not be opened further to admit more steam.

Figure 4.8 illustrates the changing exhaust enthalpy and required steam mass flow rate. Note that at pressures greater than or equal to the base case, no choking was observed. As the pressure was reduced, from 13 kPa and lower, Stage 1a exhibited choking. As the pressure was reduced from 12 kPa and lower, Stage 9 also exhibited choking. The 12 kPa case exhibited choking on Stage 1d. At a signal pressure of 604.56 kPa, only Stage 1a choked with a power of 15.593 MW and a mass flow rate of 23.063 kg/s. At a signal pressure of 604.57 kPa, Stage 1a and Stage 1d choked, with a power of 15.800 MW and a mass flow rate of 23.195 kg/s. The required power lay between these values but the system was so sensitive at this point that a solution could not be found.

The significance of this graph is that one can anticipate an increased bled steam requirement of approximately 3 kg/s as vacuum deteriorates from 11 kPa towards 26 kPa. Furthermore, vacuum may only be allowed to deteriorate to 25.85 kPa before the BFPT is unable to meet the full-load demands of the unit. In this case, a Unit might book a load loss if vacuum deteriorates past this point, or switch over to EFPs.

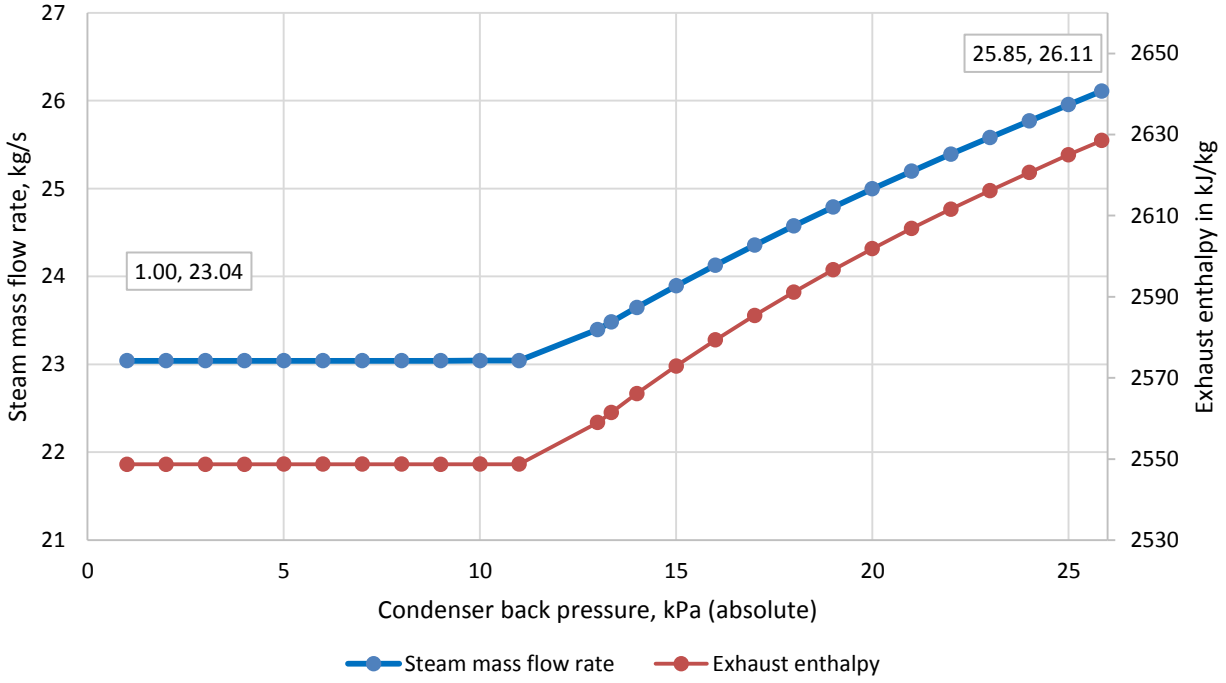

Figure 4.8: Exhaust enthalpy and required steam mass flow rate at 100 % generator load for different condenser back pressures

Figure 4.9 illustrates the change in stage-by-stage power distribution for several of the vacuum cases. It is particularly noteworthy that at increased condenser back pressure, the power output from the last stage reduces substantially, with the difference having to be made up by other stages. This has implications for the stresses placed on the earlier stages as well as for the likelihood of recirculation and blade flutter on the last stages. A detailed consideration of these phenomena is beyond the scope of this study. This model allows for this distribution to be visualised and quantified for further consideration as needed.

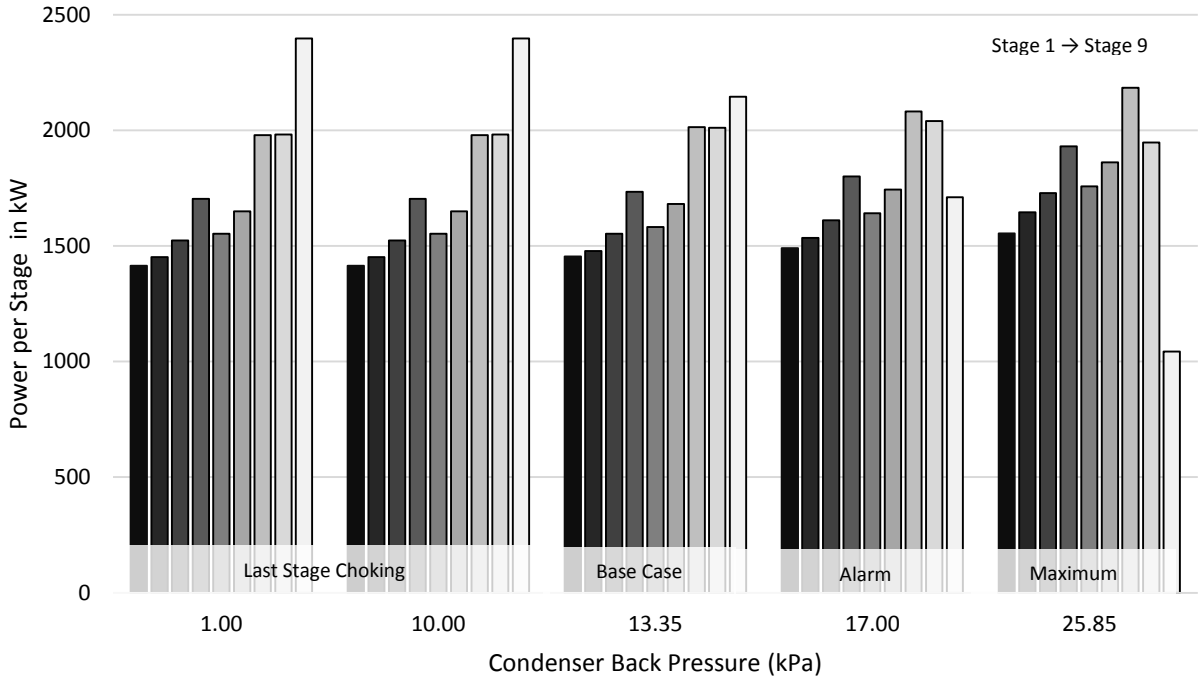

Figure 4.9: Stage-by-stage power distribution at different condenser back pressures

Noting that the feedwater demand of the boiler could not be met above a back pressure of 25.85 kPa, the steam admission valves were kept at their maximum position and the back pressure was increased to the point that the last stage began "reverse-powering" or "fanning". This occurs because the last stage pressure drop is so low that the nozzle velocity becomes less than the blade speed and so no power can be transferred. This occurred at a pressure of 47 kPa, as shown in Figure 4.10. The feedwater flow rate reduces from 538 kg/s to 480 kg/s. It is however appreciated that the automatic trip activates at 34 kPa, well before this point, in order to limit damage to the blades. In Figure 4.10 the last stage power contribution is -1 kW and the blade efficiency is -0.3 %.

Figure 4.10: Illustration of reverse-powering on the final stage

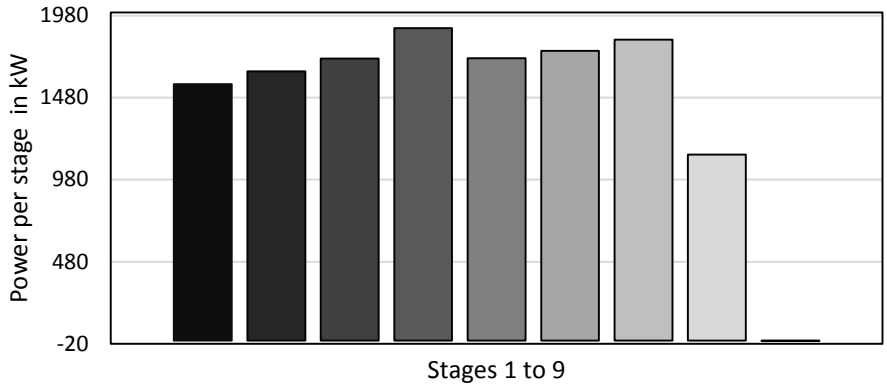

Figure 4.11: Stage-by-stage power distribution at 47 kPa, signal oil pressure maximum, 100 % generator load boundary conditions

4.2.2 DCS stroking with Cold Reheat

Because the BFPT was unable to provide the required power at pressures above 25 kPa, cold reheat might help to push this limit. As shown in Figure 4.12, the BFPT is able to meet the feedwater demand up to the tripping value of 34 kPa. The valves are fully open at approximately 40 kPa but this is not a realistic scenario owing to the trip value being 34 kPa. Whereas in the previous consideration, the inlet enthalpy was constant, here it reduces as the cold reheat valve is opened and this colder steam mixes with the hotter steam of the IP bled steam supply.

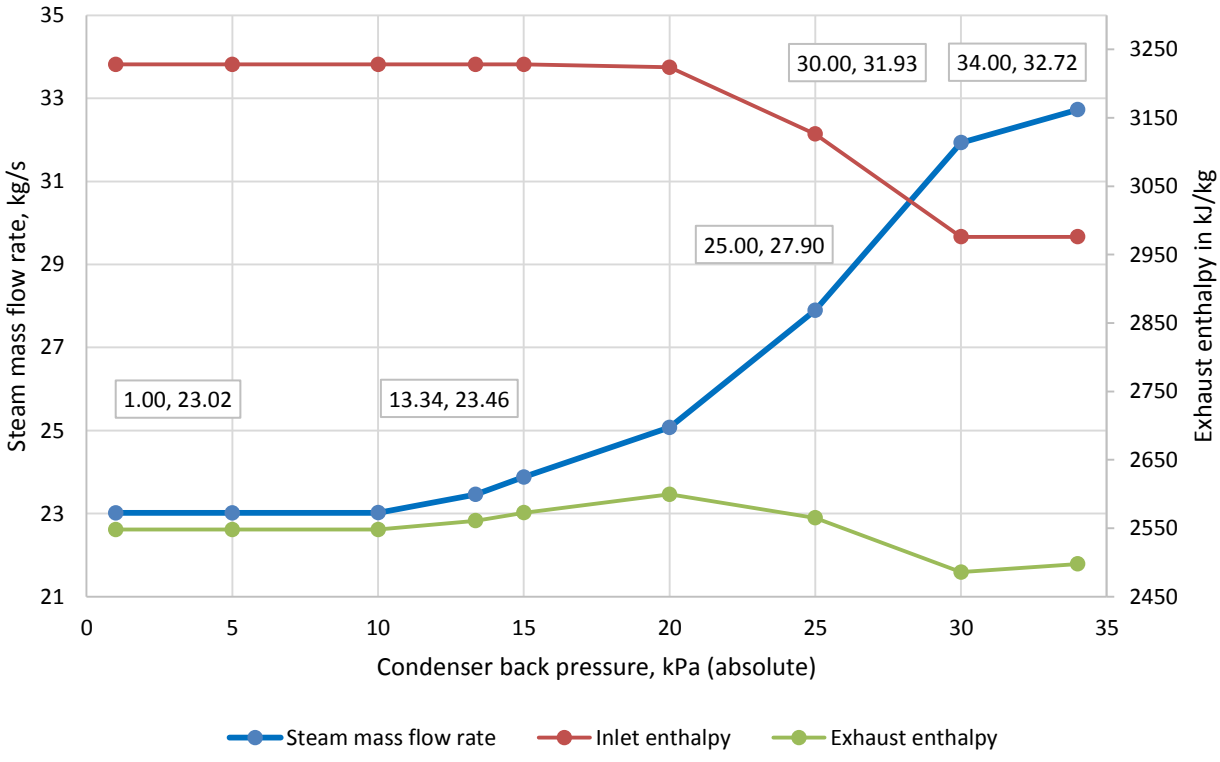

Figure 4.12: Inlet and exhaust enthalpies with required steam mass flow rate at 100 % generator load for different condenser back pressures, cold reheat supply available and valves stroked according to design

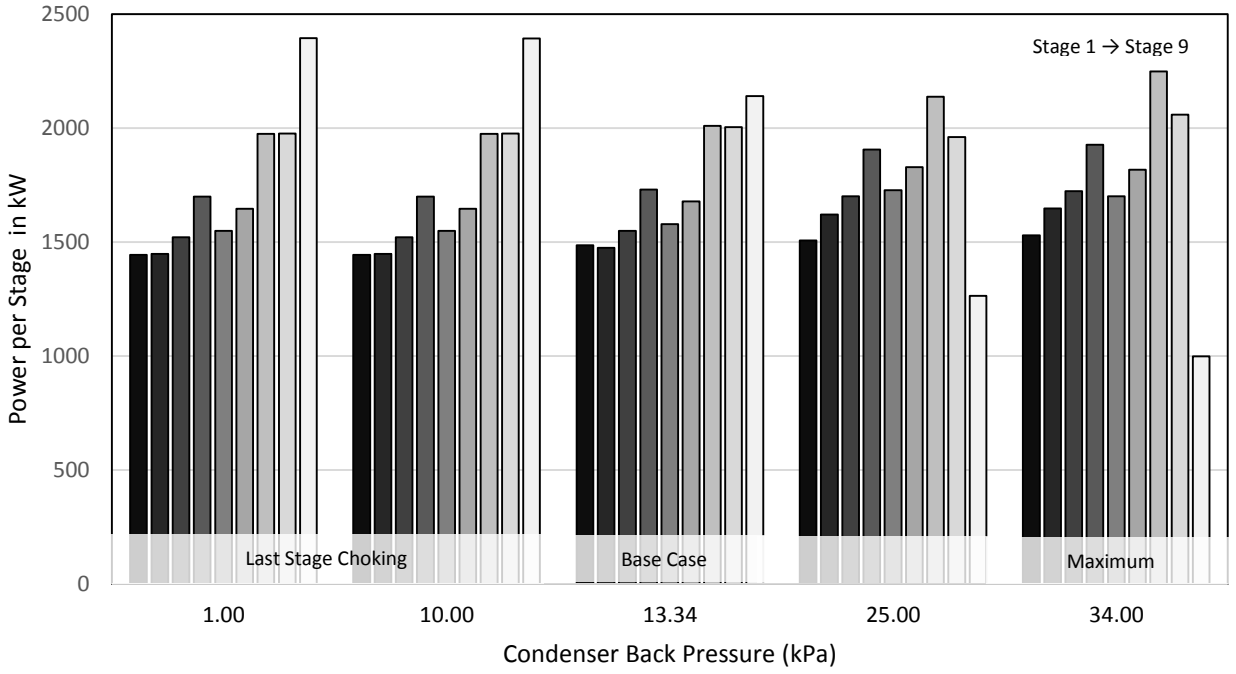

Figure 4.13: Stage-by-stage power distribution at different condenser back pressures, with cold reheat and valve stroking according to design

It is appreciated that increased bled steam mass flow rates with the same feedwater mass flow rate would result in a reduced power output from the turbine centreline. The BFPT would compensate for this by pumping more feedwater to the boiler, which would in turn require more bled steam. A detailed consideration of the centreline is beyond the scope of this study, however, and so for this case study, the feedwater demand at a given load has been kept constant. Also, this increase is less than 2% the total feedwater being pumped, hence is relatively insignificant.

4.2.3 Comment on Choking

In both cases, choking of the last stage coincides with a flattening of the mass flow rate curve, which is expected. Choking was seen from 12 kPa and lower on the normal steam supply. Based on the discussion by Cotton (1998), it is anticipated that for design conditions, choking would occur at the design back pressure of 8.46 kPa.

Because of the 1D nature of the nozzle model, it cannot consider the three-dimensional effects occurring especially in the last stage. The choking limitation may therefore be slightly exaggerated. Also, in setting up the model, the stages have been "chosen" to be close to but below the choking limit at design conditions. Further tuning of the model might show an arrangement where the last stage is slightly less susceptible to choking. However, during the model tuning it was quite challenging to arrive at a configuration where choking does not occur at some stage. This is an indication of a turbine which possibly has too few stages for the mass flow

and mean diameter, or otherwise stated, the turbine is designed at the limit of its steam swallowing capacity.

4.3 Case Study 3: Effect of Changing the Leak-Off Valve Control Philosophy

Sections 2.2.4 and 3.13 discussed the different philosophies with respect to leak-off valve control. This case study considers what occurs when the minimum mass flow rate requirement is increased. The flow rate at nominal best efficiency, Q_{00} is 550 L/s for Station A1. As discussed previously, there are three recommended leak-off points applicable here: 15 %, 25 % and 40 %; or 82.5 L/s, 137.5 L/s and 220 L/s. In addition, there is the curve associated with the OEM pump curves. The base case will be considered here – i.e. DCS valve stroking, without cold reheat.

In the base case, the discharge flow rate associated with the lowest achievable load is 194.970 L/s. This exceeds the 25 % and 15 % flow rate requirements. If the 40 % requirement were to be met, the leak-off valve would need to open as the discharge flow fell below 220 L/s, occurring at just below 37 % load. Considering the scenario of the leak-off valve opening at 37 % load, without changing the BFPT steam admission valve positions, the feedwater flow would drop significantly to 75.9 kg/s. The signal oil pressure will then rise to meet the demand, but even at its maximum value, the turbine will be underpowered, as shown in Figure 4.14.

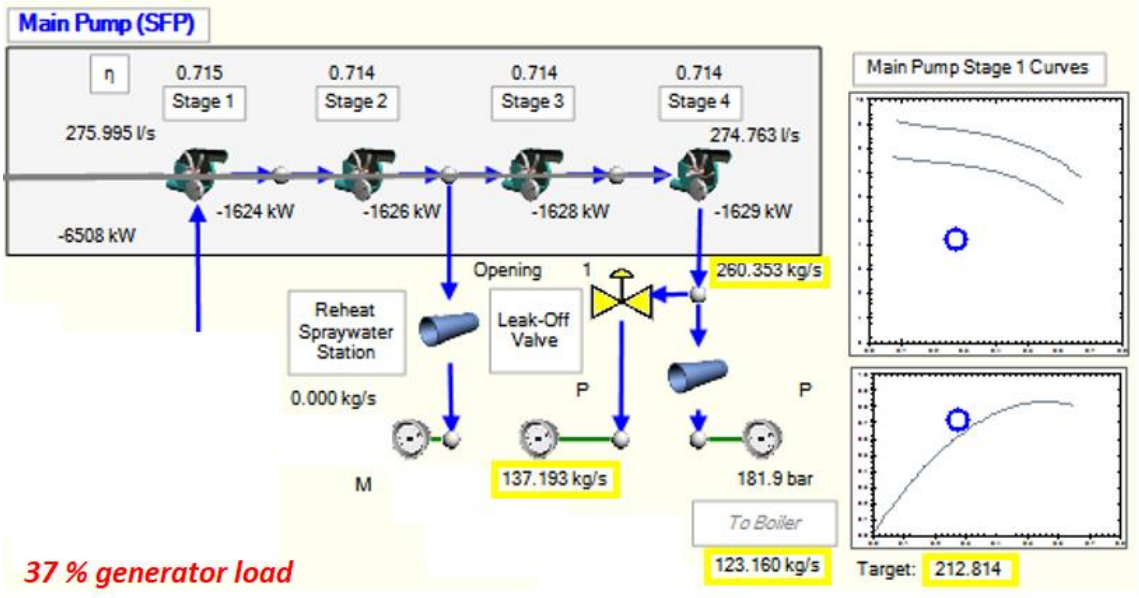

Figure 4.14: Snapshot of current plant configuration with leak-off valve open at 37 % load, signal pressure at maximum, showing only the main feedpump

This example illustrates the impracticality of utilising a binary leak-off valve to run the pump in a leak-off mode at such a high load.

Design Stroking with Cold Reheat Supply Available

The most extreme minimum load considered occurred when the valves were stroked according to the design values and the cold reheat supply was available. Here a minimum load of 23.7 % was achieved and this corresponds to a minimum of 152.0 L/s. This meets the 15 % and 25 % requirements.

If the 40 % flow rate requirement were to be met, a similar scenario would result. The leak-off valve would open at about 37 % load, the signal oil pressure would rise to its maximum, the steam admission valves would all be fully open, and the feedwater demand would not be met. This is illustrated in Figure 4.15.

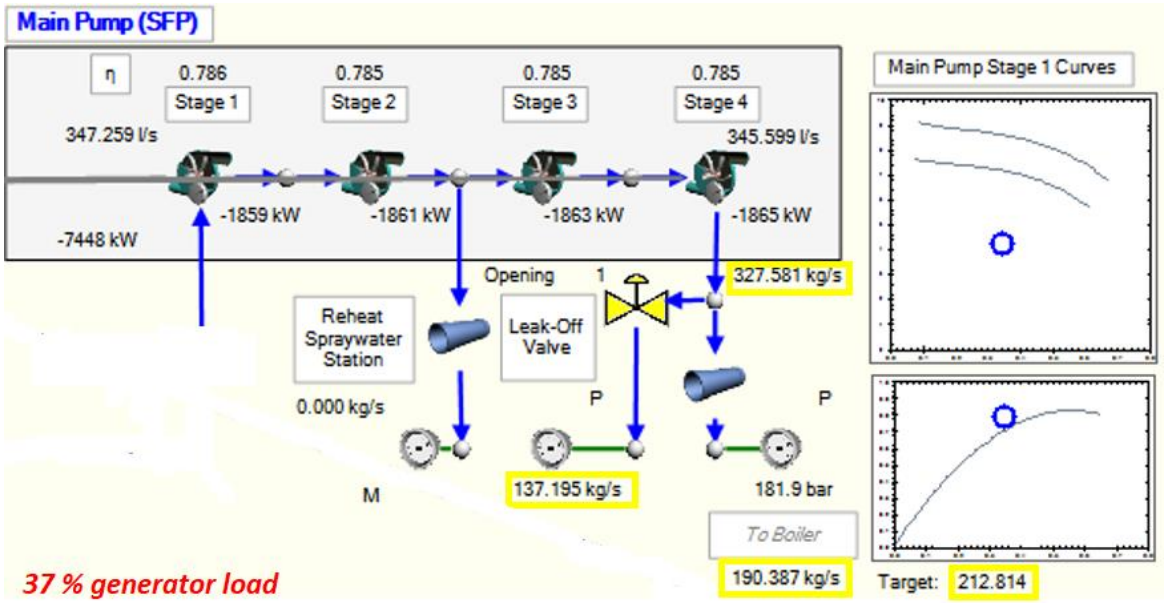

Figure 4.15: Snapshot of design plant configuration with leak-off valve open at 37 % load, signal pressure at maximum

The OEM recommendations of 25 % and 40 % are considered to be conservative and feedback from site engineers was that no issues associated with low flow (for example, in the form of vibrations) had been encountered.

4.4 Case Study 4: Electric Feed Pumps

The merit of running the steam feed pump versus the electric feed pumps at low loads is considered here. In the following considerations, the base case will be the current plant configuration – that is, stroking according to the DCS without cold reheat steam supply available.

The *Flownex* model that was built in Section 3.15 was used to compare the operation of EFPs vs an SFP at different generator load conditions. A snapshot of the EFP model at full load is shown in the

model development chapter. The appearance of the SFP model at different loads has also been presented in previous sections.

The results of this case study are presented in Table 4.4 and graphically in Figure 4.16.

Table 4.4: Power Consumed in Different Feed Pump Train Configurations

Generator load	100%	90%	80%	70%	60%	50%	40%	30%
Number of EFPs in service	2	2	2	2	1	1	1	1
Total EFP motor power consumption (MW)	24.184	22.766	21.222	19.47	12.031	11.540	10.692	5.011
Hydraulic coupling slip	15.208%	19.258%	22.897%	26.094%	13.362%	20.389%	26.189%	29.778%
Total BFPT shaft power generated (MW)	15.656	13.350	11.381	9.734	8.405	7.321	6.456	5.892
Isentropic power of turbine (bled steam potential)	20.340	17.523	15.076	12.981	11.232	9.752	8.508	9.742

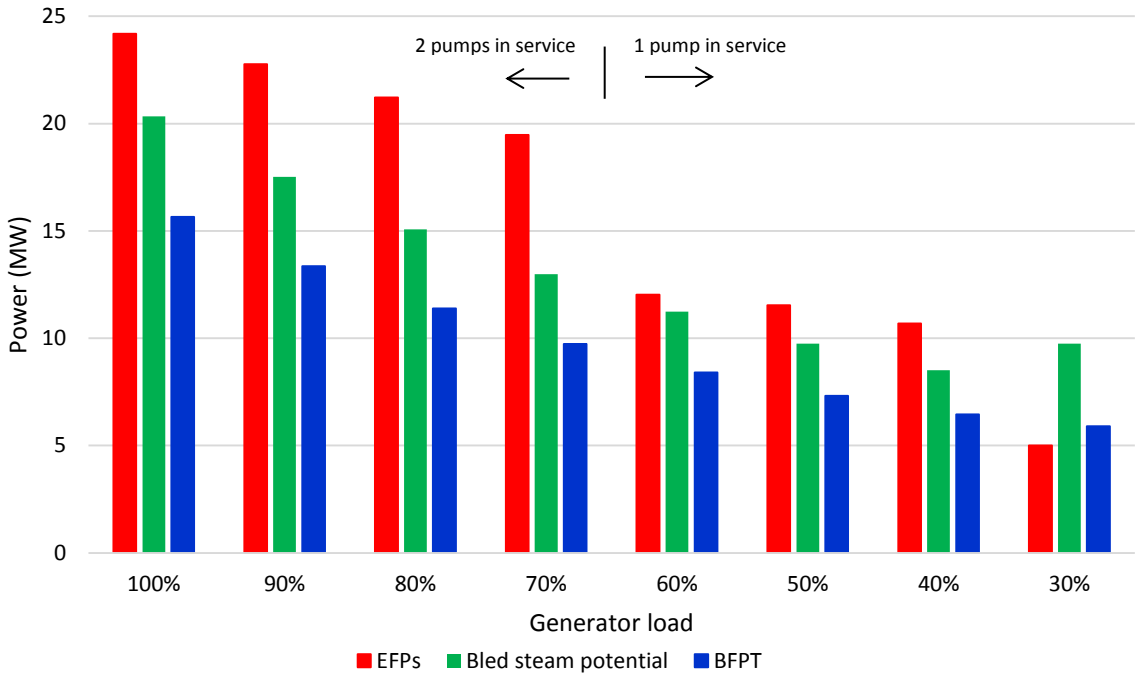

Figure 4.16: Differences in power consumption between SFP and EFPs

This demonstrates that from 100 % down to 40 % generator load, the electric power consumed by the EFPs exceeds the shaft power output from the BFPT. Furthermore, the "bled steam potential" or isentropic power of the turbine is still less than the power consumed by the electric motor. This represents the power which could be generated by expanding the bled steam through an isentropic turbine to the condenser back pressure. A difference is observed below 40 % as the cold reheat is utilised.

Furthermore, running the EFPs at full generator load instead of the BFPT results in the auxiliary power consumption increasing by 24.184 MW. With the maximum (gross) generator load constrained to 609 MW, this means that the net power output is reduced by an amount of 24.184 MW, representing a substantial amount of lost revenue.

It can be seen that at 60 % load, running one EFP is almost as efficient as running the BFPT but this deteriorates again as the load is reduced.

4.5 Case Study 5: Blade Temperatures

There was a request from a system engineer to predict the blade temperatures on Stage 8 on the range 60 – 100 % load in order for some metallurgical considerations to be made. This information is readily extracted from the model and reported in tabular form and the results are shown in Table 4.5 and Figure 4.17 for stages 2 to 9 (stage 1 was omitted from this consideration as the partial arc admission means that the different sections experience different conditions) .

Total temperatures were used because this is conservative (they are always higher than static temperatures) and a no-slip boundary condition applies to the blade surfaces which means the metal typically experiences static temperature.

This example highlights the usefulness of a stage-by-stage model such as the one developed.

Table 4.5: Predicted Blade Temperatures, Total Temperature Upstream of Row (°C)

		60% load	70% load	80% load	90% load	100% load
Stage 2	Stationary row	340.62	343.22	345.43	347.74	350.20
	Rotating row	319.07	321.36	323.23	325.19	327.29
Stage 3	Stationary row	309.50	311.85	313.83	315.95	318.26
	Rotating row	286.91	288.93	290.57	292.33	294.28
Stage 4	Stationary row	276.62	278.70	280.43	282.33	284.47
	Rotating row	252.56	254.30	255.69	257.22	258.96
Stage 5	Stationary row	239.94	241.66	243.05	244.63	246.44
	Rotating row	219.12	220.57	221.71	223.03	224.57
Stage 6	Stationary row	205.99	207.40	208.53	209.88	211.49
	Rotating row	184.31	185.45	186.31	187.38	188.73
Stage 7	Stationary row	169.80	170.85	171.64	172.68	174.04
	Rotating row	144.39	145.16	145.67	146.41	147.46
Stage 8	Stationary row	126.37	126.97	127.30	127.92	128.84
	Rotating row	101.31	101.66	101.72	102.07	102.79
Stage 9	Stationary row	82.53	82.70	82.55	82.76	83.43
	Rotating row	59.30	59.19	58.56	58.01	59.14
Exhaust steam		42.69	45.25	47.55	49.65	51.57

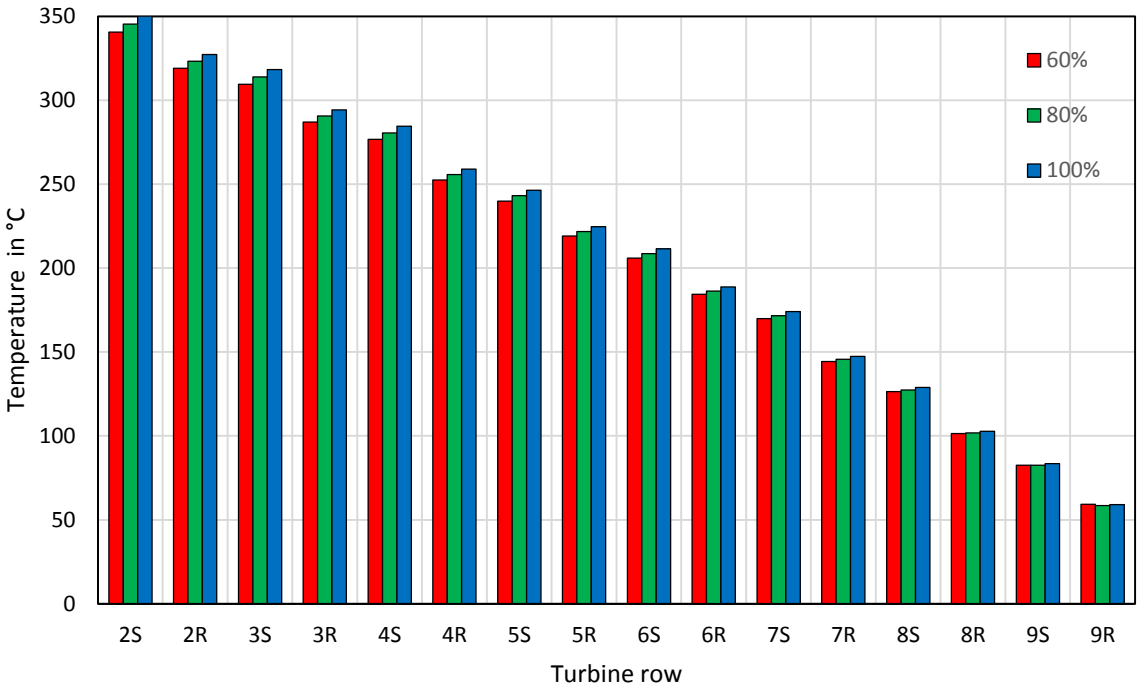

Figure 4.17: Total temperatures at inlet to each row

It can be observed from Figure 4.17 that the reduction of temperature is approximately linear from inlet to outlet, therefore it is reasonable to make a linear assumption for a quick temperature estimate. There is also very little temperature difference at different loads as the main steam temperature exiting the superheaters of the boiler is kept approximately constant regardless of Unit load. The more noticeable temperature reduction with reducing Unit load that can be seen on Stage 2 is largely due to the throttling effect of the steam admission valves.

5. Conclusions and Recommendations

5.1 Conclusion on Minimum Generation and Steam Supplies

Case Study 4 on the EFPs provides a strong motivation for keeping the BFPT in service wherever possible at all generator loads where IP bled steam is used, based on the inherent inefficiency of the EFP trains and based on the unit's net power sent out at full load.

Case Study 1 predicts a minimum achievable load of 23.7 % (144 MW) with the valve configuration as per the design setup. Removing the cold reheat steam supply, a minimum achievable load of 30.3 % (184 MW) is predicted. With the governor valves stroked as per DCS results, there is not a significant change to these values (less than 10 MW difference). Changing from design configuration to actual plant configuration has a negligible effect on the overall isentropic efficiency of the turbine with steam admission valves. However, changing from IP bled steam to cold reheat steam supply has a significant effect on this efficiency, changing from 76 % - 77 % on the load range 40 % to 100 % down to 61 % at a load of 25 %.

To place these results in context, the low load tests of November 2017 took the Unit to a minimum load of 33 % (200 MW) with 39 % (240 MW) being the load at which the limit of "Benson" mode was encountered. This was a feasible limit to aim for as below this load, collecting vessel level was accumulated. The BFPTs have been shown to remain in stable service down to a minimum of 53 % (320 MW).

For comparison, Station B1 (600 MW) was during the same tests operated down to a minimum of 39 % (235 MW), based on limits imposed by the Fossil Fuel Firing Regulations.

5.2 Conclusion on Condenser Vacuum

Case Study 2 illustrates that poor condenser vacuum is expected to result in a partial load loss from a back pressure of 25.85 kPa and higher, if only the IP bled steam is available. However, with the cold reheat supply available, the BFPT is expected to be able to meet feedwater demand up to the trip value of 34 kPa. It also illustrates that with a base case bled steam mass flow rate of 23.5 kg/s, the bled steam utilised could increase to as much as 32.7 kg/s for the 34 kPa limit. This emphasises the value of avoiding operating with poor condenser back pressures.

Relative power contribution from the final stage dropped substantially with deteriorating vacuum. The loading is shifted to the earlier stages and this is expected to have an effect on blade stresses and blade "flutter". It appears that the current warning and safety limits provide an adequate safety margin in this respect.

5.3 Conclusion on Leak-Off Valves

In Case Study 3, it was considered that whereas the current philosophy is to open the leak-off valve to maintain a minimum of 15 % of the volumetric flow rate at the best efficiency point, current recommended practice from the OEM is for this value to be between 25 % and 40 %. It was considered possible that at minimum generation the minimum flow requirements might not be met.

It was confirmed that the 25 % requirement would be met without opening the leak-off valve at the minimum load of 23.7 % (144 MW) but that the 40 % criterion would not be met. Due to the binary nature of the current valve configuration, this could not be achieved without significant plant modification. As no concerns have been noted on these pumps in connection with minimum flow, the 40 % target is not considered justifiable.

5.4 Recommendations from Case Studies

Recommendation 1

During future outages, the steam admission valves should be stroked according to the design charts as this will allow for a lower minimum load to be achieved without modification to plant, it will allow for the flow to be better spread between the valves (preventing choking occurring on the one quarter stage) and it will allow for better standardisation across Units.

Recommendation 2

During future low load tests, the limits of the BFPT's operation should be further explored as this model predicts that the BFPT should be capable of being run at a load 127 MW lower than the current limit. It is appreciated that this is based on typical operating conditions and so the specific conditions at the time may shift this value somewhat. However with a margin of over 100 MW, there is good motivation to attempt to test these limits. It is possible that the control system may need to be considered as a limiting factor, even if the load is physically achievable. Noting that the rest of the Unit is currently constrained to a limit of 40 % with EFPs running, this load would be a sensible initial target.

Recommendation 3

The pump leak-off philosophy should remain unchanged. If the 40% limit is to be imposed, a variable leak-off valve system should be incorporated.

Recommendation 4

Condenser fouling should continue to be addressed with periodic cleaning and/or through maintaining suitable cooling water chemistry, and cooling towers should be suitably maintained in order to ensure condensers are subjected to appropriate cooling water inlet temperatures. This point is already appreciated by the station; this study just serves to emphasise the importance of proper maintenance on the cooling water side.

Recommendation 5

The recommissioning of the cold reheat supply should be considered for feasibility by the relevant system engineer. However, it is appreciated that the cost of such a modification may be significant and the benefit might be marginal. This should depend on the outcome of further low load tests without the cold reheat. If the current limit imposed by the boiler – 240 MW – can be achieved without cold reheat steam supply, as predicted, then there will be no immediate benefit of recommissioning the cold reheat supply without first making modifications to the boiler. This consideration should also be made in view of the benefits associated with being able to run at poorer condenser back pressures.

Recommendation 6

The SFPs should be utilised in favour of EFPs at all generator loads.

5.5 Comments Concerning Use of the Model

This specific model may be utilised to predict interstage conditions and other results, as demonstrated in Case Study 5. Care should however be taken to note that the model is set up to show **typical boundary conditions** as a function of load and this may differ quite significantly over time and from Unit to Unit. As an example, condenser vacuum is typically significantly worse during summer than during winter, and there is quite often a significant difference in tube fouling (and hence vacuum) from one Unit to the next. Care should also be taken to cater for **changing component characteristics** over time and from Unit to Unit. For example, if a stage is removed from the turbine, as has been the case on some main turbines, then this should be reflected in the model to be used. If the turbine efficiency is known to have deteriorated significantly from design values – for example, if blade surfaces become rougher due to adverse steam conditions – then loss coefficients might be increased accordingly.

If one considers applicability to other Units at the same power station, assuming that the Units are all according to the same design, then the design/heat balance values would be unchanged and all that would need to change in terms of inputs would be the inputs based on DCS data. For initial

model tuning, this would include the bled steam temperature and pressure, the condenser pressure and the pressure after Stage 1 for the tuning case (preferably full load).

Examples on the boundary conditions would include typical back pressures as a function of load (because different condensers have different levels of fouling), different feedwater mass flow rates required as a function of load (because of steam leaks and cycle efficiency differences) and bled steam conditions as functions of load.

If any modifications are implemented on a specific Unit, then this would also need to be reflected in the new model – for example, on one Unit the cold reheat supply might be recommissioned, the steam admission valve stroking philosophy might be different, or a stage might be removed on the turbine. Such factors would need to be considered when revising the model.

5.6 Concluding Remarks

A model has been built in *Flownex* based on careful consideration of relevant theory as well as site-specific design data and plant measurements, and this model has been used to predict behaviour of the system in modes which cannot readily be tested in practice. In particular, the limits of low load operation, the impact of poor condenser vacuum, the impact of different leak-off valve philosophies and the contrasts between running with turbine-driven pumps and running with electric feed pumps, have all been successfully explored.

Case studies such as these allow for a better understanding of the system in question, which informs operating and maintenance strategies as well as possible plant modifications. The conclusions of these specific case studies have been used to produce useful recommendations for the station under consideration. The model in question may be used to study other problems of interest, and the methodology employed here may be applied to similar systems at other power stations.

6. List of References

The Harvard referencing system is used in this document, with acknowledgement to the University Library of the Anglia Ruskin University for their guide (Anglia Ruskin University Library, 2017).

6.1 Document References

- ABB, 2017. ABB motor sets world record in energy efficiency – saves half a million dollars. ABB News Center, [online]. Available at: https://new.abb.com/news/detail/1789/ABB-motor-sets-world-record-in-energy-efficiency-saves-half-a-million-dollars [Accessed 3 October 2018]
- Anglia Ruskin University Library, 2017. *Guide to Harvard Style of Referencing (version 6.1).* [online] Anglia Ruskin University. Available at: <https://libweb.anglia.ac.uk/referencing/files/Harvard_referencing_201718.pdf> [Accessed 08/01/2018]
- British Standards Institution, 2003. BS EN ISO 5167: 2003 *Measurement of fluid flow by means of pressure differential devices*. London: BSI.
- Christie, A.G., 1920. Steam Turbines **In**: F.W. Sterling ed. 1920. *Marine Engineer's Handbook.* New York: McGraw-Hill Book Company, Inc.
- Church, E.F., 1928. *Steam Turbines*. New York: McGraw-Hill Book Company, Inc.
- Cotton, K., 1998. *Evaluating and Improving Steam Turbine Performance.* 2nd ed. Rexford, NY: Cotton Fact Inc.
- Dixon, S.L., and Hall, C.A., 2014. *Fluid Mechanics and Thermodynamics of Turbomachinery*. 7th ed. Oxford: Elsevier Inc.
- Fuls, W., 2017a. Accurate stage-by-stage modelling of axial turbines using an appropriate nozzle analogy with minimal geometric data. Applied Thermal Engineering 116 (2017), pages 134-146.
- Fuls, W., 2017b. Enhancement to the Traditional Ellipse Law for More Accurate Modelling of a Turbine with a Finite Number of Stages. Journal of Engineering for Gas Turbines and Power Vol. 139, November 2017, pages 112603-1 to 112603-12.
- M-Tech Industrial, "Flownex Simulation Environment," January 2019. [Online]. Available: https://www.flownex.com/
- Nag, P.K., 2008. *Power Plant Engineering*. 3rd ed. New Delhi: Tata McGraw-Hill Publishing Company Limited.
- Rousseau, P. and Fuls, W., 2017. *Course Notes. MEC 411 6Z Power Plant Systems Analysis.* University of Cape Town, unpublished.

- Siemens AG, 2015. Siemens Steam Turbine SST-600. *Siemens Global Website,* [online]. Available at: https://www.siemens.com/content/dam/webassetpool/mam/tag-siemens-com/smdb/power-and-gas/steamturbines/sst-600/sst600-interactivepdf-v10.pdf [Accessed 26 August 2018]
- van der Westhuizen, W., 2016. *Course Notes. 50420944 Pumps*. Eskom Electrical Power Plant Engineering Institute, unpublished.
- van der Westhuizen, W., and Cattaert, T., 2010. Power Station Pump Selection: Part 2. *World Pumps,* January 2010, pages 14 – 17.
- Wagner et al., 2000. The IAPWS Industrial Formulation 1997 for the Thermodynamic Properties of Water and Steam. Journal of Engineering for Gas Turbines and Power Vol. 122, January 2000, pages 150-182.
- Wildi, T., 2006. *Electrical Machines, Drives and Power Systems.* 6th ed. Upper Saddle River, New Jersey: Pearson Education Inc.
- Woell, F.X., 2016. Steam Turbines: Thermodynamic Velocity Triangle and Blade Design, *D 50266921 Turbines*. Eskom Electrical Power Plant Engineering Institute, unpublished.

6.2 Image References

- Beck, S., and Collins, R., (2012) [revised by Deramaux, M, 2016]. *Moody Diagram*. [image online] Available at: < https://commons.wikimedia.org/w/index.php?curid=52681200> [Accessed 14 September 2018].
- Bentley, J.R. (2007). *The Aeolipile: A Replica of the World's First Rotating Steam Engine*. [image online] Available at: <http://modelengines.info/aeolipile/> [Accessed 08 January 2018].
- Christie, A.G., 1920. *Fig. 70 – Design of an Impulse Blade.* Reproduced on p. 614 in: Christie, A.G., 1920. Steam Turbines **In**: F.W. Sterling ed. 1920. *Marine Engineer's Handbook.* New York: McGraw-Hill Book Company, Inc.
- Christie, A.G., 1920. *Fig. 83 – Design of a Semi-Wing Blade.* Reproduced on p. 620 in: Christie, A.G., 1920. Steam Turbines **In**: F.W. Sterling ed. 1920. *Marine Engineer's Handbook.* New York: McGraw-Hill Book Company, Inc.
- Christie, A.G., 1920. *Fig. 84– Design of a Full-Wing Blade.* Reproduced on p. 621 in: Christie, A.G., 1920. Steam Turbines **In**: F.W. Sterling ed. 1920. *Marine Engineer's Handbook.* New York: McGraw-Hill Book Company, Inc.

- Cotton, 1998a. *Figure 3-5. Approximate stage reactions – fossil-fired turbines.* Reproduced on p. 41 in: Cotton, K., 1998. *Evaluating and Improving Steam Turbine Performance.* 2nd ed. Rexford, NY: Cotton Fact Inc.
- Cotton, 1998b. *Figure 3-6. Approximate stage reactions – nuclear cycle turbines.* Reproduced on p. 41 in: Cotton, K., 1998. *Evaluating and Improving Steam Turbine Performance.* 2nd ed. Rexford, NY: Cotton Fact Inc.
- Emoscopes (2006). *Schematic diagram summarising the differences between impulse and reaction turbines*. [image online] Available at: <https://commons.wikimedia.org/wiki/File:Turbines_impulse_v_reaction.png> [Accessed 09 January 2018].
- Faizan, A., n.d. *Figure 1: Characteristic curves of an induction motor.* [image online] Available at: http://electricalacademia.com/induction-motor/three-phase-induction-motor-performance/ [Accessed 17 November 2018]
- Frolov, B., n.d. *Figure 2: Steam turbine stage losses (impulse design).* [image online] Available at: http://blog.softinway.com/en/steam-turbine-aerodynamic-improvements-for-significant-efficiency-gains/ [Accessed 19 November 2018]
- Fundacja na rzecz Czystej Energii [Foundation for Clean Energy], (2018a). *Turbina Peltona o wale poziomym z dwiema dyszami* [A Pelton turbine with a horizontal shaft with two nozzles]. [image online] Available at: <http://fundacjaenergia.pl/baza-wiedzy/technologie/energia-wod/turbiny-wodne> [Accessed 08 January 2018].
- Fundacja na rzecz Czystej Energii [Foundation for Clean Energy], (2018b). *Turbina Peltona o poziomym wale* [A Pelton turbine with a horizontal shaft]. [image online] Available at: <http://fundacjaenergia.pl/baza-wiedzy/technologie/energia-wod/turbiny-wodne> [Accessed 08 January 2018].
- Rousseau, 2015a. *Figure 6-12: General layout of typical drum-type (or two-pass) boiler*. Reproduced on p. 245 in: Rousseau, P. and Fuls, W., 2017. *Course Notes. MEC 411 6Z Power Plant Systems Analysis.* University of Cape Town, unpublished.
- Rousseau, 2015b. *Figure 6-13: General layout of typical once-through (or tower-type) boiler*. Reproduced on p. 246 in: Rousseau, P. and Fuls, W., 2017. *Course Notes. MEC 411 6Z Power Plant Systems Analysis.* University of Cape Town, unpublished.
- Senanayake, N., 2016. *Turbine Isentropic Efficiency*. [image online, slide from presentation "Applied Thermodynamics – Gas Turbine Cycles"] Available at: <https://www.slideshare.net/nssen/gas-turbine-1> [Accessed 04/05/2017]

- Siemens AG, 2004. *Steam turbine* (reference number EOG20041001-02). [image online] Available at: <https://www.siemens.com/press/en/presspicture/?press=/en/presspicture/2009/oil_gas/eog20041001-02.htm&content[]=EO&content[]=EP&content[]=PG> [Accessed 1 June 2018]
- UTK-EBPO, 2017. *Vorecon Type RW*. [image online] Available at: <http://ctkeuro.ru/?LANG=ENG&p=Voith_turbo> [Accessed 05/05/2017]
- Voith, 2017. *Variable Speed Fluid Couplings.* [image online] Available at: <http://www.voith.com/en/products-services/power-transmission/variable-speed-drives/variable-speed-fluid-couplings-57899.html> [Accessed 04/05/2017]
- Wildi, 2006. *Figure 14.16: Complete torque-speed curve of a 3-phase induction machine*. Reproduced on p. 322 in: Wildi, T., 2006. *Electrical Machines, Drives and Power Systems.* 6th ed. Upper Saddle River, New Jersey: Pearson Education Inc.
- Zajaczkowski, K., 2011. *Stodola's cone when the turbine nozzles are not choked. Graph of a formula.* [image online] Available at: https://commons.wikimedia.org/wiki/File:Stodola%27s_cone_not_choked.svg

7. List of Appendices

Appendices relating to the Flownex *model:*

- Appendix A: Extract from Script for Boundary Conditions
- Appendix B: Extract from Script for Steam Admission Valves
- Appendix C: Equations for Signal Oil Pressures

Appendices relating to heat balance data:

- Appendix D: Data from Heat Balance Diagrams for Station A1
- Appendix E: Data from Heat Balance Diagrams for Station B1

Appendices relating to theory and model development:

- Appendix F: Considerations of Optimum Turbine Blade Efficiency
- Appendix G: Orifice Plate Theory and Modelling of Leak-Off Valves
- Appendix H: Boundary Conditions – Pump Discharge Pressure
- Appendix I: Flow Resistance Component – Linear Characteristic

Appendices relating to Eskom-specific information:

- Appendix J: Fleet Overview
- Appendix K: Relevant AKZ Signals for Station A1
- Appendix : List of Reference Drawings

General appendices:

- Appendix M: General *Flownex* Notes

Appendix A. Extract from Script for Boundary Conditions

The boundary conditions are represented in Figure 7.1. Content from the script component describing these boundary conditions as a function of the percentage generator load, "W_1", appears below ("W_1" ranges from 0 to 100). The content is expressed with the correct syntax here and in the following appendix in order that the reader may readily reconstruct these scripts in *Flownex* if so required.

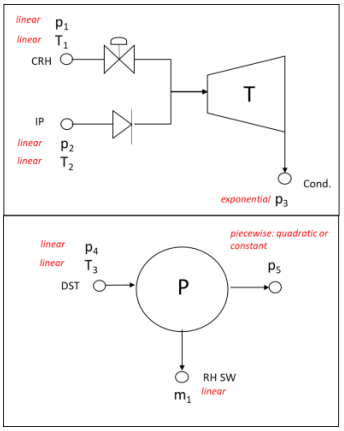

Figure 7.1: Key to boundary conditions

```
//Cold reheat boundary conditions
p_1.Value=35.914*W_1.Value/100 + 3.5799;
T_1.Value=57.73*W_1.Value/100 + 246.85;
//IP bled steam boundary conditions
 p_2.Value=11.251*W_1.Value/100 + 0.6529;
T_2.Value=26.63*W_1.Value/100 + 357.84;
//Condenser boundary condition
p_3.Value=0.1208*W_1.Value/100 + 0.0126;
//Pump suction boundary conditions
p_4.Value=3.0613*W_1.Value/100 + 3.0015;
T_3.Value=37.601*W_1.Value/100 + 106.36;
//Pump discharge boundary condition
 if(W_1.Value<40)
        {
        p_5.Value=181.8754;
        }
     else
        {
          p_5.Value=57.229*Math.Pow(W_1.Value/100, (2.0)) - 14.203*(W_1.Value/100) + 178.4;
        }
```

```
//Reheat spraywater boundary condition
if (W_1.Value<69)
   {
    m_1.Value=0;
   }
else
   {
    m_1.Value=-0.3696*W_1.Value+25.872;
    }
     //Required output: feedwater mass flow rate to boiler
 m_2.Value=517.29*W_1.Value/100 + 21.417;
```

Appendix B. Extract from Scripts for Steam Admission Valves

Content from the script components describing valve admittances and valve opening as a function of signal oil pressure ("Signal") appears below. The content is expressed with the correct syntax here as in the previous appendix in order that the reader may readily reconstruct these scripts in *Flownex* if so required.

Valve Admittances (A_f)

```
Admittance_1.Value=7.6367E-05;
Admittance_2.Value=Admittance_1.Value;
Admittance_3.Value=Admittance_1.Value*0.7994;
Admittance_4.Value=Admittance_3.Value;
Admittance_5.Value=0.5194*Admittance_1.Value;
Admittance_NRV.Value=1.0;
```

Valve Opening (A_0) – Position

There are two variations, depending on whether the valves are stroked according to the DCS trends or according to the station manuals.

```
//Four governor valves - quadratic - DCS stroking
Pos_1.Value=1.380E-03*Signal.Value + 1.246E-01;
Pos_2.Value=8.765E-04*Signal.Value + 1.278E-01;
Pos_3.Value=7.013E-04*Signal.Value + 2.843E-01;
Pos_4.Value=3.967E-04*Signal.Value + 2.574E-01;
Pos_5.Value=2.083E-03*Signal.Value-1.646E+00;

//Four governor valves - quadratic - station manual stroking
Pos_1.Value=1.741E-03*Signal.Value - 3.471E-01;
Pos_2.Value=Pos_1.Value;
Pos_3.Value=3.408E-03*Signal.Value - 2.012E+00;
Pos_4.Value=Pos_3.Value;
Pos_5.Value=2.083E-03*Signal.Value-1.646E+00;
```

Valve Opening (A_0) – Logics to Prevent Errors

Similar logics were used for all the steam admission valves and so only one valve will be shown here.

```
//Valve 1
if (Pos_1.Value<0)
  {
```

```
    Pos_1.Value=0;
  }
else
  {
    if (Pos_1.Value>1)
      {
       Pos_1.Value=1;
      }
    else
      {
        Pos_1.Value= Pos_1.Value;
        }
  }
```

Valve Opening (A_0) – A_0 Values

```
Valve_1.Value=Math.Pow(Pos_1.Value, (2.0));
Valve_2.Value=Math.Pow(Pos_2.Value, (2.0));
Valve_3.Value= Math.Pow(Pos_3.Value, (2.0));
Valve_4.Value=Math.Pow(Pos_4.Value, (2.0));
Valve_5.Value=Math.Pow(Pos_5.Value, (2.0));
```

Appendix C. Equations for Signal Oil Pressures

The following table may be utilised in order to estimate the signal oil pressure required in order to achieve the correct feedwater mass flow rate at percentage load "x" ("x" ranges from 0 to 1).

Table 7.1: Equations for Estimating Signal Oil Pressure vs Load for Different Configurations

DCS stroking, CRH			
Mode 1	V4, CRH controlling	1270 ≥ p > 1000	$y = 3.099E+03x^2 - 2.625E+03x + 1.719E+03$
Mode 2	V2, V3, V4, CRH controlling	1000 ≥ p > 780	$y = 1.514E+06x^2 - 1.112E+06x + 2.050E+05$
Mode 3	V2,V3,V4 controlling	780 ≥ p > 640	$y = 2.667E+04x^2 - 2.427E+04x + 6.073E+03$
Mode 4	V1,V2,V3,V4 controlling	640 ≥ p	$y = 2.045E+03x^2 - 2.804E+03x + 1.414E+03$
DCS stroking, no CRH			
Mode 1	V4 controlling	1270 ≥ p > 1000	y = -2.111E+04x + 7.952E+03
Mode 2	V2,V3,V4 controlling	1000 ≥ p > 640	$y = 4.063E+04x^2 - 3.453E+04x + 7.952E+03$
Mode 3	V1,V2,V3,V4 controlling	640 ≥ p	$y = 2.045E+03x^2 - 2.804E+03x + 1.414E+03$
Design stroking, CRH			
Mode 1	CRH controlling	1270 ≥ p > 883	$y = 2.962E+03x^2 - 2.545E+03x + 1.706E+03$
Mode 2	V3,V4,CRH controlling	883 ≥ p > 780	y = -2.000E+04x + 7.789E+03
Mode 3	V1,V2,V3,V4 controlling	780 ≥ p > 590	y = -1.000E+03x + 1.139E+03
Mode 4	V1,V2 controlling	590 ≥ p > 200	$y = 5.429E+02x^2 - 7.573E+02x + 9.702E+02$
Design stroking, no CRH			
Mode 1	V3,V4 controlling	883 ≥ p > 775	$y = 1.659E+04x^2 - 1.277E+04x + 3.226E+03$
Mode 2	V1,V2,V3,V4 controlling	775 ≥ p > 590	$y = 5.429E+02x^2 - 7.573E+02x + 9.702E+02$

Appendix D. Data from Heat Balance Diagrams for Station A1

This appendix provides heat balance data for Station A1, used for model development.

Table 7.2: Summary of Main Heat Balance Diagrams for Station A1

			Steam side					Feedwater side	
			IP BS	CRH	Steam supply to BFPT	To BFPT condenser	From BFPT condenser	Pump suction	Pump discharge
100% without reheat spraywater (dwg [redacted]66)	Pressure	*bar*	12.13	41.07	N/S	0.048	0.0477	7.110	200.8
	Temperature	*°C*	377.7	334.0	N/S	32.0	32.0	140.9	144.8
	Enthalpy	*kJ/kg*	3213.2	3051.6	3213.2	2447.8	134.3	589.6	622.8
	Mass flow rate	*kg/s*	N/A	N/A	16.668	16.668	16.668	501.027	501.027
	Steam quality	*kg/kg*	1	1	1	0.954	0	0	0
100% with reheat spraywater (dwg [redacted]67)	Pressure	*bar*	12.13	41.07	N/S	0.048	0.0477	7.110	223.4
	Temperature	*°C*	373.9	334.0	N/S	32.0	32.0	141.9	145.2
	Enthalpy	*kJ/kg*	3205.0	3051.6	3205.0	2443.5	134.3	597.5	626.0
	Mass flow rate	*kg/s*	N/A	N/A	18.746	18.746	18.746	502.525	491.438
	Steam quality	*kg/kg*	1	1	1	0.952	0	0	0
80% (dwg [redacted]68)	Pressure	*bar*	9.81	33.08	N/S	0.04	0.0403	6.380	203
	Temperature	*°C*	374.8	324.7	N/S	29.1	29.1	134.5	137.7
	Enthalpy	*kJ/kg*	3211.2	3049.0	3211.2	2465.9	121.9	565.5	592.9
	Mass flow rate	*kg/s*	N/A	N/A	14.610	14.610	14.610	402.889	399.193
	Steam quality	*kg/kg*	1	1	1	0.964	0	0	0

			Steam side					Feedwater side	
			IP BS	CRH	Steam supply to BFPT	To BFPT condenser	From BFPT condenser	Pump suction	Pump discharge
60% (dwg [redacted] 69)	Pressure	*bar*	7.39	24.81	N/S	0.036	0.036	5.620	188.5
	Temperature	*°C*	370.0	314.8	N/S	27.2	27.2	125.0	128.6
	Enthalpy	*kJ/kg*	3205.4	3046.8	3205.4	2498.6	113.8	525.1	553.8
	Mass flow rate	*kg/s*	N/A	N/A	11.954	11.954	11.954	296.968	296.968
	Steam quality	*kg/kg*	1	1	1	0.979	0	0	0
45 % (dwg [redacted]70)	Pressure	*bar*	5.68	19.13	N/S	0.033	0.0332	5.080	180.2
	Temperature	*°C*	364.1	308.0	N/S	25.8	25.8	116.6	121.4
	Enthalpy	*kJ/kg*	3196.2	3046.0	3196.2	2537.8	108.1	489.6	528.4
	Mass flow rate	*kg/s*	N/A	N/A	11.628	11.628	11.628	227.987	227.987
	Steam quality	*kg/kg*	1	1	1	0.996	0	0	0

Notes on Table 7.2:

1. The temperature of the steam to the BFPT condenser was calculated using steam tables as the saturation temperature corresponding to the given pressure.
2. The steam quality to the BFPT condenser was calculated from the provided pressure and enthalpy.
3. The enthalpy of the condensate was calculated as the liquid enthalpy (i.e. x=0) at the condenser pressure.
4. Grey highlighted cells have unclear values on the diagram.
5. The feedwater mass flow rate values for the 80 % case have an uncertainty of ± 14 kg/s based on the legibility of the drawing.
6. The IP BS extraction point temperature was calculated from the given pressure and enthalpy using steam tables.
7. The suction pressure was taken as the DA steam supply pressure plus 3.3 bar (for the height of the DST).
8. The SFP discharge pressure was taken from the outlet of HP heater 6 in the absence of other values.
9. The BFPT condenser pressure is assumed to be the same as that of the cold condenser.
10. The reheat spraywater flow is zero for the cases shown except for the 100 % (TS 18 967) and 80 % (TS 18 968) cases. These have flow rates and enthalpies of 11.088 kg/s, 609.0 kJ/kg, 3.696 kg/s and 577.9 kJ/kg respectively.
11. All pressures are absolute.

Appendix E. Data from Heat Balance Diagrams for Station B1

This appendix provides heat balance data for Station B1 which, while not the station of interest in this study, is used for comparison in some respects.

Table 7.3: Summary of Main Heat Balance Diagrams for Station B1

			Steam side					Feedwater side	
			IP BS supply	CRH supply	Steam supply to BFPT	To BFPT condenser	From BFPT condenser	Pump suction	Pump discharge
600 MW	Pressure	*bar*	9.611	41.0	9.322	0.061	0.0607	9.130	195.1
	Temperature	*°C*	343.2	333.0	342.9	36.4	36.4	176.0	179.2
	Enthalpy	*kJ/kg*	3145.0	3049.2	3145.0	2417.3	152.4	745.3	769.3
	Mass flow rate	*kg/s*	N/A	N/A	17.694	17.694	17.694	505.179	505.179
	Steam quality	*kg/kg*	1	1	1	0.938	0	0	0
480 MW	Pressure	*bar*	7.668	32.45	7.438	0.05	0.0504	7.284	184.4
	Temperature	*°C*	344.8	322.6	344.6	33.0	33.0	166.6	169.5
	Enthalpy	*kJ/kg*	3152.3	3045.4	3152.3	2439.1	138.3	704.1	726.7
	Mass flow rate	*kg/s*	N/A	N/A	13.357	13.357	13.357	396.919	396.919
	Steam quality	*kg/kg*	1	1	1	0.949	0	0	0
360 MW	Pressure	*bar*	5.806	24.51	5.632	0.047	0.0465	5.516	178.5
	Temperature	*°C*	339.1	313.6	339.0	31.6	31.6	155.6	158.8
	Enthalpy	*kJ/kg*	3144.1	3044.6	3144.1	2467.7	132.4	656.3	680.6
	Mass flow rate	*kg/s*	N/A	N/A	11.461	11.461	11.461	297.831	297.831
	Steam quality	*kg/kg*	1	1	1	0.962	0	0	0
240 MW	Pressure	*bar*	4.021	17.05	3.901	0.045	0.0449	3.820	169.2
	Temperature	*°C*	304.9	301.4	304.8	31.0	31.0	142.0	146.6
	Enthalpy	*kJ/kg*	3077.4	3036.4	3077.4	2473.6	129.9	597.5	626.3
	Mass flow rate	*kg/s*	N/A	N/A	10.703	10.703	10.703	208.171	208.171
	Steam quality	*kg/kg*	1	1	1	0.965	0	0	0
180 MW	Pressure	*bar*	3.124	13.35	3.030	0.045	0.0448	2.967	165.9
	Temperature	*°C*	284.2	285.3	284.1	30.9	30.9	133.2	138.4
	Enthalpy	*kJ/kg*	3037.2	3010.7	3037.2	2479.6	129.6	559.8	593.0
	Mass flow rate	*kg/s*	N/A	N/A	10.606	10.606	10.606	163.576	163.576
	Steam quality	*kg/kg*	1	1	1	0.968	0	0	0

Notes on Table 7.3:

1. The pump suction pressure was not given so the pressure of the bled steam to DST was used. This will possibly be about 3 bar higher due to the height of the DST.
2. The temperature of the steam to the BFPT condenser was calculated as the saturation temperature corresponding to the given pressure.
3. Various other heat balance diagrams exist for miscellaneous loads but those shown in this table are the most important ones.
4. All pressures are taken as absolute.

Appendix F. Considerations of Optimum Turbine Blade Efficiency

It was stated previously that for optimal efficiency,

$$\Gamma \approx 2 \cdot (1 - R) \tag{105}$$

This follows from:

$$\rho_{opt} = \frac{\cos \alpha}{2(1 - R)} \tag{106}$$

The optimal ρ -value will be considered in more detail here so that the above equation's use may be justified.

This discussion is partially based on Church (1928) and Nag (2008).

Definitions Revised

In the preceding sections, the following dimensionless descriptors were defined:

$$R = \frac{\Delta h_{row,rotating}}{\Delta h_{stage}} = \frac{h_2 - h_3}{h_1 - h_3} \tag{107}$$

$$\rho = \frac{v_b}{v_2} \tag{108}$$

$$\psi = \frac{h_{02} - h_{03}}{{v_b}^2} = \frac{w}{{v_b}^2} \tag{109}$$

$$\phi = \frac{\sin \alpha}{\rho} \tag{110}$$

$$\Gamma = \Delta h_{stage(isentropic)} \cdot \left(\frac{\cos \alpha}{v_b} \right)^2 \tag{111}$$

General Assumptions

For the following scenarios, consider one stage with a reaction ratio R between 0 and 1. Assume perfect, frictionless nozzle behaviour of the blades, and perfect carry-over of velocity from the stationary row to the rotating row. Further, assume that v_1 is negligible and can be taken as zero.

The total energy available for the stage to convert into work is equal to the total static enthalpy drop over the stage, $h_1 - h_3$. In a pure impulse turbine, this enthalpy drop all occurs over the stationary row, and so the energy can be expressed as $\frac{v_2^2}{2}$. In a turbine with a non-zero reaction ratio, part of the nozzle effect is over the stationary blade and part is over the rotating blade. This may therefore be expressed with a fictitious v_3, as discussed in Section 2.3.2, derived from the total stage enthalpy drop. This may also be written as a function of reaction ratio, as shown below.

Stationary Row

From the definition of total (stagnation) enthalpy and reaction ratio:

$$h_1 + \frac{1}{2}\cdot v_1^2 = h_2 + \frac{1}{2}\cdot v_2^2 \therefore h_1 - h_2 = \frac{1}{2}\cdot\left(v_2^2 - v_1^2\right) \tag{112}$$

$$1 - R = \frac{h_1 - h_2}{h_1 - h_3} \therefore h_1 - h_2 = \left(1 - R\right)\cdot\left(\Delta h_{stage}\right) \tag{113}$$

Equating,

$$\Delta h_{stage} = \frac{v_2^2 - v_1^2}{2\cdot\left(1-R\right)} \therefore \Delta h_{stage} = \frac{v_2^2}{2\cdot\left(1-R\right)} \tag{114}$$

Case 1: Ideal Impulse Stage

With reference to Figure 7.2 and applying Euler's turbomachinery equation,

$$w = v_b\cdot\left(v_2\cos\alpha + v_3\cos\delta\right) = v_b\cdot\left(v_{2r}\cos\beta + v_b + v_{3r}\cos\gamma - v_b\right) \tag{115}$$

$$\therefore w = v_b\cdot\left(v_{2r}\cos\beta + v_{3r}\cos\gamma\right) \tag{116}$$

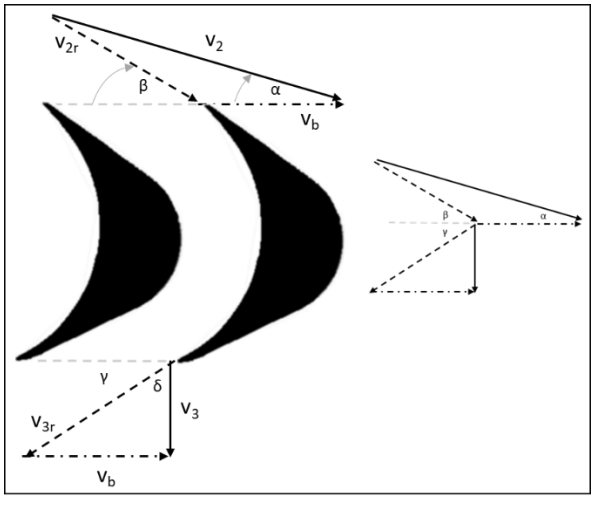

Figure 7.2: Typical velocity triangles for the impulse turbine case

Assuming symmetrical rotating blades, which is the norm for 0 % reaction stages, $v_{2r}\cos\beta = v_{3r}\cos\gamma$ and:

$$w = 2\cdot v_b \cdot \left(v_{2r}\cos\beta\right) = 2\cdot v_b \cdot \left(v_2 \cdot \cos\alpha - v_b\right) \tag{117}$$

Writing in terms of ρ,

$$w = 2\cdot {v_b}^2 \cdot \left(\frac{\cos\alpha}{\rho} - 1\right) \tag{118}$$

Applying R=0 to the equation (110):

$$\Delta h_{stage} = \frac{{v_2}^2}{2\cdot\left(1-R\right)} = \frac{{v_2}^2}{2} \tag{119}$$

Therefore the blade efficiency is:

$$\eta_{bl} = \frac{w}{\Delta h_{stage}} = \frac{2\cdot {v_b}^2 \cdot \left(\frac{\cos\alpha}{\rho} - 1\right)}{\frac{{v_2}^2}{2}} = 4\cdot\left(\rho\cdot\cos\alpha - \rho^2\right) \tag{120}$$

Differentiating with respect to ρ:

$$\frac{d\eta_{bl}}{d\rho} = 4\cdot\left(\cos\alpha - 2\cdot\rho\right) \tag{121}$$

Setting this derivative to zero,

$$\rho_{opt} = \frac{\cos\alpha}{2} \tag{122}$$

And

$$\eta_{bl(\max)} = 4\cdot\left(\rho\cdot\cos\alpha - \rho^2\right) = \cos^2\alpha \tag{123}$$

Axial Exhaust

Note that this result implies that δ = 90 °, which is expected for optimal efficiency. This is shown in the following equations.

From Euler's equation:

$$w = v_b \cdot \left(v_2\cos\alpha + v_3\cos\delta\right) \tag{124}$$

And in terms of blade efficiency:

$$w = \Delta h_{stage} \cdot \eta_{bl} = \frac{v_2^{\,2}}{2} \cdot \eta_{bl} \tag{125}$$

For optimal ρ:

$$w = \frac{v_2^{\,2}}{2} \cdot \cos^2 \alpha \tag{126}$$

Equating this to the Euler work:

$$v_b \cdot \left(v_2 \cos \alpha + v_3 \cos \delta \right) = \frac{v_2^{\,2}}{2} \cdot \cos^2 \alpha \tag{127}$$

Since

$$\rho = \frac{v_b}{v_2} = \frac{\cos \alpha}{2} \tag{128}$$

This becomes:

$$\frac{v_2^{\,2}}{2} \cdot \cos^2 \alpha + \frac{1}{2} \cdot v_2 \cos \alpha \cdot v_3 \cos \delta = \frac{v_2^{\,2}}{2} \cdot \cos^2 \alpha \tag{129}$$

Comparing the left- and right-sides, it is clear that δ = 90 ° and the absolute velocity at exhaust is axial.

<u>Case 2: Ideal (50 %) Reaction Stage</u>

With reference to Figure 7.3 and applying Euler's turbomachinery equation,

$$w = v_b \cdot \left(v_2 \cos \alpha + v_3 \cos \delta \right) = v_b \cdot \left(v_2 \cos \alpha + v_{3r} \cos \gamma - v_b \right) \tag{130}$$

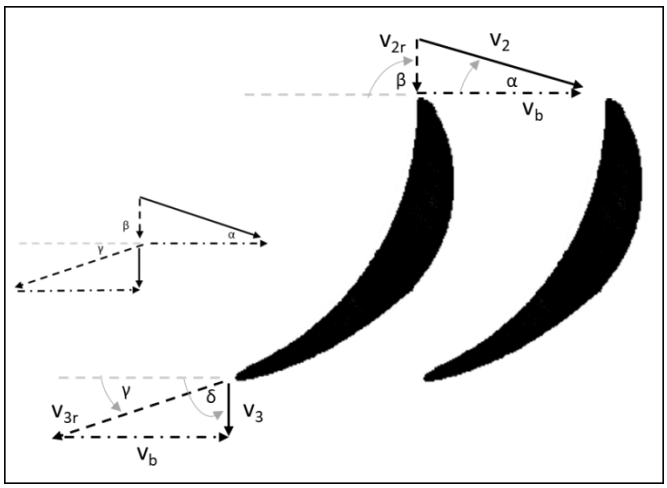

Figure 7.3: Typical velocity triangles for the 50 % reaction turbine case

Assuming symmetrical stationary and rotating rows, which is expected for 50 % reaction stages, $v_2 \cos\alpha = v_{3r} \cos\gamma$ and:

$$w = v_b \cdot \left(2 \cdot v_2 \cos\alpha - v_b\right) = v_2^{\,2} \cdot \left(2 \cdot \rho \cdot \cos\alpha - \rho^2\right) \tag{131}$$

Applying the same stage enthalpy drop equation as before but now setting R=0.5:

$$\Delta h_{stage} = \frac{v_2^{\,2}}{2 \cdot (1 - R)} = v_2^{\,2} \tag{132}$$

$$\eta_{bl} = \frac{w}{\Delta h_{stage}} = \frac{v_2^{\,2} \cdot \left(2 \cdot \rho \cdot \cos\alpha - \rho^2\right)}{v_2^{\,2}} = 2 \cdot \rho \cdot \cos\alpha - \rho^2 \tag{133}$$

Differentiating with respect to ρ:

$$\frac{d\eta_{bl}}{d\rho} = \left(2 \cdot \cos\alpha - 2 \cdot \rho\right) = 2 \cdot \left(\cos\alpha - \rho\right) \tag{134}$$

Setting this derivative to zero,

$$\rho_{opt} = \cos\alpha \tag{135}$$

And:

$$\eta_{bl(\max)} = \cos^2\alpha \tag{136}$$

Axial Exhaust

Note that this result implies that δ = 90 °, which is expected for optimal efficiency. This is shown in the following equations.

From Euler's equation:

$$w = v_b \cdot \left(v_2 \cos\alpha + v_3 \cos\delta\right) \tag{137}$$

And in terms of blade efficiency:

$$w = \Delta h_{stage} \cdot \eta_{bl} = v_2^{\,2} \cdot \eta_{bl} \tag{138}$$

For optimal ρ:

$$w = v_2^{\,2} \cdot \cos^2\alpha \tag{139}$$

Equating this to the Euler work:

$$v_b \cdot \left(v_2 \cos\alpha + v_3 \cos\delta\right) = v_2^{\,2} \cdot \cos^2\alpha \tag{140}$$

Since

$$\rho = \frac{v_b}{v_2} = \cos\alpha \tag{141}$$

This becomes:

$$v_2^{\,2} \cdot \cos^2\alpha + v_2 \cos\alpha \cdot v_3 \cos\delta = v_2^{\,2} \cdot \cos^2\alpha \tag{142}$$

Comparing the left- and right-sides, it is clear that δ = 90 ° and the absolute velocity at exhaust is axial in this case as well.

Case 3: Ideal Stage with Different Reaction Values

As noted above,

$$w = v_b \cdot \left(v_2 \cos\alpha + v_3 \sin\delta\right) \tag{143}$$

When considering a single stage, an axial exhaust is desirable as no whirl velocity is then wasted. This requirement is also consistent with the previous two cases as they both imply purely axial exhaust flow.

With an axial exit velocity, δ = 90 ° and the work expression simplifies to:

$$w = v_b \cdot \left(v_2 \cos\alpha\right) \tag{144}$$

Writing in terms of ρ,

$$w = \rho \cdot v_2^{\,2} \cdot \cos\alpha \tag{145}$$

The blade efficiency is then:

$$\eta_{bl} = \frac{w}{\Delta h_{stage}} = \frac{\left(\rho \cdot v_2^{\,2} \cdot \cos\alpha\right) \cdot \left(2 \cdot \left(1-R\right)\right)}{v_2^{\,2}} = 2 \cdot \rho \cdot \cos\alpha \cdot \left(1-R\right) \tag{146}$$

In the two extreme cases shown above, the maximum efficiency for each ideal stage is $\cos^2\alpha$, whether impulse or reaction. It is reasonable to expect the same maximum efficiency to be achieved at different R-values provided the correct ρ-values are set.

Thus:

$$\eta_{bl} = 2 \cdot \rho \cdot \cos\alpha \cdot \left(1-R\right) = \cos^2\alpha \Rightarrow \rho_{opt} = \frac{\cos\alpha}{2 \cdot \left(1-R\right)} \tag{147}$$

Implications

$$\rho_{opt} = \frac{\cos\alpha}{2\cdot(1-R)} \tag{148}$$

$$\Delta h_{stage} = \frac{v_2^{\,2}}{2\cdot(1-R)} = \frac{v_b^{\,2}}{\rho^2\cdot 2\cdot(1-R)} = \frac{v_b^{\,2}}{\left(\frac{\cos\alpha}{2\cdot(1-R)}\right)^2\cdot 2\cdot(1-R)} = 2\cdot(1-R)\cdot\frac{v_b^{\,2}}{\cos^2\alpha} \tag{149}$$

From the definition of Γ,

$$\Delta h_{stage} = \Gamma\cdot\frac{v_b^{\,2}}{\cos^2\alpha} \tag{150}$$

By comparison of these two equations, $\Gamma = 2(1-R)$

Similarly, applying the optimal ρ to the other dimensionless descriptors,

$$\phi = \frac{\sin\alpha}{\rho} = \frac{\sin\alpha}{\frac{\cos\alpha}{2\cdot(1-R)}} = 2\cdot(1-R)\cdot\tan\alpha = \Gamma\cdot\tan\alpha \tag{151}$$

$$\psi = \frac{w}{v_b^{\,2}} = \frac{\rho\cdot v_2^{\,2}\cdot\cos\alpha}{v_b^{\,2}} = \frac{\cos\alpha}{\rho} = \frac{\cos\alpha}{\frac{\cos\alpha}{2\cdot(1-R)}} = 2\cdot(1-R) = \Gamma \tag{152}$$

Note that although for these circumstances they are equal, Γ and ψ are definitionally different parameters and so it was convenient to write all these expressions in terms of Γ.

More generally, if δ ≠ 90 °, then:

$$\psi = \frac{w}{v_b^{\,2}} = \frac{\cos\alpha}{\rho} + \frac{v_3\cos\delta}{v_b} = \Gamma + \frac{v_3\cos\delta}{v_b} \tag{153}$$

Summary

For ideal stages, considered in isolation, the following relationships may be applied:

$$\Gamma = 2\cdot(1-R) \tag{154}$$

$$\rho = \frac{\cos\alpha}{\Gamma} \tag{155}$$

$$\psi = \Gamma = 2\cdot(1-R) \tag{156}$$

$$\phi = \Gamma\cdot\tan\alpha \tag{157}$$

Figure 7.4 illustrates the effect of changing reaction ratio on these parameters for an ideal stage with α set to 20 °.

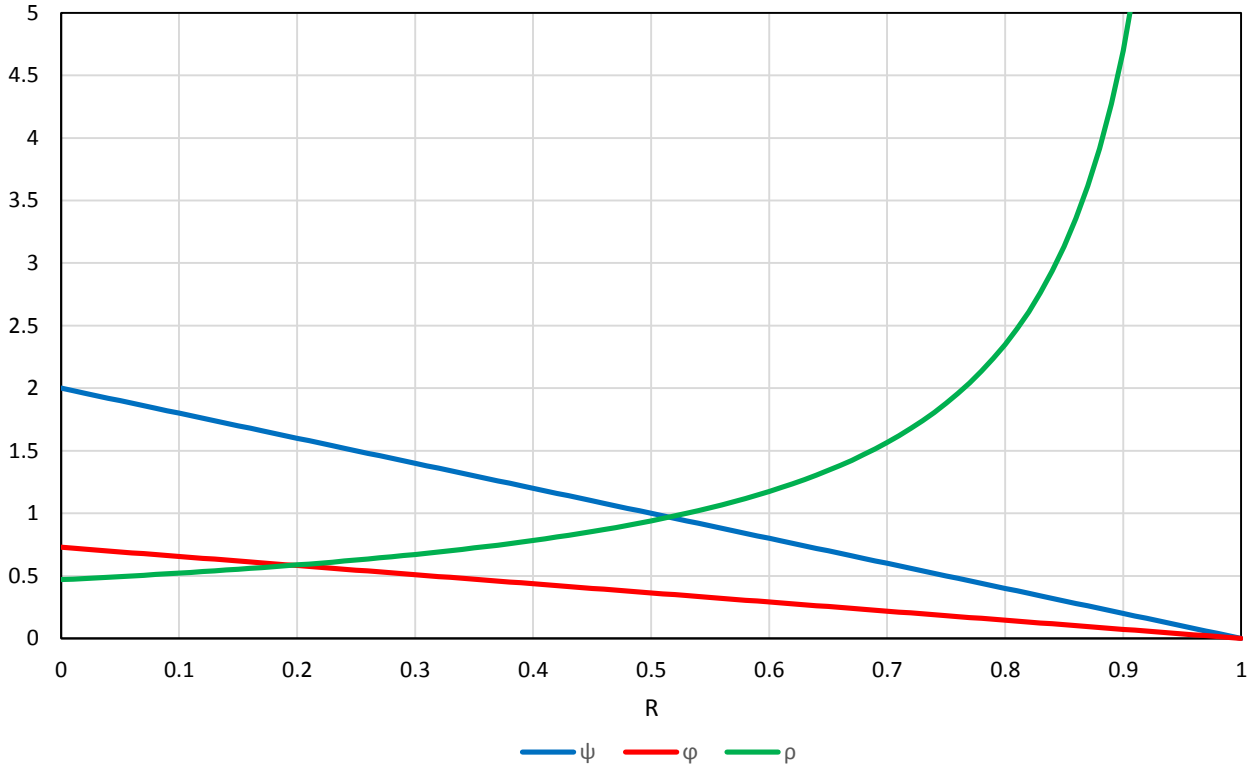

Figure 7.4: Dimensionless descriptors for ideal stages with α = 20 °

Appendix G. Orifice Plate Theory and Modelling of Leak-Off Valves

Orifice Plate Theory

The following discussion is based on the text "Experimental Methods for Engineers" by Holman (2001). Applying Bernoulli's equation and mass flow continuity, the volumetric flow rate of an incompressible fluid through an ideal orifice can be expressed as follows:

$$Q = \frac{A_2}{\sqrt{1-\left(\frac{A_2}{A_1}\right)^2}} \cdot \sqrt{\frac{2}{\rho}\left(p_1 - p_2\right)} \tag{158}$$

To account for real effects, a discharge coefficient C is applied such that:

$$C = \frac{Q_{actual}}{Q_{ideal}} \tag{159}$$

C may be determined from empirical correlations, noting the following definitions:

- Velocity of approach factor: $M = \frac{1}{\sqrt{1-\left(\frac{A_2}{A_1}\right)^2}}$
- Flow coefficient: $K = C \cdot M$
- Diameter ratio: $\beta = \frac{d}{D} = \sqrt{\frac{A_2}{A_1}}$

C is a function of Reynolds number ($\mathrm{Re}_D = \frac{\rho \cdot \bar{v} \cdot D}{\mu}$) as well as β. It is typically in the range 0.6 to 0.85, as illustrated in Figure 7.5 (Holman, 2001).

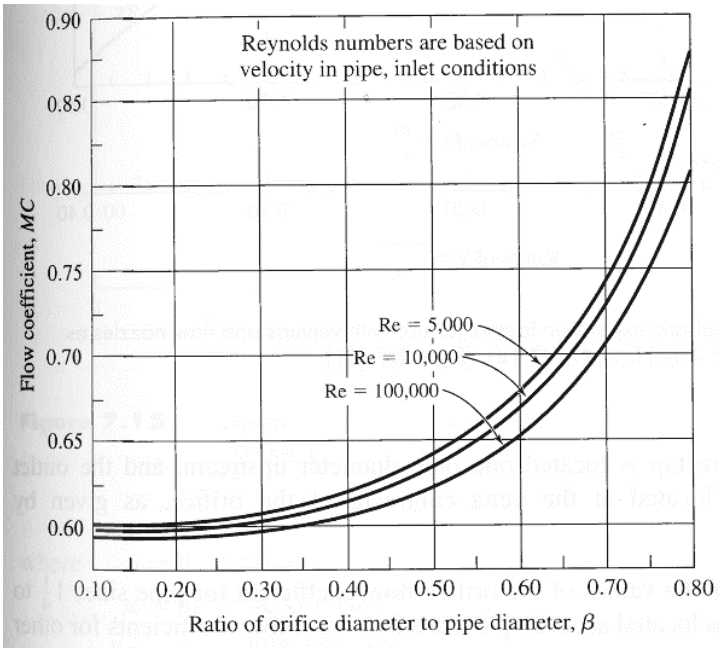

Figure 7.5: Empirical correlation for loss coefficient on orifices for 1.25'' < D < 3.00" (Holman, 2001)

Applicable Standard

Standard BS EN ISO 5167, Part 2 (2003), "Measurement of fluid flow by means of pressure differential devices" will be considered here as in general stations A1 and A2 were built according to British standards.

This standard expresses the mass flow rate, q_m, as follows:

$$q_m = \frac{C}{\sqrt{1-\beta^4}} \cdot \varepsilon \cdot \frac{\pi}{4} \cdot d^2 \sqrt{2 \cdot \Delta p \cdot \rho_1} \qquad (160)$$

This is equivalent to the equation introduced previously, multiplied by density in order to obtain mass flow rate, with the addition of an expansibility factor ε , which will be taken as 1 for an incompressible fluid. The discharge coefficient is obtained through use of the Reader-Harris/Gallagher (1998) equation, which depends on the diameter ratio, β, the Reynolds number with reference to the pipe diameter, Re_D, and the tapping arrangements. For pipes with diameters not less than 71.12 mm:

$$C = 0.5961 + 0.0261 \cdot \beta^2 - 0.216 \cdot \beta^8 + 0.000521 \cdot \left(\frac{10^6 \cdot \beta}{Re_D}\right)^{0.7} + \left(0.0188 + 0.0063 \cdot A\right) \cdot \beta^{3.5} \cdot \left(\frac{10^6}{Re_D}\right)^{0.3}$$
$$+ \left(0.043 + 0.080 \cdot e^{-10 \cdot L_1} - 0.123 \cdot e^{-7 \cdot L_1}\right)\left(1 - 0.11 \cdot A\right) \cdot \frac{\beta^4}{1-\beta^4} - 0.031 \cdot \left(M`_2 - 0.8 \cdot M`_2{}^{1.1}\right) \cdot \beta^{1.3}$$

(161)

Where:

$$A=\left(\frac{19000\cdot\beta}{\mathrm{Re}_D}\right)^{0.8} \quad (162)$$

$$M`_2=\frac{2\cdot L`_2}{1-\beta} \quad (163)$$

L_1 and $L`_2$ are defined according to three recognised tapping arrangements, as the ratio of upstream or downstream displacement of the tapping points to the pipe diameter:

For corner tappings, $L_1=L`_2=0$, for tappings at D and D/2, $L_1=1$, $L`_2=0.47$, and for a flange tapping configuration, $L_1=L`_2=\frac{25.4}{D}$, with D in mm.

Note that this correlation is only applicable for 0.1 ≤ β ≤ 0.75, 50 mm ≤ D ≤ 1000 mm and d ≥ 12.5 mm. There are also requirements with respect to minimum Reynolds numbers.

Orifice Plate on SFP Leak-Off Line

The pipe in which the orifice plate is located has the following characteristics:

1. Outer diameter: 168.3 mm (nominal bore of 150 mm).
2. Thickness: 7.11 mm

However, information about the orifice plate itself was not available.

Applying the operating conditions from the 45 % heat balance diagram, the Reader-Harris/Gallagher (1998) equation was applied for different values of β (the diameter ratio) for the three tapping cases – corner tappings (case i), D and D/2 tappings (case ii), and flange tappings (case iii). The results are shown in Figure 7.6. It is assumed here that based on the BS codes to which the station was built, BS EN ISO 5167 is applicable here.

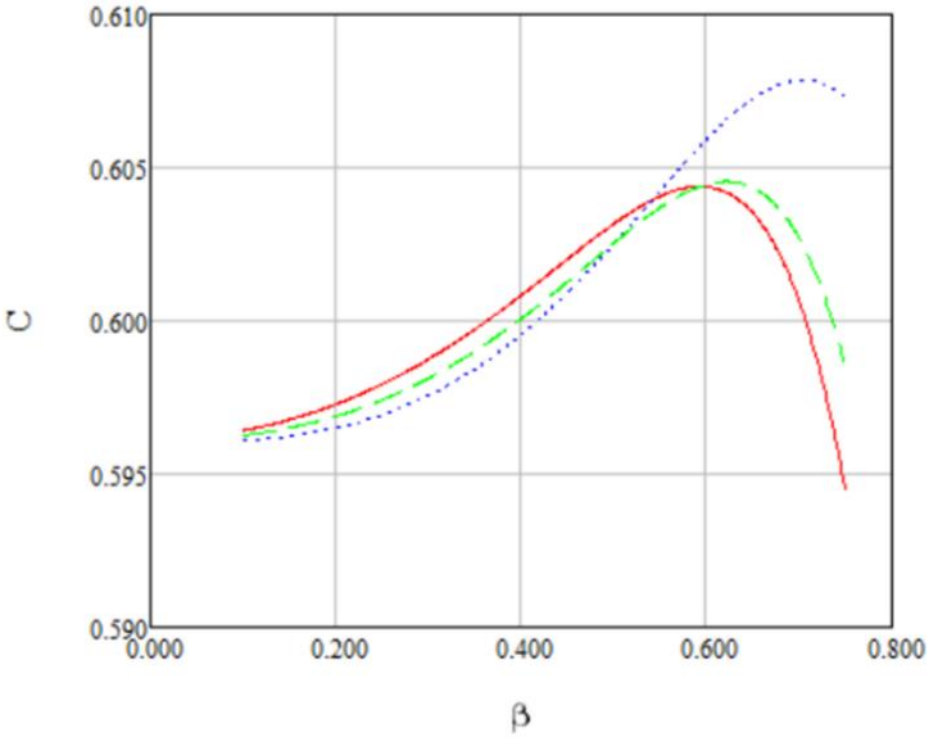

Figure 7.6: Station A1 discharge coefficient vs diameter ratio for SFP leak-off

It can therefore be seen that C ranges from about 0.595 to about 0.608 for the possible scenarios. In the absence of more detailed information, a C-value of 0.6 will be assumed. Re-arranging the equation introduced in Section 2.2.5, the required orifice diameter may be expressed as follows, relating the differential pressure to the flow rate measured.

$$d = D \cdot \left(\frac{C^2 \cdot \pi^2 \cdot D^4 \cdot \Delta p}{8 \cdot {Q_{FW}}^2 \cdot \rho_{FW}} + 1 \right)^{-\left(\frac{1}{4}\right)} \tag{164}$$

Assuming that Q_{FW} is 15 % of Q_{00} with Δp of 206 kPa, and utilising C=0.6, an orifice diameter of 89.03 mm is obtained. Applying this value, the following curve in Figure 7.7 is obtained, relating volumetric flow rate to differential pressure measured, through use of the following equation:

$$Q = \frac{C}{\sqrt{1-\beta^4}} \cdot \frac{\pi}{4} \cdot \beta^2 \cdot D^2 \sqrt{\frac{2 \cdot \Delta p}{\rho}} \tag{165}$$

A constant ρ was applied based on the 45 % heat balance pressure and temperature.

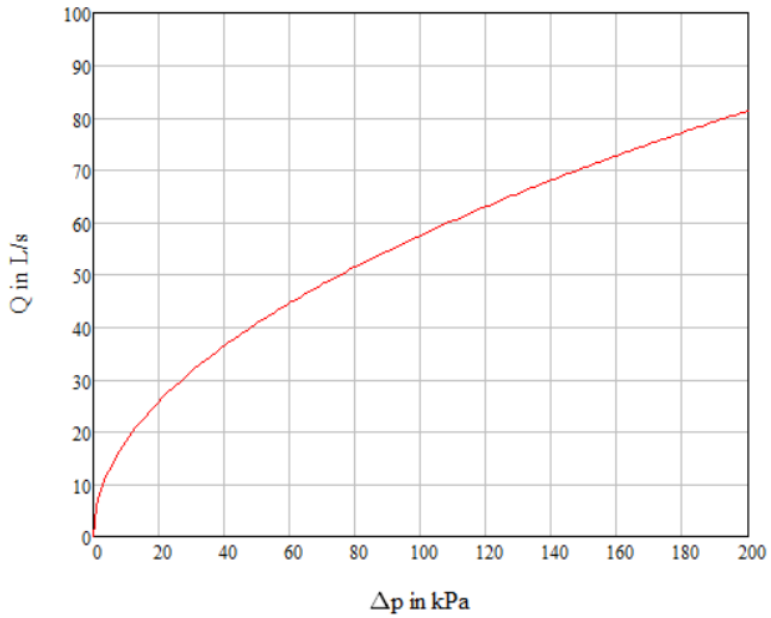

Figure 7.7: Graph illustrating Q vs Δp for Station A1 leak-off orifice plate

In the absence of information about the orifice plate, this exercise has allowed for the leak-off flow rate to be estimated from the available data from the DCS.

Appendix H. Boundary Conditions – Pump Discharge Pressure

Figure 7.8 illustrates measured (DCS) pump discharge pressures. Whereas the normal operation on 60 % to 100 % has an approximately linear relationship with load, this becomes more non-linear on the 30 % to 60 % range, becoming approximately constant below 40 %. Therefore it will not suffice to make this boundary condition linear.

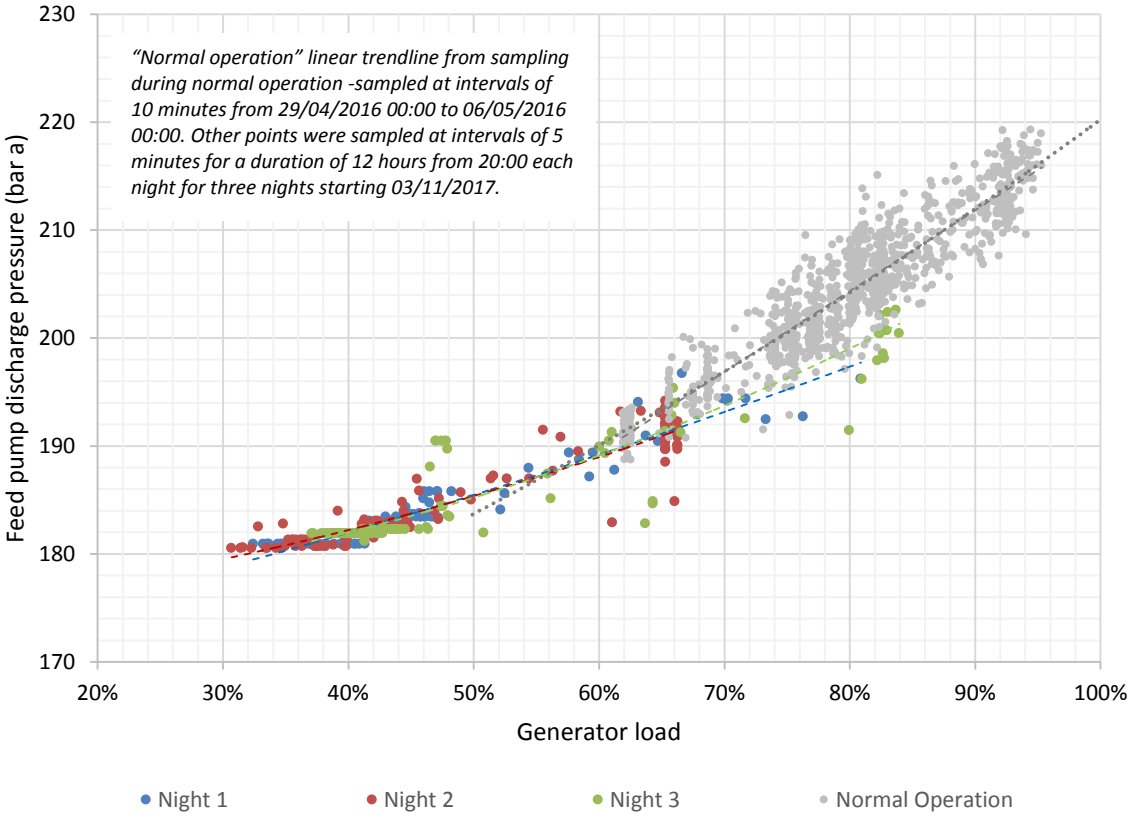

Figure 7.8: Chart of feed pump discharge pressure vs load during normal operation and low load tests

Figure 7.9 illustrates the digitised boiler resistance curve from the pump OEM. This may be represented with a trendline of the fifth order with a maximum deviation of 12 m head from the digitised plot, an acceptable correlation.

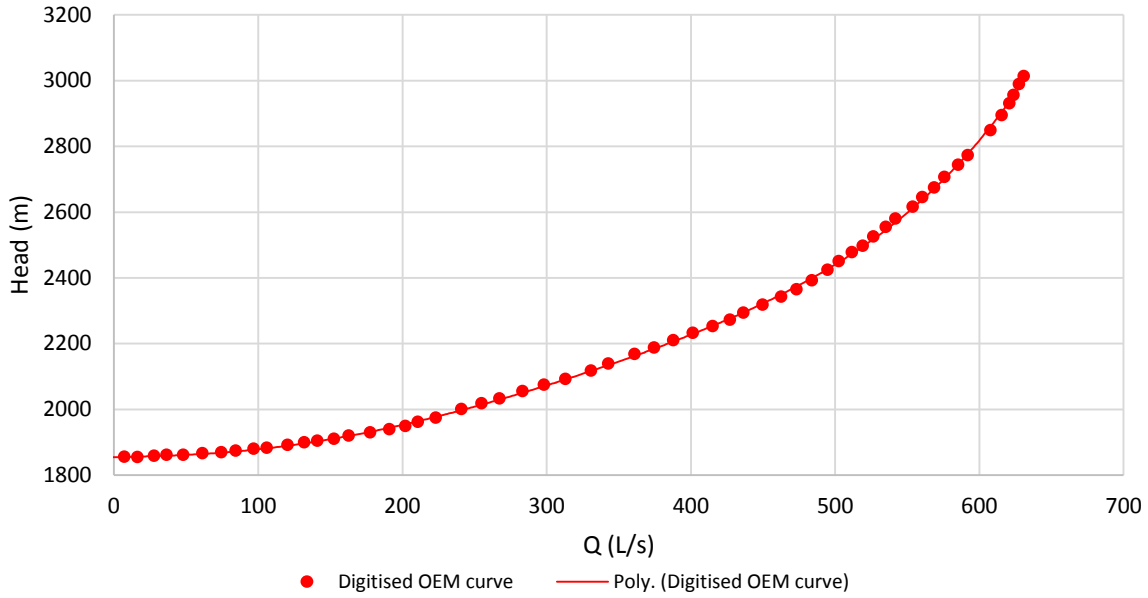

Figure 7.9: Boiler resistance curve from OEM

In Figure 7.10 this boiler resistance curve is converted to an approximate pressure vs generator load curve by applying the pump's reference density and utilising the linear correlation obtained for mass flow rate vs generator load. This neglects the possible effect of opening the leak-off valve at low loads. The mass flow rate is simply extrapolated to lower loads. It is observed that this differs significantly from the data points from the DCS and so the usefulness of this curve in predicting actual plant behaviour is questionable. The red curve is the quadratic trendline for all of the data points used in Figure 7.10. Its turning point is however to the right of the y-axis. Therefore to make this more realistic, the discharge pressure will be defined piecewise, with a quadratic expression above 40 % and a constant value below this.

Although the discharge pressure is a function of velocities through the boiler, with associated pressure losses increasing as the flow rate increases, it was considered practical for modelling purposes to represent the boundary condition as a static back pressure solely dependent on generator load.

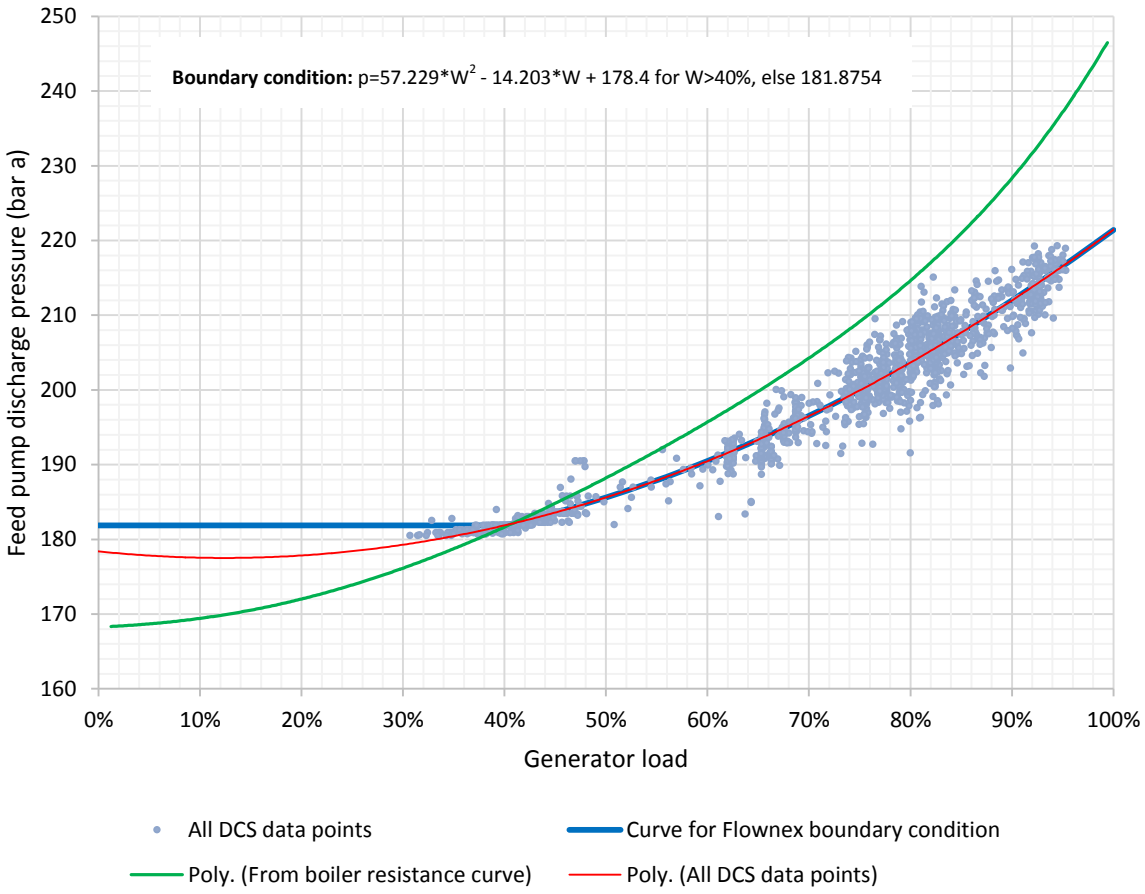

Figure 7.10: Feed pump discharge pressure vs generator load

Appendix I. Flow Resistance Component – Linear Characteristic

The linear characteristic was not used for any of the flow resistance components representing valves in the *Flownex* model. It is therefore discussed in this appendix.

The Moody diagram is shown in Figure 7.11 (Beck and Collins, n.d.).

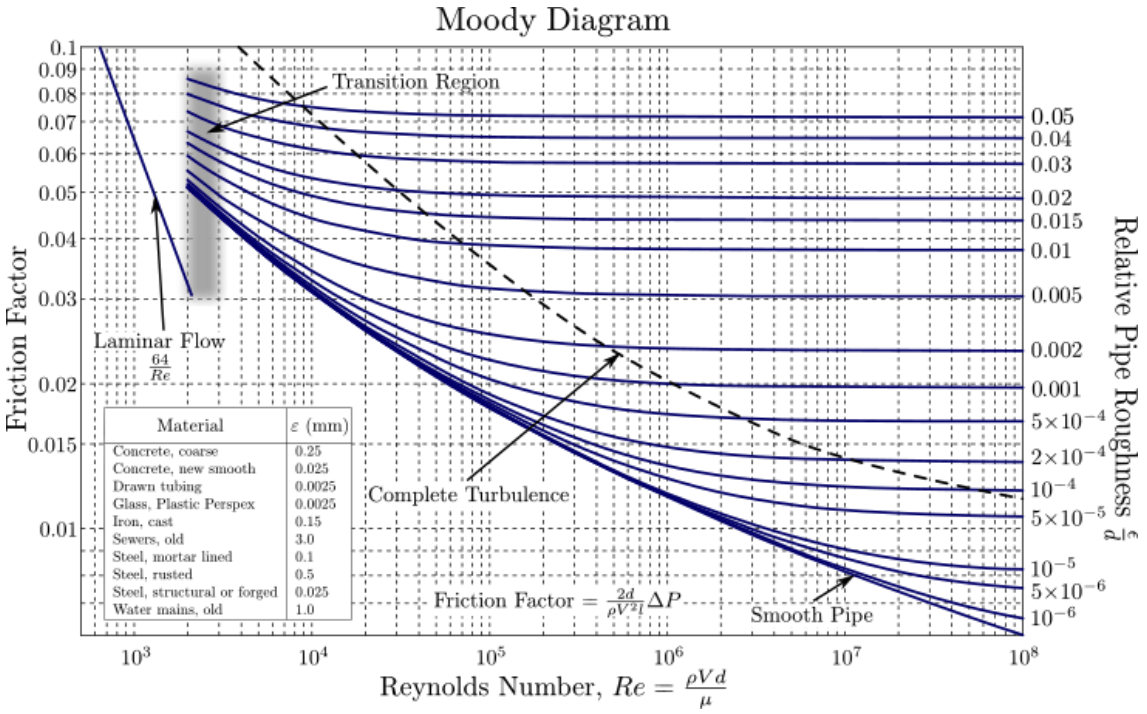

Figure 7.11: Moody diagram (Beck and Collins, 2012)

In general, the pressure drop over a valve can be expressed as follows, as noted previously:

$$\Delta p_{0L} = \left[\frac{1}{2}\cdot(f)\cdot\left(\frac{L}{D}\right)\cdot\left(\frac{1}{A^2}\right)\right]\cdot\left[\frac{1}{\rho}\cdot|\dot{m}|\cdot\dot{m}\right] \tag{166}$$

For laminar flow,

$$f = \left(\frac{64}{\mathrm{Re}}\right) \tag{167}$$

With

$$\mathrm{Re} = \frac{\rho\cdot\bar{v}\cdot D}{\mu} \tag{168}$$

Thus:

$$f = \frac{64 \cdot \mu}{\rho \cdot \overline{v} \cdot D} \tag{169}$$

Since

$$\dot{m} = \rho \cdot \overline{v} \cdot A \Rightarrow \overline{v} = \frac{\dot{m}}{\rho \cdot A} \tag{170}$$

The pressure drop may be represented as follows:

$$\Delta p_{0L} = \left[\left(\frac{64 \cdot \mu \cdot L}{D^2} \right) \left(\frac{1}{2 \cdot \rho \cdot A} \right) \right] \dot{m} \tag{171}$$

From this, it is clear that the assumption of laminar flow results in a linear valve characteristic.

The constant factor is again expressed in terms of A-coefficients as defined previously, so that:

$$\Delta p_{0L} = \left[\frac{1}{A_f \cdot A_{sf} \cdot A_o} \right] \cdot \dot{m} \tag{172}$$

Thus:

$$\left[\frac{1}{A_f \cdot A_{sf} \cdot A_o} \right] = \left[\left(\frac{64 \cdot \mu \cdot L}{D^2} \right) \cdot \left(\frac{1}{2 \cdot \rho \cdot A} \right) \right] \tag{173}$$

It is implied that the density is also constant.

Appendix J. Fleet Overview

Table 7.4 provides an overview of the most noteworthy features of the power stations in Eskom's fleet. *Due to confidentiality reasons, some content of this appendix can only be provided upon special request. Please contact the author or Study Leader.*

Table 7.4: Overview of Key Features of the Eskom Fleet

Station capacity (MW)	Units	Year[7]	Comments	Turbine OEM	Boiler operation mode	Cooling system	Feed pump configuration
2352	6	1974	See Note 1				
3600	6	1984					
2000	10	1976					
4116	6	1993					
1940	2	1985	See Note 2				
3000	6	1979	See Note 3				
3708	6	1990					
4110	6	2001					
3990	6	1993					
3600	6	1983					
3654	6	1990					
1510	8	1969	See Note 4				
1200	6	1977	See Note 5				
940	9	1966	See Note 6				
4788	6	In progress					
4800	6	In progress					

Notes for Table 7.4:

1: [redacted]

2: [redacted]

3: [redacted]

4: [redacted]

5: [redacted]

6: [redacted]

7: [redacted]

8: [redacted]

Key for Table 7.4:

Wet: Indirect wet cooling (natural draught towers)

Dry (CT): Indirect dry cooling (natural draught towers)

Dry (ACC): Direct dry cooling (forced draught ACCs)

OEM: Original Equipment Manufacturer

RTS: return to service

Table 7.5: Selection and Naming of Test Stations

Station capacity (MW)	Year	Unit size (average)	Fuel source	SFP?	Comments
			Coal	Yes	Low capacity units
			Coal	Yes	Station A2
			Coal	Yes	Low capacity units
			Coal	No	Station D
			Nuclear	Yes	Possibly include
			Coal	Yes	Station C
			Coal	Yes	Station B2
			Coal	No	No SFP
			Coal	No	No SFP
			Coal	Yes	Station B1
			Coal	Yes	Station A1
			Coal	No	No SFP; low capacity units
			Coal	Yes	Low capacity units
			Coal	No	No SFP; low capacity units
			Coal	No	No SFP
			Coal	No	No SFP

Table 7.6: Key Characteristics of Stations Considered

Station	Station / Unit capacity (MW)	Units	Year[8]	Boiler mode	Cooling system	Feed pump config.	T_{MS}[9] (°C)	p_{MS} (bar)	T_{RH}[10] (°C)	p_{RH} (bar)
A1					Closed loop with wet natural draught cooling towers	1 x 100 % SFP, 2 x 50 % EFP	535	161	535	37
A2							535	161	535	37
B1							535	160	535	36
B2							535	160	535	36
C							510	110	510	30
D						2 x 100 % SFP, 1 x 50 % EFP	286	69	N/A	N/A

[8] Year of commissioning completion
[9] Main steam
[10] (Hot) reheat steam

Appendix K. Relevant AKZ Signals for Station A1

Table 7.7 contains references of signals used from the data capture system for model development. This information will only be of value to the reader having access to Eskom data and wishing to expand upon this work. *Due to confidentiality reasons, some content of this appendix can only be provided upon special request. Please contact the author or Study Leader.*

Table 7.7: List of Relevant AKZ Numbers for DCS Signals for Station A1

AKZ number from P&ID	Signal on PGIM system for Unit [redacted]	Signal description (PGIM)
Misc.		
		GEN LOAD
		EFP A MOTOR CURNT
		EFP B MOTOR CURNT
		BFPT SHAFT SPEED
Steam / Condensate Pressures		
		BFPT STM BEF LH ESPV PTX
		BFPT C R/H CV IN STM PTX
		BFPT C R/H STM SUP PTX
		BFPT STM AFT LH ESPV PTX
		BFPT STM AFT RH ESPV PTX
		BFPT DRN STM PTX
		BFPT NOZ BOX 4 STM PTX
		BFPT NOZ BOX 2 STM PTX
		BFPT NOZ BOX 3 STM PTX
		BFPT NOZ BOX 1 STM PTX
		BFPT COND PTX 1
		BFPT COND PTX 2
		BFPT COND PTX 3
		BFPT COND PRESS 2v3
Steam / Condensate Temperatures		
		BFPT STM BEF LH ESPV TCT
		BFPT C R/H STM SUP TCT
		BFPT CSG MDW MET TCT
		BFPT COND IN STM TCT
		BFPT COND HW TCT
Condensate Levels		
		BFPT COND LTX 1
		BFPT COND LTX 1
		BFPT COND LTX 2
		BFPT COND LTX 2
		BFPT COND LTX 3
		BFPT COND LTX 3
		BFPT COND LTX 2v3
FW Pressures		
		EFP A BP SUC PTX
		EFP A SUC STRN DPTX

		EFP A LEAK DETN PTX
		EFP B BP SUC PTX
		EFP B SUC STRN DPTX
		EFP B LEAK DET PTX
		SFP BP SUC PTX
		SFP SUC FLTR DPTX
		SFP L/DETN 1st CSG PTX
		EFP A MP DEL AFT NRV PTX
		EFP A MP DEL BFR NRV PTX
		EFP B MP DEL AFT NRV PTX
		EFP B MP DEL BEF NRV PTX
		SFP DEL AFT NRV PTX
		SFP DEL BEF NRV PTX
FW Temperatures		
		EFP A SUC TCT
		EFP A FW IN TCT
		EFP B SUC TCT
		EFP B FW IN TCT
		BFPT SUC TCT
		DA TO BFPT FW IN TCT
		SFP FW IN TCT
		EFP B FW OUTL TCT
		SFP FW OUTL TCT
FW Flows		
		EFP A FW DISCH FTX 1
		EFP A FW DISCH FTX 1
		EFP A FW DISCH FLOW 2v3
		EFP A FW DISCH FTX 2
		EFP A FW DISCH FTX 2
		EFP A FW DISCH FTX 3
		EFP A FW DISCH FTX 3
		EFP A L/0 FTX
		EFP A L/O FTX CORR
		EFP B FW DISCH FTX 1
		EFP B FW DISCH FTX 1
		EFP B FW DISCH FLOW 2v3
		EFP B FW DISCH FTX 2
		EFP B FW DISCH FTX 2
		EFP B FW DISCH FTX 3
		EFP B FW DISCH FTX 3
		EFP B L/O FTX
		EFP B L/O FTX CORR
		SFP DISCH FW FTX 1
		SFP DISCH FW FTX 2v3
		SFP DISCH FW FTX 2
		SFP DISCH FW FTX 3
		SFP L/O FTX

Control Signals		
		SFP LH ESPV TRP CYL PTX
		SFP RH ESPV TRP CYL PTX
		BFPT GOV SIG AIR PTX
		BFPT GOV ACT
		BFPT SHAFT SPEED
		BFPT SHAFT SPEED WINDOW
		SFP FW FLOW CONTROL
		BFPT GOV POS
		BFPT SENS OIL NOZ PTX
		BFPT ST/UP VLV CALC POS
		BFPT PWR OIL SUP PTX
		BFPT PWR OIL DMP VLV PTX
		BFPT PWR OIL FLTR DPTX
		BFPT BARGR MTR SPEED
		BFPT PWR OIL RES PTX

Table 7.8: List of EtaPro Servers

Server address	Station

Appendix L. Lists of Reference Drawings

Table 7.9, Table 7.10, and Table 7.11 contain references of drawings used from station manuals for model development. This information will only be of value to the reader having access to Eskom data and wishing to expand upon this work. *Due to confidentiality reasons, the content of this appendix can only be provided upon special request. Please contact the author or Study Leader.*

Table 7.9: List of P&IDs for Station A1

Drawing reference number	Drawing title	Comment
		Feedwater side
		Feedwater side
		Feedwater side
		Feedwater side
		Feedwater side
		Steam side
		Steam side
		Steam side

Table 7.10: List of Rotor Drawings for Station A1/A2

Drawing reference number	Drawing title

Table 7.11: List of Pump Curves

Drawing reference number	Drawing title	Comment
		Station A1 EFPs
		Station A1 SFP booster pump
		Station A1 SFP main pump

Appendix M. General *Flownex* and *Mathcad* Notes

General lessons learnt / observations:

- Data transfer links must be set to transfer before/after each iteration. This is not the default setting. In general, scripts were set to be executed during steady state.
- Power matching: shafts were assigned to the gearbox within its own component window, and then the actual shaft components were each linked to a gearbox shaft; if this is not done, one can inadvertently assign speed ratios incorrectly. If the gearbox is set to calculate speed, it will adjust the reference shaft speed until the net power into the gearbox is zero. In other words, set up a gearbox with three "stubs", then set up three shafts. On each shaft, connect to the correct stub on the gearbox.
- Aesthetics: the colour "white smoke" was used as the fill colour for the blocks to denote different subsystems. Bends were used in the data transfer links in order to makes these lines neater. Disabling "snap to grid" also allowed for components to be better aligned. Coloured blocks were placed in front of data transfer links in order to make the model easier to read.
- Snaps are useful for loading conditions from an earlier run. However, parametric cases will stay in force when a new snap is loaded.
- A node which is a source on the boundary of a system will have a positive mass flow rate whereas a sink on a system boundary will have a negative mass flow rate. A node within a system where the flow in is equal to the flow out will have a mass flow rate of zero.

The following figures are useful shortcuts and functions in Mathcad.

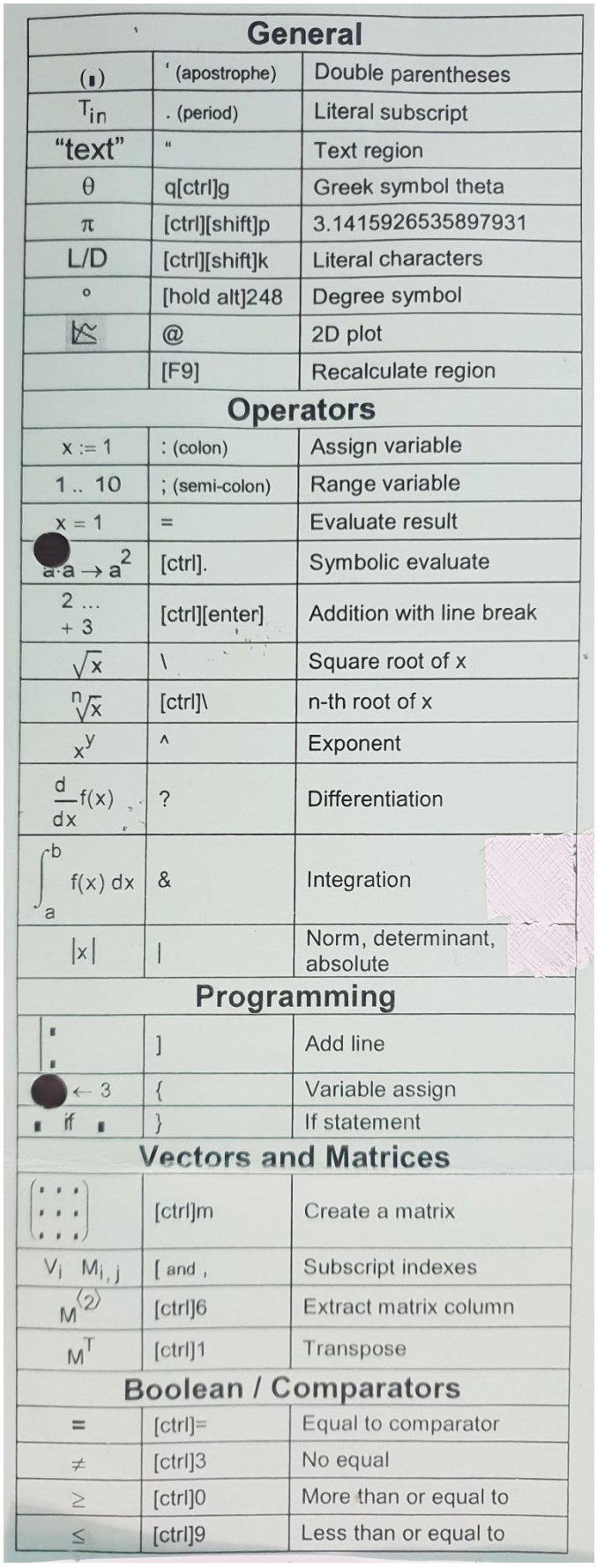

General		
(▮)	‘ (apostrophe)	Double parentheses
T_{in}	. (period)	Literal subscript
“text”	“	Text region
θ	q[ctrl]g	Greek symbol theta
π	[ctrl][shift]p	3.1415926535897931
L/D	[ctrl][shift]k	Literal characters
°	[hold alt]248	Degree symbol
	@	2D plot
	[F9]	Recalculate region
Operators		
x := 1	: (colon)	Assign variable
1 .. 10	; (semi-colon)	Range variable
x = 1	=	Evaluate result
$a \cdot a \rightarrow a^2$	[ctrl].	Symbolic evaluate
2 … + 3	[ctrl][enter]	Addition with line break
$\sqrt{x}$	\	Square root of x
$\sqrt[n]{x}$	[ctrl]\	n-th root of x
x^y	^	Exponent
$\frac{d}{dx} f(x)$	?	Differentiation
$\int_a^b f(x)\,dx$	&	Integration
$\lvert x \rvert$	|	Norm, determinant, absolute
Programming		
▮ ▮	]	Add line
← 3	{	Variable assign
▮ if ▮	}	If statement
Vectors and Matrices		
$\begin{pmatrix} ▮ & ▮ & ▮ \\ ▮ & ▮ & ▮ \\ ▮ & ▮ & ▮ \end{pmatrix}$	[ctrl]m	Create a matrix
V_i $M_{i,j}$	[and ,	Subscript indexes
$M^{\langle 2 \rangle}$	[ctrl]6	Extract matrix column
M^T	[ctrl]1	Transpose
Boolean / Comparators		
=	[ctrl]=	Equal to comparator
≠	[ctrl]3	No equal
≥	[ctrl]0	More than or equal to
≤	[ctrl]9	Less than or equal to

Figure 7.12: List of Mathcad *shortcuts*

Temperature [K] :	$T_{steam}(p, v, h, s)$	p, s, p+v, p+h, p+s, h+v, h+s, s+v
Pressure [Pa] :	$p_{steam}(T, v, h, s)$	T, s, T+v, T+h, T+s, h+v, h+s
Specific volume [m^3/kg] :	$v_{steam}(p, T, x, h, s)$	p+T, p+h, p+s, p+x, T+x, T+s, h+s
Density [kg/m^3] :	$\rho_{steam}(p, T, x, h, s)$	p+T, p+h, p+s, p+x, T+x, T+s, h+s
Enthalpy [J/kg] :	$h_{steam}(p, T, v, x, s)$	s, p+T, p+x, p+s, p+v, T+x, T+s
Entropy [J/kg*k] :	$s_{steam}(p, T, v, x, h)$	p+T, p+x, p+h, p+v, T+x, T+v, T+h
Internal energy [J/kg] :	$u_{steam}(p, T, v, x, h, s)$	p+T, p+x, p+h, p+s, p+v, T+x, T+v, T+h, T+s, h+s
Specific heat, isobaric [J/kg*K] :	$Cp_{steam}(p, T, v, x, h, s)$	p+T, p+x, p+h, p+s, p+v, T+x, T+v, T+h, T+s, h+s
Specific heat, isochoric [J/kg*K] :	$Cv_{steam}(p, T, v, x, h, s)$	p+T, p+x, p+h, p+s, p+v, T+x, T+v, T+h, T+s, h+s
Sonic speed [m/s] :	$w_{steam}(p, T, v, x, h, s)$	p+T, p+x, p+h, p+s, p+v, T+x, T+v, T+h, T+s, h+s
Quality [0-1] :	$x_{steam}(p, T, v, h, s)$	s, p+v, p+h, p+s, T+v, T+h, T+s, h+s
Phase number [-x to +x] :	$x'_{steam}(p, T, v, h, s)$	s, p+v, p+h, p+s, T+v, T+h, T+s, h+s
Phase state :	$state_{steam}(p, T, v)$	p+T+v
Dynamic viscosity [Pa/s] :	$\mu_{steam}(p, T, v, x, h, s)$	p+T, p+x, p+h, p+s, p+v, T+x, T+v, T+h, T+s, h+s
Thermal conductivty [W/m*K] :	$\lambda_{steam}(p, T, v, x, h, s)$	p+T, p+x, p+h, p+s, p+v, T+x, T+v, T+h, T+s, h+s
Surface tension [N/m] :	$\sigma_{steam}(p, T)$	p, T
Prandtl number :	$Pr_{steam}(p, T, x)$	p+T, p+x, T+x
Cp/Cv (isentropic expansion coeff):	$\gamma_{steam}(p, T, x)$	p+T, p+x, T+x

Figure 7.13: List of steam functions in Mathcad